Characterisation of Ovine and Human Vertebral Endplates using X-ray Microtomography: the Effects of Degeneration on Structure.

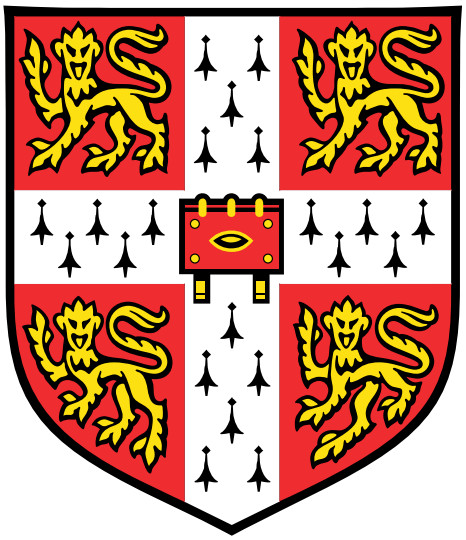

Sheen Gurrib

Department of Materials Science and Metallurgy
University of Cambridge

This dissertation is submitted for the degree of
Doctor of Philosophy

Hughes Hall

May 2020

"Mischief Managed!"
-Harry Potter

Declaration

This dissertation is the result of my own work and includes nothing which is the outcome of work done in collaboration except as specified in the text.

It is not substantially the same as any that I have submitted, or, is being concurrently submitted for a degree or diploma or other qualification at the University of Cambridge or any other University or similar institution except as declared in the Preface and specified in the text. I further state that no substantial part of my dissertation has already been submitted, or, is being concurrently submitted for any such degree, diploma or other qualification at the University of Cambridge or any other University or similar institution except as declared in the Preface and specified in the text.

In accordance with the Degree Committee of the Faculty of Physics and Chemistry, this dissertation does not exceed 60,000 words, including summary/abstract, tables, footnotes and appendices, but excluding table of contents, photographs, diagrams, figure captions, list of figures/diagrams, list of abbreviations/acronyms, bibliography and acknowledgements.

Sheen Gurrib
May 2020

Abstract

Thesis Title: Characterisation of Ovine and Human Vertebral Endplates using X-ray Microtomography: the Effects of Degeneration on Structure.

Name: Sheen Gurrib

Back pain is a significant and debilitating problem worldwide. It can be caused by several factors, but the cause of pain is only identified successfully in a minority of cases. There has been significant evidence indicating that the vertebral endplate (VEP) plays a major role in low back pain. The VEP balances two conflicting biophysical functions: providing both a nutritional pathway and mechanical support to the disc, therefore making it prone to damage. However, the VEP is still poorly characterised.

This thesis describes work undertaken to characterise the structure of normal and degenerative VEPs. Initially, ovine VEPs were used to investigate the effect of location along the spine on the structural properties of the VEP. Next, the network of canals within the VEP was characterised in terms of canal architecture, content and endings at the disc boundary. Finally, the effect of degeneration on the structural properties was investigated in human endplates.

Sheep spines were used as a model for the human spine to develop experimental protocols, due to similarities in their morphological and biomechanical features. A protocol was developed, using micro-computed tomography (micro-CT), for the structural characterisation of sheep VEPs. This is the first time that simultaneous assessment of different structural properties of the same VEP has been reported, allowing the comparison of structural features at different VEP locations on the same spine. The central region of the VEP was thinner than the periphery at all spinal levels and this could be explained by the increased biochemical exchange with the central nucleus pulposus of the disc and by the requirement of strong anchorage of disc fibres for mechanical support in the peripheral regions. Cranial VEPs were thicker, more porous and showed higher bone mineral density than their caudal counterparts. VEPs at different spinal levels also exhibited different structural properties. The thickest VEP measured was 1.010 ± 0.014 mm at the anterior region at cranial side of L5/L6 and the thinnest VEP was 0.455 ± 0.025 mm at the central region at caudal side of L3/L4.

A series of intricate 3D canal networks within the ovine VEP layer was analysed. These networks were found to connect the marrow spaces in the vertebra to the soft tissues of the disc. Evidence of the presence of blood within these canals was shown using photoacoustic imaging, and the ending of the vessels were identified as bud-like protrusions, emerging out of the VEP layer. The individual canals were characterised in terms of their length, cross-sectional diameter and orientation. A high density of canals perpendicular to the VEP surface and emerging out of the VEP boundary was seen in the central region, of up to 39 $\pm$ 8 canal openings / mm^2 for the caudal VEP at the spinal level L3/L4, providing further evidence for the increased nutritional exchange with the nucleus pulposus. This study is the first to characterise the structure of the individual canals, and simultaneously investigate the contents and the endings of these canals.

A novel approach was also developed for the comparison of the clinical assessments of disc degeneration, from magnetic resonance imaging (MRI) scans, to laboratory characterisation of the human VEP from micro-CT imaging, using samples from patients undergoing elective surgery. The results suggest that the hindered nutritional pathway within the VEP was more likely to be an initiating factor of disc degeneration, rather than the effect. The structural properties of the VEP were seen to change with levels of disc degeneration, assessed by Modic types, Pfirrmann grades and VEP erosion grades. The bone mineral density showed an increasing trend from Modic type I (0.108 $\pm$ 0.007 gcm^{-3}) to type III (0.139 $\pm$ 0.004 gcm^{-3}). The Pfirrmann grading system was found to be limited in its assessment of progressive degeneration, while advancing VEP erosion grades was correlated with increasing sizes of the canal openings on the VEP surface. The findings also showed that the sheep model, although useful for optimising testing protocols, was not a realistic representation of the human spine.

This body of work shows the importance of the VEP in maintaining the healthy functioning of the disc, given its key role in providing nutrition and mechanical support to the disc. Evidence is also provided to correlate spinal degeneration with structural changes in the VEP. Equipped with knowledge of the structure and functions of the VEP, it will be possible to identify the areas prone to damage and therefore the aetiology of degeneration can be clarified.

Acknowledgements

I would like to thank my supervisor, Prof Ruth Cameron, and my advisor, Prof Serena Best for their guidance through this new territory for us, and their constant support throughout this journey, even during the COVID19 pandemic! I would also like to acknowledge the Cambridge Malaysian and Commonwealth Studies Centre and the Currimjee Group in Mauritius for generously funding my studies.

I am grateful to all of the Cambridge Centre for Medical Materials PhD students and postdocs for their company and technical advice throughout my PhD. Special thanks goes to Dr Jennifer Shepherd for training me in X-ray micro-computed tomography. I would also like to thank Dr Malavika Nair for patiently debugging my messed up codes, Dr Joanne Kwon for being a universal problem solver, Dr Daniel Bax for his assistance with the ethics and collections of biological samples, Wayne Skelton-Hough for general lab matters and fireworks chat, and Anna Perkins for being so helpful at all times.

I would also like to thank Karin Newell and Dr Frances Henson from the Division of Trauma and Orthopaedic Surgery at the University of Cambridge for their generous supply of sheep spines. I am grateful to Prof Matthew Allen for kindly allowing me to use the blade saw at the Veterinary School, and for even helping me wipe the floor when the machine flooded! Special thanks to Alastair Houston for answering my numerous questions about the analysis software Simpleware.

Thank you to the wider collaboration team at Ipswich Hospital and Exeter University. Thank you to the orthopaedic surgeons Mr. David Sharp and Mr. Saaj Kaleel for their enthusiasm and expert advice throughout. Special thanks to Tom Marjoram for making sure sample sharing went smoothly and for patiently answering my basic clinical questions. To Fay Manning, thank you for the never ending chats to figure out the blood vessels, for being an amazing conference buddy and for the awesome time in Exeter.

The skills I learnt during my time at Oxford University have been indispensable for my PhD and I would also like to thank Prof Peter Nellist for inspiring me to pursue research, and Prof Jan Czernuszka for introducing me to the field of biomaterials.

I am also very grateful to my college Hughes Hall, the Cambridge Philosophical Society, The Bone Research Society, Armourers and Brasiers' Company and the British Association

of Spine Surgeons for their generous contributions, allowing me to present my work at several national and international conferences, in Japan, Germany, Belgium and the Netherlands.

My friends and family have been a constant source of support and I have been so lucky to have a collection of beautiful memories from my time at Cambridge. I would like to thank my Oxford ride-or-dies, Mehreen and Sabah. To Nabila, thank you for being such an inspiring and supportive friend, always only a phone call away. To LokYi, thank you for being on this OxBridge journey with me for the past eight years! Special shout out to my best friend Yashna, thank you for being my rock from across oceans! I would also like to thank the amazing humans I was lucky to spend the last four years with: Yasmin, Droper, Jamie, Isabella, Else, Sofia, Olivia. To the lads, Rob and Matt, thank you for the numerous McDonald's road trips and for generally making Cambridge a second home. Finally, to my parents and sister, thank you for making me believe that I can do anything and everything in life.

Table of contents

List of figures

List of tables

Chapter 1

Introduction

1.1 Context and Motivation

Chronic low back pain is the leading cause of disability around the world [1]. Up to 80% of adults will experience back pain at least once in their lifetime. However, back pain still remains difficult to diagnose and to treat [2]. It represents a huge financial burden globally due to lost days of work and the cost of treatments, which are often unsuccessful. With the acutely increasing rates of disability and associated research costs, there is an urgent need for further research to better understand the causes of low back pain [3].

Back pain is a condition that may result from ageing or from spinal diseases including: degenerative disc disease, lumbar disc herniation and osteoporosis. Degenerative conditions of the spine relate to the deterioration or break down of one or more intervertebral discs, causing pain and discomfort. However, the specific cause of most cases cannot be diagnosed and the understanding of the structural changes of the spine remains incomplete. The lumbar spine is made up of a combination of 33 vertebrae and 23 intervertebral discs. Each disc is constrained on both sides by the vertebral endplates (VEP), the main focus of this thesis. Whilst there is a very large body of research into the biomechanics and cellular structure of the normal and degenerate intervertebral discs [4–6], there is relatively limited understanding of the VEP, in particular in degenerative diseases of the spine, despite several reported evidence identifying the VEP as a source of chronic low back pain [3]. This is at a time when there are rapid and exciting developments of potential methods for the treatment of symptomatic degenerative disc disease, the efficacy of which will be dependent on a thorough knowledge of the function and the mechanical properties of the VEPs, which has not yet been acquired.

In order to provide targeted treatment to the source of back pain and to develop successful discal implants for the human body, it is crucial to first acquire a clear understanding of the complexities of the biomechanical demands of the VEPs.

1.2 Thesis Outline

This thesis will aim to investigate the structural properties of the VEP, the nutritional function of the VEP and the effect of disc degeneration on the VEP, as outlined below:

- Chapter 2 consists of a review of the existing literature relevant to the work in this thesis. A brief summary of the physiology of the lumbar spine and the endplates is included and the studies on the structure, functions and degenerations of the endplates are critically reviewed.
- Chapter 3 investigates the structural properties of the endplates with respect to their location along the spinal levels, their position and side with respect to the disc. This was carried out using a micro-computed tomography X-ray scanner and a sheep model. The structure of the VEP was characterised by its thickness, porosity, bone mineral density and curvature. Furthermore, the relationship with the epiphyseal ring and the underlying trabecular bone was also investigated.
- Chapter 4 focuses on the isolation and characterisation of the 3D canal network present within the endplate layer, acting as a nutritional pathway to the avascular disc. The canal network was quantitatively characterised and the presence of blood within the network was investigated. Furthermore, the nature of the endings of these canals at the disc boundary with the endplate was investigated.
- Chapter 5 investigates the effect of different degrees of disc degeneration on the structure of the endplate and its nutritional pathway. This was carried out using samples obtained from patients undergoing spinal surgeries, enabling the correlation of laboratory findings with clinical observations. The validity of the sheep model for spinal investigations was also explored.
- Chapter 6 summarises the main findings of this thesis and identifies the main avenues for future investigations of the endplate's role in chronic back pain.

Chapter 2

Literature Review

2.1 Introduction

This literature review chapter aims to provide an overview of the anatomical and structural properties of the healthy vertebral endplates (VEPs), their interaction with the surrounding disc and vertebra, as well as the effect of changes due to ageing and pathological degeneration.

2.2 Chronic Low Back Pain

There is considerable information about the prevalence and incidence of back pain but limited understanding of chronic back pain, partly due to the disagreement about definitions in the research community [7]. Chronic back pain is generally defined as back pain that persists longer than 7-12 weeks. Chronic back pain can also be defined as pain that is frequently recurring over a long period of time or pain that persists post normal healing period [8]. However, due to the lack of understanding of the underlying pathological causes for chronic low back pain, the diagnosis and therefore treatment, present a clinical challenge. This is why a combination of drugs, physical therapies and pain management treatment can be ineffective for some patients [2]. The different underlying pathologies involved and the effect of age on the prevalence of back pain will be discussed in more details in Section 2.7.

The prevailing understanding is that at the site of injury, trauma or degeneration in the spine, usually in or around the intervertebral disc, the free nerve endings of the nociceptors are activated. These sensory neurons then respond to the stimuli by sending "possible threat" signals to the central nervous system: the spinal cord and the brain, where the sensation of pain is registered and the pain is felt. However, there is growing interest and evidence identifying innervated or damaged VEPs as the initiation points for the pain pathway, which

will be discussed in more details in Section 2.7 [3]. Previously, the role of the VEP has been undrappreciated, especially by clinicians, because VEPs are poorly visualised on current diagnostic imaging tools.

Therefore, it is crucial to properly identify the source of the pain and the role of the VEP in the onset of low back pain to be able to offer the optimal treatment to patients.

2.3 The Lumbar Spine

Although pain can be felt anywhere along the spine, low back pain is most common and originates from the lumbar spine [7]. The lumbar region is often referred to as the lower back. This area is of key interest as it is shown to be a common site of intervertebral disc protrusion and other degenerative issues [9]. This is why, the focus of this thesis will be only on the lumbar region of the spine.

A brief description of the main anatomy and functions of the whole lumbar spine and its main components is necessary to understand the role of the VEP in the normal and degenerate conditions of the spine, as well as its interaction with the other components of the spine, such as the intervertebral disc and the vertebra.

2.3.1 Anatomy of the Lumbar Spine

The spine has a complex anatomy which is the combination of 33 vertebrae with only 23 intervertebral discs (there are no discs between the Atlas (C1), Axis (C2), and Coccyx areas of the spine) and multiple joints, tendons, ligaments, nerves, vascular supply and muscles which together play a major role in maintaining vital bodily functions [10]. The lumbar region of the spine is located between the thoracic and sacral regions and is made up of five moveable vertebrae, as seen in Figure 2.1. The vertebrae are numbered, from the top to the bottom, as L1 to L5. They are stacked on top of each other with the intervertebral discs in between each pair [11].

Fig. 2.1 Schematic of the human lumbar spine, showing the 5 levels labelled L1 to L5, the vertebral bodies and the discs with the surrounding bone parts which support and protect the spinal cord. [11]

The vertebrae are made up of 3 main functional components: the vertebral body, the pedicles and the posterior elements comprising the laminae and their spinous and transverse processes, as shown in Figure 2.2. The lumbar vertebrae have no rib facets and the outer shell of each vertebra is made of cortical bone, a dense and strong bony structure whereas the inside is made up of cancellous bone, a spongy and honeycomb-like structure. The cavities of the cancellous bone are filled with bone marrow [12].

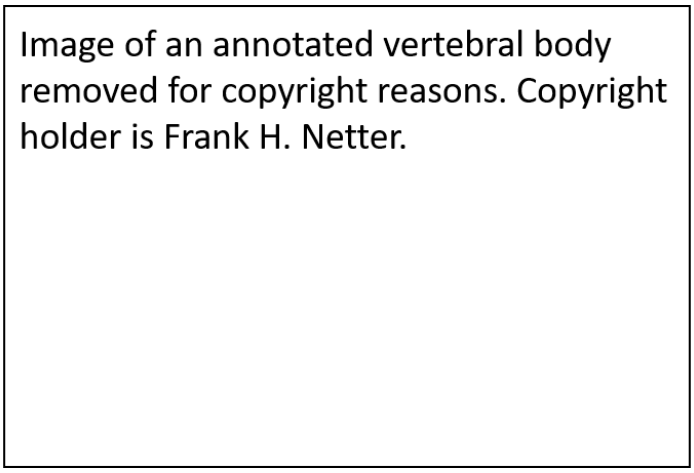

Fig. 2.2 Superior view of the vertebra showing the positions of the spinal processes and the pedicles. The schematic also highlights the shell structure of the cortical bone surrounding the sponge-like bone marrow of the main body of the vertebra. [11]

Each pair of vertebrae is separated by an intervertebral disc. The discs are the largest avascular structure in the body, approximately 7-10 mm thick [13, 14]. The complex structures of the discs are made up of a thick outer ring of fibrous cartilage, called the annulus fibrosus surrounding the nucleus pulposus, the gelatinous core [6]. The highly hydrated core is made of proteoglycan gel held tightly in a network of type-II collagen fibrils with a water content of 70-80 % [15] and is surrounded by 15-25 concentric lamellae of highly organised type-I collagen fibres [16]. The proteoglycan concentration and therefore the hydration content decrease radially from the core to the periphery whereas the collagen content increases in the same direction [17, 18].

The nucleus is constrained on both sides by the vertebral endplates, as shown in Figure 2.3, the focus of this project which will be discussed in further details in Section 2.4 of this chapter [3].

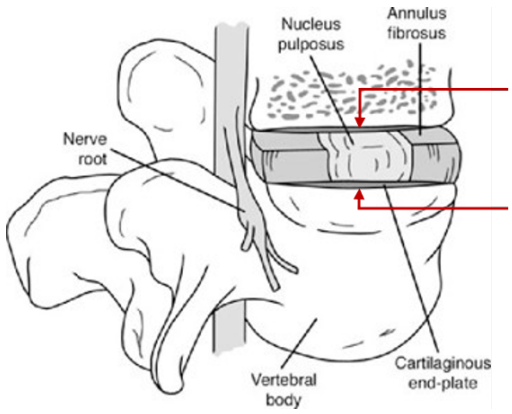

Fig. 2.3 Schematic of the cross section of a disc in between its two neighbouring vertebrae, showing the position of the endplate relative to the disc, as shown by the red arrows [14].

The endplate does not extend to the extremities of the annulus fibrosis, instead it is surrounded by a ring apophysis, a bony growth referred to as the epiphyseal ring, as shown in Figure 2.4 [19]. The epiphyseal ring is composed of slighty raised dense bone which overlaps with the external sides of the vertebral body and slants internally to fuse with the edges of the endplates [20]. Most previous research agree on the main function of the ring as an anchor for the fibres from the annulus fibrosus of the disc, providing mechanical stability [20–22]. However, the structural properties of the ring and the correlation with the morphology of surrounding structures still remain unclear.

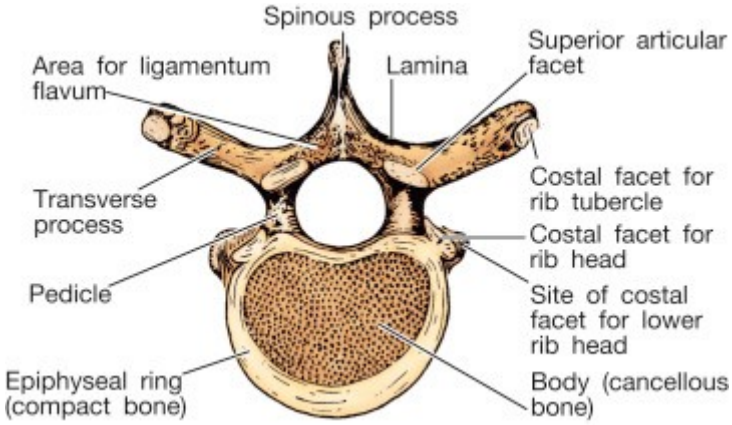

Fig. 2.4 Schematic of the anatomy of a vertebra showing the relative location of the epiphyseal ring. It is shown as a ring of compact bone encapsulating the top surface of the vertebra, made of cancellous bone [19].

2.3.2 Biomechanics of the Spine

The lumbar spine is inherently very strong. One of its main functions is to protect and support the spinal nerve roots and the very fragile spinal cord which regulate the exchange of messages from the brain to the rest of the body and from the body to the brain [23]. The spine is also responsible for mobility, flexion, extension and rotation of the body, which requires it to be very flexible [24, 25].

The vertebrae have very high compressive breaking load of 0.8-16 kN to enable them to carry and transmit the weight of the upper body while the body is vertical and in motion [26–28]. The intervertebral discs deform as a result of the loading process of the spine during daily activities, allowing the spine to move and flex. To do so, the nucleus undergoes compression while the annulus carries the tensile stresses, as shown in Figure 2.5. The nucleus has a high water content and together with the inner annulus experiences hydrostatic pressure when the disc is compressed [29, 30] while the lamellae present in the peripheral annulus experience tensile stresses to contain the fluid pressure [31, 29]. The annulus can deform to a considerable extent because the adjacent lamellae are loosely bonded together allowing them free motion and the collagen fibres can realign when they experience tension [32, 15]. The discs also transmit mechanical loads by dissipating the energy as heat and this process has been compared to the action of shock-absorbers [33]. The ultimate compressive strength of the nucleus pulposus of the disc has been reported to be 5.4-8.0 MPa [34, 35], while the tensile strength ranges from 1.5-7.8 MPa [5, 34, 36–38].

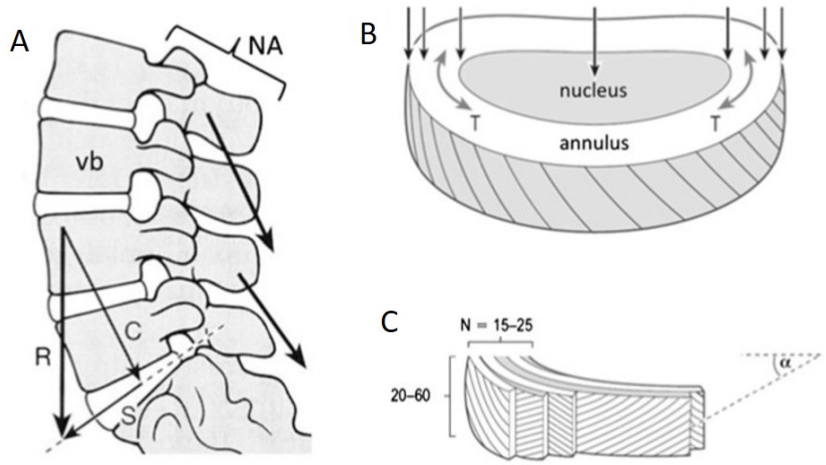

Fig. 2.5 Schematics showing the different forces experienced by different areas of the disc as a result of mechanical loading of the spine. (A) Forces acting on the vertebrae (vb) and the neural arches (NA) of the lumbar spine from gravity and from tension in the surrounding muscles are shown by the arrows. Spinal compression shown by the arrow C and shear, shown by S lead to a resultant force R acting on each disc during loading. (B) Compression of the disc causes an increase of the hydrostatic pressure of the disc, generating a tension (T) in the annulus. (C) Schematic showing the lamellae in the annulus, each made of 20-60 collagen fibres. [15]

2.4 The Vertebral Endplates

The endplate is described as a bilayer of cartilage and bone, which acts as a boundary between the vertebral bone and intervertebral disc. Endplates can be classified as cranial or caudal with respect to the intervertebral disc. Cranial endplates have the vertebra on top and the disc underneath whereas the caudal endplates have the disc on top and the vertebra underneath, when the spine is fully stretched vertically. From the earliest stage of the development of the skeleton in the foetus and throughout maturing of the spine, the cartilage endplates can be identified as discrete components. The cartilage endplate has a very similar chemical composition to the nucleus of the disc but with a more prominent complex network of type-II collagen fibrils [39]. There is also the presence of an ossification line in early stages of growth known as the growth plates which advances and fuses to form the bony endplate at the disc boundary once maturity is reached [40, 41].

The endplate is made of 3 main components: the cartilage region, the calcified cartilage region and the bony region, also referred to as the vertebral endplate (VEP) [33]. In the context of this thesis, the bony endplate will be referred to as the VEP. There has been considerable debate on whether the endplate should be considered as part of the disc or part

of the vertebra [33, 40]. Even though this distinction is not crucial for the understanding of the role of the endplate in the spine, it is imperative to distinguish the 3 components [42, 43]. Using histological studies, Lotz et al. showed the presence of a dense cartilage region (orange region) in between the disc (white region) and the osseous part of the VEP which has a similar structure to trabecular bone [3] as shown in Figure 2.6.

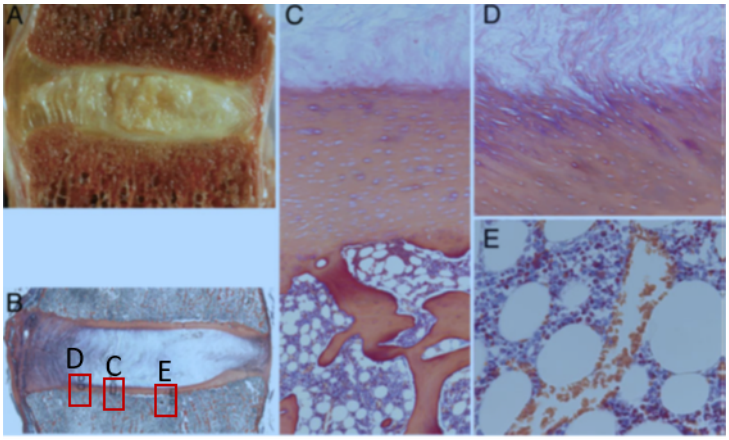

Fig. 2.6 The series of images show the presence of cartilage endplate between the disc and the bony endplate. A: Gross morphology of the intervertebral joint from human cadavers showing the disc in between two vertebrae. B: Histological representation of the sample in A, with the annotated locations of the regions of interest C, D and E. C: Cartilage endplate was shown in purple just underneath the disc tissues shown in white and osseous endplate was shown in orange, above the large pores of the trabecular bone in the vertebra. D: Discal fibres from the annulus pulposus are shown to embed in the cartilage endplate. E: The presence of vasculature is shown as pale brown, present in the bone marrow in the pores of the underlying trabecular bone [3].

The cartilage component of the endplate is similar to that of the articular cartilage, consisting of a hydrated extracellular matrix of proteoglycans, reinforced by a complex network of collagen fibrils (types I and II) [44]. This is illustrated in Figure 2.7. However, in the VEP the fibres are arranged horizontally parallel to the ends of the vertebra unlike the articular cartilage which has different zones with different fibre organisations [45]. Antoniou et al. reported that in a young healthy lumbar spine, the VEP cartilage has a proteoglycan content of approximately 300 μg / mg with 55 % percent water and 0.9 ng / mg of collagen fibrils [18].

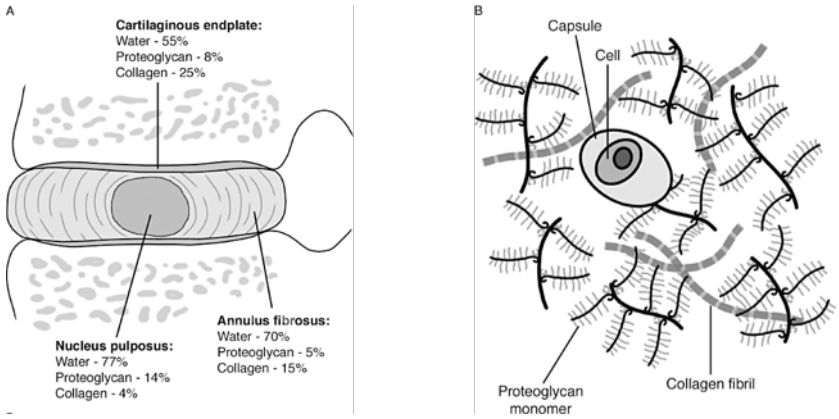

Fig. 2.7 A: Schematic showing the chemical structure of the intervertebral disc and the endplate. B: The proteoglycan aggregates present in the intervertebral disc responsible for maintaining tissue hydration [14].

The cartilage component itself is split up into the hyaline cartilage and the fibrocartilage. The hyaline part lies on the vertebral bone side whereas the fibrocartilage surrounds the nucleus pulposus. The fibrocartilage is the extension of collagen fibres from the annulus fibrosus and is replaced permanently by the hyaline cartilage with age [10]. The cartilage endplate is therefore indirectly connected to the vertebra via its osseous component but directly connected to the disc through the lamellae of annulus fibrosus, as shown in Figure 2.8 [46]. The osseous component resembles a dense layer of spongy trabecular bone, embedded with osteocytes [47].

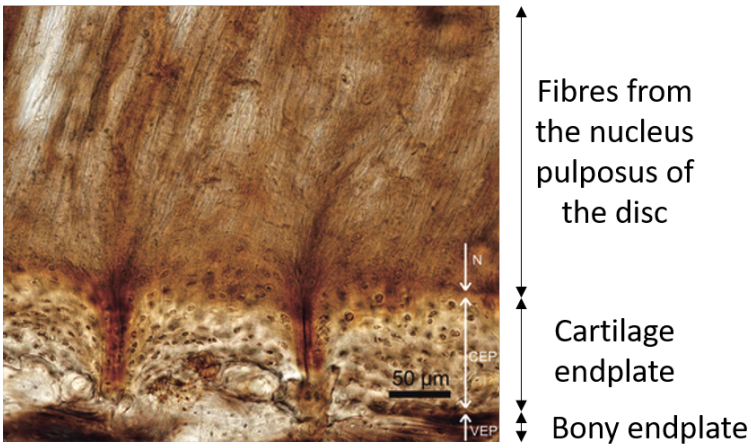

Fig. 2.8 The differential interference contrast optical microscopy (DIC) image shows how collagen fibrils in an ovine nucleus pulposus bind to the cartilage endplate and underlying bony component of the VEP [48]. The scale bar represent 50 μm

.

2.5 Structure of the Vertebral Endplates

Bone is currently characterised by a common set of histomorphometric parameters: bone volume, thickness of the bone area, thickness of the trabecular struts, separation of the trabecular struts, curvature of the endplate surface and bone density [49–52]. Given that the VEP is described as a layer of compact bone, the structure of the VEP can be defined by the thickness, porosity (bone volume), bone density and curvature of the VEP surface. These will be discussed further in this section by comparing previous findings from the literature.

2.5.1 Histomorphometric Properties

Thickness and Porosity

The VEPs are generally considered as thin layers of bone about 0.6-1.0 mm thick [53–56]. Thickness is minimal at the centre of the VEP and increases to its maximum at the periphery [4, 53, 57]. The thickness of the VEP also varies with the level (anatomical level in the spine) such that thickness is maximal at upper levels [58]. The central region of the VEP is more porous than the edges [13]. Histological experiments showed that the number and size of pores at the central region of the VEP are greater than at the peripheral regions with areas of the pore structures (5 ± 3) x10^5 μm^2 and (0.8 ± 0.6) x10^5 μm^2 in the central and peripheral groups, respectively, as shown in Figure 2.9 [56].

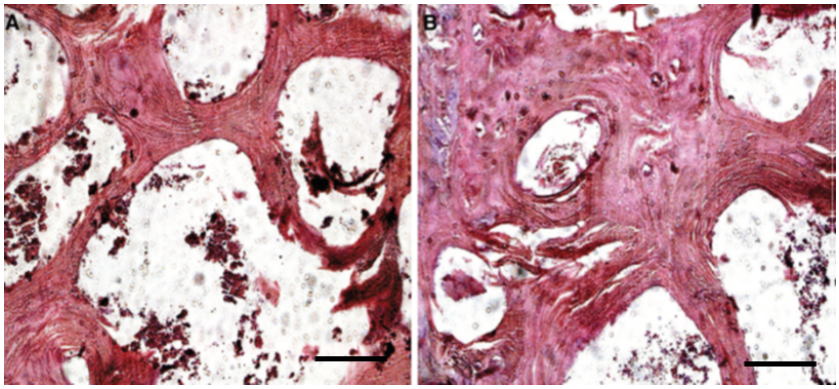

Fig. 2.9 Histological images from cadaveric human samples using haematoxylin and eosin staining show the differences in porosity and pore structures at different locations of the VEP The bone is stained in pink. A:The central region of the endplate showed several large pores, with thinner bone cortex. B: Smaller and fewer pores were seen in the peripheral regions of the endplate with thicker bone cortex [56]. Slides were imaged at 10 times magnifications using a light microscope and the scale bars represent 500 μm.

Curvature of the Endplate Surface

The surface of the VEP in contact with the intervertebral disc has been suggested by Van der Houwen et al. to be curved [59]. This theory was confirmed by the work of Wang et al., showing an asymmetry between the two VEPs bordering the same lumbar disc in humans, referring to the cranial and caudal VEPs with respect to the same disc [60]. Both studies showed that the cranial endplates to the disc were concave, with a mean concavity depth of 0.8 mm greater than the caudal ones which were observed as mainly flat on radiographs. Although this asymmetry was consistently observed irrespective of the spinal level, the mechanism leading to this characteristic structure remains unexplained.

Bone Mineral Density

The micro-CT has been shown to be a useful means of measuring the bone mineral density (BMD) of bone. The reconstructed micro-CT image is a 3D map of local X-ray absorption by the bone. The reconstructed grey-scale intensity of each image voxel does not relate directly to mass density alone. The measured X-ray absorption is defined as attenuation coefficient in units of 1/distance, which is determined by both the mass density and the elemental composition of the material, bone in this study. If the X-ray absorption of material is known to be heavily dominated by one specific element of the material, then the X-ray attenuation coefficient can be directly related to the mass density of that element. For the case of bone mineral density (BMD), the X-ray attenuation of mineralised tissues, such as bone, is dominated by, and therefore can be approximated as, the X-ray attenuation of the mineral compound calcium hydroxyapatite (CaHa) [61]. This enables the measurement of CaHa density or bone mineral density in gcm^{-3} of bone samples from their corresponding attenuation coefficients measured from their micro-CT images.

The BMD of the VEPs from 48 male human cadaveric spines were reported to be independent of age but higher for cranial VEPs with respect to the disc compared to the corresponding caudal ones, using micro-computed tomography (micro-CT), as shown in Figure 2.10 [62]. The hypothesis of a close association between the BMD of VEPs and disc degeneration was rejected by Wang et al. This is in contradiction to the repeated findings by Gruber et al., showing a strong association between higher VEP bone mineral density and severe cases of disc degeneration [63–65]. The latter were based on animal models while the former was carried out with human spines, which could potentially explain the discrepancies. Furthermore, Gruber et al. used the dual-energy X-ray absorptiometry (DXA) method to assess BMD in vivo and this method uses a projection technique which is unable to distinguish the VEP from either the adjacent trabecular bone or the vertebral cortical shell

and could therefore explain the substantial overestimation [66]. It has also been reported that several lumbar spine degenerative features such as the presence of osteophytes can also interfere with the DXA bone mineral density measurements [67]. However, it is worth noting that the improved measurement of BMD using the micro-CT done by Wang et al., consisted of BMD values which were averaged across the whole volume of the VEP layer, meaning that if the new deposited mineralised tissue on the VEP, as a result of degeneration, had the same mineral density as the original endplate, this effect of degeneration would not have been detected [62].

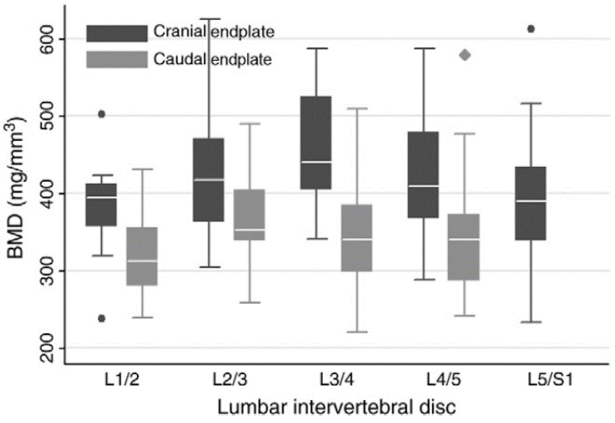

Fig. 2.10 The distribution of the BMD of lumbar vertebral endplates from cadaveric human spines, at different spinal levels is shown. The plots show that the BMD of cranial endplates were always greater than that of corresponding caudal endplates. The box describes the middle 50% of the distribution, with the white line in the middle indicating the median of the data. The two whiskers represent the minimal and maximal measurements while the dots or diamonds represent the outliers in the data [62].

2.5.2 Structural Characterisation Techniques

The literature has several reviews on the different characterisation techniques used for the purposes of visualising the regional morphology of the VEP in three-dimensions as well as its boundary with the underlying trabecular bone, especially from cadaveric human samples [13, 47, 59, 68, 69]. This section of the literature review aims to describe and compare the most commonly used investigations to characterise the endplates, such as scanning electron microscopy (SEM), micro-computed tomography (micro-CT) and histological studies.

Computed Tomography

Micro-computed tomography (micro-CT) scanning is non-invasive, requires minimal sample preparation and allows wet condition imaging, mimicking the biological environment. Micro-CT is commonly used for bone characterisation as a single scan provides high resolution images of the bone's internal 3D structure and accurate bone specific parameters [70].

The micro-CT works by illuminating the sample with a micro-focused X-ray source. The sample rotates, creating a series of angular views which are then collected by an X-ray detector as magnified projection images. The software then creates a stack of virtual cross-sections slices of the sample. This is further explained in Figure 2.11.

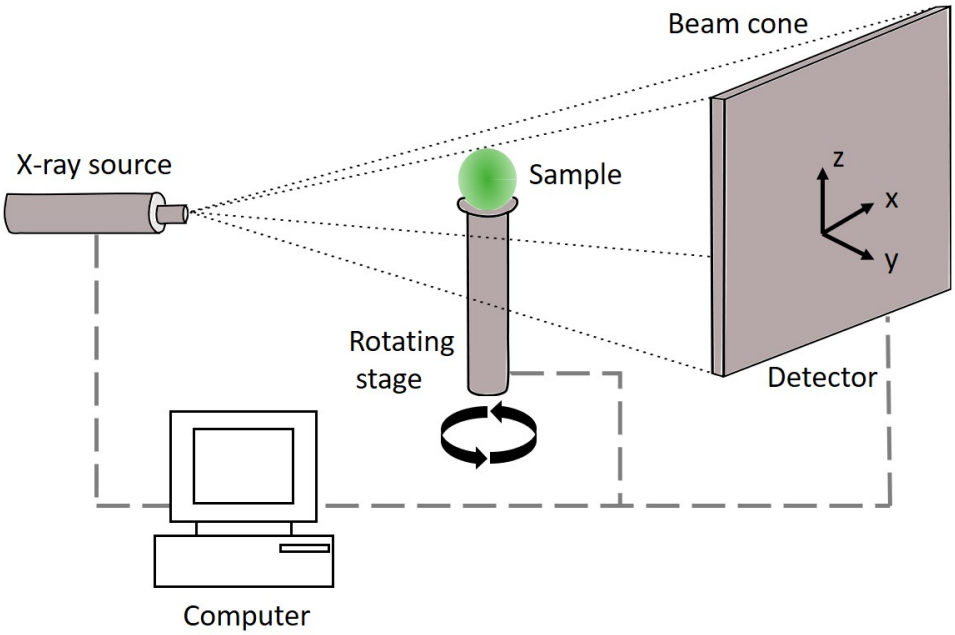

Fig. 2.11 Schematic showing a simplified version of how the imaging system works within the micro-CT. A micro-focus X-ray source illuminates the object, shown in green, and a planar X-ray detector collects magnified projection images. Based on hundreds of angular views acquired while the object rotates, a computer synthesises a stack of virtual cross section slices through the object.

Micro-CT has been used to show that although VEP from female donors are smaller than those from male donors, the elliptical overall shape is similar [71]. Van der Houwen et al. showed that CT scanning is a reliable method to measure the geometry of the VEP, with a mean difference in measurement of 0.18 mm (95 confidence interval) between CT measurements and Vernier caliper measurements [59]. Similarly, Zhou et al. used CT scans from patients to report the average circumference of the lower VEP to be 141 mm and the

average surface area as 1492 mm^2 [72]. However, the findings available from the CT scan are limited by the pixel size and spatial resolution. Recent technical advances have made high resolution micro-CT images, with pixel size in the micron range, a possibility for biological investigations [73].

Micro-computed tomography enables non-destructive scanning, capable of volumetric CT analysis with isotropic voxel spacing ranging from 10-75 μm [73, 74]. Scanning of sections made up of a whole functional spine unit, comprising the intervertebral disc, the VEP and the underlying trabecular bone is possible. This allows the scanned samples to be used for further tests, such as strain under compression, and correlation of data [75, 52]. Changes in bone structure, volume and microstructure can also be precisely measured using the micro-CT [74]. Similarly, the reliability, validity and precision of the micro-CT for the measurement of bone mineral densities and bone volume have been well established [62]. Rodriguez et al. showed that micro-CT can be used to quantitatively investigate the morphology of the VEP in cadaveric human samples and correlate these findings to the degree of disc degeneration [76]. Their data reported that VEP morphology was dependent on the depth at which measurement was taken, from the VEP surface adjacent to the disc, with peak bone density measured at a depth of 0.29 ± 0.20 mm from the VEP boundary, as shown by the graph in Figure 2.12. The bone density was measured as the ratio of bone volume to the total volume of the sample. The micro-CT scans also showed architectural changes from a heterogeneous structure to a homogeneous one as the disc degeneration increases, as shown by the bone density loss in Figure 2.13.

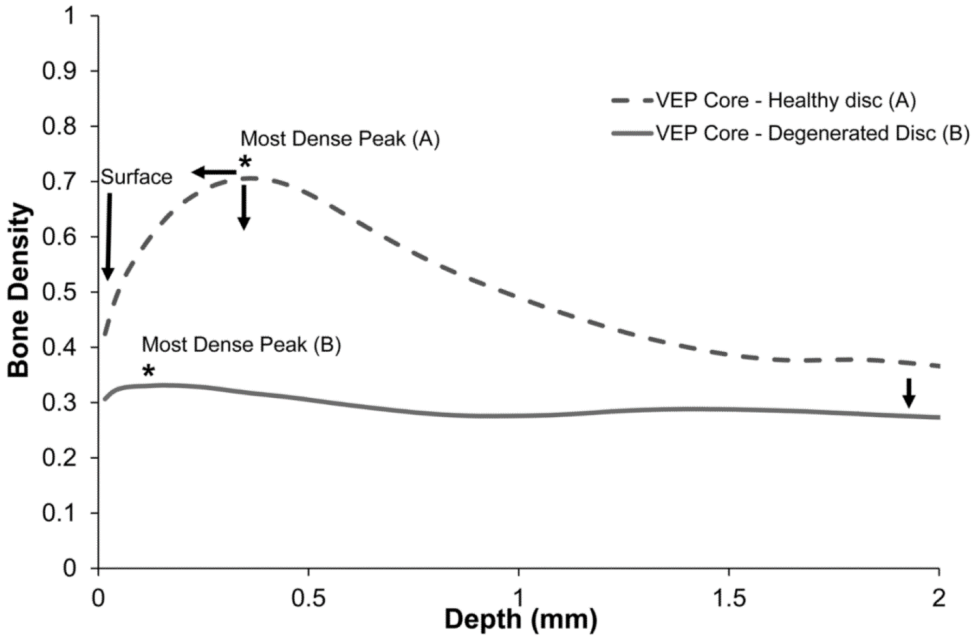

Fig. 2.12 The graph shows the variation of bone density at different depths from the VEP surface with the disc for healthy and degenerated samples. A: adjacent to healthy disc, B: adjacent to degenerative disc. The most-dense peak moves closer to the surface and bone density decreases with disc degeneration [76].

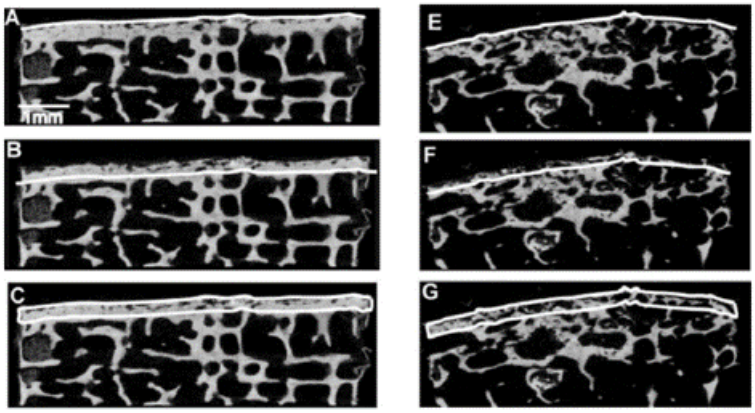

Fig. 2.13 The reconstructed micro-CT images of the VEP and underlying trabecular bone from two specimens of human cadavers are shown. Left column (A, B, C) shows VEP next to healthy disc and right column (E, F, G) shows VEP next to a degenerated disc. The white lines in A and E show the surface region of VEP; the white lines in B and F show the most dense region of VEP; the white boundaries in C and G highlight the maximum thickness region. The scale bar is shown in A and it represents 1mm [76].

The micro-CT images also showed the presence of the 'double-endplate' phenomenon, previously reported, in a subset of the samples, as shown in Figure 2.14 [54, 76]. The

main limitations of their study were the use of cadaveric samples, making the findings non conclusive, and the investigation of the central VEP region only, making results non-applicable to the rim.

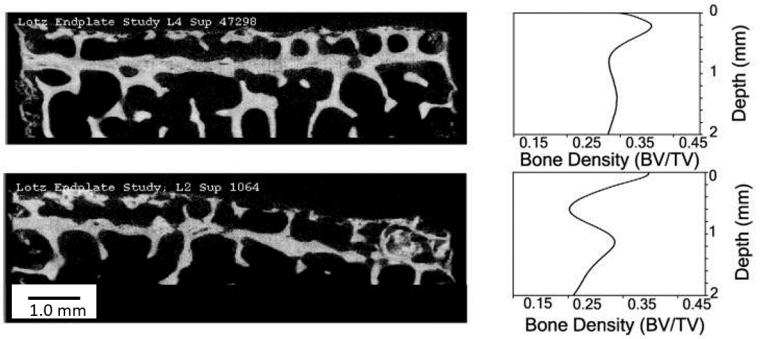

Fig. 2.14 The micro-CT images and their corresponding bone density distributions show the presence of double layer endplates in cadaveric human samples. Two layers of compact bones can be seen on the micro-CT images and the presence of the double layer VEP is further represented by the two separate peaks shown on the bone density distributions. [76].

The bone loss was also seen as the increased surface porosity with increasing Pfirrmann grade of degeneration as shown by the graph in Figure 2.15. Pfirrmann et al. identified 5 incremental levels of disc degeneration, based on the homogeneity of the structure of the disc, the structural distinction between the nucleus pulposus and annulus fibrosus of the disc, and the disc height [77], which will be explored in more details in Section 5.2.4. The results, showing an increased porosity by 50 % in the VEP with disc degeneration were in line with Grant's work, reporting a 30-60 % decrease in VEP indentation strength [68].

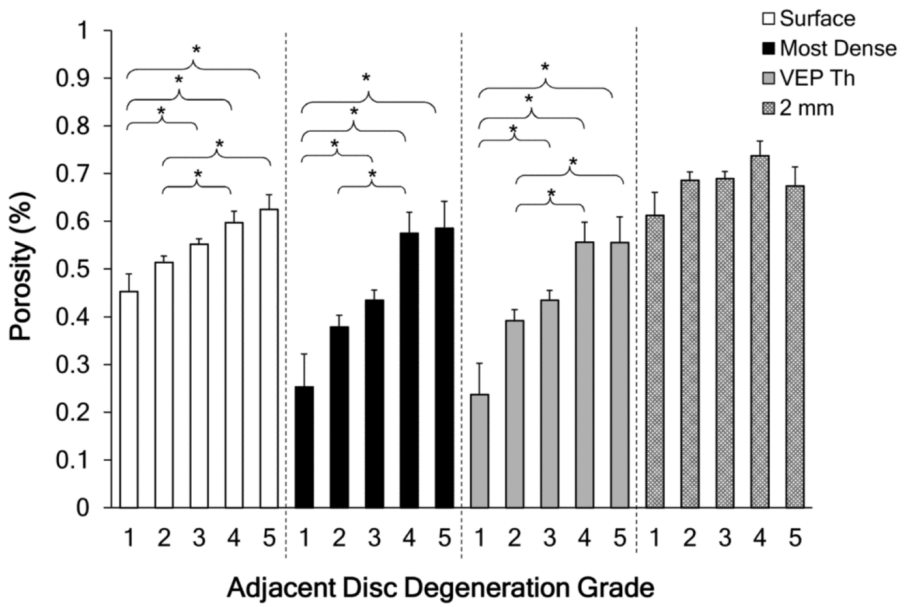

Fig. 2.15 Porosity variations of the vertebral endplates with different degeneration grade of adjacent disc is shown for 4 different sections: the surface of the VEP, the most dense layer of the VEP, the whole thickness of the VEP and at 2mm depth from the VEP surface. The degeneration grades refer to the Pfirrmann degeneration grades from 1 to 5, with one being healthy and 5 being the worst case of degeneration. The asterisks and corresponding brackets represent statistically significant differences. Porosity of the VEP increases with increasing degeneration for all the categories shown [76].

Similarly, Laffosse et al. used reconstructed micro-CT images of porcine samples to show the morphological location and thickness of the VEP layer, as well as the presence of growth plates, as shown in Figure 2.16 [78].

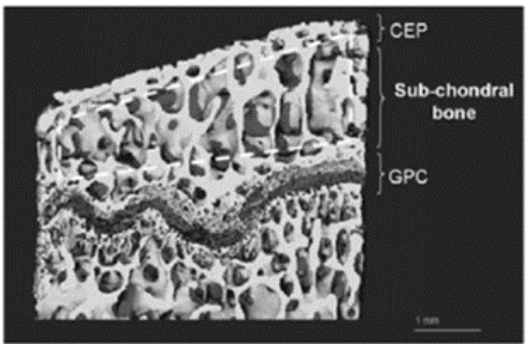

Fig. 2.16 The reconstructed micro-CT image from a porcine sample shows the presence of the cartilage end-plate (CEP), and the growth plates (GPC), which then fuses with the underlying trabecular bone. The scale bar represents 1mm [78].

Wang et al. used micro-CT to show that VEP thickness and bone mineral density are independent of age but cranial VEP to the disc were thicker with higher bone mineral density than their caudal counterparts [62]. Given the non-destructive nature of the micro-CT, samples usually require very little or no preparation at all. It is essential to clean the fresh samples by using tissues papers to rip out as much of the soft tissue as possible. One commonly used method for sample preparation is to fix the bone samples with 10% buffered formalin followed by long term storage in 70% alcohol [79]. These samples are then scanned dry and is ideal for studying bone morphology [80]. However, this technique does not work if calibrated measurements such as the bone mineral density must be measured. Instead Campbell et al. reported that bone samples soaked in physiological saline and stored frozen work better for biomechanical testing or histomorphometric analysis [70]. During the scan, it is crucial that the sample does not move independently. This can compromise the scan quality due to drying-related shrinkage. One advantage of the micro-CT technique is the possibility of scanning bone samples in the medium, such as saline or alcohol [81]. The sample holder should also be held in place securely. This has been done previously using plasticine, dental wax, parafilm [70, 76]. The sample holder as well as the sticking material should absorb X-rays.

Scanning Electron Microscopy

Vertebral trabecular bone structure and its remodelling have been extensively investigated using scanning electron microscopy (SEM) [82–86]. Whitehouse et al. showed that SEM is a reliable imaging tool for vivid representation of the architecture of trabecular bone from cadaveric human vertebral body and they suggested that it would also enable the comparison of bone remodelling due to pathological or physiological changes [87]. Their SEM image in Figure 2.17 shows a very clear representation of the sponge-like structure of trabecular bone as well as the dense cartilage layer at the bottom surface, which is where the VEP would be expected to be seen.

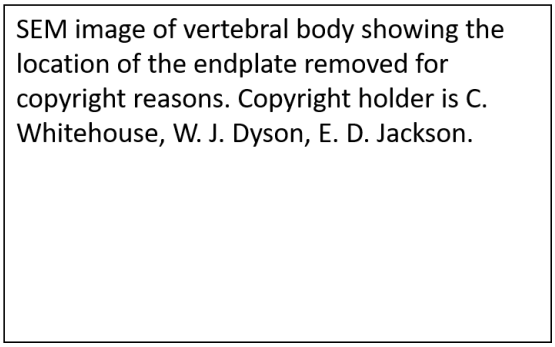

Fig. 2.17 The SEM image of cadaveric human samples from the vertebra shows the high resolution and distinction enabled by the imaging tool. The sample was cut at the region labelled G on the vertebral body, as shown by the red square in the left hand side schematic. The inferior endplate as labelled in the schematic refers to the cranial VEP. The dense layer of bone at the bottom lies in between the vertebra and the disc, identified as the red bracket, showed the VEP. The scale bar represents 1mm [87].

Nosikova et al. used SEM to characterise the interface between the annulus fibrosus of the disc and the vertebral body of bovine samples and to measure the thickness of the VEP, referred to as the hyper mineralised layer and highlighted by the white arrows shown in Figure 2.18 [88].

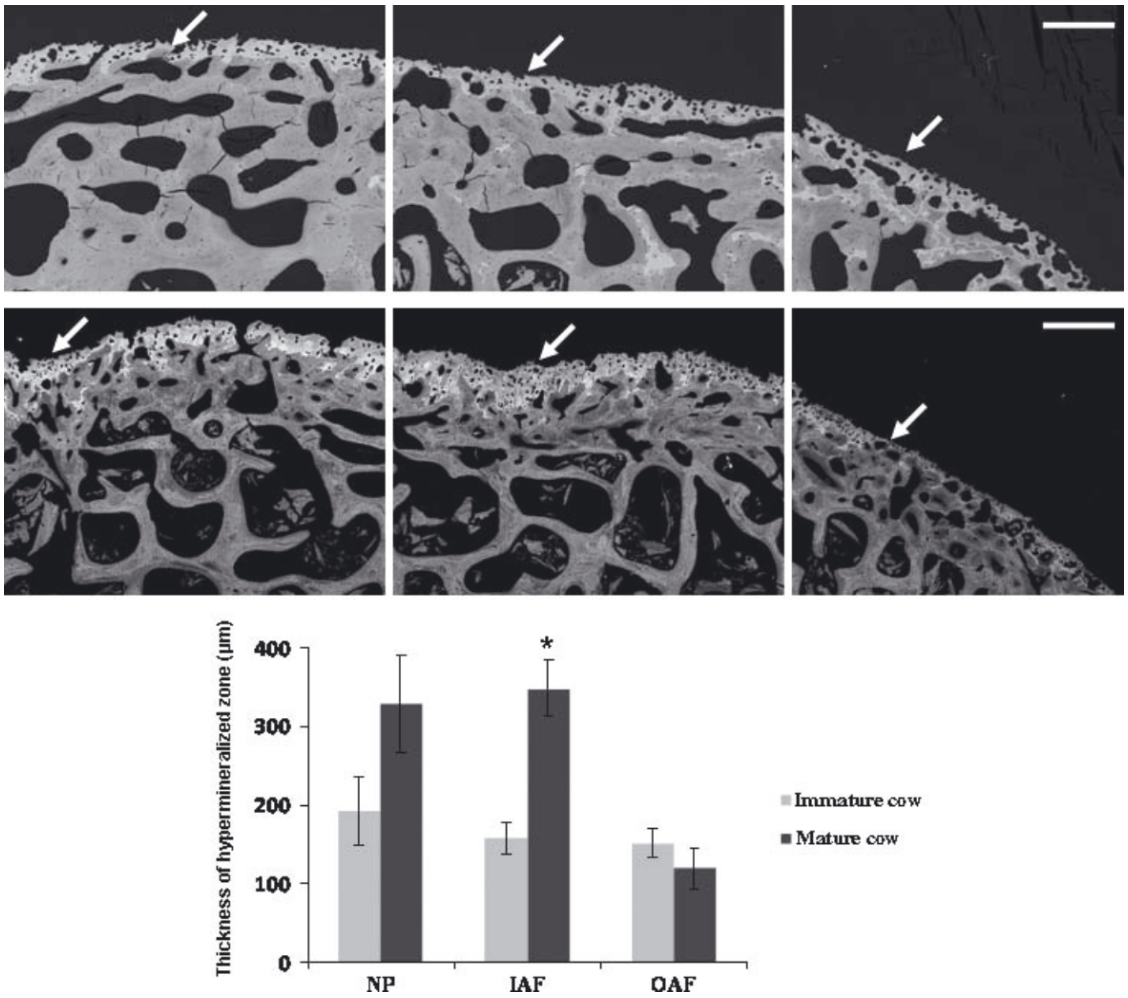

Fig. 2.18 The VEP, referred to as hypermineralised zone in this context, from mature and immature cows are imaged using the SEM and the thickness of the VEP was measured and compared. The interface between vertebra and disc with VEP layers was shown by white arrows. The graph highlights the VEP thickness measured in mature and immature cows for the nucleus pulposus region (NP), inner annulus fibrosus (IAF) and outer annulus fibrosus (OAF) regions. The asterisk represent statistical significance of the IAF mature cow data. The error bars represent the standard error of the mean for each dataset. The scale bars in the SEM images represent 500 μm. The VEP was thicker in the mature cow samples in the NP and IAF region but the contrary was observed in the OAF region [88].

In SEM, the outermost surface is examined and to visualise the sponge-like structure of the bone, it is crucial to clean the bone of any adherent tissues and bone marrow. Nosikova et al. prepared the samples for SEM by embedding in epoxy, polishing and carbon coating [88]. Whitehouse used samples 3-5 mm thick which were sawn from vertebral units, cooled with liquid nitrogen and hand polished with silicon carbide paper under more liquid nitrogen. This process freezes the bone marrow so that it is hard enough to protect the trabecular structure

from damage and embedding of broken pieces of bone during polishing. The samples were then allowed to come to room temperature and a jet of cold water was used to wash out the marrow and samples were eventually dried over silica gel before coating with a layer of Duron antistatic agent in alcohol to make the surface conducting for SEM imaging. This protocol avoided the use of metal or carbon coating which can lead to isolated areas of coating because of the open structure of the trabecular bone [87].

Several other preparatory techniques have been used in the literature. In each protocol, there is a series of steps for which several recipes have been reported. The first step in the sample preparation is to preserve the biological sample [89]. This can be done either by physical or chemical fixation. Cryopreservation is the preferred physical fixation and it rapidly inactivates all cellular activities using a very low temperature. However, the instruments and methods can prove to be technically challenging. The most commonly used chemical fixatives are glutaraldehyde and paraformaldehyde [90]. They are the most preferred approach for fixation, even though penetration rate of the fixatives is very slow, making quality of fixation not ideal in some cases [91]. A standard SEM protocol for biological samples includes fixation, drying, mounting sample onto a stub and coating with a conductive layer [92]. The adherent soft tissues can be removed to enable better visualisation of the intricate sponge-like structure. This can be done using mechanical force, detergents (non-ionic, ionic, zwitterionic) or enzymes [93]. For the decellularisation protocol to be effective, the protocol should ideally comprise a combination of all 3 approaches. Table 2.1 summarises the most commonly used methods.

Method	**Example**	**References**
Physical	Snap Freezing	[94]
	Mechanical Force	[95]
	Mechanical Agitation	[96]
Chemical	Acid/Alkali	[97]
	Triton X-100	[98]
	Sodium Dodecyl Sulfate	[99]
	Ethylene Diamine Tetraacetic Acid	[100]
Enzymatic	Trypsin	[101]
	Endo/Exo Nucleases	[102]

Table 2.1 Summary of the commonly used methods for decellularisation from literature.

Propagation Phase Contrast Synchrotron X-ray Tomography

In 2017, Cao et al. used mice samples and propagation phase contrast synchrotron X-ray tomography (PPCST) to simultaneously investigate the age-related 3D micro-architectural changes in the VEP and the disc. They provided further evidence that the PPCST provides a better alternative to conventional micro-CT for high spatial resolution and 3D imaging of both the disc and the endplate [103]. This comparison can be seen in Figure 2.19 where the soft tissue contrast (purple) and VEP demarcation line (green) are markedly more defined in PPCST reconstructed images than micro-CT ones [104]. However, the VEP and vascular canals were equally visible with both techniques.

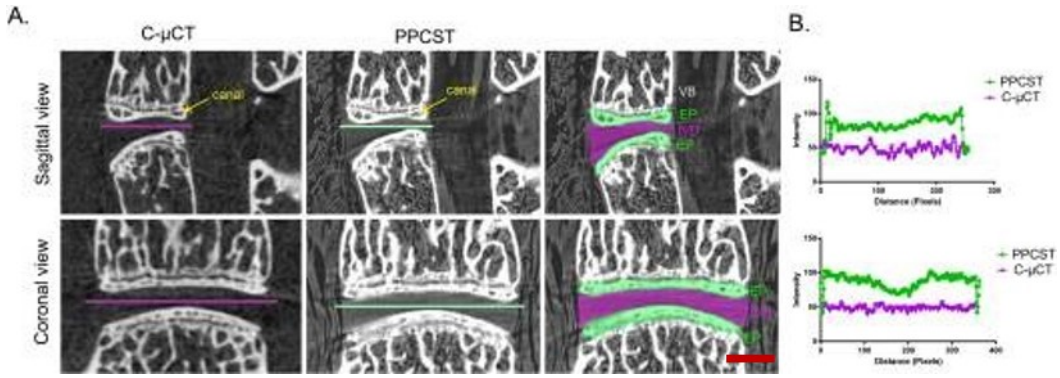

Fig. 2.19 The images of the vertebral functional units and corresponding intensity profiles highlight the observed differences when using the micro-CT as compared to the PPCST. A:PPCST reconstructed images show markedly better soft tissue contrast in the disc (purple line) and delineation of the VEP (green line) than conventional micro-CT images. The canals in the VEP could be detected in both images. B: intensity profile of the matching coloured lines in A. The red scale bar represents 1mm [104].

PPCST was used to measure VEP thickness and porosity for caudal and cranial VEPs with aging. The comparison of these findings is shown in Figure 2.20. Their work confirmed that VEP is thinnest centrally and opposite to anterior and posterior regions. The porosity distribution with age was found to follow same trend as for thickness. It was concluded that both VEP thickness and porosity are associated with ageing.

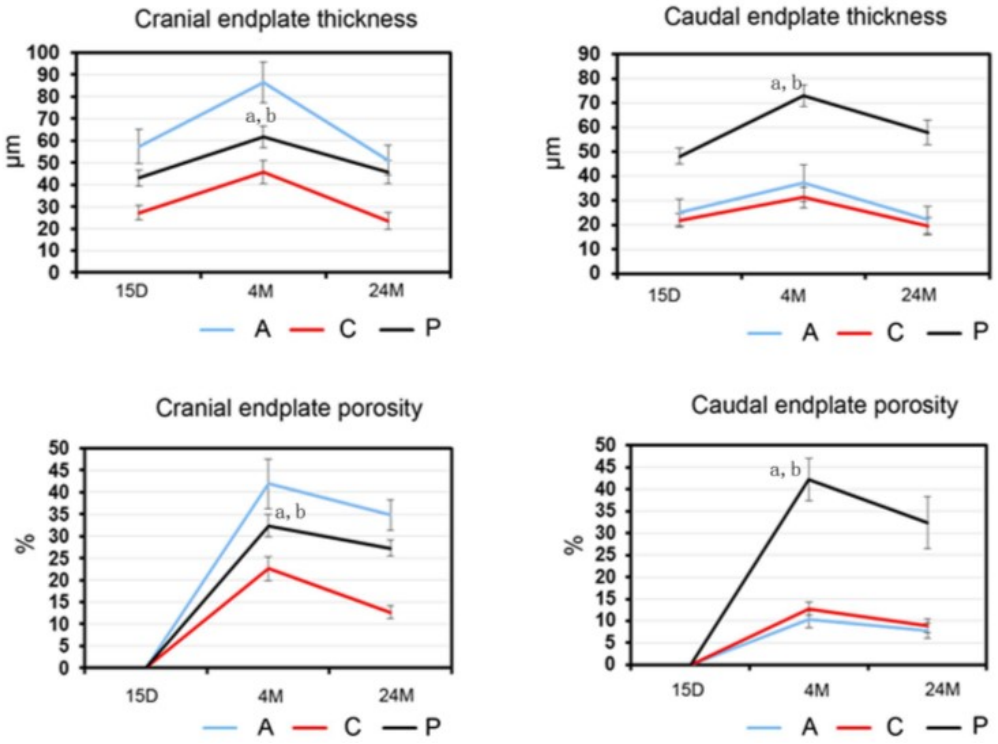

Fig. 2.20 The 4 graphs show the comparison of the VEP thickness and porosity for caudal and cranial mice VEP after ageing. The lines A. B and C represent the VEP location from which the sample was taken (A:anterior, C:centre, P:posterior). Samples used were from mice ages 15 days (15D), 4 months (4M) and 24 months (24M). The data shown were mean values with the standard deviation shown by the error bars (n:8 mice for each group). The label (a) indicates a significant difference between the posterior region and the center region and the label (b) indicates a significant difference between the posterior region and the anterior region ($P < 0.05$) [104].

Surface-rendered images from PPCST were also compared to histological samples as shown in Figure 2.21. It was observed that the features of the disc and VEP seen, such as the canals, from PPCST were in line with the histological studies.

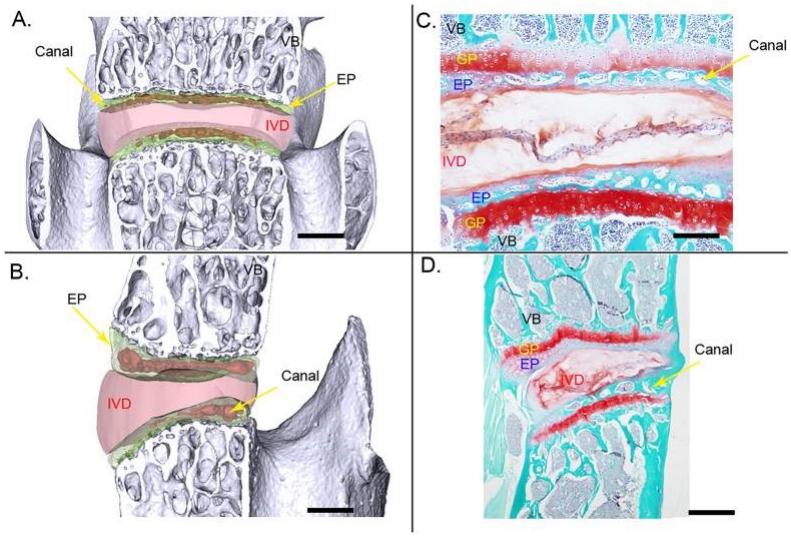

Fig. 2.21 Surface-rendered images from PPCST (A and B) compared to histological slides (C and D). Corresponding section images were stained with Saf-O. Scale bar represents 1mm. VB: vertebral body, EP:endplate, GP:growth plate, IVD: intervertebral disc. Canals were clearly seen in the histological slides and the gross morphology of VEP and disc were clearly imaged [104].

Reconstructed PPCST images were also used to identify and compare the canal network present in caudal and cranial VEPs. The 3D digitalised images showed a higher concentration of such canals in cranial VEP than caudal but these decrease with age, as shown in Figure 2.22. The result was in line with previous findings, suggesting an intricate 3D network canals which is different from the Haversian system seen in cortical bone [63].

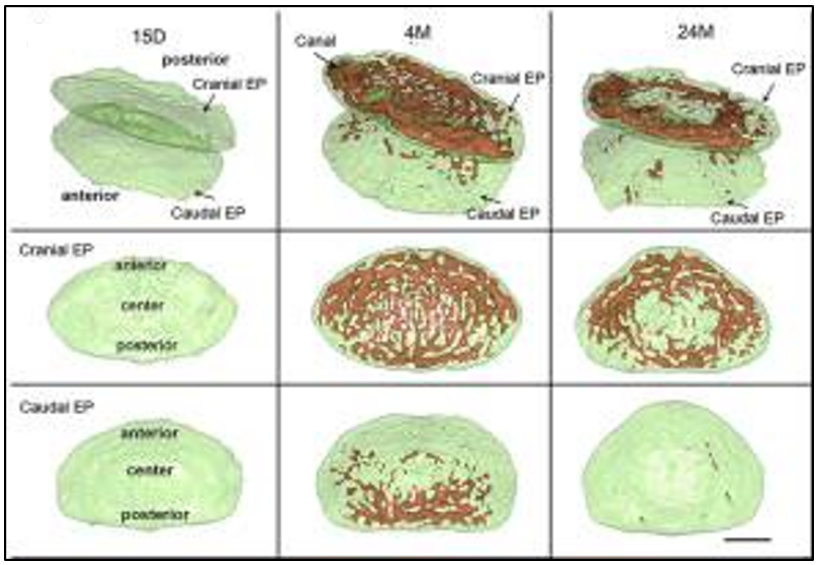

Fig. 2.22 The 3D digitalised maps show the intricate 3D network of canals in cranial and caudal VEP for mice of 3 different ages (15D:15 days, 4M:4 months and 24M:24 months). The canals were more prominent in the cranial VEPs as compared to the caudal VEPs for the 4M and 24M but canals were absent in the 15D samples. Scale bar represents 1mm [104].

2.5.3 Animal Models

Ideally, human cadaveric spines are the most suited model for lumbar spine investigations. However, the availability of large numbers of healthy and appropriate samples, providing the full in-depth analysis is limited. Therefore, several spinal studies have used different animal models, such as mouse, rat, rabbit, dog, sheep, cow and apes [105]. Although animal models are not representative of the degeneration route and effect, they enable proof of concept, development of laboratory techniques and collection of baseline data [106]. Therefore, the choice of an animal model depends on the criteria under investigation, for example, structural or mechanical properties. When investigating the vertebral body, the bone density and histomorphometric bone properties would be important to be considered whereas investigating the disc would require similar proteoglycan and biochemical parameters. Furthermore, degenerative models of the spine can be classified as induced or spontaneous and the onset of degeneration also dictates the suitability of the animal model [107].

The choice of which animal model to use therefore depends on several factors, such as the spinal area of focus, availability of samples and synergies between the biomechanical properties and the scientific question at hand.

Furthermore, histological studies have been used to characterise VEP layers in ovine models and for comparison purposes with human VEP. Zhang et al. used standard staining

techniques coupled with light microscopy to show that although there were several morphological similarities between human lumbar VEP, rabbit and goat ones, the most significant difference was the presence of calcified cartilage in human VEP whereas animal VEP was made of non-calcified cartilage and bony endplate. In addition, animal samples showed the presence of growth plates which were absent in human samples. These findings suggest that animal models do not represent a complete representation of human VEP [108]. These findings are shown in VEP samples from rabbit, goat and human as shown in Figures 2.23, 2.24 and 2.25 respectively.

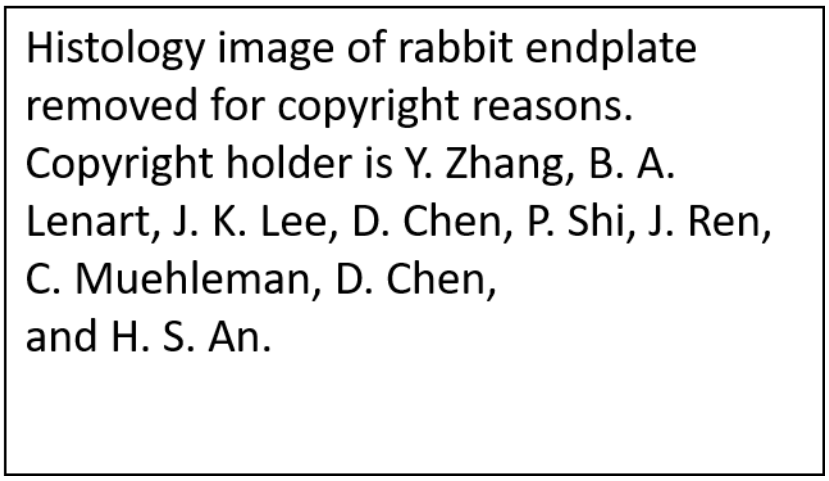

Fig. 2.23 The histological images using Alcian Blue, counterstained with hematoxylin and eosin, show the rabbit VEP. The intervertebral disc was stained pale purple and labelled IVD. Rabbit VEP had a thin layer of cartilaginous VEP, shown in pink and labelled as bony endplate (BEP) in this study and growth plates (GP). The thin green arrow shows the tidemark line, demarcating the line between the bony endplate and the cartilage endplate. The blue arrows show vascular channels. The images shown are at different magnifications: (A) low magnification, (B) and (C) high magnifications [108]. The scale bar in C represents 250 μm

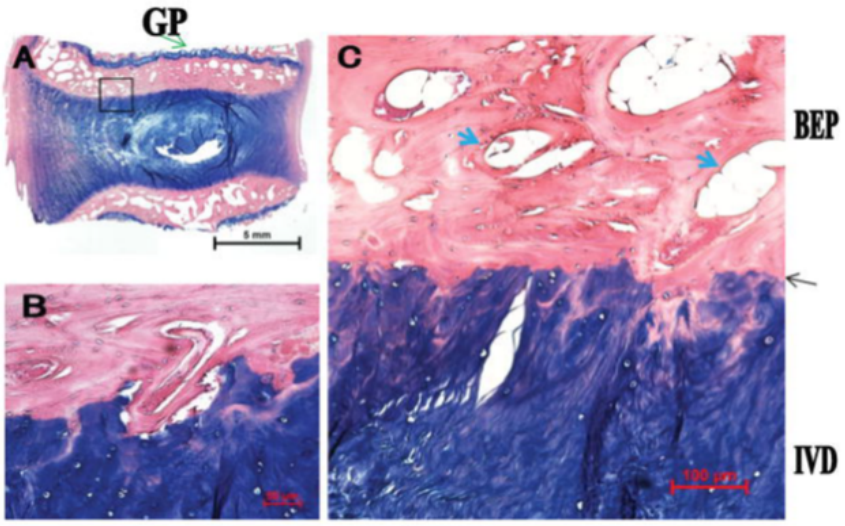

Fig. 2.24 The histological images using Alcian Blue, counterstained with hematoxylin and eosin show the endplate and disc boundary from a goat. The goat endplate consisted of a thin layer of cartilaginous endplate, bony endplate (BEP) and growth plates (GP). The bony area was stained pale pink while the soft tissues of the disc were stained dark purple. Green arrow shows GP,black arrow shows tidemark and blue arrows show vascular channels. (A) low magnification, (B) and (C) high magnification. The scale bar in C represents 100 μm [108].

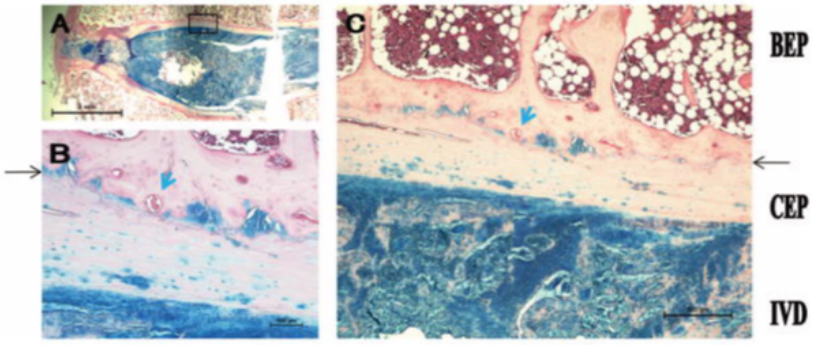

Fig. 2.25 Histological images with Alcian Blue, counterstained with hematoxylin and eosin, showing the structure of human endplates. The endplate was mostly composed of the calcified cartilage (CEP) and bony endplates (BEP). The scale bar in C represents 500 μm. Black arrow shows possible location of the tidemark, blue arrows show vascular channels. (A) low magnification, (B) and (C) high magnification [108].

These histological findings also identified the presence of vascular channels in the VEP layer. This confirmed the earlier work of Nachemson et al. where they used the diffusion of a dye and histological studies to show that the presence of these vascular channels in human specimens, or vascular projections which provide contacts between the marrow space of the

vertebral body and the VEP, is related to the permeability of the central region of the VEP [109].

Given that the bony VEPs are closely related to the vertebral body, it is crucial to take into account the physical properties of the trabecular bone and the process of bone growth [110]. This is because these parameters define the mechanical properties of the bone and inform on the suitability of age and spinal levels of the animals to match the human equivalent parameters. The ovine model has been shown to be a close match with the human spine, especially the VEP regions, with similar weight range, bone and joint structure and remodelling processes [111–113]. Furthermore, sheep spines are readily available and easy to handle, providing large number of samples to negate the effect of biological variability. Although sheep are quadrupeds, the loading of the spine has been shown to be by axial compression and mainly along the long axis, matching the loading of the human spine [114]. This can be explained by the additional tensile forces from surrounding muscles and ligaments acting to maintain posture in a quadruped to resist bending.

Daly et al. found that none of the animal models they reviewed, such as mice, rabbits, dogs, goats, sheep, and primates, accurately mimicked the clinical conditions of disc degeneration [115]. This is because of the complex pathology of disc degeneration, caused by different levels of influence of the changes in the cellular matrix, the VEP or the neurovascular components of the disc, as well as the effect of pain in determining patients outcome.

Although the human VEP has been shown to share similarities in histological characteristics with animal models explored above, significant differences also exist. Therefore, these findings support the claim that no single animal model provides a complete representation of the human endplate. As such, although animal models are essential for perfecting research on the human endplates, one must be cautious in extrapolating data.

2.5.4 Summary of Structural Properties of the Endplates

The VEP has been shown to be characterised by their thickness, porosity, bone mineral density and curvature. Furthermore, the structural properties of the VEPs has been shown to vary with their location in the spine, their position with respect to the side of the disc and the region of the disc they are in contact with.

The central region of the VEP has been shown to be thin but porous while the peripheral regions are thick and less porous. The central surface of the VEP has also been shown to have the largest dip, creating a curved surface for the VEP, and providing space for the nucleus pulposus of the intervertebral disc to swell. The cranial VEPs with respect to the disc were also shown to have the higher curvature and higher BMD than their caudal counterparts.

Several characterisation techniques have been used to measure the structural properties of the VEP in vitro, such as the micro-CT, SEM and PPCST. Although the existing literature has successfully identified isolated trends in structural properties, there still has not been any study which considered all the structural properties simultaneously, while taking into account the effect of spine level, side of the disc and region of the VEP. Furthermore, the trends in structural properties of the VEP reported in the existing literature were based on several animal models, and on human samples. Therefore, there is still a need to investigate the trends across the the different positions of the VEP and for the different structural properties simultaneously. This will provide a more holistic understanding of the interplay between the structure of the VEP and the mechanical loading of the spine. It will also aid the understanding of how the VEP fulfils its biophysical functions, which will be discussed in further details in the next section.

2.6 Functions of the Vertebral Endplates

The VEP plays an important role in the crucial daily functions of the spine. It balances two conflicting biophysical demands: providing a nutritional pathway between the vertebra and the disc, and providing mechanical stability to the vertebra during daily loading of the spine.

2.6.1 Nutritional Pathways

The first main function of the VEP is to provide a nutritional pathway between the vertebra and the avascular disc. The VEP acts as a permeable membrane to the disc for biological and chemical exchange [58, 68, 109]. The disc being avascular relies on different mechanisms to obtain the essential quantities of nutrients such as glucose, oxygen, amino acids and sulfates. Metabolic waste, such as lactic acid, produced by the disc also needs to be extracted [116, 117]. Early in vivo studies used small dye molecules as tracers to investigate the transport mechanisms and reported that there are two distinct paths for transport to the disc: from the vertebral bone via the VEP and from surrounding tissue through the annulus of the disc, as shown in Figure 2.26 [118]. Surrounding capillaries in the soft tissues around the disc are 7-8 mm away from the nearest nucleus pulposus [116]. The nutrients diffuse from these capillaries into the dense extracellular matrix of the nucleus and waste products are removed in a reverse mechanism. The transport mechanism was found to be very slow and dependent on the loading rate and shape of the disc [119, 120]. Most of the disc however, relies on the transport route via the VEP [109, 121]. The central regions of the VEPs are freely permeable. This was shown using several techniques, including radiology, histology and fluorescent dye

injection techniques [116, 122, 123]. However, the differentiation between the transport into the disc and transport of metabolic waste out of the disc has not been successfully achieved yet. There is considerable information about the blood supply through the VEP unlike the one from the annulus periphery [124].

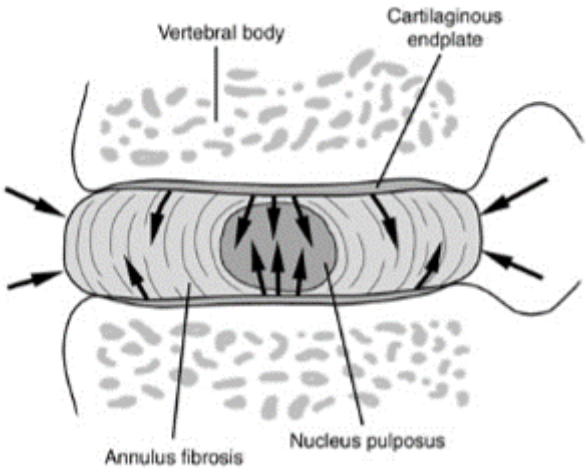

Fig. 2.26 Schematic showing the nutritional pathways to a healthy disc, sandwiched between the 2 endplates and their corresponding vertebral bodies. The disc is avascular and relies on the blood supply from the capillaries through the endplates and the direction of the flow of nutrients to the disc is shown by the arrows [14].

Crock et al. used vascular injection techniques to show the presence of an intricate network of arteries and veins in the centre of vertebrae and their corresponding VEPs, as shown in Figure 2.27 [125]. In vitro and in vivo studies have showed that this network is the primary route of solute exchange and the main mechanism by which solute exchange occurs is diffusion [126]. The diffusion is controlled by the size and ionic charge of the diffusing molecule [126, 127]. The VEPs have high proteoglycan concentration giving them an overall negative charge, coupled with their low hydration coefficients, restricts solute transport to the disc [58]. Water, oxygen and amino acids are small and uncharged molecules and therefore easily diffuse across whereas bigger anions would be partially or completely restricted to the disc [128].

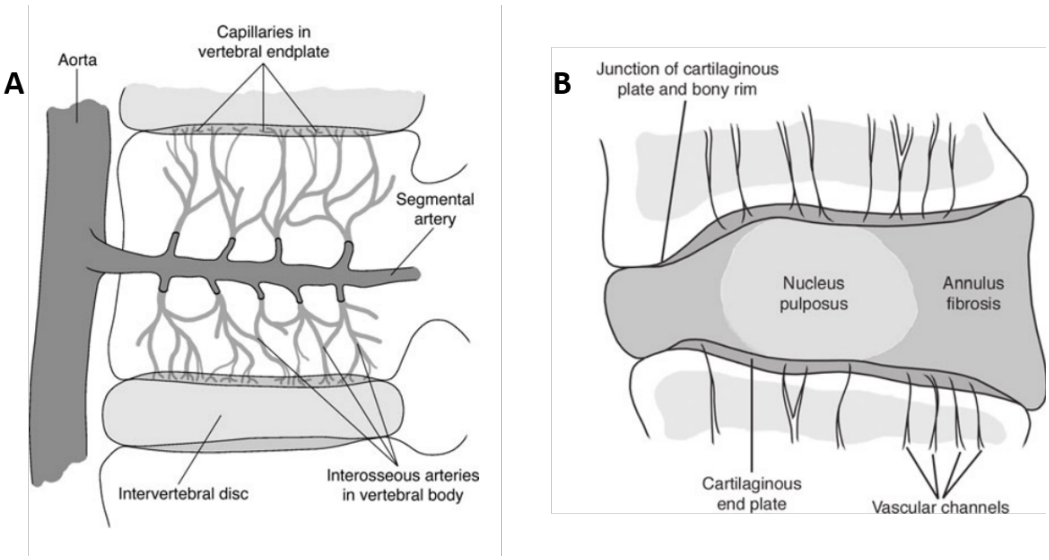

Fig. 2.27 Schematics showing the proposed location and architecture of blood vessels near the disc and bone boundaries. A: Schematic showing the organisation of blood vessels from the vertebral body into the capillaries found in the VEP. B: A schematic of an axial section of a human adult disc showing the thin VEPs and the vascular channels penetrating the VEP to bring blood supply to the annulus fibrosus and nucleus pulposis of the disc [14].

The central regions of the VEPs are permeable. Maroudas et al. used histological studies to show that this permeability was associated with the presence of small vascular "buds" beneath the VEP layer [44]. These findings were later confirmed using several techniques, including radiology, fluorescent dye injections and hydrogen washout techniques [116, 122, 123]. Throughout growth and ageing, the cartilage in the VEP undergoes mineralisation and this tissue undergoes resorption to be replaced by bone [129, 130]. This impedes diffusion across the VEP and disc boundary. Furthermore, the vascular network in the VEP undergoes calcification and therefore is blocked [55]. A considerable change in solute flow has been noted and is attributed to these modifications of the VEP structure.

3D Canal Structure

The presence of active blood flow in the VEPs has been shown using vascular tracers, scanning electron microscopy and histological staining. These will be explored in further details in the next sub-section. However, the architecture of the canal network containing the blood network is still poorly characterised due to the complexity and intricate nature of the 3D network.

Yamaguchi et al. used the micro-CT to quantitatively characterise this 3D canal structure in rabbit VEPs, as shown in Figure 2.28 [131]. They reported the presence of large scale

canals running parallel in the VEP surface with a mean diameter of 152.1 mm at a mean depth of 224.1 mm from the VEP boundary with the disc. These canals were connected to the disc and the marrow spaces of the vertebral bone by longitudinally oriented canals. These vertically aligned canals were the most dominant and could be classified as short length (57.6 mm) and small diameter (45.7 mm) canals. However, the study did not discriminate between caudal and cranial VEPs or between central and peripheral regions of the VEP. The spine of the animal model used, rabbits, is also a much smaller scale than the spine of humans, therefore the architecture of the canal network in human VEPs has not been quantitatively characterised to date.

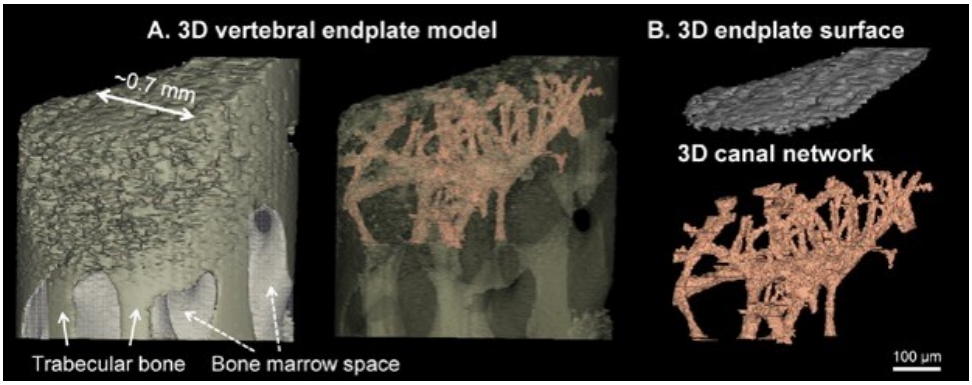

Fig. 2.28 Micro-CT image of rabbit VEP with corresponding 3D canal network within the endplate layer are shown. A: Representative high-resolution micro-CT-based 3D canal network models in the rabbit lumbar VEP. B:Representative 3D VEP surface and the corresponding 3D canal network topology. The scale bar represents 100 μm [131].

Cao et al. also quantitatively characterised the structural paramaters of the canals in the caudal and cranial VEPs of mice specimens [104]. They also confirmed the presence of the 3D interconnected canal system, which was different from the Haversian canal system usually found in cortical bone [132]. However, they concluded that further investigations were required to understand the morphology of the canal structure and the effects of aging and degeneration, especially in humans VEPs.

Vascular Network

The intervertebral disc is the largest avascular tissue in the human body and therefore the nutrient concentration of the matrix decreases with increasing distance from capillaries [133, 134]. Cells in the disc require a critical level of 0.2 mM glucose and a pH of 6.7 to survive. As discussed in the previous sections, the VEP is the main pathway for nutritional exchange to the intervertebral disc, with a small amount of diffusion through the outer annulus

of the disc [116]. The VEP also provides the pathway for the removal of metabolic waste and degraded matrix molecules from the intervertebral disc, which is crucial for maintaining an appropriate cellular environment [128].

The main artery and vein which run parallel to the spine are the abdominal aorta and the inferior vena cava respectively. The aorta further divides into the lumbar artery which penetrate into the vertebral body. Once inside the vertebra, the lumbar artery branches further into the equatorial branches and the nutritional arteries. These then form the capillary network which extends all the way to the VEP [125, 135]. Crock et al. suggested the presence of a venous drainage system in the VEPs and identified the presence of large vessels running horizontally in the trabecular bone, leading to the capillary network in the VEP [136]. Crock and Goldwasser also imaged the terminations of the blood vessels in the VEP of adult dogs, using the decalcified specimens post-infusion with Japanese ink mixed with a suspension of barium sulfate [123]. The photo-micrographs from this study identified the capillary bed present at the VEP-disc boundary and also described the terminations of the blood vessels at this boundary, especially near the nucleus pulposus of the disc as "suckers on the tentacles of an octopus", as shown in Figure 2.29. They found that these capillaries then drain into venules which connect to the postcapillary network in the trabecular bone of the underlying vertebra. However, this study did not address the flat and discontinuous nature of the capillary endings.

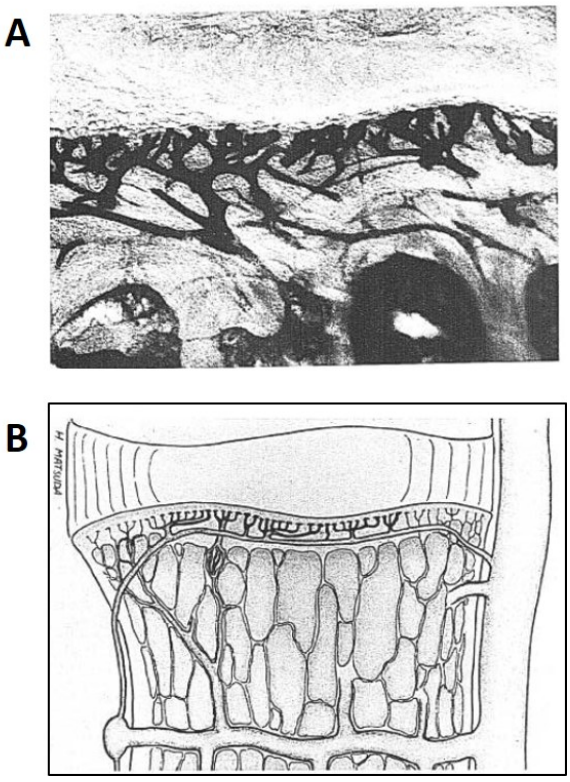

Fig. 2.29 The micrograph and schematic show the proposed architecture of the canal endings at the boundary of the endplate and the disc. A: Photomicrograph of a sagittal section showing the capillary terminations in the VEP at the boundary with the disc, underlying the nucleus pulposus. B: Schematic showing the detailed anatomy of the capillary bed in the VEP of an adult dog based on the findings from this study [123].

Scanning electron microscopy coupled with resin injection has been used by Oki et al. to also image the vascular network in the VEP of rabbits [137]. As shown in Figure 2.30, the blood vessels were shown to extend from the trabecular bone in the underlying trabecular bone, into the VEP where the capillaries coiled into loops, referred to as vascular buds. This is the only paper that successfully imaged these vascular buds in the VEP at the discal boundary. However, several studies have alluded to the presence of a capillary bed in the VEP and the presence of such loops to account for the requirement of the blood system to be a closed and continuous network to be physiologically viable. However, there is still little evidence to back these suggestions.

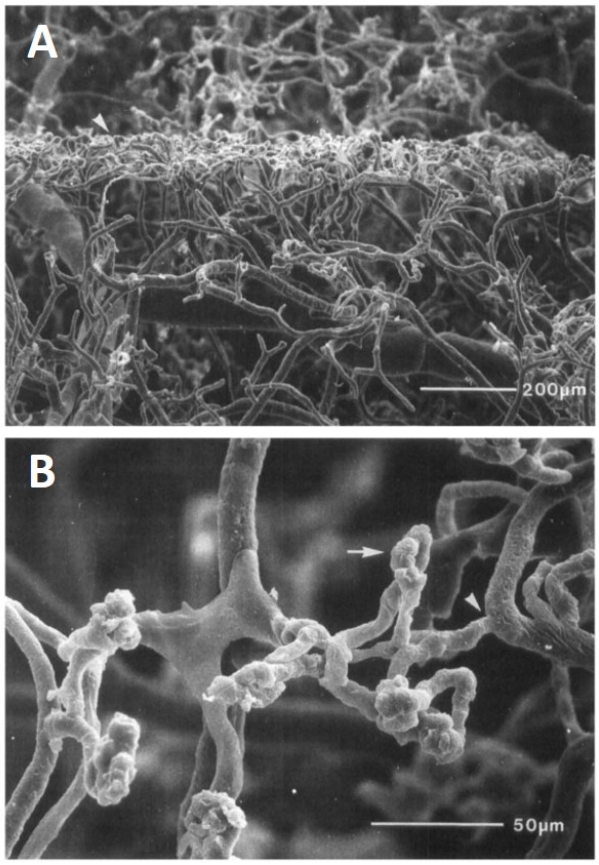

Fig. 2.30 The SEM images show the bud-like nature of the canal endings and the loops seen in the canal network of a rabbit endplate. A: Lateral view of the vascular network in the rabbit VEP showing the blood vessels reaching the boundary between the VEP and the disc, as shown by the arrowheads. B: Top view of the same rabbit VEP with the arrowheads pointing to the branching of the capillaries and the arrow showing a microvessel loop [137].

The visualisation of blood vessels and a clear understanding of the architecture and sizes of vessels are crucial for the planning of several vascular interventions. Manual segmentation of blood vessels is impractical as they present very complex 3D structures, therefore an automatic or semi-automatic segmentation is preferred [138]. Centreline analysis is a commonly used semi-automatic vessel segmentation to characterise blood vessels. It provides a a fast and reproducible method to measure the length, diameter and orientation of vessels [139]. The only limitation reported is the dependence on the quality of vessel segmentation which in turn is determined by the resolution of the imaging technique and the anatomy of the specimen under investigation [140]. This technique has been used extensively to characterise blood vessels in aortic tissues and hepatic tissues but, so far as the author is aware, has not been applied to the spine or the VEP.

Lymphatic System

The lymphatic network is crucial for the normal function of the high-pressure, closed blood system in the human body. It has been shown to transport lipids absorbed from the digestive tract and to provide an outlet for plasma components from capillaries and post-capillary venules [141]. Lymphatic vessels return the capillary filtrates and the excess plasma proteins to the central circulation, therefore maintaining normal tissue fluid volumes across the whole system. Furthermore, lymphatic vessels form a vast distribution network, connecting all parts of the body with blind-ended capillaries which convey interstitial fluid and cellular debris.

The spine also has lymphatic vessels that co-exist with the blood supply, however, the presence of lymphatic vessels in relation to the disc or the VEP still remains unclear. A histological study with a wide age range of human specimens was the first to suggest the presence of lymph vessels in the annulus of the disc, up to the age of 20 years. They showed the presence of the lymph vessels surrounding the annulus tissues but did not consider the VEPs, only the soft tissues of the disc [142]. However, Kashima et al. later disagreed with these earlier findings, despite using the same method. The newer study included the VEPs and the vertebrae as well as the disc but reported the absence of lymphatic vessels in both the healthy vertebrae and the discs, of all human specimens irrespective of age [143]. They did however suggest the presence of lymphatic vessels in pathological degeneration of the disc as a result of in-growth of lymphatics from surrounding connective tissues. Therefore, both the presence and the role of the lymphatic network in relation to the disc and the VEP are inconclusive at this stage.

Diffusion and Convection Processes

It is understood that the transport of fluids and solutes from the vertebra to the disc is carried out through the blood vessels in the VEP and surrounding the annulus fibrosus of the disc. However, two mechanisms for the exchange of fluids and solutes from the blood vessels to the discal tissues have been hypothesised: firstly, through molecular diffusion of metabolites influenced by the concentration gradients and secondly, by convective flow of metabolites alongside fluid being pumped across the VEP [144]. When nutrients reach the VEP boundary at the disc, small solutes such as glucose, lactate and oxygen pass through to the disc matrix by diffusion [145]. Conversely, larger solutes are subjected to convective fluid flow induced by the concentration gradient between blood plasma and tissue matrix, until there is a balance between the concentration between the nutrient density in the capillaries and the disc cells [146].

Urban, Maroudas and Holm used injection techniques using radioactive tracers in the VEP specimens from dogs to show that diffusion of solutes from the blood vessel to the discal tissue was the main transport mechanism [126]. They concluded that the driving force for the diffusion process under normal physiological conditions in vivo was the concentration gradient between plasma and the discal tissue which is caused by the consumption and production of solutes by cells in the discs.

As discussed previously, the VEP not only provides a nutritional pathway but also provides the pathway for metabolic waste and fluid removal [128]. Metabolic waste is composed of larger molecules, for example lactate is 89 g / mol, and therefore would more likely be transported to the disc by convection than by diffusion [147].

During daily activities, the disc experiences load-induced pressure which can be 3 to 5 times larger than the physiological osmotic swelling pressure of the disc [148]. This leads to fluid being pushed out of the disc, by convection, and a decrease in the hydration of the disc, resulting in an increase in the swelling pressure. This is why, it is crucial for the disc to rehydrate during rest and the osmotic swelling pressure to draw fluid back into the disc so as the disc rehydrates, the swelling pressure decreases [149, 150]. Given the short period of rest and the weaker swelling pressure, the driving force for flow into the disc is weaker than for flow out. This implies the presence of direction-dependency to ensure the recovery of lost fluid of the disc. Ayotte et al. measured the resistance ratio between the flow in and flow out of the intervertebral disc of the VEP of ex-vivo sheep specimens [151]. They confirmed the hypothesis that the resistance to the convective flow is direction-dependent, with a greater inhibition to flow out of the disc due to the cartilage endplate obstructing the marrow contact channels (holes) at the disc-bone boundary, resulting in larger drag forces, as shown in Figure 2.31. This also ensures the recovery of fluid lost from the discs during daily activities.

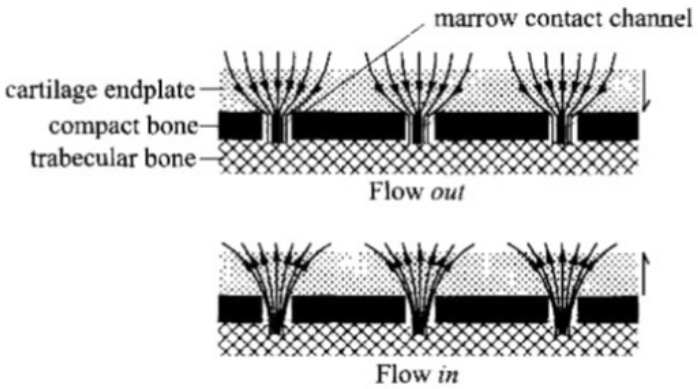

Fig. 2.31 Schematic illustrating the direction-dependent flow of fluid in and out of the intervertebral disc through the marrow contact channels at the boundary between the disc and the VEP [151]. It is shown here that the holes at the boundary of the endplate and the disc are labelled as marrow contact channel. It has been suggested by Ayotte et al. that the flow out of the disc experiences a higher resistance than the flow into the disc from the trabecular bone of the vertebra.

2.6.2 Biomechanical Support

The second biophysical function of the VEPs is to provide mechanical stability to the spine by dissipation of the loading stresses [3]. Lumbar compression forces can go up to 800 Nin the human spine, while standing vertically, but up to 3000 N during heavy lifting [152]. The VEP evenly distributes the stresses in the discs onto adjacent vertebrae due to significant loading during daily activities [3]. Oxland et al. showed that there is a 33 % reduction of the average failure load of the human vertebral body and significant decrease in stiffness when the VEP has been previously removed by a high-speed burr [3, 56, 153]. The graphs in Figure 2.32 illustrate this comparison. This shows that the VEP contributes to the mechanical stability of the vertebral body and the spine.

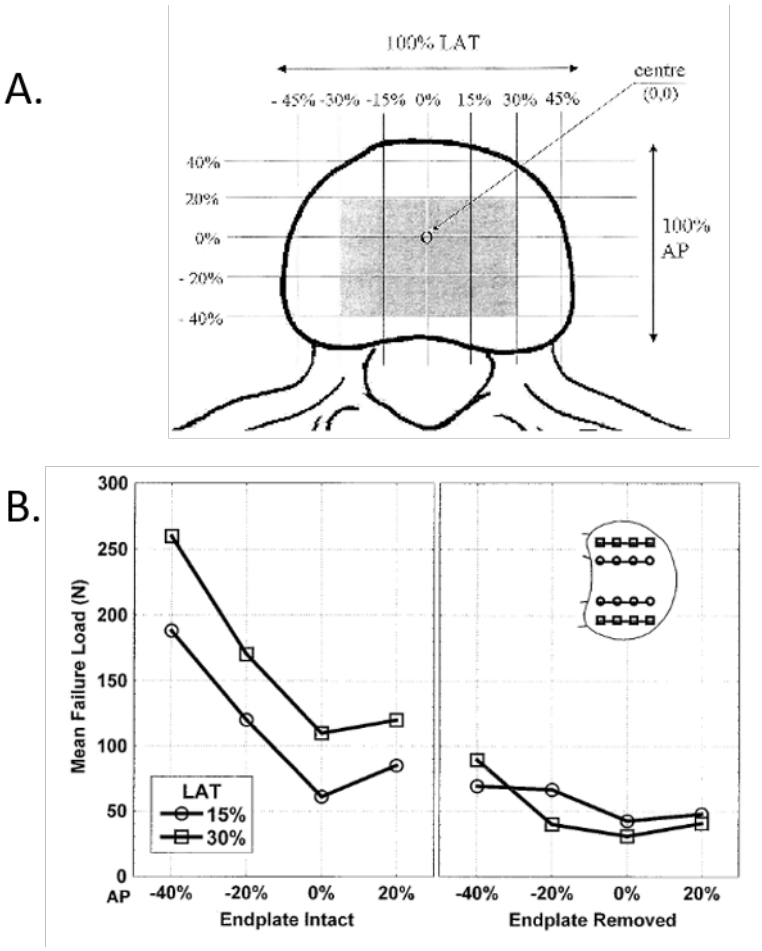

Fig. 2.32 The schematic and graphs show the effect of location of the VEP on the mechanical strength and the effect of endplate removal on the failure load of the vertebra. A: Schematic showing the coordinates of the test sites on the VEP surface. B: Graphs comparing the maximum anterior-posterior and lateral-to-lateral (LAT) failure load in specimens with and without VEP [153]. There was no signifcant difference between the shapes of the 2 failure load maps. However, the sites with the VEP intact were significantly stronger than the sites where the VEP has been removed (P=0.04)

During axial compression of the spine, the VEPs as well as the discs and the underlying trabecular bone undergo deformation [154]. All components of the spinal unit contribute to the deformation and recovery during loading and unloading cycles of daily movement such as standing (1000 N) or light manual work (1500-2000 N) [155]. Loading can occur in compression, flexion, extension and torsion. Bovine studies have demonstrated that application of a compressive load on the spine causes hydrostatic pressure within the nucleus pulposus. This in turn leads to hoop stresses with radial bulging of the annulus but the nucleus is incompressible, being made of ninety percent water. Therefore, the central VEP also bulges [156, 157] to transmit the applied stress away from the disc. A young and healthy

VEP will automatically revert to its original shape if the load is moderate. However, if a continuous and very high load is applied over a long period of time, the VEPs can be considerably and permanently damaged [68, 153, 157]. This will be discussed in further details in the next section addressing degenerative states of the VEP.

2.6.3 Summary of Biophysical Functions of the Endplates

The 2 main functions of the VEP have been identified as the provision of mechanical support and nutritional pathway to the intervertebral disc.

The nutritional pathways have been identified as a 3D intricate network of canals within the VEP layer. This network has been isolated, visualised and quantified, however only in small scale animal models to date, such as rabbits and mice. Although studies have shown that the canal network within the VEP must contain blood vessels which are responsible for bringing nutrients and oxygen to the disc and extracting waste products, the organisation of the blood vessels is still unclear. The nature of bud-like structures reported at the endplate-disc boundary remains unresolved, given the requirement for any blood system to be closed and not open-ended. The mechanism for movement of water from the disc to the VEP has been shown to be dependent on the load-induced disc pressures. However, the mechanism for the biochemical exchange between the blood vessels and the fibres of the disc is also not fully understood.

The VEP provides mechanical support to the disc by evenly distributing the stresses from daily loading of the spine through the strong anchorage of the disc fibres. Given the conflicting requirement for the VEP to be porous for nutritional exchange but thick for mechanical support to the disc, the VEP is also prone to damage. The pathology and the onset of degeneration in the VEP will be discussed in more details in the next section.

2.7 Degeneration of the Vertebral Endplates

The VEP lies in between the very rigid vertebral bone and gelatinous disc. It must be strong enough to disperse significant loads to protect the vertebra bones from fracture but it must also be porous to allow for nutrients to diffuse to the avascular disc. The VEPs have to balance these conflicting biophysical requirements, increasing the likelihood of damage [3, 23]. The VEPs can be subjected to the effects of both ageing and pathological degeneration of the intervertebral disc.

2.7.1 Physiological Degeneration

As previously mentioned, the human VEP also undergoes gradual thinning and slow calcification with age, due to the changes in proteoglycan and collagen content [18, 58, 129, 158]. Antoniou et al. reported that proteoglycan content decreases by 50 % from age of 2 to 80 years whereas the water content decreases by 11 % and the collagen content decreases by about 72 % [18]. The mechanisms causing these compositional changes are still not well understood. However, Aigner et al. used markers of chondrocyte hypertrophy to show that these age-related changes are linked to degenerate discs [159]. This is because an increased concentration of type X collagen shows the presence of hypertrophic chondrocyte which explains calcification. The works of Adams and Wong suggested that changes in the hydrostatic pressure could be controlling degeneration of the VEP, given that hydrostatic pressure regulates chondrocyte functions [29, 160].

Section 2.6.2. explained how the VEPs are subjected to tensile stresses during mechanical loading of the spine. When subjected to very high stresses, the VEP is likely to undergo damage [154]. Irrespective of age, cranial VEPs injuries are more common than caudal VEPs and according to Zhao et al. this could be because the cranial VEPs are thinner and supported by less dense trabecular bone [161]. Similarly, the thinner central region of the VEP register more damage than the thicker peripheral regions [68]. Several factors could be responsible for VEP damage, such as the local morphology of the VEP structure, size and type of mechanical loading and the condition of the adjacent intervertebral disc [3]. The pile up of VEP damage can lead to the creation of localised weak points that then make their way to the edges [162, 163]. Ageing worsens this effect because the central VEP becomes more porous and therefore weaker, leading to the degeneration of the adjacent disc [76, 164, 165]. These changes could be the result of bone remodelling as a response to the stimuli of reduced proteoglycan concentration in the disc or changes in the hydrostatic pressure [166]. Ageing being a major contributor to degeneration, it is difficult to differentiate between degeneration and ageing related health issues [167]. To allow for distinction, it is the general agreement that degeneration includes structural change of the disc because of mechanical loading [168]. As in any other physiological processes, genetics are also involved, such that some genes could be more prone to weaker extracellular matrix in the disc [39, 169, 170].

2.7.2 Pathological Degeneration

Degenerative disc disease is a term used to describe the changes that occur, most commonly in the lumbar region of the spine, that can cause pain [171]. Some characteristic features of disc degeneration include circumferential and radial fissures of the annulus, disc herniation,

biochemical changes and VEP fractures. A theoretical requirement for discogenic pain is pathologic innervation [172, 173].

The VEP region has been shown to be highly populated with blood vessels and highly innervated, with similar densities of nerve endings as the annulus of the disc [136, 174]. The presence of nerve endings explain the implications of VEP as the cause of lower back pain. Lotz et al. found that VEPs removed from patients suffering from chronic lower back pain had high concentrations of proliferated blood vessels, calcitonin gene-related peptide (CGRP) which are marrow pain indicators, and nerve fibers in the underlying trabecular bone [3]. Furthermore, Crock et al. suggested that bone marrow lesions in vertebrae could be caused by the diffusion of inflammatory constituents from the intervertebral discs as the discal tissues have the ability to trigger autoimmune response due to increased concentrations of pro-inflammatory factors [175]. This would imply the VEP has been damaged, leading to increased permeability and communication between the nucleus of the disc and the bone marrow in the vertebra. There is evidence of reported endplate damage association with bone marrow lesions having pain indicators [176, 177] and direct association between endplate damage and increased permeability between the verterba and the disc has been shown [178, 179]. Therefore, different types of endplate defects have been linked to degenerative states of the disc in patients suffering from lower back pain [77, 180, 181]. Endplate defects have been broadly classified under four groups: Schmorl's node, fracture, erosion and calcification. Three of these are shown in Figure 2.33.

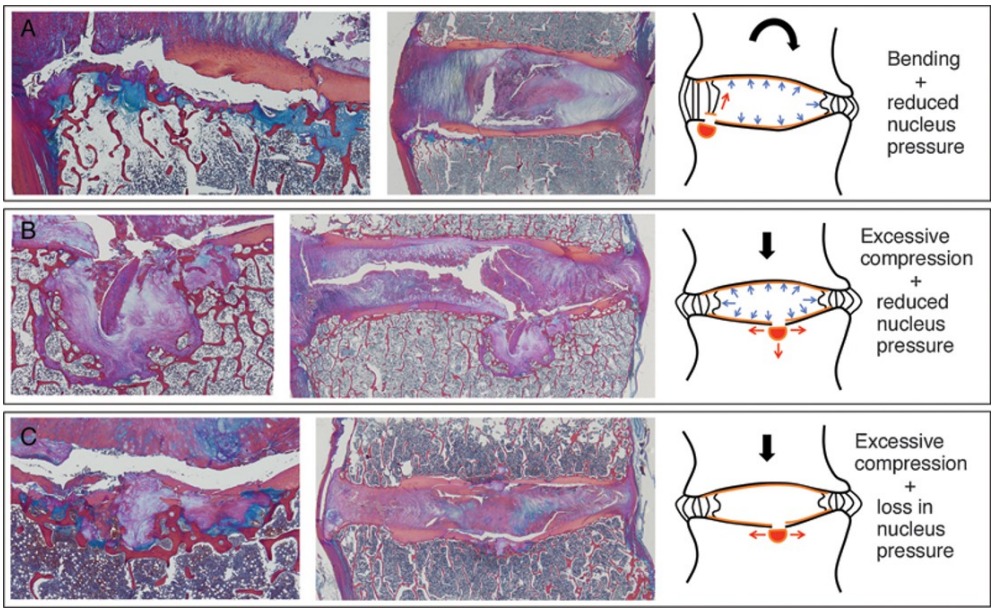

Fig. 2.33 Three groups of endplate defects with their hypothesised etiologies are shown in histological images, stained with hematoxylin and eosin. The red circles on the right hand side schematics represent the areas of the endplate that have been damaged. A: Cartilage endplate avulsion caused by bending motion, leading to traction between the VEP and the inner annulus of the disc. B: Excessive compression of the nucleus pulposus of the disc led to traumatic Schmorl's node with endplate fragments. C: Central portion of the endplate fracture, exposing the trabeculae of the vertebra as a result of excessive compression with a degenerate disc [3]

Although minor endplate defects are hard to image or detect on radiographs, they are considered to be part of the normal aging process of the spine [22, 182]. However, Schmorl's nodes are larger, focal defects on the endplate surface leading to herniations of disc tissue into the adjacent vertebra, resulting in severe back pain [183]. Wang, Videman and Battié began addressing the relationship between the aetiology of endplate lesions and, spinal level and endplate location [60]. They showed that different types of endplate defects had different extents of prevalence at distinct spinal levels and different endplate locations, suggesting unique etiologies for each type of defect. Defects like the Schmorl's nodes were more commonly observed in the central region of the endplate [77], adjacent to the nucleus pulposus of the disc, and in the upper lumbar region of the spine, where the bone mineral density is lower [184] and the endplates have been reported to be weaker than other parts of the spine [56]. Therefore the bone in the VEP and the trabecular bone tend to undergo more severe softening, allowing for the occurrence of nodes [56, 185]. Conversely, erosions and calcifications of the endplate were more common at the peripheral regions of the VEP and in the lower lumbar region of the spine, where the spine undergoes a wider range of motion in

flexion, causing increased extension of the spine and therefore increased traction between the discal tissues and the endplate [186–189]. Calcification and sclerosis in this region could also be the result of consecutive traumatic compression. However, the varying etiologies of the endplate lesions and their role in the onset or advancement of disc failure and lower back pain are still unclear. This suggests the need for further investigation into the VEP function along the spine and the effect of degeneration on the structure of the VEP.

Lotz et al. claimed that the strongest evidence for the role of the VEP in lower back pain is the strong association between discogenic pain and vertebral bone marrow abnormalities [3]. In 1988, Modic et al. were the first to classify vertebral marrow changes seen on magnetic resonance imaging (MRI) into 3 distinct groups and since then, Modic changes are commonly referenced in the literature in relation to pathologies of both the endplates and disc degeneration [190]. Modic classifications of the vertebral body and the VEP in degenerative conditions of the disc are characterised according to the signal intensity from both the T1-weighted and T2-weighted images [190].

Tissue can be characterized by two different relaxation times - T1 and T2. T1 (longitudinal relaxation time) is the time constant which determines the rate at which excited protons return to equilibrium. It is a measure of the time taken for spinning protons to realign with the external magnetic field. T2 (transverse relaxation time) is the time constant which determines the rate at which excited protons reach equilibrium or go out of phase with each other. It is a measure of the time taken for spinning protons to lose phase coherence among the nuclei spinning perpendicular to the main field. The most common MRI sequences are T1-weighted and T2-weighted scans. T1-weighted images are produced by using short time to echo (TE) and repetition time (TR). The contrast and brightness of the image are predominately determined by T1 properties of tissue. Conversely, T2-weighted images are produced by using longer TE and TR times. In these images, the contrast and brightness are predominately determined by the T2 properties of tissue.

Modic type I changes are hypointense on T1-weighted imaging but hyperintense on T2-weighted imaging and are known to represent bone marrow oedema (swelling due to fluid accummulation) and inflammation. MRI images are in black and white with shades of grey. A hyperintensity is an area that appears lighter in color than the surrounding tissues; a hypointensity would be darker in color. Type II changes are hyperintense on T1-weighted imaging, slightly hyperintense on T2-weighted imaging and are associated with conversion of normal red hemopoietic bone marrow into yellow fatty marrow as a result of marrow ischemia, or an inadequate blood supply. Modic type III changes are described as hypointense on both types of imaging and are thought to represent subchondral bone sclerosis, which is the formation of new bone. Certain cases of mixed Modic changes, such as I/II and II/III

have also been reported, suggesting that these changes can convert from one type to another and that they all present different stages of the same pathologic process [191]. The absence of Modic changes represent a normal anatomic appearance of the disc and VEP on the MRI.

Modic changes have also been referred to as 'verterbal endplate signal changes' on the MRI [192]. However, Modic changes on the MRI can affect up to 75 % of the vertebral body and considering the size of the VEP, it is unlikely to be able to resolve the degeneration of the VEP only on the MRI images [193]. This implies that Modic changes cannot be used to assess specific degenerative states of the VEP. Furthermore, it has been reported that innervated endplate damage is poorly visualised on MRI scans because of the short T2 of the endplate, therefore showing little signal with the pulse sequences that have long echo times (TE) [3]. It has been suggested that newer imaging techniques, with shorter TE might provide a better way to differentiate between patients with and without VEP pathological degeneration, as shown in Figure 2.34

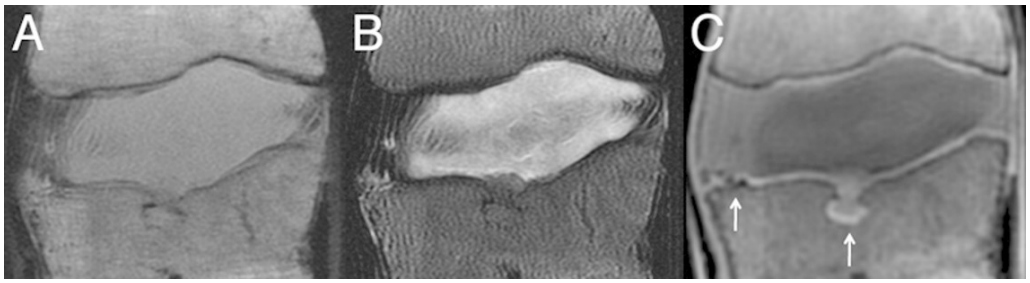

Fig. 2.34 Comparison of 3 different imaging techniques to assess the optimum settings to visualise the VEP with the MRI. A: Midsagittal T1-weighted MRI of L1-L2 motion segment with poor end plate signal. B: T2-weighted MRI of L1-L2 motion segment with poor end plate signal. C: Corresponding ultrashort time-to-echo (UTE) MRI image showing enhanced end plate signal. Arrows indicate end plate defects [3].

2.7.3 Summary of Degenerative States of the Endplates

Given that the VEP has to balance conflicting biophysical demands, it is prone to damage. With age, the VEP experiences wear from constant loading of the spine. The loading mechanism of the spine is also reflected in the patterns of damage in VEP, such that cranial VEPs have been shown to be have higher probability of showing sign of damage than their caudal counterparts. Furthermore, damage of the VEP can also be caused by different pathological degenerations. A close correlation between the degenerative states of the disc and damaged VEP has been shown. However, it is still unclear whether the disc or the VEP is the initiator of the degeneration process. The damage or erosion of VEPs has also been linked with the Modic changes seen in the vertebrae from MRI scans.

Several studies have shown evidence of VEP damage in patients suffering from chronic back pain. Although it is clear that the VEP undergoes damage which eventually leads to pain, the role of the VEP in the origin and pathological development of the pain is still unclear. Degeneration could be starting from the vertebra and leaking through the VEP to the disc. Conversely, the disc could be experiencing degeneration in the first place which leads to erosion of the VEP and the vertebra. Damage occurring in the VEP could also impede the nutrient transport to the disc, leading to degeneration. Therefore, at this stage, the exact precursor to degeneration is still unclear, making diagnosis and treatment of back pain less targeted and with low success rates.

2.8 Relevance of Endplates to Disc Regeneration

The VEP must balance conflicting biophysical functions which means it is subjected to physiological wear and challenges, contributing to its failure. However, it plays a key role in the functioning of the spine. Reviewing the existing literature and experimental designs, the main functions of the VEP as well as its role in maintaining a healthy disc are very clear. There are still considerable gaps in the understanding of the VEP, especially in degenerative conditions, and how failure can be prevented or cured. This is at a time when there are rapid developments of potential methods for the symptomatic treatment of degenerative disc diseases or regeneration of discs. These include intra-discal gene and stem cell therapies, growth factors and biogels to supplement the biomechanically and structurally failing disc [194]. The aims of these trials would be to re-establish nuclear swelling of the disc and introduce more cells in the acellular disc. Figure 2.35 shows a comparison between healthy and degenerated discs and a summary of the potential therapies, taking into account the permeability of the endplates. Regenerative approaches in tissue engineering of the disc aim to restore or preserve the anatomy and function of the whole disc, that is, both the annulus fibrosus and the nucleus pulposus. Therefore, an ideal scaffold for disc replacement should have good biocompatibility, porosity, and the shape, structure and mechanical properties similar to the healthy disc, and surface compatibility with the neighbouring endplates as well. The efficacy of such cellular techniques will depend on a thorough knowledge of the structural integrity of the VEP and its ability to provide a continuous supply of water and oxygen, and mechanical support to the repaired disc.

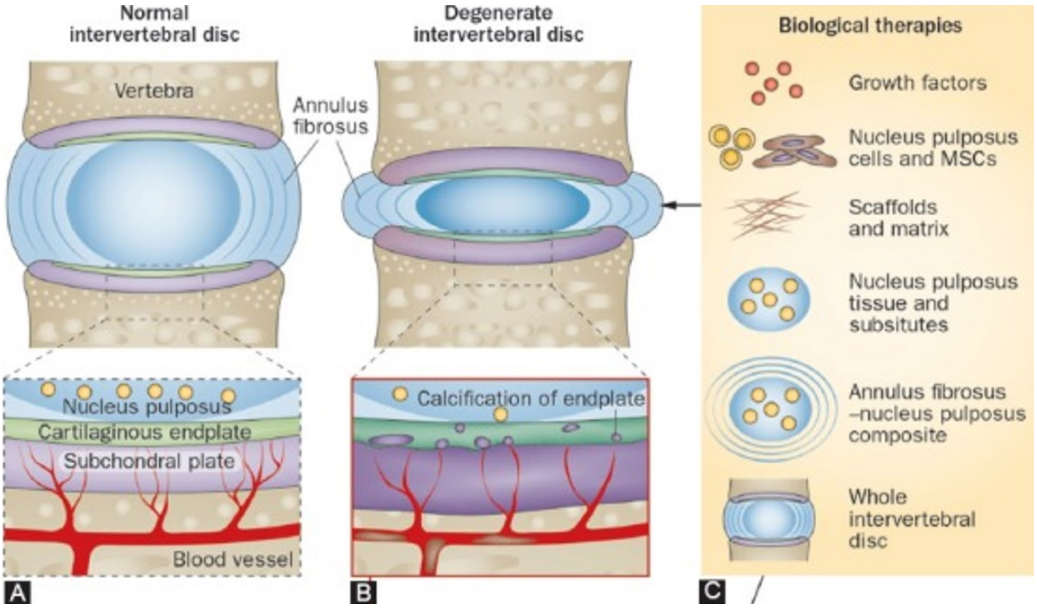

Fig. 2.35 The schematic shows the structure of both healthy and degenerated discs and the possible therapeutic approaches are summarised. A: Nutrient pathways in normal disc through the blood vessels in the bony endplate (labelled as subchondral plate here). B: Nutrient pathways in a degenerate disc which could be caused by the calcification of cartilaginous endplate, occlusion of marrow spaces, atherosclerosis of vertebral arteries, or reduced capillary density, among others. C: Different types of biological therapies for disc repair are listed [195].

Spinal fusion with either autologous graft material or implantable devices are potential procedures of spinal reconstruction. Interbody fusion allows for direct load transmission through the vertebral bodies, restoration of disc height and reduced damage to muscles during surgery. A successful spinal interbody fusion technique needs to address distinct issues such as the provision of axial compressive strength sufficient to resist implant subsidence or collapse, thereby maintaining disc space height and the creation of a biological environment compatible with the process of bone substitution, leading to interbody fusion [196].

In these cases, mechanical stability is crucial for the success of the implants and these require the VEP to be structurally intact for even distribution of the stresses. This is because when the disc is replaced by an interbody fusion implant, most of the axial load is transmitted through the implant and the implant-endplate contact area. If the implant-endplate contact area is too small or incongruent, the implant can create excessive stress at the implant-bone interface, leading to subsidence of the implant. Conversely, if the implant-endplate contact area is too large, there is not enough space left for the graft material to interact with the host bone to create fusion of the vertebral bodies [197].

It has been argued that preservation of bony VEP is desirable for the prevention of implant subsidence. Conversely, a partial removal of the endplate facilitates the incorporation of graft material, increasing the likelihood of the solid interbody fusion [196]. For instance, it has been suggested that both the disc and the VEP should be replaced by titanium cage constructs which would provide better biomechanical properties for successful anterior thoracolumbar column reconstruction [198]. This method has been tried, as illustrated in Figure 2.36, but met with serious complications including recurrent disc herniation, post-operative back pain and subsidence of the cage into the underlying vertebra [199]. This implies that the pre-operative removal of the VEP might not be ideal, and the next steps should be the investigations of the outcome of these surgeries with the VEP intact. Furthermore, the VEP has been shown to provide mechanical support to both the disc and the vertebra, and the VEP should therefore be given due consideration as part of implant design and surgical procedures in the case of spinal reconstructions and disc degeneration. This is why a thorough understanding of the structural and mechanical properties of the healthy VEP would help with disc regeneration therapies and surgical planning.

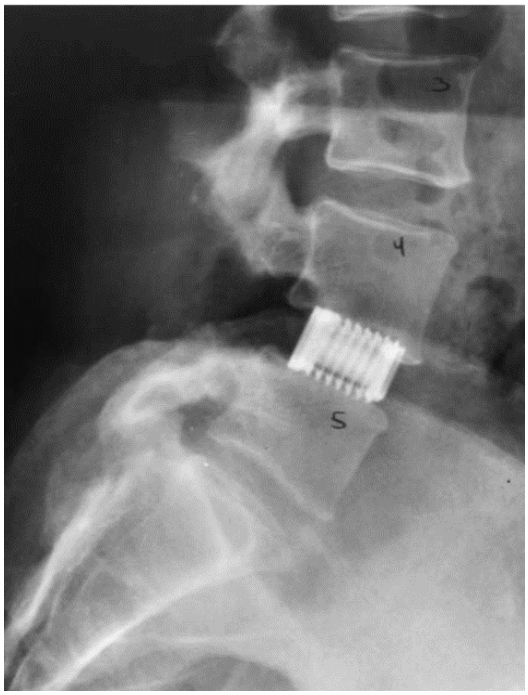

Fig. 2.36 Post surgery radiograph showing the successful implantation of a titanium cage in between the vertebrae at levels L4 and L5 in a patient [199].

2.9 Conclusions and Guiding Questions

Overall, this chapter considered the current understanding of the role of the VEP in the physiological functions of the spine and in the onset of chronic low back pain. This has involved a consideration of the structural properties of the VEP and the characterisation techniques generally used in the research community. This chapter also explored the two main functions of the VEP: offering a nutritional pathway and mechanical stability to the disc. Given the requirements to balance conflicting biophysical demands, the chapter also considered the different mechanisms for degeneration and damage of the VEPs.

It became clear from the discussion in this chapter that there is a lack of a complete understanding of the VEP's structural properties and the 3D network supporting the blood supply in the VEP, acting as the main nutritional pathway to the disc remains poorly visualised or quantitatively characterised. Furthermore, the association of the VEP's structure and the nutritional pathway with degenerative conditions of the spine is also unclear at this stage. Therefore, as shown in the schematic in Figure 2.37, this thesis will aim to investigate these points further, including:

- Characterising the structural properties of the VEP in a sheep model (Chapter 3)
- Understanding the blood supply to the disc and investigating the presence of vascular buds at the disc-VEP boundary in a sheep model (Chapter 4)
- Quantitatively characterising the complex 3D network of canals in the VEP of a sheep model (Chapter 4)
- Investigating the effects of degenerative states of the disc on the structure and nutritional pathway of the VEP in the human spine (Chapter 5)
- Assessing the validity of the sheep model for the investigations of the VEP (Chapter 5)

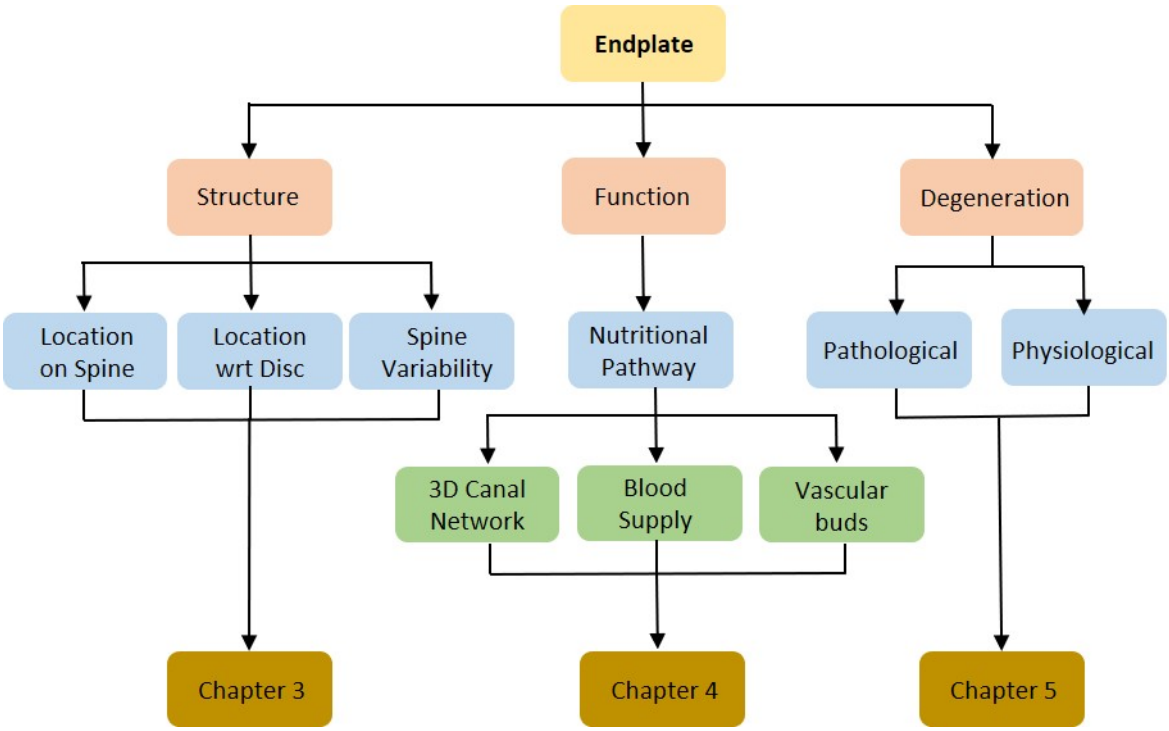

Fig. 2.37 Schematic representing the outline of the thesis with respect to the VEP's structure, nutritional function and changes in degenerative conditions of the spine.

Chapter 3

Investigation of the Structure of Sheep Vertebral Endplates and Vertebrae

3.1 Introduction and Relevance

As discussed in the Literature Review, the verterbal endplates (VEPs) are prone to damage due to conflicting biomechanical functions requiring them to be porous but simultaneously strong. To understand the mechanism of failure in the VEP and the causal relationship between disc degeneration and endplate damage, it is important to first understand how biomechanical function governs the structural properties of healthy endplates. However, as mentioned previously, the structure of the VEP described in the literature is confused with differing nomenclature and an incomplete understanding of the effect of spinal level and location with respect to the disc on the structure of the VEP.

This chapter investigates the use of micro-computed tomography (micro-CT) to visualise and characterise the structure of the VEP and the underlying trabecular bone of the vertebra. This chapter will also investigate the structure of the epiphyseal ring and its role in the mechanical support of the intervertebral disc. This was achieved by quantifying the thickness, porosity, bone mineral density, curvature, trabecular thickness and trabecular separation of the different bone areas under investigation. The VEP samples were grouped according to their spinal level, side and position relative to the disc. All samples were harvested from the same spine and 2 VEPs were used from a second spine to assess the spine to spine variability. The effect of age on the structure of the VEP was also investigated in the sheep model.

3.2 Materials and Methods

3.2.1 Acquisition and Preparation of Sheep Spines

As discussed in the Literature Review, the sheep spines are more readily available than human spines, easy to handle and represent a good biomechanical match to the human spine. This is why the ovine model was used in this study.

In the first instance, a spine from young sheep were sourced, with the central nervous system, the spinal cord, previously removed for biosafety reasons as it can contain the prion protein which causes spongiform encephalopathies such as scrapie, which can also be transmissible. This was based on the advice sought from the Veterinary Medicine Department of Cambridge University. Two additional spines from mature sheep were also sourced, with the spinal cord previously extracted. All spines were frozen at - 80 °C until used. The age and sex of the sheep were recorded. However, only male sheep were used in this study and the breed was unknown. Therefore, the effects of gender and breed were not investigated in this study. Sheep lumbar spines were obtained as summarised in Table 3.1 below:

Sheep	Number of Spines	Age (months)	Sex	Supplier
Young	1	9	Male	Leech and Sons Butchers (Melbourn, Cambridgeshire)
Mature	2	36	Male	Division of Trauma & Orthopaedic Surgery (Cambridge University)

Table 3.1 Details of the number of spines, age and sex of the sheep and the suppliers of the sheep spines used in this study.

Throughout the experiments for this chapter, the cut samples were kept in wet conditions for scanning, to prevent the introduction of artefacts due to partial drying of the samples with the X-rays. There is no loss of contrast due to the attenuation properties of the medium due to the high contrast of bone tissue [79]. The sample holders used were 2 ml graduated Sigma-Aldrich centrifuge plastic vials, as they are transparent to X-rays. The cut samples were individually wrapped in phosphate buffered saline (PBS) soaked tissue paper, stored in the tubes and kept in the fridge for up to five days, the time during which they were imaged, and then frozen at -80 °C. The spines were thawed in the fridge overnight before use. The centrifuge tube was then mounted on the stage of the micro-CT and held upright using dental wax.

3.2.2 Sample Selection and Preparation

Three discs were identified, from levels L3/L4 to L5/L6, from the first mature sheep spine as shown in Figure 3.1. To separate the 2 VEPs of each disc, the soft disc was first identified. Using a scalpel, the disc was sliced into two halves along its transverse plan such that the two neighbouring vertebrae and therefore VEPs were then separated as shown in Figure 3.2, into the cranial and caudal VEPs. This prevents tearing of the disc fibres out of the VEP from any excessive pulling and protects the VEP from any damage or debris from cutting hard bone surfaces. Therefore 3 pairs of VEPs were harvested from this spine. From the second mature spine, 1 pair of VEPs was harvested from spinal level L4/L5. As for the young sheep spine, 2 VEPs were harvested from level L3/L4.

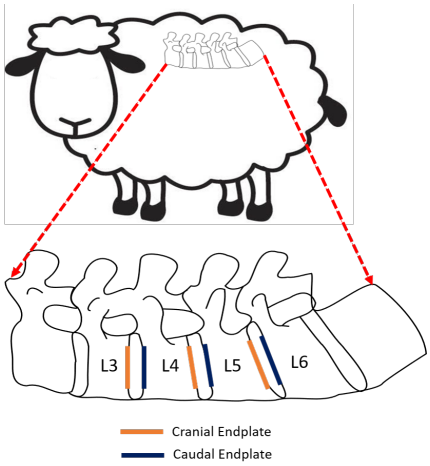

Fig. 3.1 Schematic highlighting the location of the L3/L4, L4/L5 and L5/L6 levels from which cranial and caudal VEPs were harvested in a sheep spine.

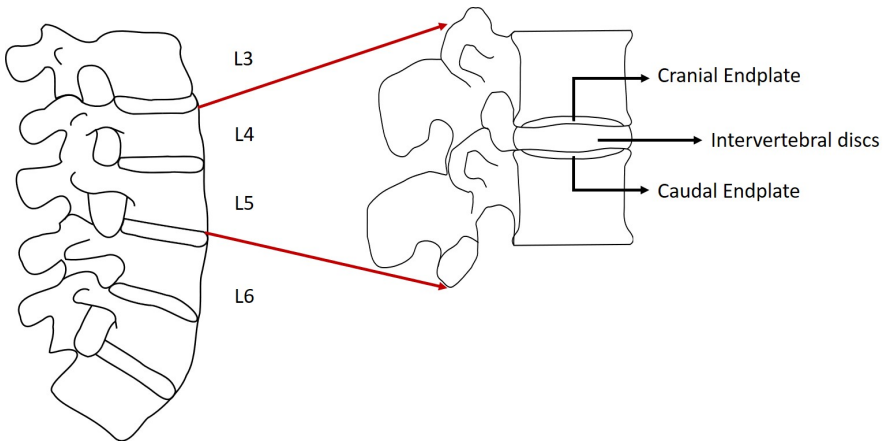

Fig. 3.2 Schematic of the sheep lumbar spine showing a close up on the right of a disc sandwiched between the two types of VEPs, caudal and cranial.

To successfully map the properties of the whole endplate, the area was split into a grid of 9 areas to be imaged This will enable distinction between anterior/posterior, central/peripheral and right/left regions. The 9 regions were cut using an IsoMet 1000 Precision Sectioning Saw at the Veterinary School in Cambridge and the layout of the ROIs were selected while avoiding the epiphyseal ring, as shown in Figure 3.3. Therefore, 54 samples were used from the 6 VEPs in the first mature spine and 18 samples were used from the 2 VEPs from the second mature spine. The samples were imaged using a micro-CT scanner which will be discussed in mored details in the next section.

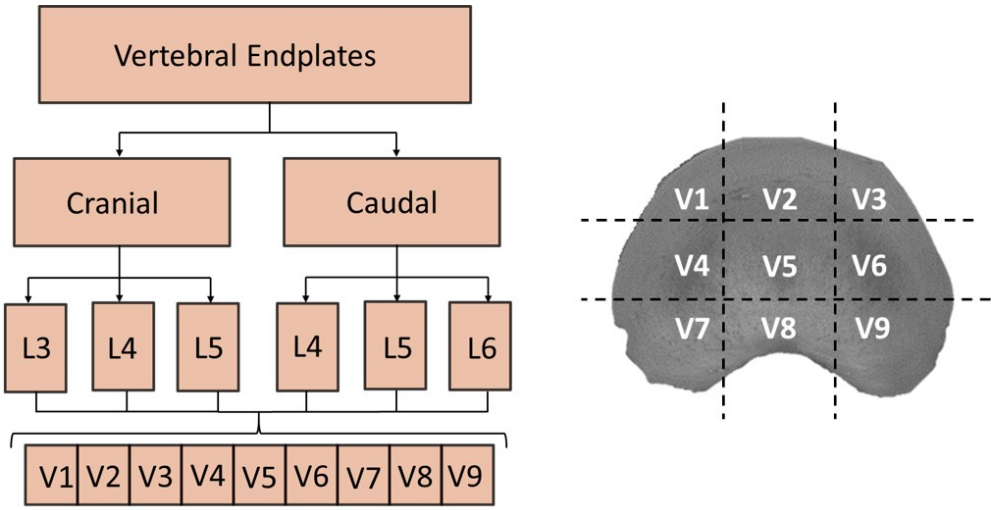

Fig. 3.3 Flowchart showing the different categories of the VEP used, namely their position with respect to the disc as cranial or caudal, their spinal level L3 to L6 and the area of the VEP denoted by V1 to V9 which are shown in the right-hand side schematic.

From the grid of 9 samples, 14 circular regions of interest (ROIs) each of radius 2.5 mm were used for analysis, as shown in Figure 3.4.

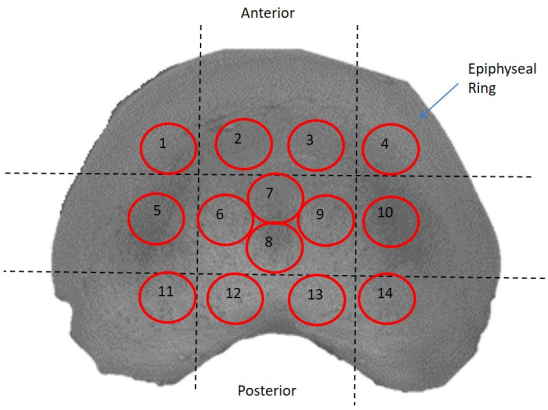

Fig. 3.4 The grid lines represent the cutting line to make 9 separate samples, from which 14 ROIs were selected, as indicated by the red circles.

3.2.3 Micro-Computed Tomography Procedure

For this study, micro-computed tomography (micro-CT) was used to image the bone samples for structural characterisation. Samples from the mature spines and the young spine were scanned using a Bruker Skyscan 1172 micro-CT scanner. Following a "scout" scan, a voltage of 65 kV and current of 153 μA were used in this study. A 0.5 mm aluminium filter was used to further reduce the beam hardening by absorbing low-energy X-rays to optimise transmission. Samples were centered carefully on the stage within the apparatus. Before scanning, flat-field correction was carried out to remove artefacts caused by variations of the pixel-to-pixel sensitivity of the detector.

A compromise between the size and time of the scans was reached from the "scout" scan and all further scans were taken with the camera in the medium range, a rotation step size of 0.4 °, frame averaging of 2 and exposure time of 7.5 seconds. To image the smaller features of the bone architecture, a pixel size of less than 10 μm is recommended. In this study, the scanner allowed for a pixel size of 4.89 μm to be used.

Reconstructions of the scanned images were carried out using the software, NRecon. Thresholding was kept constant (minimum: 0, maximum: 0.1) for all the scans to ensure reliability for comparison purposes. NRecon allows smoothing, ring artefact reduction and beam hardening correction. Based on trial runs, the optimum settings were one pixel, 20 % and 10 respectively.

3.2.4 Histomorphometric Properties of the Endplate

The structure of the VEP from the mature sheep spines only was quantitatively characterised by the histomorphometric parameters which will be explained in this section. From the images, the upper boundary of the VEP was identified as the clear contrast boundary between bone and soft tissue as the latter is shown as empty space in the greyscale thresholding. The lower boundary was chosen as the first marrow space encountered vertically underneath the VEP in the trabecular bone of the vertebra.

Thickness

Thickness of the VEP was measured by loading the reconstructed images in the software CTAnalyser (CTAn). Thickness varies greatly in the VEP, therefore for each of the 54 samples, 3 distinct regions were selected. On both sides of the 2D image, 0.5mm from the edge was measured. Given that the radius of the circular ROI is 2.5mm, as explained in Section 3.2.2, the middle point of the remaining length of 1.5mm was found. The 3 regions, shown by the orange arrows, selected were therefore 1 in the centre and at 2 of them at 0.5mm from the edges, as shown in Figure 3.5. Vertical lines were drawn from the upper boundary of the VEP to the lower boundary at each region, shown as white lines, and the vertical height of each line represented the VEP thickness at that specific location. The average thickness of the 3 regions was then used as the mean thickness of the VEP sample and the standard deviation of the thickness for the 3 regions was calculated as the error in the thickness measurement.

The VEP was split into 9 samples V1 to V9 but some of these samples have more than one region of interest (ROI), such that V2 and V8 have 2 ROIs each and V5 has 5 ROIs. The thickness measurements for these samples were therefore averaged for all their ROIs. The schematic in Figure 3.6 shows the visual representation of the location on the VEP surface for each data point used for plotting the data.

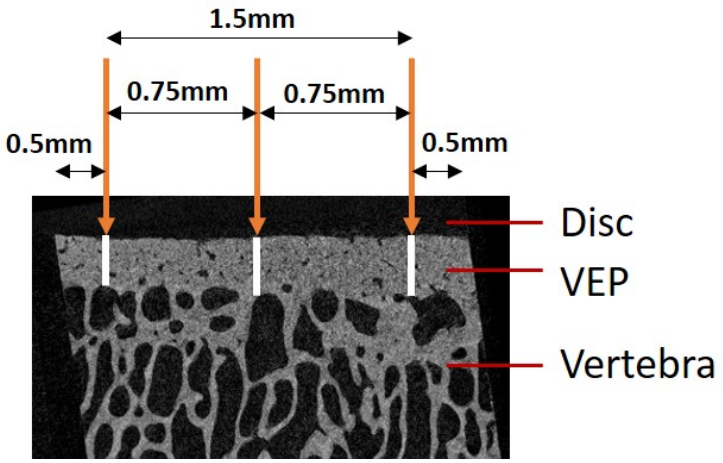

Fig. 3.5 Schematic showing the location of the 3 different points where the thickness of the VEP was measured. The orange arrows represent the locations where thickness was measures, determined by the 0.5mm distance from the edges and the middle point. The white lines indicate the thickness measured at these locations.

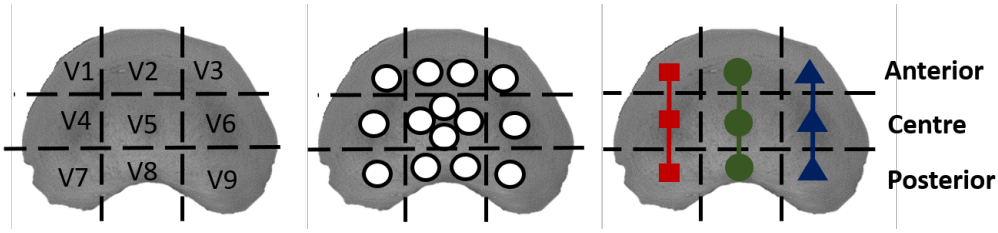

Fig. 3.6 Schematic showing the 14 regions of interests from which VEP thickness were measured and the visual representations of the 9 regions for which data points were plotted in the following graphs.

Bone Volume Fraction and Porosity

Using the CTAn software, the reconstructed images of the VEP region were thresholded from greyscale levels 80 to 255 to segment the foreground from the background, then the image was de-speckled by removing all smaller objects created by background noise. Finally, the bone volume fraction as a percentage $(\frac{BV}{TV})$ was generated, with the associated confidence intervals, as the ratio of volume occupied by bone material (BV) to the total volume (TV) of the region of interest. Porosity of the VEP was defined as the difference between full volume fraction and bone volume fraction, as shown in Equation 3.1. The error associated with each measurement was calculated from the confidence intervals.

$$Porosity = 100 - \frac{BV}{TV} \tag{3.1}$$

The VEP was split into 9 samples V1 to V9 but some of these samples have more than one region of interest (ROI), such that V2 and V8 have 2 ROIs each and V5 has 5 ROIs. The porosity measurements for these samples were therefore averaged for all their ROIs. The schematic in Figure 3.6 shows the visual representation of the location on the VEP surface for each data point used for plotting the data.

Bone Mineral Density

For the case of bone mineral density (BMD), the X-ray attenuation of mineralised tissues, such as bone, is dominated by, and therefore can be approximated as, the X-ray attenuation of the mineral compound calcium hydroxyapatite (CaHa) [61]. Using 2 phantoms of known CaHa densities, a high concentration and a low concentration, their corresponding X-ray attenuation coefficients were measured and used to calibrate the CTAn software. This enabled the measurement of CaHa density or bone mineral density in gcm^{-3} of the VEP from their corresponding attenuation coefficients measured from their micro-CT images.

BMD in this study was therefore defined as the density of calcium hydroxyapatite (CaHa) per volume of bone tissue, expressed as gcm^{-3}. The density measurement was restricted to within the volume of the calcified bone tissue of the VEP only, excluding surrounding soft tissue. The software generated the BMD values with their associated standard deviation values for each of the ROI of the samples from the mature sheep spine.

Epiphyseal Ring

The average thickness, d, of the epiphyseal ring was measured, using Fiji ImageJ. The reconstructed micro-CT images were loaded in the programme and a straight line was drawn from the visible epiphyseal boundary and the edge of the sample, as shown in the schematic in Figure 3.7. The whole VEP surface can be split into 4 sections: anterior, posterior, left and right sides. Given that the VEP surface was sectioned into 9 distinct samples in this study, the anterior section was therefore assumed to be made up of V1, V2, V3, the right section consisted of V6, V9, the left section consisted of V4 and V7 while the posterior section was made up of V8, as shown in Figure 3.7. For each of the V sections, 3 lines were drawn and 3 values of d measured. The average ring size was then calculated from all the V samples making up the specific ring region, as shown in Table 3.2. The standard deviation of the measurements for each of the 4 sections was also calculated.

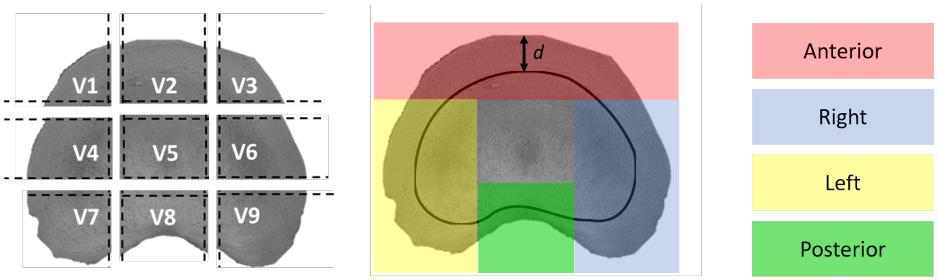

Fig. 3.7 Schematic showing the original 9 sections of the sectioned surface of the VEP on the left. In the middle, the colours identify the 4 sections of the epiphyseal ring, labelled as anterior, right, left and posterior. An example of the ring thickness d is also marked between the boundary of the epiphyseal ring and the edge of the surface of the bone.

Ring region	**Region of VEP covered**
Anterior	V1, V2, V3
Right	V6, V9
Left	V4, V7
Posterior	V8

Table 3.2 Summary of the 4 sections of the epiphyseal ring and the V regions of the VEP surface which make up each of these sections.

Curvature

In order to measure the curvature across the sagittal and coronal planes, the images across different samples had to be "stitched" back together to provide a continuous image of the transverse plane of the VEP, which was discontinuous due to the VEP being cut into a grid of 9 regions. As shown in Figure 3.8, the images were "stitched" together such that lines A, B, C consist of samples V2, V5 and V8. Lines D, E and F comprise samples V4, V5 and V6. As shown in Figure 3.8, curvature was measured at 3 sagittal lines (A to C) and at 3 coronal lines (D to F). Lines A, B and C measured the curvature from anterior to posterior edges whereas lines D, E and F measure the curvature from right to left sides of the VEP, as shown in Figure 3.9. A curve was drawn, mapping the curved surface of the VEP at the specific line location and the curvature of each curve was measured using the Kappa Plugin in Fiji. The average curvature and standard deviation in the measurements for anterior to posterior for each VEP were then calculated as an average of lines A, B and C, and the distribution of the data respectively. Similarly, the average curvature and standard deviation in the measurements for right to left curvature for each VEP were calculated from lines D, E and F. A summary of the analysis is shown in Table 3.3.

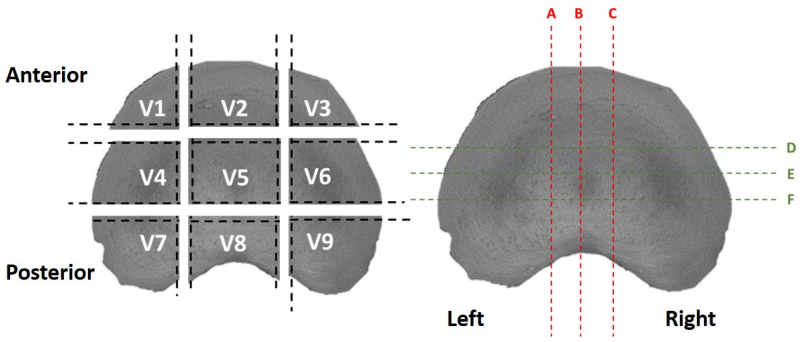

Fig. 3.8 Schematic of the location of categories V1 to V9 of the VEP (left) and the sagittal lines A, B and C shown in red, coronal lines D, E and F shown in green (right).

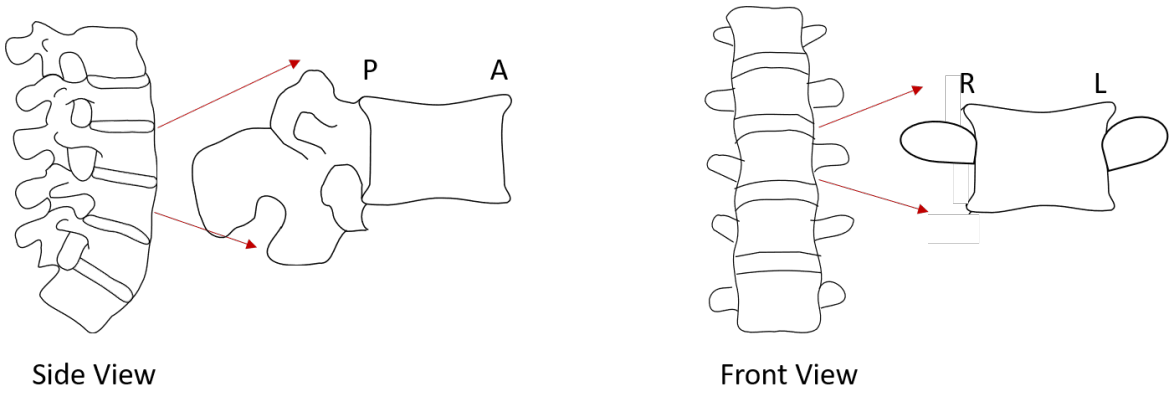

Fig. 3.9 Left: Schematic showing the side view of the lumbar spine with a close up of the curved edge of the VEP surface at the top and bottom of the vertebra from anterior (A) to posterior (P) sides. Right: Schematic showing the front view of the lumbar spine with a close up of the curved edge of the VEP surface at the top and bottom of the vertebra from right (R) to left (L) sides.

Curvature	Curvature of lines averaged	Regions on VEP joined by the lines
Anterior-Posterior	A, B, C	V2, V5, V8
Right-Left	D, E, F	V4, V5, V6

Table 3.3 Summary of the curvature analysis of the VEP. The lines A, B and C join the regions V2, V5, V8 of the VEP and therefore their individual curvatures can be averaged to calculate the curvature from the anterior to posterior edges of the VEP. Similarly, line D, E and F are drawn through regions V4, V5 and V6. Their individual curvatures can be averaged to obtain the curvature of the right to left edges of the VEP.

3.2.5 Analysis of the Trabecular bone of the Vertebrae

The upper boundary of the trabecular bone is at the boundary with the VEP. Therefore, a cylindrical region of interest at 5mm below this boundary of 10 mm in depth and 2.5 mm cross-sectional diameter was selected, as shown in Figure 3.10. The cylindrical ROI was always selected to be at the middle point of the sample to avoid edge effects. The samples were then analysed using CTAn. The average thickness of the trabeculae (Tb Th), the average distance (separation) between the trabeculae (Tb Sp), the bone volume fraction (BV/TV) and the bone mineral density (BMD) for the trabecular bone of the vertebra were generated by the software and recorded. This was carried out for the samples from the mature spines.

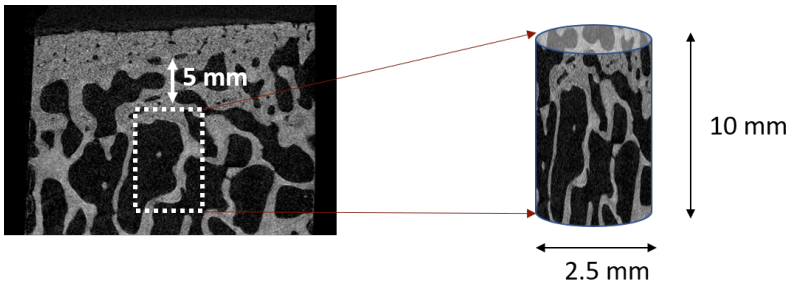

Fig. 3.10 The white dotted outline shows the region of interest of the trabecular bone, beneath the boundary with the VEP. The enlarged cylindrical region of interest on the right shows the 10 mm depth and diameter of 2.5 mm selection for analysis of the trabecular bone.

3.2.6 Statistical Analysis

Statistical analysis was carried out using the software OriginLab to check for statistical significance of the measurements for this study. Normality of the data distributions was first checked, then a Levene's test was used to ensure homogeneity of variances between the different groups of data. If the data passed both tests, a one-way ANOVA parametric test was used. If either one of the two conditions were not met, a non-parametric test, Kruskal-Wallis ANOVA test was used instead. In both ANOVA tests, the data was considered statistically significant only if the evaluated P-value was smaller than 0.05. When comparing 3 or more groups of data, the ANOVA test identifies if the results are significant overall, but a post-hoc Tukey test is carried out to identify exactly where those differences lie.

3.3 Results

3.3.1 Imaging the Vertebral Endplates

The VEP was clearly identified as the denser layer of bone at the boundary between the soft tissue of the disc and the hard tissue of the vertebra as shown in the coronal images of Figure 3.11. This layer showed marked differences from the spongy-type of bone observed in the trabecular bone of the vertebra. The soft tissues of the disc, despite being still attached to the VEP, was not visible on the CT images due to their naturally lower absorption of X-rays compared to the mineralised bone tissues. The transverse section of the VEP appears smaller than the one of the trabecular bone because of the curved nature of the top layer of the VEP. Furthermore, a layer of cortical bone was observed as a dense layer of bone surrounding the trabecular bone in the vertebrae, as indicated by the white arrows in Figure 3.11

There are considerable observed structural differences in the different VEP areas, for example, samples from the central region of the VEP (sample marked as region V5) are seen to be thinner than samples from the peripheral regions of the VEP (sample marked as V2). A representative comparison is shown below in Figure 3.12. These differences are further investigated and quantified for all samples in the next section.

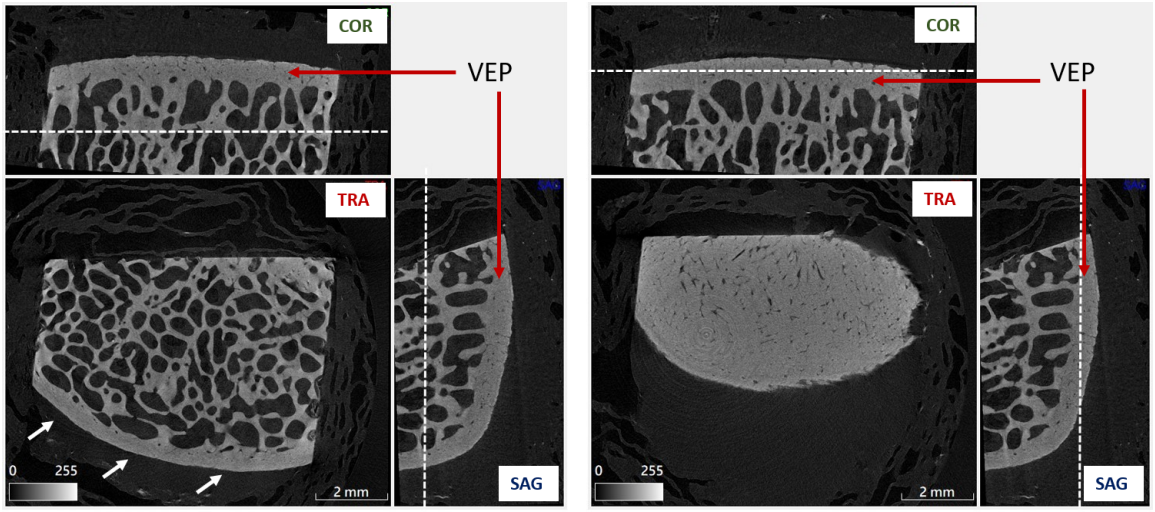

Fig. 3.11 Reconstructed images of the samples from L3/L4 cranial VEP at the V2 cut section. The white dashed lines show the slice location on the coronal (COR) and sagittal (SAG) views exhibited in the corresponding transverse (TRA) view. The soft tissue of the disc are still attached to the VEP but are not visible on the micro-CT images. The greyscale bar represents the X-ray absorption with zero showing no absorption as white and 255 showing maximum absorption as black and the scale bar shows 2 mm. Left: The trabecular bone is shown as spongy with relatively large pores. Right: The VEP is shown as a dense layer of bone with small pores. The VEP transverse slice appears smaller than the trabecular bone due to the curved shape of the top layer of the VEP. The white arrows show the cortical bony casing enclosing the trabecular bone in the vertebra.

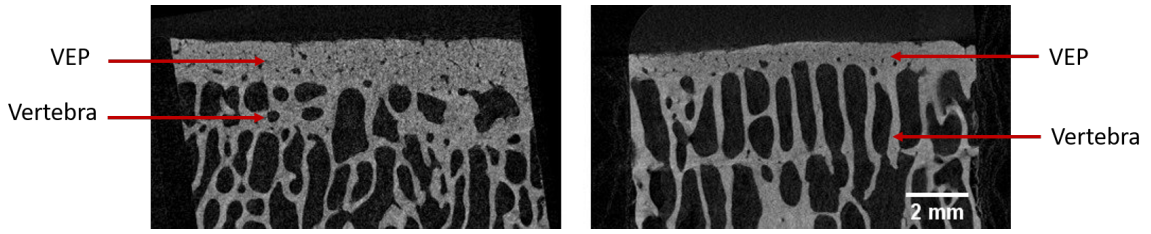

Fig. 3.12 Reconstructed micro-CT images from L3/L4 cranial VEPs from an anterior region (V2) on the left and from the centre (V5) on the right. The anterior region has a thicker VEP than the central one. The scale bar represents 2 mm for both images.

Samples from the young sheep showed the absence of clear boundaries delineating the dense layer of bone of the VEP from the trabecular bone. However an area of tangled bone projections was seen, extending from beneath the disc layer to eventually merge with the trabecular bone as shown in Figure 3.13. These projections were absent in samples from the mature sheep spine. In the latter case, VEP boundaries could be distinctively identified from the trabecular bone and the disc surface, and was seen as a dense layer of bone.

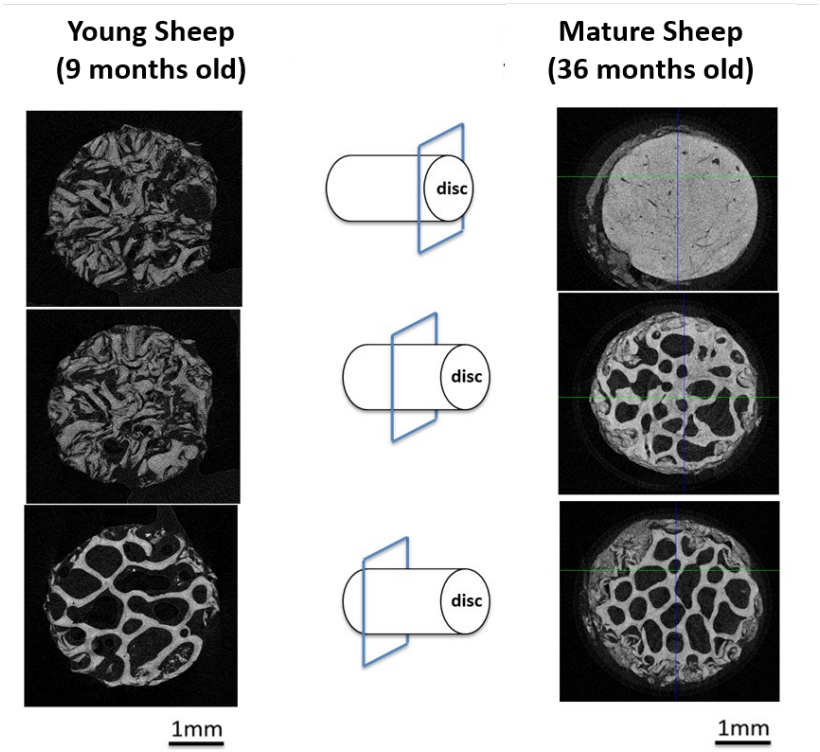

Fig. 3.13 A ROI from the central region of a caudal VEP at level L3/L4 from the young sheep spine (left) and a similar ROI from caudal VEP at level L3/L4 from a mature sheep spine (right) were compared. The image slice from the ROI at the boundary with the disc showed the presence of the dense layer of bone of the VEP in the mature sheep but was absent in the young sheep sample. The slice further down the ROI further from the disc showed the presence of the trabecular bone of the vertebra in the mature sheep but the presence of bony protrusion in the younger one. Further down the cores, the slices showed the sponge-like structure of the trabecular bone structure in both cores, although the struts were further apart in the young sheep vertebra than the mature one.

3.3.2 Structural Properties of the Vertebral Endplates

Thickness

The distribution of VEP thickness across the VEP surface and along the spinal levels is shown in Figure 3.14. Across all VEPs, the central regions were significantly thinner than the surrounding areas. Cranial VEPs with respect to the disc were significantly thicker ($P < 0.05$) than their caudal counterparts. Cranial VEPs also had thicker anterior regions than posterior region but caudal VEPs had thicker posterior regions compared to the anterior ones. The thickness of VEPs also increased moving down the spinal levels.

The VEPs from L4/L5 of Spine 2 exhibited the same trends in thickness as the VEPs from the same level in Spine 1, and the thickness measurements were of similar magnitudes. The cranial VEPs were also significantly thicker ($P < 0.05$) than the caudal VEPs in Spine 2.

The thickness measurements with the associated standard deviations as error bars were plotted in Figure 3.15. The thickest measured VEP was 1.010 ± 0.014 mm at the anterior region at cranial side of L5/L6 and the thinnest VEP was 0.455 ± 0.025 mm at the central region at caudal side of L3/L4.

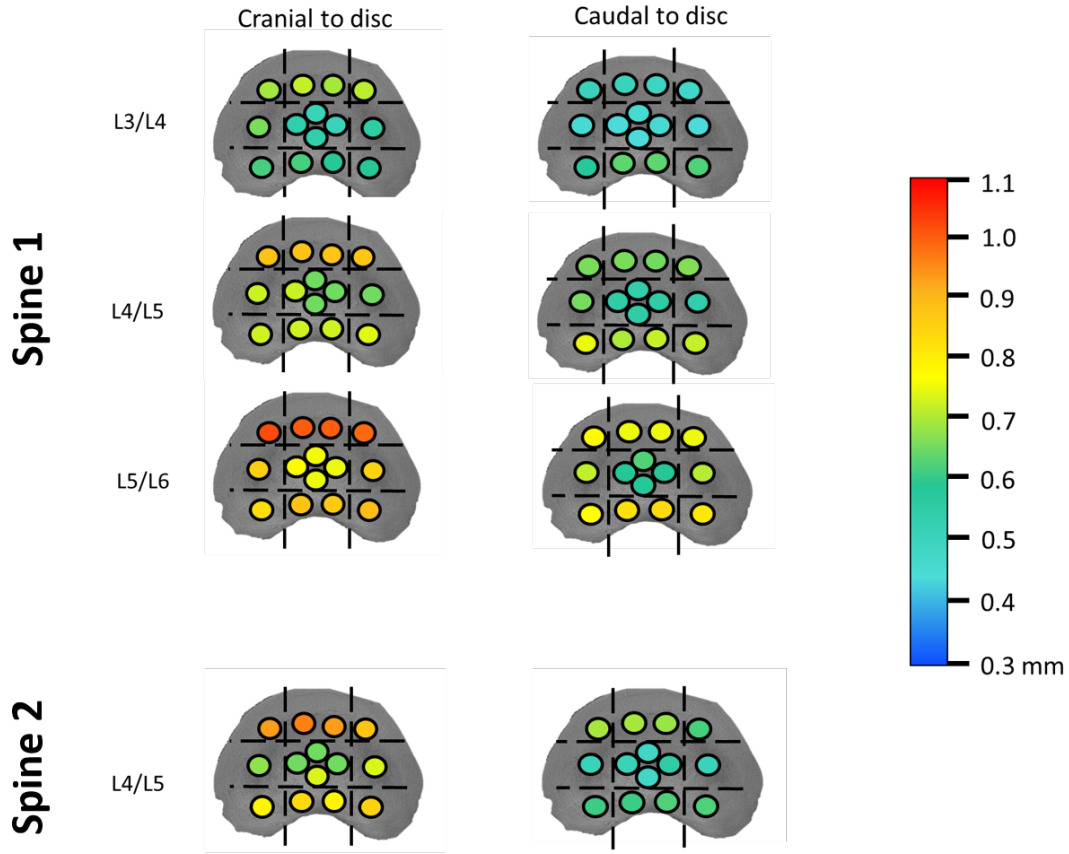

Fig. 3.14 The colour maps represent the thickness of specific regions of interest of the VEP at different spinal levels and on different sides of the disc for the 2 mature spines used in this study. The central regions of the VEP are always thinner than the peripheral regions. The cranial VEPs are significantly thicker than the cranial ones at the same spinal level for both spines 1 and 2. The anterior region of the VEP are thicker than the posterior ones in the cranial VEPs, but the opposite is true for the caudal VEPs. The VEP samples from Spine 2 showed the same trends as the the VEPs from the same spinal level from Spine 1. The colour bar on the right shows the thickness (mm) assigned to the colours.

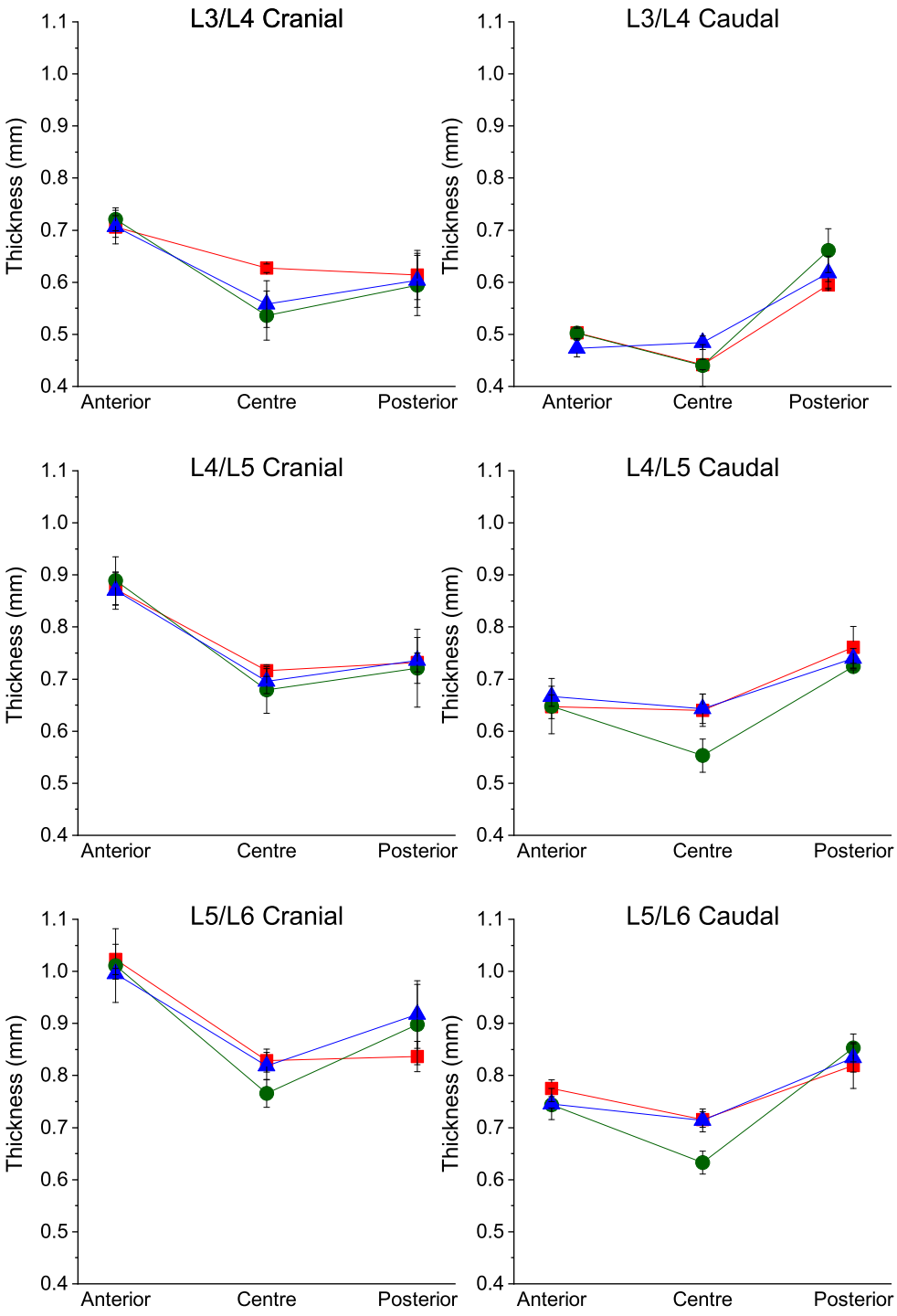

Fig. 3.15 The series of graphs shows the thickness variation of the VEP from the mature sheep spine at different spinal levels, side of disc and region of the VEP. Thickness of the VEP is always lowest at the central regions in all 6 graphs. The left hand side graphs show that cranial VEPs are always thicker than their counter caudal VEPs, shown in the right hand side graphs. Thickness increases down the spine from L3/L4 to L5/L6. Anterior regions are thicker than posterior ones for the cranial VEPs but are thinner than posterior ones for caudal VEPs. The error bars represent the standard deviation of the data. The schematic in Figure 3.6 shows the physical locations on the VEP surface of each point on the graphs, labelled with different colours and shapes of markers.

Porosity

Porosity of the VEP at different spinal levels and regions of the VEP are shown in Figure 3.16. Across all VEPs the central region was significantly the most porous compared to the peripheral regions. The cranial VEPs were significantly less porous ($P < 0.05$) than their caudal counterparts. Anterior regions of cranial VEPs were less porous than the posterior regions but anterior regions of caudal VEPs were more porous than the posterior ones. Furthermore, VEPs further down the lumbar spine (L5/L6) were less porous than those higher up (L3/L4).

The VEPs from L4/L5 of Spine 2 exhibited the same trends in porosity as the VEPs from the same level in Spine 1 and the porosity measurements were of the same magnitudes. The cranial VEPs were also significantly less porous ($P < 0.05$) than the caudal VEPs in Spine 2.

The porosity measurements with the associated standard deviations as error bars were plotted in Figure 3.17. The schematic in Figure 3.6 showed the visual representation of the location on the VEP surface for each data point plotted in the graphs below. The least porous region of the VEP was measured as 13.46 ± 1.67 % at the anterior edge of the cranial L5/L6 VEP and the most porous was measured as 32.22 ± 10.40 % at the central region of the L3/L4 caudal VEP.

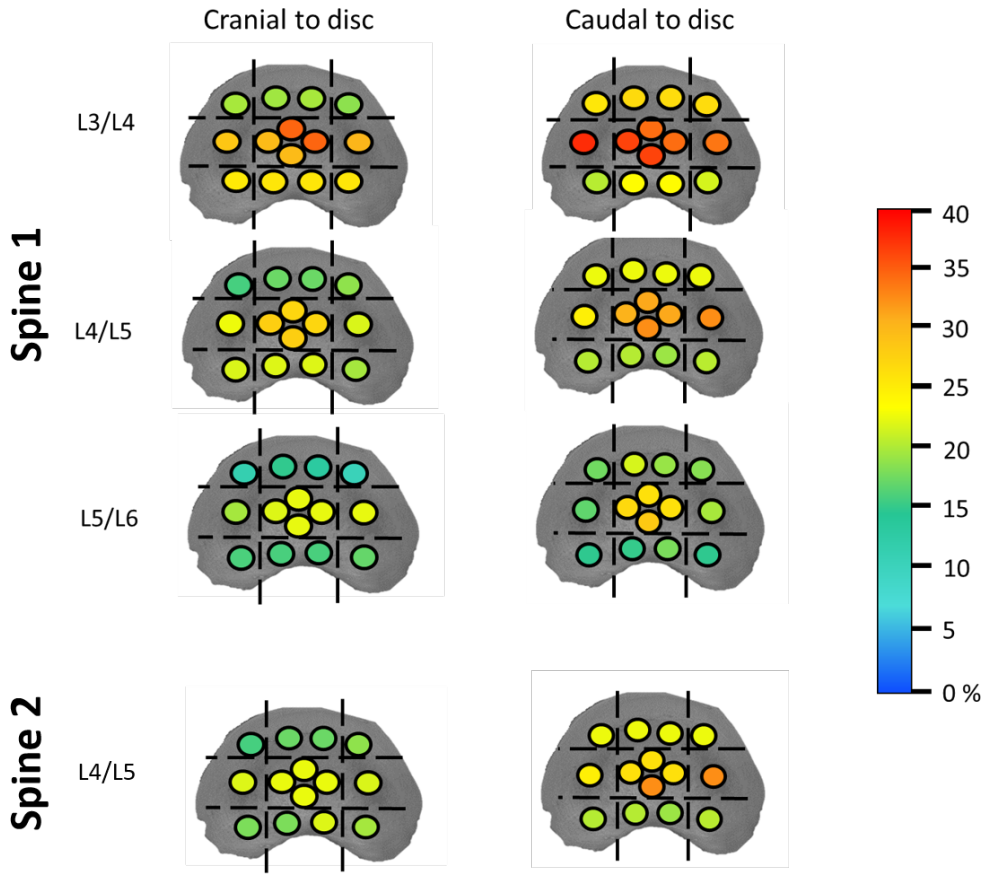

Fig. 3.16 The colour maps represent the porosity of specific regions of interest of the VEP at different spinal levels and on different sides of the disc for the 2 spines used in this study. Porosity of the VEP is always highest at the central regions in all the VEPs. The cranial VEPs were significantly less porous than their counter caudal VEPs. The VEP samples from Spine 2 showed the same trends as the the VEPs from the same spinal level from Spine 1. The colour bar on the right shows the porosity (%) assigned to the colours.

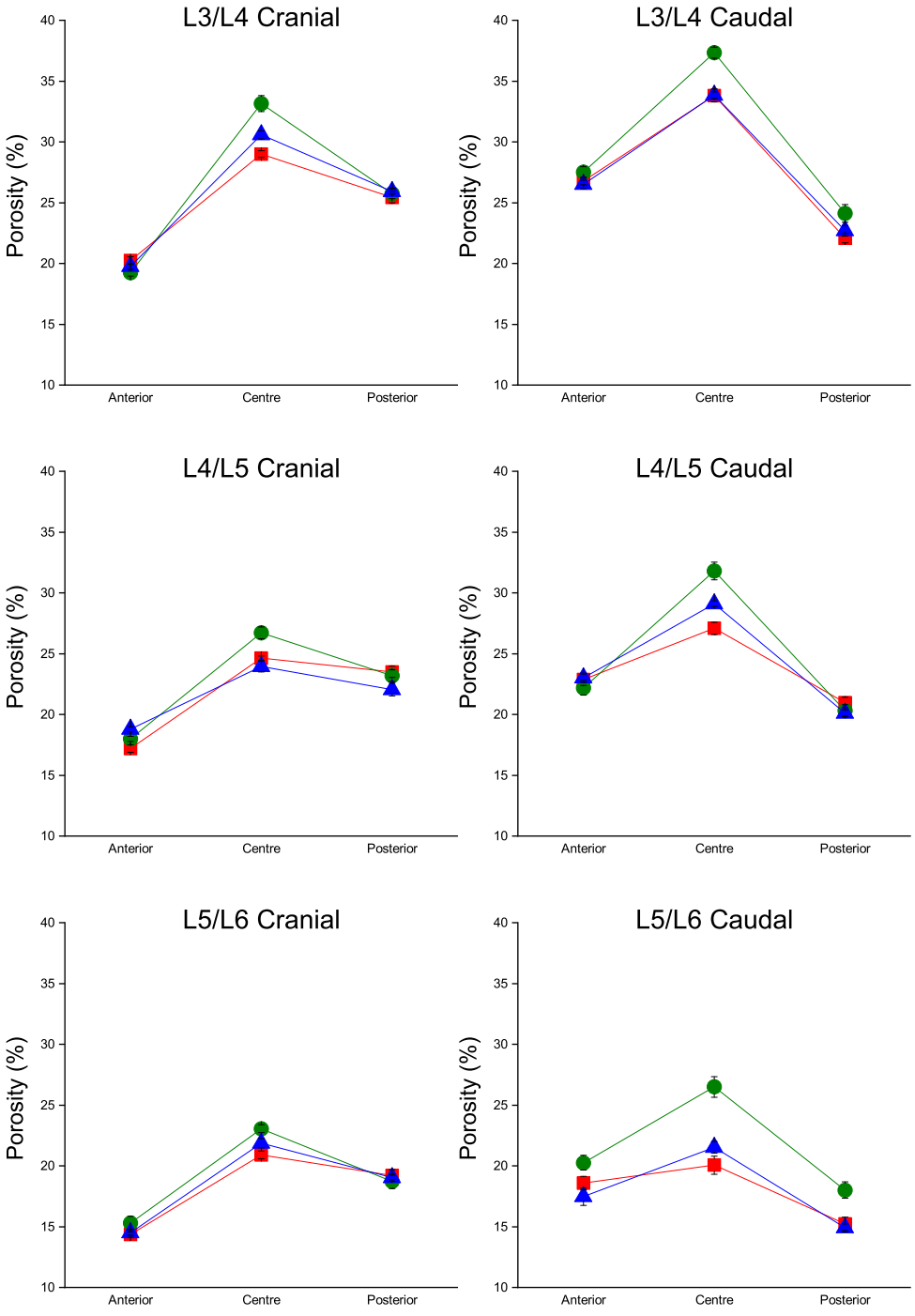

Fig. 3.17 The series of graphs shows the porosity variation of the VEP from the mature sheep spine at different spinal levels, side of disc and region of the VEP. Porosity of the VEP is highest at the central regions in all 6 graphs. The left hand side graphs show that cranial VEPs are always less porous than their counter caudal VEPs, shown in the right hand side graphs. Porosity decreases down the spine from L3/L4 to L5/L6. Anterior regions are less porous than posterior regions for the cranial VEPs but are more porous than the posterior regions in caudal VEPs. The error bars represent the standard deviation of the data.The schematic in Figure 3.6 shows the physical locations on the VEP surface of each point on the graphs, labelled with different colours and shapes of markers.

Bone Mineral Density

BMD measured from the reconstructed micro-CT images showed a significant decreasing trend down the spine from L3/L4 to L5/L6, as shown in Figure 3.18. At each spinal level the cranial VEP had a significantly higher mean BMD ($P < 0.05$) than the corresponding caudal VEP. There were no observed trends of the BMD at different locations (V1 to V9) on the same VEP surface and therefore the measurements were plotted as box plots, to compare the BMD values at different spinal levels and sides of the disc, as shown in Figure 3.19. The measurements of the BMD at the 9 regions for each VEPs were averaged and the standard deviation from the mean were shown as the whiskers.

The samples from Spine 2 showed the same trends, of significantly higher BMD ($P < 0.05$) in the cranial VEPs than caudal VEPs with no clear trend across the VEP surface. However, the BMD values were smaller than the ones from the same L4/L5 level in Spine 1.

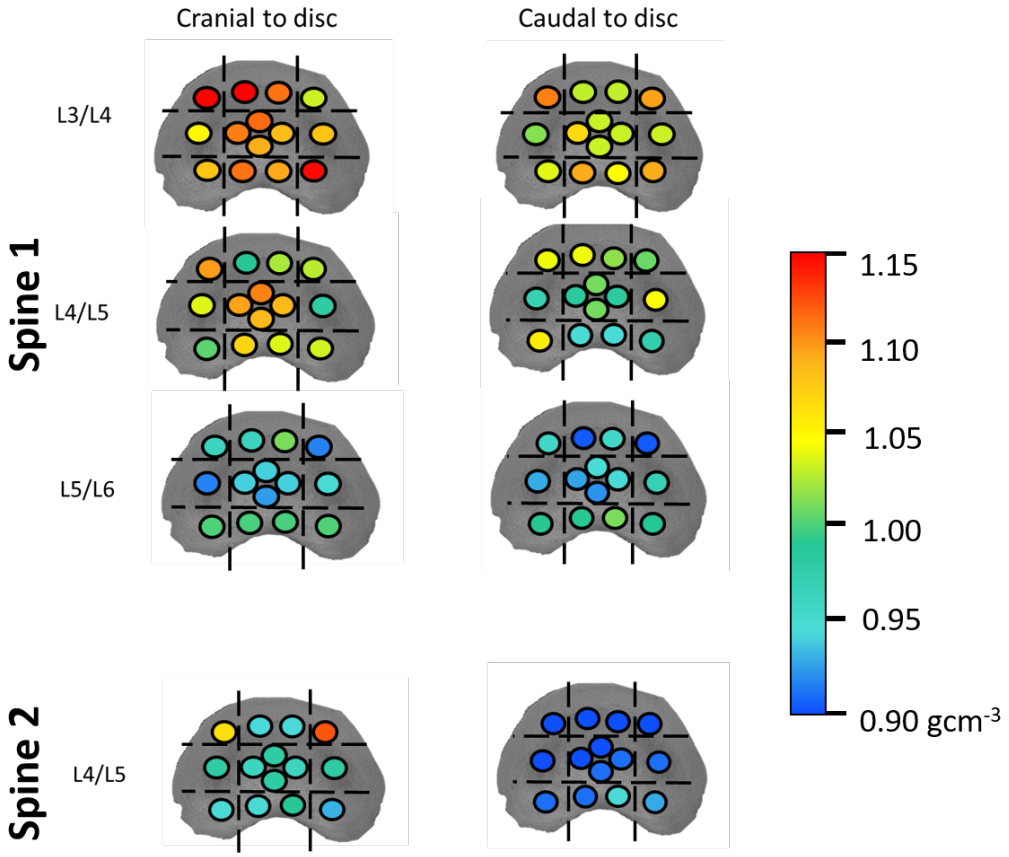

Fig. 3.18 The colour maps represent the bone mineral density (BMD) of specific regions of interest of the VEP at different spinal levels and on different sides of the disc for the 2 spines used in this study. The VEP samples from Spine 2 showed the same trends as the the VEPs from the same spinal level from Spine 1. The colour bar on the right shows the BMD (gcm^{-3}) assigned to the colours.

There was a significant trend of decreasing BMD from L3/L4 to L5/L6 ($P < 0.05$). The caudal VEPs had significantly lower mean BMD values ($P < 0.05$) than their cranial counterparts at each spinal level, as shown in Figure 3.19.

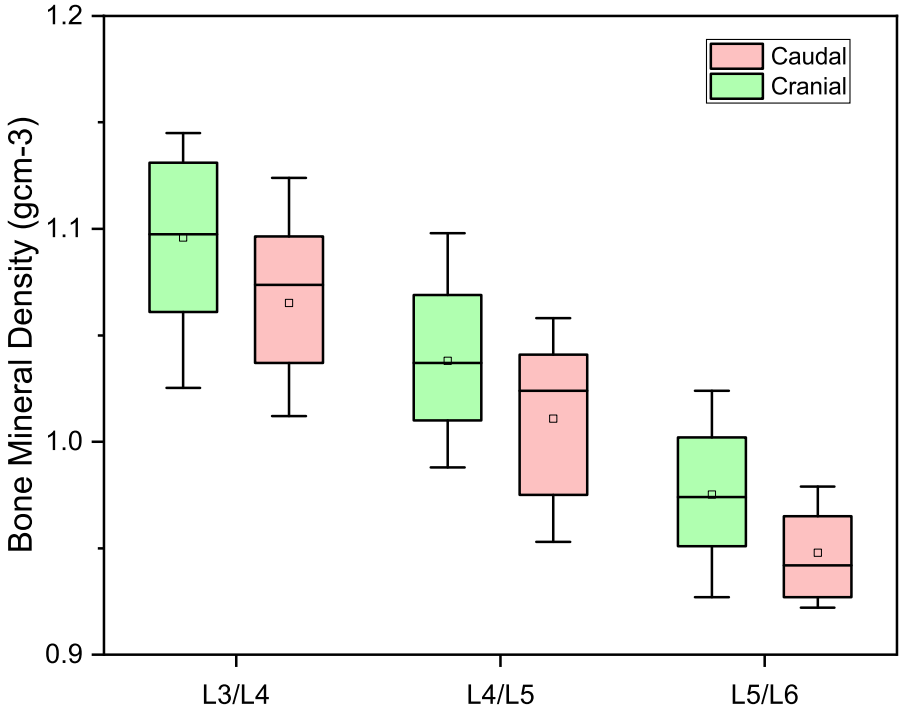

Fig. 3.19 The box plots show the distribution of the BMD for each VEP, with the whiskers showing the standard deviation and the line in the middle of each box represents the median. The mean BMD, shown by the square in the middle of each box plot, was lower for caudal than for cranial VEPs at each spinal level and the BMD decreases from L3/L4 to L5/L6.

Curvature

The curvature for the anterior-posterior (AP) line in the caudal VEPs were the highest measured curvature in both spines 1 and 2 at the spinal level L4/L5. The AP curve was significantly higher ($P < 0.05$)) for the caudal VEPs than the cranial ones in both spines. Similarly, the right-left (RL) curvature was significantly higher ($P < 0.05$) in the caudal VEPs than the cranial ones in both spines, as shown in Figure 3.20.

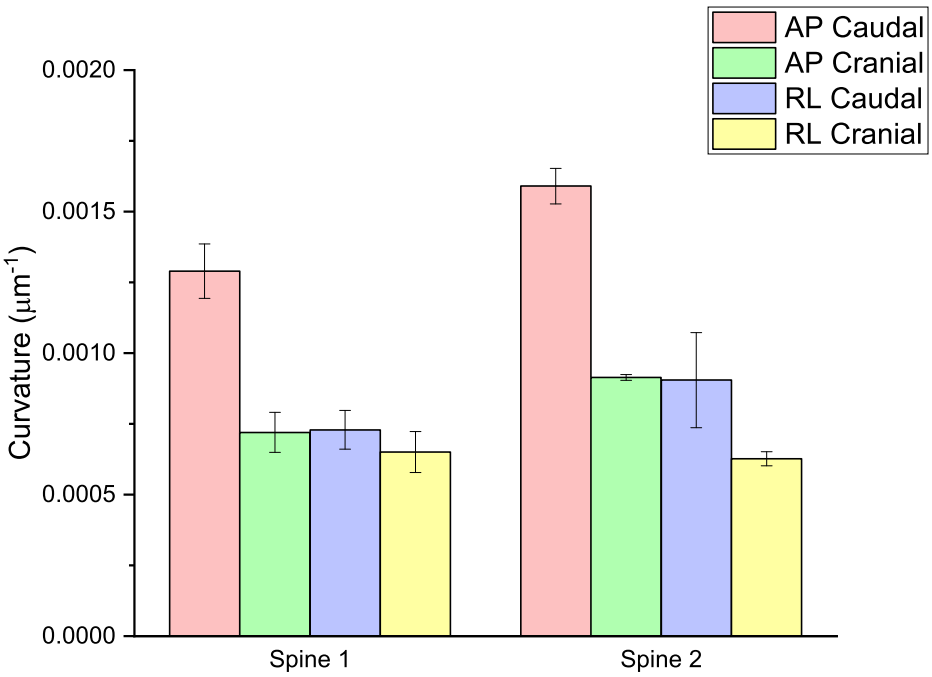

Fig. 3.20 The curvature of the anterior-posterior caudal VEPs were highest in both spines, at the spinal level L4/L5. The error bars show the standard deviation of the datasets. (AP: anterior-posterior, RL: right-left)

The VEP has a concave shape, with the maximum curvature occurring at the center of the VEP surface. The caudal VEPs showed significantly higher ($P < 0.05$) curvatures than the cranial ones at all spinal levels, with the most curved surfaces along the anterior-posterior lines, on both VEPs at the L5/L6 level as shown by the stitched reconstructed images in Figure 3.21.

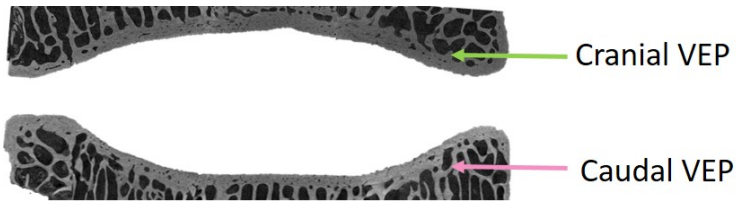

Fig. 3.21 Single slices of each of the cranial and caudal VEPs from the L5/L6 level, along the anterior-posterior line B, covering regions V2, V5 and V8 of the VEP, show the maximum recorded curvatures in this study.

The shape of the VEP surface was most curved from anterior to posterior, through the central region, compared to the shape from right to left sides of the VEP. The mean curvature increased from L3/L4 to L5/L6, as shown in Figure 3.22, but the curvature of the cranial VEPs increased at a faster rate than the caudal ones, along both directions investigated in this study.

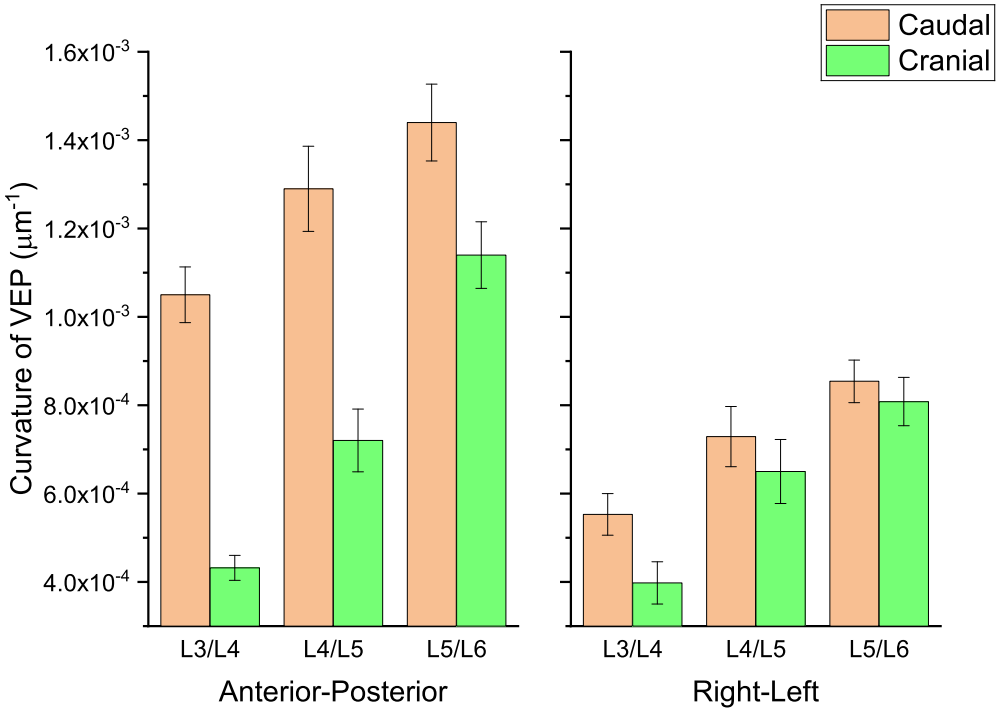

Fig. 3.22 The VEP surface exhibits a more concave shape along the anterior-posterior direction compared to the right-left one across all spinal levels. Caudal VEPs are more curved than their counter cranial VEPs in all cases. Curvature increases for all VEPs down the spine from L3/L4 to L5/L6, with the cranial VEPs curvature increasing at a faster rate than the caudal ones. The error bars represent the standard deviation of the measurements.

3.3.3 Epiphyseal Ring

The thickness of the epiphyseal ring was significantly highest ($P < 0.05$) in the anterior region than the other regions of the VEP surface across all VEPs, as shown in Figure 3.23. The posterior region of the ring, on the contrary, was the thinnest region across all VEPs ($P < 0.05$). Furthermore, the cranial VEPs had significantly smaller ($P < 0.05$) epiphyseal rings compared to their caudal counterparts across all spinal levels. The ring on the right and left sides of the same VEP surface exhibited similar range of sizes. The caudal VEPs had larger

differences between the anterior and posterior ring sizes than for the cranial VEPs in both spines. The size of the epiphyseal ring from the VEPs of the level L4/L5 of Spine 2 was in the same range as the ones measured from the same spinal level in Spine 1.

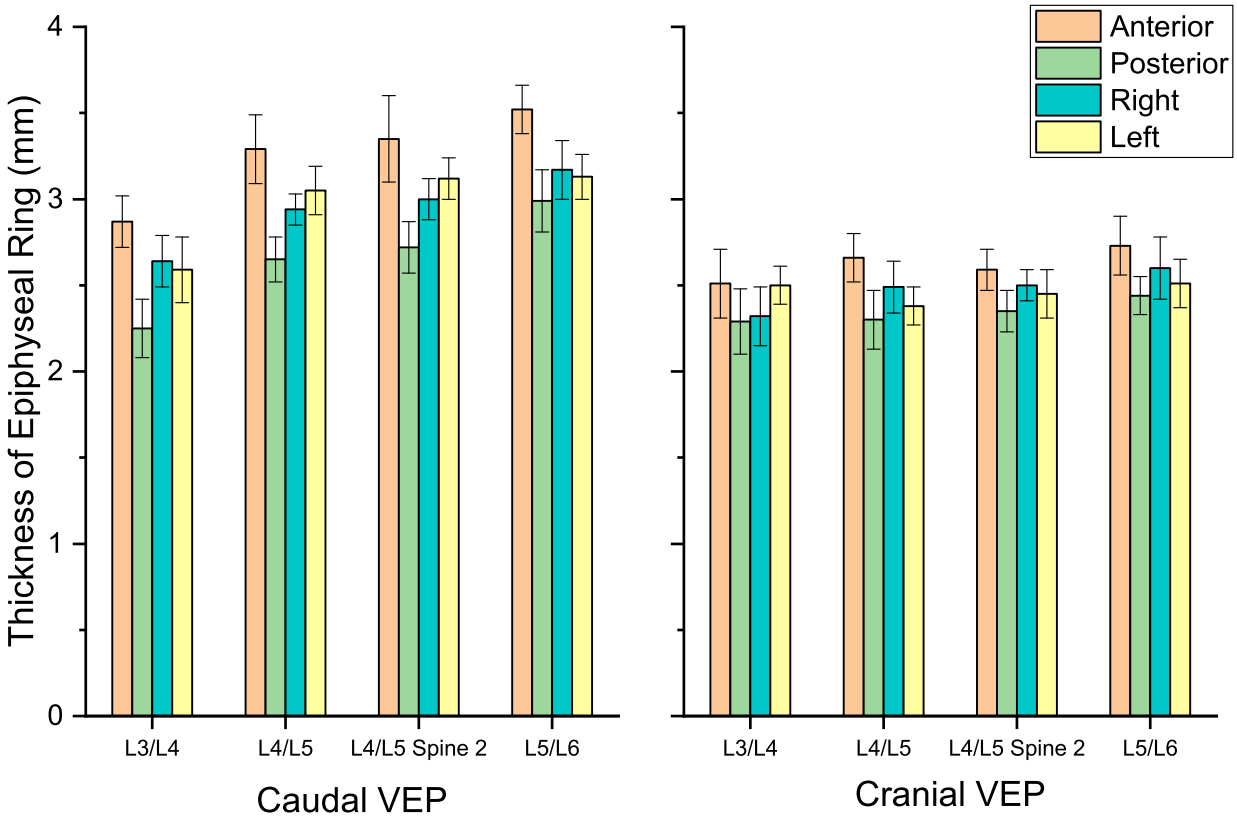

Fig. 3.23 The size of the epiphyseal ring was measured at 4 sections of the VEP: anterior, posterior, left and right sides for the caudal and cranial VEPs. The anterior region showed the largest size of the ring for all samples whereas the posterior region showed the smallest size. The caudal VEPs had a larger total ring size than their cranial counterparts. The VEPs from Spine 2 showed the same range of values for the size of the ring. The error bars represent the standard deviation in the measurements.

3.3.4 Structural Properties of the Trabecular Bone

The bone properties of the trabecular bone calculated from the regions V1 to V9 showed no trend for either of the histomorphometric properties measured. Instead, the effect of the spinal level of the vertebrae and the side of the disc are therefore compared in this section.

Porosity of Trabecular Bone

The porosity of the trabecular bone in the vertebrae showed no statistically significant differences ($P < 0.05$) between caudal and cranial samples from the same spinal level, in both Spine 1 and Spine 2 as shown in Figure 3.24. There was no apparent trend of the trabecular porosity with respect to the side of the disc or the spinal level.

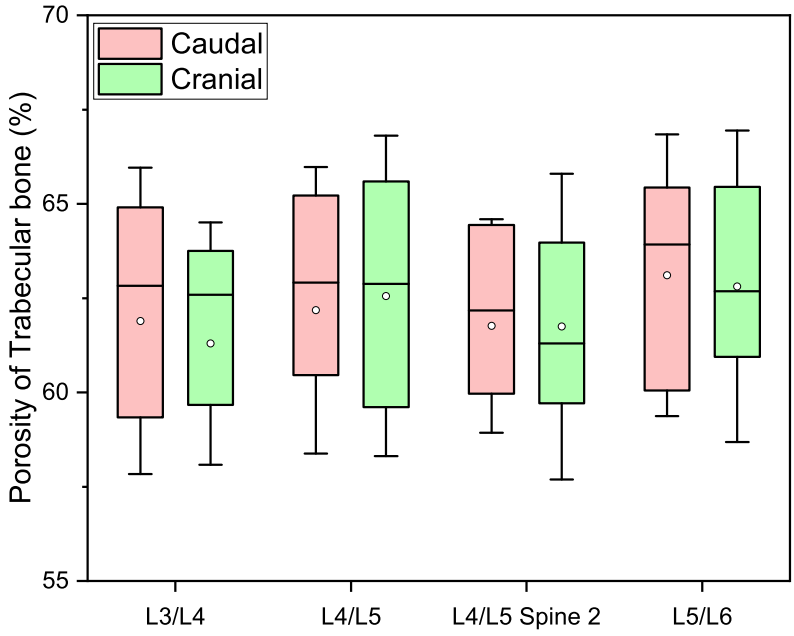

Fig. 3.24 The box plots show the distribution of the caudal and cranial datasets, with the whiskers indicating the standard deviation, the square in the middle shows the mean and the horizontal line is the median. No significant differences was observed between the caudal and cranial samples and down the spine from L3/L4 to L5/L6.

Bone Mineral Density of Trabecular Bone

The trabecular bone in the underlying vertebrae showed increasing BMD down the lumbar spine, as shown in Figure 3.25, which is the opposite trend observed for the VEP in Section 3.3.2. However, the caudal samples had significantly smaller average BMD values ($P < 0.05$) than cranial ones in both VEPs and the trabecular bone of the vertebrae, in both spines.

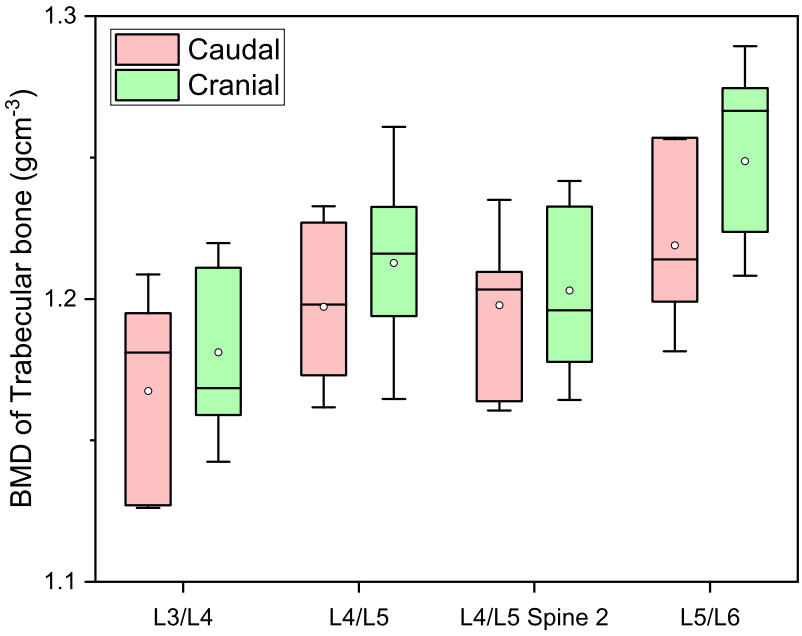

Fig. 3.25 The box plots show the distribution of the caudal and cranial datasets, with the whiskers indicating the standard deviation, the square in the middle shows the mean and the horizontal line is the median. The BMD is observed to increase for both caudal and cranial samples down the spine from L3/L4 to L5/L6 and the cranial samples have significantly higher BMD than their caudal counterparts. The error bars represent the standard deviation in the measurement.

Trabecular Thickness and Separation

The average trabecular thickness was 0.154 ± 0.012 mm for both caudal and cranial samples from Spine 1, as shown in Figure 3.26. The caudal samples had a trabecular separation of 0.35 ± 0.06 mm while the cranial samples were 0.34 ± 0.05 mm, as shown in Figure 3.26. Therefore, there are no marked changes in terms of trabecular thickness and separation across all samples, irrespective of location with respect to the disc and spinal position.

The average trabecular thickness of Spine 2 was higher than Spine 1 but the opposite trend was observed for the trabecular separation, as shown in Figure 3.26. The cranial and the caudal samples had statistically significant differences for both parameters (trabecular separation and thickness) with $P < 0.05$.

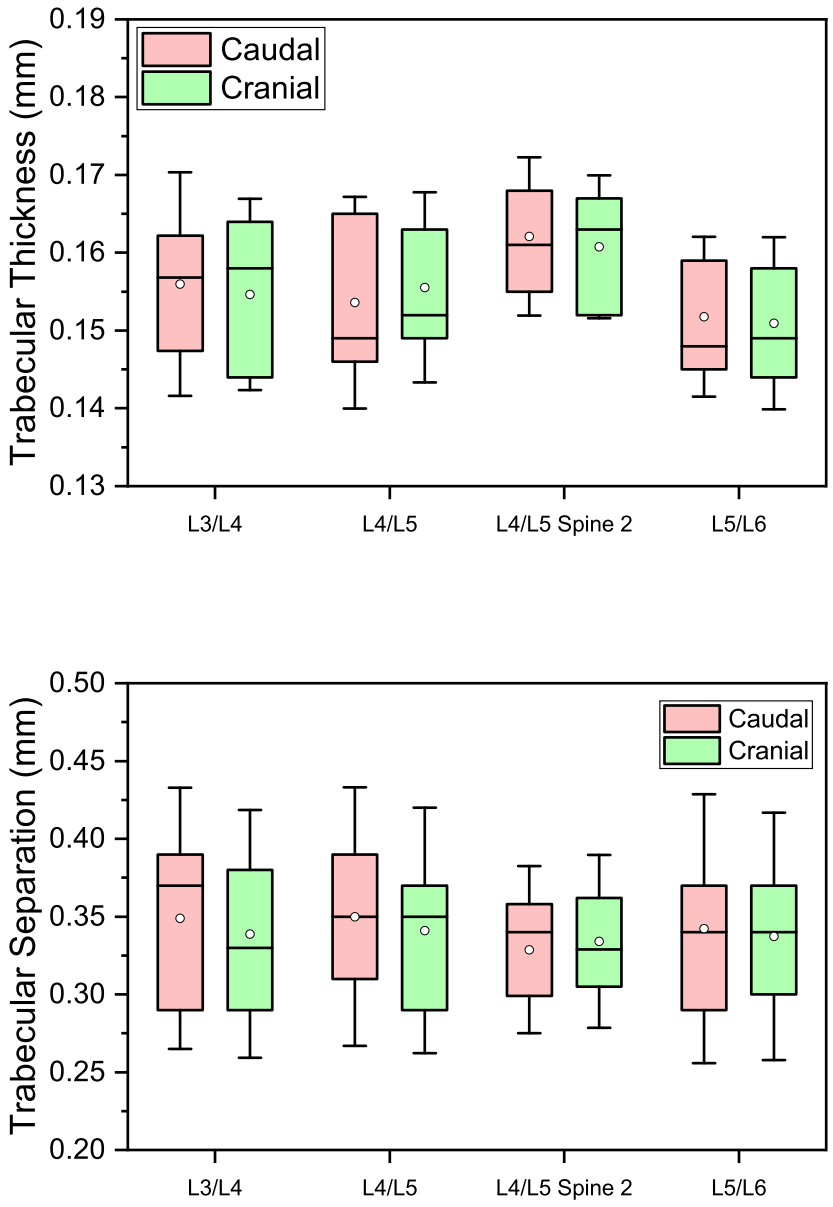

Fig. 3.26 Top: The average trabecular thickness of the struts of the trabecular bone of the vertebrae showed no clear trend for different spinal levels or sides of the disc. The samples from Spine 2 had similar range of thickness. Bottom: The average trabecular separation of the struts of the trabecular bone of the vertebrae showed no clear trend for different spinal levels or sides of the disc. The samples from Spine 2 had similar range of thickness measurements. The error bars represent the standard deviation of the measurements.

3.4 Discussion

3.4.1 Imaging of the Vertebral Endplates

This study used the micro-CT as a non-invasive, high resolution 3D imaging tool for the visualisation and structural characterisation of the VEP and its underlying trabecular bone. Although micro-CT has been used previously for the characterisation of the VEP, the animal models used were mice [63, 200], immature pigs [78] and rabbits [201] which were shown to not be the best models for human spines due to their differences in terms of size and characteristic features. These animal models have shown the presence of growth plates which are absent in the mature human VEP, and the persistence of larger cartilage endplate with smaller central bony endplate than the human VEPs [108]. Some studies used sheep but imaging the VEP as one whole sample meant a limit to the resolution. Most studies have used pixel sizes ranging from 7 μm to 25 μm [104, 202, 203]. As discussed in more details in Section 2.5.3. of the Literature Review, the ovine model has been shown to be a close match with the human spine biomechanically, especially the VEP regions, with similar weight range, bone and joint structure and remodelling processes [111–113]. Furthermore, sheep spines are more readily available than human spines and are easy to handle. Although sheep are quadrupeds, the loading of the spine has been shown to be by axial compression and mainly along the long axis, matching the loading of the human spine [114]. This can be explained by the additional tensile forces from surrounding muscles and ligaments acting to maintain posture in a quadruped to resist bending.

This current study successfully used a pixel size as small as 4.89 μm. Smaller pixel size allows for high resolution imaging of smaller features on the sample. Moreover, previous studies have focussed on the thoracic and cervical regions of the spine but the lumbar region is most relevant when considering the lower back pain [202, 204]. The novel aspect of this study is also the combination of several categories of the VEP such that samples were collected from the same spine at different levels, both caudal and cranial VEPs and across the whole VEP region. From the images, 3 distinct regions of hard tissue underneath the disc were distinguished:

- The VEP as a dense bone layer lodged between the disc and the vertebra.
- The epiphyseal ring encasing the VEP.
- The sponge-like trabecular bone in the vertebra, underlying the VEP.

The structural properties of each of these 3 regions will be discussed separately, in terms of how they vary with spinal level, side of the disc and location on the VEP surface. The

findings will then be summarised to provide a holistic image of the interaction of the 3 regions with each other.

Furthermore, the presence of the bone projections seen in the younger sheep sample, as shown in Figure 3.13, made the identification of the VEP layer uncertain. The observed bony structure could be part of the growth plates, but this has not been confirmed in this study. Growth plates have been shown to be present during the early years of animals, using histological staining, acting as a growth front for the bone [105]. Influenced by growth hormones, new cartilage is formed on one side of the growth plate, also known as an epiphyseal plate, and damaged cartilage is removed or replaced by new spongy bone on the other side. This ensures the continuous process of bone growth during early stages of growth of mammals. At the end of the growth period, which varies for animals and humans and is governed by the increased concentrations of sex hormones during puberty, the epiphyseal plate thins until eventual replacement by trabecular bone [205]. The sheep spine has been shown to attain skeletal maturity after 15 to 18 months [206] and given that the focus of this thesis is the VEP, spines from mature sheep, 36 months old, were preferentially used for the rest of the study to ensure maturity was reached.

3.4.2 The Vertebral Endplate

As discussed previously, the VEP has 2 main functions: providing a nutritional pathway to the avascular disc and redistributing the mechanical loads across the vertebra. The trends observed in the structural properties from this study reflected these functional requirements, as will be discussed in more details in the next subsections.

Mechanical Stability of the Disc

During the diurnal loading of the vertebral column, the nucleus pulposus of the disc exerts an evenly distributed strain onto the adjacent vertebrae. This is because the high water content of the gel-like nucleus pulposus exerts hydrostatic pressure which reacts to compressive loading [149]. The VEP evenly distributes the stresses from the discs onto the adjacent vertebrae, providing biomechanical support [3]. The complex collagen fibres arrangement provides strength in tension to the annulus fibrosus, preventing the nucleus from expanding radially [30]. The pressure is mainly controlled through the slow water loss of the disc to the vertebrae through the canal openings of the VEP [207]. The daily mechanical loading of the spine causes an increase in the intradiscal pressure, or the hydrostatic pressure of the fluid, of the intervertebral discs, and to counteract the pressure, water is forced out of the disc. As water is expelled out of the disc, the swelling pressure within the disc increases until

it balances out the loading pressure. The swelling pressure is osmotic pressure generated by the proteoglycans in the nucleus pulposus which attract and bind to water molecules. When equilibrium is reached, the flow of water out of the disc stops. When the load has been removed from the spine, the swelling pressure increases and therefore water flows back into the disc. As the disc rehydrates, the swelling pressure decreases and the intradiscal pressure increases. Once again, once equilibrium is reached, the flow of water stops.

The spine of the sheep has been shown to be mainly loaded along its long axis, similar to the human spine which is why the quadruped is a comparable model for spine research. This is because spinal segments do not have the ability to withstand considerable bending moments. Therefore additional tensile forces from adjoining muscles and ligaments provide the necessary additional support to maintain the posture of the quadruped spine [114]. This is why the sheep spine is loaded primarily by axial compression. Furthermore, the trabecular bone in goat's vertebrae have been shown to follow a horizontal course between the 2 VEPs of the opposite edges, implying that the compression force is indeed in the axial direction of the spine [208]. Given that similar size, weight and quadruped nature of the goats and sheep and the fact that it has been shown that goat and sheep bones are very similar in architecture and structural properties, it can be assumed that the trabecular bone follows the same course in sheep vertebrae [209]. Given that the sheep spine is loaded along its long axis, similar to the human spine, and that structural properties of bone are dominated by the directionality of mechanical loading [210], the trends observed in this study will be compared to the trends reported in the literature from other sheep models as well as human models.

The VEP thickness in this study ranged from 0.45 mm to 1.01 mm. Previous studies investigating human VEP reported thickness ranging from 0.2 mm to 0.8 mm [53, 62, 76, 211]. As shown by Mageed et al., the structural properties of the sheep spine is comparable to human ones in the VEP region [110]. According to Wolff's law, bone being a highly vascularised tissue has the ability to remodel in accordance with changes in mechanical loading. An increase in mechanical loading will produce high strain which influences the bone cells leading to an increased production of bone matrix, giving thicker and stiffer bone to withstand the new load [212]. The reverse is also true for decreased mechanical loading. The differences observed in the thickness of the VEP can therefore be explained by the different loads experienced at different locations of the VEP. The central VEP for all 6 samples were thinner than their peripheral regions. The nucleus pressure is lower than the maximum compressive stress experienced by the annulus fibres. Anatomically, this can be explained by the annulus fibrosus fibres being deeply anchored to the peripheral regions of the VEP. Rodrigues et al. showed that the fibres split into bundles and sub-bundles before anchoring into the VEP. The subdivision of the fibres offers a higher interface area which

reduces the shear stress at the disc-bone interface caused by the tensile forces in the fibres during mechanical loading [69]. Thus, the thicker the VEP layer, the more surface there is for anchorage of disc fibres and the higher the tensile forces that can be withstood before disc failure or VEP pullout. Inoue et al. also concluded that the firm anchorage is why these regions are able to withstand higher compressive strains and shear stresses than the central region which is underneath the nucleus pulposus of the disc [213]. The fine collagen type II fibrils of the nucleus pulposus on the other hand, insert into the cartilage endplate, therefore not requiring a strong anchorage into the bony VEP [48].

Across the 3 spinal levels, the caudal VEPs were thinner than their cranial counterparts. Compression of the spine is transmitted through tensile forces along the muscles, through the pedicles to the vertebra. This means that the compressive load increases by intervals at each pedicle, along the spine. Caudal VEPs to the disc are compressed by the disc above it and by the muscles attached to the corresponding pedicle. Cranial VEPs are only loaded by their corresponding discs. This could explain the asymmetry in thickness of caudal and cranial VEPs, and the higher prevalence of VEP fracture in the caudal side [214, 215]. Furthermore, the cranial VEPs exhibited higher BMD than the caudal ones, confirming the higher strength of the cranial VEP as it has been shown previously that bone strength increases with an increase in BMD, with a correlation of about 80 % [216]. Grant et al. also concluded that the cranial, or inferior to the vertebra, VEPs are stronger than the caudal ones due to their higher mineral content [68].

The anterior regions of the cranial VEPs were thicker than the posterior ones. However, for the caudal ones, the opposite was observed. In the lumbar spine, the anterior sides of the discs have been reported to be thicker than the posterior ones [207]. This is because during daily movement, the anterior region withstands the highest torsion and bending. This has been shown by Xie et al. using finite element modelling, as shown in Figure 3.27 [217]. The thicker anterior disc provides flexibility to the lumbar spine and the thicker anterior VEP cranially is required for strong anchoring of the increased density of annulus fibres to prevent the disc from bulging out anteriorly. The mirrored symmetry in the caudal VEPs can be explained by the requirement to counterbalance the anchoring of the disc to ensure the disc is not pulled out from the VEP.

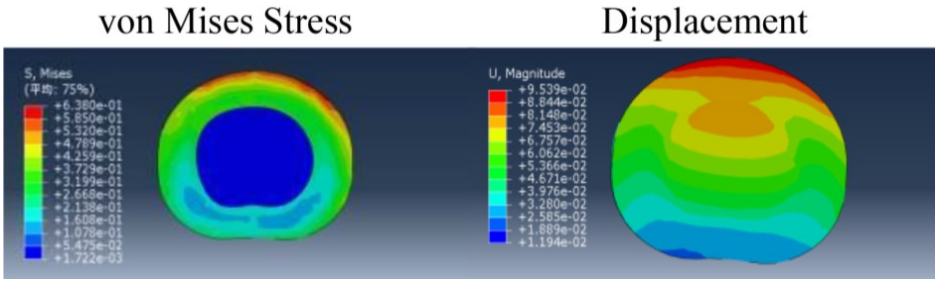

Fig. 3.27 Hyperelastic finite element model of a healthy human disc under everyday loading from walking and lifting showing the distribution of the von Mises stress and tissue displacement. Both show the anterior region experiences the highest stress and displacement during mechanical loading [217].

Thickness of the VEP was observed to increase from spinal level L3 to L6. The stress distribution and the size of the vertebral body increase down the lumbar spine, as shown by Zahaf et al. in Figure 3.28 [218]. This suggests that the VEP therefore needs to be thicker to withstand the increased load.

Conversely, the BMD was seen to decrease along the spine from L3 to L6. Similar trends have been reported previously by Wang et al. [62] in cadaveric human spine as shown in Figure 3.29 but the reason for this trend is still unclear. The BMD ranged from 0.85-1.10 gcm^{-3} for the cranial VEPs which is higher than 0.39-0.46 gcm^{-3}, reported by Wang et al. The values for caudal VEPs were also higher in this study, and this could be because Wang et al. used cadaveric human samples [62]. Furthermore, the differences seen in the absolute values of BMD in samples from Spine 1 and Spine 2, could be explained by different breed, nutrition and genetic effects of individual sheep, but the trends observed were the same.

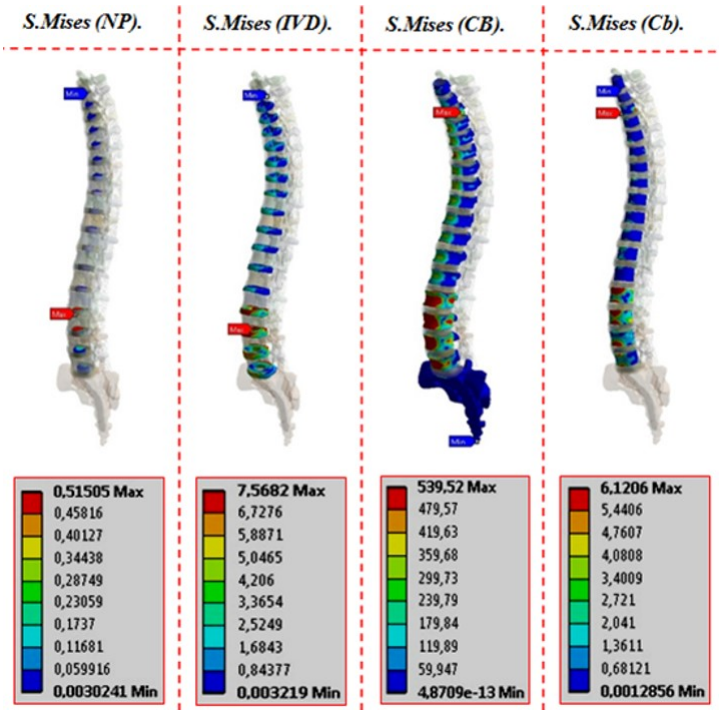

Fig. 3.28 Distribution of the von Mises stress in the human spine under posterior loading of 15 kg for the nucleus pulposus (NP), the intervertebral disc (IVD), cortical bone (CB) and cancellous/trabecular bone (Cb) showing increasing stress in the lower lumbar region as compared to upper regions. [218]

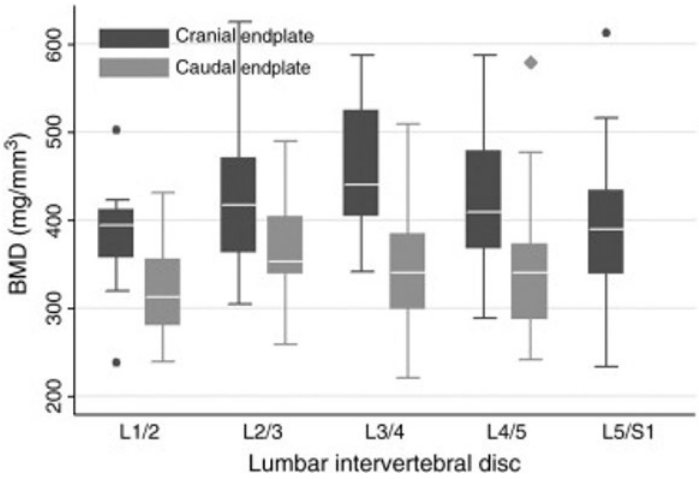

Fig. 3.29 Graph showing the BMD for cadaveric human VEPs from L1/L2 to L5/S1. The cranial VEPs have higher BMD than caudal ones and there is a clear trend of decreasing BMD from L3/L4 to L5/S1 [62].

The caudal VEPs were more concave than the cranial ones, exhibiting the opposite trend that has been reported previously in the human spine [60]. This opposite trend highligths the differences in the curved surfaces of the VEP between bipeds and quadrupeds, as reported previously by Langrana et al. [219]. The highest curvature is along the anterior-posterior direction of the VEP surface and this curvature increases along the spine. The area of highest curvature is likely to be near the central portion of the VEP, but it is not apparent from this study. Information of the surface curvature of the VEP could inform the design of surgical implants of the disc, such that an implant will follow the same curvature of the endplate, to avoid exerting additional compressive strains onto the neighbouring VEPs, or the creation of localised weak points.

Nutritional Pathway to the Disc

The results showed an inverse relationship between the porosity and thickness of the VEPs. Porosity refers to the percentage of hole volume of the bone sample, such that higher porosity allows for more metabolite transport to the disc but reduced mechanical strength [13].

The central regions of the VEP, underlying the nucleus pulposus, have the highest porosity for all VEPs. This could be explained by the high metabolic activity in the nucleus pulposus of the discs. The observed trends of the porosity for anterior/posterior regions, caudal/cranial sides and along the spine from L3/L4 to L5/L6 all follow an inverse trend to the thickness. A study carried out by Zehra et al. using the caudal and cranial VEPs in human cadaveric spines showed that porosity depends on thickness which in turn is highly dependent on the mechanical loading of the spine [13]. They also showed the same trends of central VEP being thinner and more porous than the peripheral regions. This implies that the thicker and less porous regions of the VEP offer mechanical strength while the porous and thinner regions of the VEP allow biochemical exchange to happen with the disc.

Physiologically, the pores in the VEP offer the pathway for the free transfer of water, nutrients and oxygen to the disc and the removal of waste products, through diffusion and convection as explained in the Literature Review. The water exchange with the disc ensure the disc is able to withstand the load-induced pressure by swelling and regaining its original size during rest. The nucleus pulposus of the disc is the epicentre for biochemical reactions and has a higher water content than the peripheral regions [19]. Therefore, the higher density of openings underneath the nucleus pulposus of the disc shown in this study could be related to the increased exchange of nutrients at the central region of the disc. Furthermore, these pores could also be hosting the ends or "buds" of blood vessels, which cannot be visualised on the micro-CT images. This will be explored in more detail in Chapter 4.

3.4.3 The Epiphyseal Ring

The thickness of the epiphyseal ring, also referred to as the apophysis or epiphysial ring, increases along the spine from spinal level L3/L4 to L5/L6, as shown in Figure 3.23. The size of the vertebral body has been shown to increase as a result of increasing mechanical load and tension in the annulus fibres. Hongo et al. found that the caudal epiphyseal ring represented a more densely packed region of annulus fibres from the disc than their cranial counterparts [220]. Moreover, they also reported higher tensile strain in the caudal vertebral surface than the cranial ones. As shown by previous studies [20, 221], the vertebrae widen cranio-caudally into a trapezoidal shape down the lumbar spine, with the vertebra-disc boundary being larger caudally, which could explain the larger ring area in the caudal VEP than the cranial ones as an attempt to sustain the mechanical strains. The results from this study also showed these structural differences between the ring size in caudal and cranial surfaces. Furthermore, the increase in the size of the ring down the spinal levels was seen to be larger in the caudal VEPs than in the cranial ones. This could also be explained by the fact that the vertebra widens into a trapezoidal shape down the spine, implying the caudal surface of the vertebrae with respect to the disc will widen at a higher ratio at consecutive spinal levels than the cranial ones. This would explain why the ring sizes of the cranial surfaces showed smaller incremental increase than the caudal ones.

The posterior VEP region had the thinnest ring area while the anterior one had the thickest ring area for all VEPs in this study. The left and right sections also had larger areas than the posterior ones, although still thinner than the anterior regions, for all VEPs. This could be explained by the need to provide thicker annulus anchoring to withstand the lateral flexion of the spine in the anterior regions of the disc whereas the posterior regions already have additional support by the neural arch ligaments [222]. Furthermore, other structures such as the facet joints coupled with muscles and ligaments act in conjunction to reduce the stress on the posterior annulus fibres anchored in the epiphyseal rings. During flexion, ligaments are stretched to provide stable but limited movement and therefore the posterior annular fires are unaffected. During extension of the spine, the strain is endured by the anterior region of the disc fibres and therefore this area of the ring needs to be able to provide additional strength through dense anchoring. The lateral sections of the ring (left and right sections), provide lateral flexion of the spine and being only supported by neural arch and surrounding ligaments, they could be requiring thicker regions for the dense packing of the annulus fibres [223].

It has been reported that posterior cranial ring region has the highest prevalence of fracture [224, 225]. The thin ring area coupled with the higher tensile forces and the fewer fibre attachment of the disc in the cranial area could explain this phenomenon. The epiphyseal

ring could therefore be contributing to the overall dissipation of the mechanical stresses on the disc during everyday loading of the spine and should be further investigated.

3.4.4 The Trabecular Bone of the Vertebra

From the previous sections, it has become apparent that the VEP and the epiphyseal ring could be playing an important role in dissipating the mechanical strains during loading of the spine caused by everyday movement. Therefore, they could be providing mechanical stability to the trabecular bone of the vertebra. The health of trabecular bone not only depends on the bone mineral density and porosity but also on the architecture of the sponge-like trabeculae, which is defined by the trabecular separation and trabecular thickness.

The BMD ranged from 1.1 to 1.3 gcm^{-3}, which agrees with 1.15 gcm^{-3} reported by Wu et al. previously for healthy sheep [226]. The results in this study showed that the BMD of the trabecular bone increased along the spine, which is the opposite trend recorded for the VEPs. As the vertebral body size have been reported to increase along the spine due to increasing loads, the increased BMD of the trabecular bone could be contributing to the resistance against these increasing loads down the lumbar spine. As explained in Section 3.4.3. there is a direct correlation between BMD and strength of the bone. Therefore an increasing trend down the spine implies providing the means to withstand increasing mechanical load.

The BMD of the VEP and of the underlying trabecular bone followed opposite trends, as shown in the schematic in Figure 3.30. The caudal trabecular bone of level L3/L4 (with respect to the disc)and the cranial trabecular bone of level L4/L5 are part of the same vertebra, and Figure 3.25 shows that these 2 samples exhibited BMD values in the same range. This trend was seen, especially in vertebrae L4 and L5 as samples from both the caudal and cranial sides of these vertebrae were analysed in this study. Therefore, the BMD of the trabecular bone of one vertebral body could be uniform throughout the length of the vertebra. The increasing trend in the BMD of the trabecular bone down the spine could potentially be explained by the requirement for the trabecular bone within the vertebra to remodel to withstand the differences in mechanical strength of the VEPs at opposing ends of the vertebral body. However, the reason behind the decreasing BMD in the VEP and increasing BMD in the vertebra remains unclear at this stage.

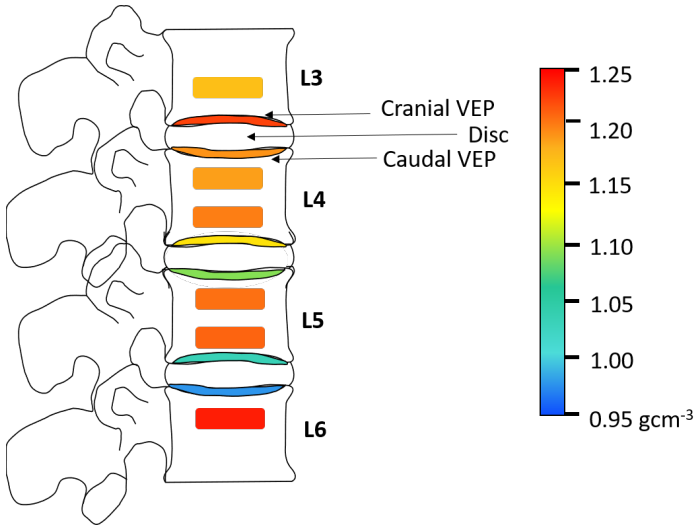

Fig. 3.30 Schematic showing the representation of the BMD values for cranial, caudal VEPs and the trabecular bone in the caudal and cranial areas of the vertebra. The colour bar on the right-hand side shows the colour assigned to each BMD values.

Trabecular porosity was measured to be 58-66 %, which is in the same order of magnitude as values reported in previous studies, showing a range of 66-69 % for sheep spines [227, 228]. Porous bone does reduce the weight of the vertebra and makes the bone more compliant. Therefore, it provides flexibility to the lower back, allowing the bone to absorb energy during impact loading and lighter bone also helps movement of lower limbs [229]. The mean porosity of trabecular bone did not change with the side of the disc or with spinal level. This could be explained by the fact that the vertebrae experience uniform strain given the fact that the VEP and the epiphyseal ring already possess adapted structures to withstand the different bio-mechanical requirements at different locations in the spine. Furthermore, trabecular bone in the vertebra is spatially heterogeneous [230], which means that the struts are arranged in different directions and it has been shown that compressive load on vertebrae is sustained primarily by the vertical trabeculae, whereas the horizontal trabeculae serve to prevent buckling of the vertical trabeculae in humans [231, 232]. In the sheep, given the horizontal nature of the spine in the quadruped but with the loading still along the long axis of the spine, the opposite is likely to be true. Irrespective of the directionality of the load bearing struts, the heterogeneous nature of the bone could be the factor withstanding the different mechanical loads on the vertebrae which would not be detected by the porosity of the bone only. Further quantitative information about the directionality of the trabeculae struts, which were not available from the micro-CT images from the current study, could contribute to the understanding of the bone mechanical stiffness.

Vertebrae have adapted to a hyperboloid shape such that they are wider at both ends than the middle section, in order to support the loading cycles of everyday activities [72]. For a healthy spine, it has been reported that load transfer is carried out primarily through the trabecular centrum (central part of the vertebra), outwards to the cortical shell of the vertebra [233]. Further studies have reinforced this theory showing that the size of the vertebral centrum increases cranio-caudally as the body weight increases [184, 234]. Studies have also shown that the mid-section of the vertebral body has different properties to the edges, where there is close proximity with the VEP [235]. The forces exerted by the vertebral discs have been hypothesised to be mostly attenuated by the VEP and the trabecular bone right next to the VEP such that it can be assumed that the optimal design of the middle section of the vertebra is to have few but thick trabecular struts. From this study, the average trabecular thickness and separation for the vertebral bone were 0.15 ± 0.03 mm and 0.34 ± 0.02 mm respectively, which are in the same order of magnitude but smaller than the values reported by Kennedy et al., which were 0.24 ± 0.02 mm for the trabecular thickness and 0.58 ± 0.09 mm for the trabecular separation of trabecular bone in ewes' vertebrae [235]. However, the values from this study showed no significant variation along the spine or between caudal and cranial vertebrae.

3.4.5 Combined Effects

The 3 main areas identified in this study were the VEP, the epiphsyeal ring and the vertebra. The fibres of the disc anchor into the VEP as well as the epiphyseal ring. The strength of this anchoring could be determining the ability of the disc to withstand the biomechanical strains of daily loading of the spine during extension and flexion. The disc is generally divided into 3 regions, the inner two-thirds and the outer third, as shown in Figure 3.31. The disc fibres of the outer third region of the disc could be anchoring into the epiphyseal ring while the fibres from the middle and central third regions would be anchored into the VEP [236].

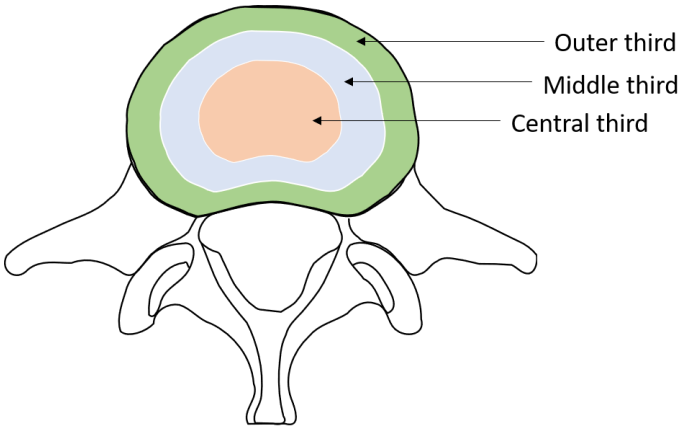

Fig. 3.31 Schematic showing the 3 regions of the disc. The disc fibres from the central and middle third regions are anchored into the VEP while the fibres from the outer third region are anchored into the epiphyseal ring.

The results from this study suggests that the central region of the VEP provides a thin and porous barrier to the nucleus pulposus of the disc to allow for water exchange during the loading-induced swelling of the disc, a nutritional pathway and a flexible layer to allow the disc to swell and occupy space. Conversely, the results indicate that the peripheral regions of the disc could be providing a thicker and less porous surface to the disc. This would ensure proper anchorage of the fibres of the annulus fibrosus to accommodate for the higher tension experienced by the fibres in this area of the disc. The VEP also showed highest curvature through the central region, reinforcing the theories of adaptation to provide space for the swelling of the nucleus pulposus.

The epiphyseal ring provides a thick region anteriorly for the Sharpey's fibres, which consist of collagen fibres and elastic fibres from the annulus of the disc, to anchor [237]. The epiphyseal ring would thus enable the spine to twist and bend without the disc slipping out of place from the edges. The VEP and the ring could therefore be acting together like a transitional boundary from the soft tissue of the disc and the hard tissue of the trabecular bone. The disc therefore has to be considered alongside these 3 regions when trying to understand the function of the disc during everyday loading of the spine, and also when investigating the onset of physiological failures.

3.4.6 Relevance for Implant Design

A substantial number of disc implants and prostheses are tested in vivo in animal models, to test for biological and mechanical responses. However, these implants are commonly designed based on data collected from cadaveric human vertebrae and VEPs [219]. As expected, this leads to considerable anatomical and biomechanical mismatch which in many

cases eventually leads to failure of the implants during the animal testing stage. The failure is not necessarily intrinsic to the implant but could be influenced by the mismatch between human and animal spines. Although it is crucial to design implants based on data collected from human VEPs and discs, it is also important to take into account the limitations of these in vivo tests based on the mismatch with animal models. A better understanding of the structural and mechanical properties of the VEP in animal models would enable the mismatch limitations to be factored in, therefore, potentially improving the outcome and the reliability of these in vivo tests.

Moreover, information pertaining to the curvature of the VEP surface in contact with the disc will improve adhesion and physical fit of disc implants to the vertebral bone and ensure a functional interface between the biological host and the implant. Furthermore, taking into account the mechanical strength of the underlying trabecular bone of the vertebra and the VEP would ensure that any implant would not cause resorption of the bone or subsidence into the bone, due to overbearing mechanical loading, or the creation of localised weak points, during interbody spinal fusion, as discussed in the Literature Review in Section 2.8.

Similarly, an in-depth understanding of the thickness, porosity and BMD of the VEP will inform the design of future endplate implants, to successfully match the requirements to withstand the mechanical loading of the spine and to still provide a permeable interface to the disc. The trends observed from this study for the structural properties across the VEP surface, between caudal and cranial VEP and along the spine from L3 to L6 are also crucial to take into consideration. Implants for the VEP will therefore have to be tailor-made, depending on where exactly in the spine they are being designed for.

3.5 Conclusions

This study used the micro-CT for the visualisation of the architecture of the VEP at very high resolution. For the first time, VEP samples from the same spine were simultaneously categorised based on their spinal level (L3 to L6), the side of the disc they were attached to (caudal and cranial) and the spatial region of the disc they were connected to (central and peripheral). Clear differences were observed in terms of thickness and porosity of the VEP, depending on their location. The differences in the curvature of the VEP surface were clearly identified. This study is also the first to have characterised the size of the epiphyseal ring alongside the VEP at different spinal levels, to the best of the author's knowledge. Furthermore, the reconstructed images were used for the structural characterisation of the VEP, quantifying the thickness, porosity, BMD and curvature. The bone quality of the underlying trabecular bone in the vertebrae were also assessed, in terms of the porostiy, BMD

and trabecular thickness and separation. Given that all 54 samples were harvested from the same sheep spine, 18 more samples from 2 VEPs of a second spine were used to assess spine to spine variability of the observations. This showed that some of the trends were statistically relevant but some require further repeats before making conclusive remarks. The results sugges that the structural properties are associated with the mechanical loading of the spine and the biophysical demands of the disc, to enable the VEP to carry out its 2 main functions of providing mechanical rigidity and a nutritional pathway to the avascular disc. The findings of this study could also guide disc implant design for the purpose of in vivo animal testing.

This study showed that the healthy VEP has a unique structure which could be a result of adapting to the mechanical loading it is subjected to, as part of one of its main roles: providing mechanical stability. The second role of the VEP, providing a nutritional pathway to the disc will be investigated in more details in the next Chapter. The conflicting biomechanical requirements the VEP has to balance make it vulnerable to damage and thus reinforce the theory that the VEP is prone to damage, which could be leading to disc degeneration and therefore, back pain. The pathological onset of degeneration will be investigated in Chapter 5.

Key Points

The main findings from this chapter can be summarised as shown below:

- The central regions of the VEP were thinner and more porous than the peripheral ones.
- The cranial VEPs were thicker, less porous, less curved and had higher BMD than the caudal VEPs.
- The anterior regions of the VEP were thinner and more porous on the caudal side.
- Along the spine from L3 to L6 the thickness of the VEP increased but the porosity and BMD decreased.
- The epiphyseal ring is thickest in the anterior region of the vertebral surface and thinnest in the posterior region, providing higher packing density of the disc fibre in the anterior region.
- The trabecular bone of the vertebra showed increasing BMD along the spine, but no changes were observed in the average porosity, trabecular separation and thickness.

Chapter 4

Qualitative and Quantitative Analysis of the Nutritional Pathways in the Endplate

4.1 Introduction and Relevance

As discussed in the Chapter 2, the prevalence of low back pain has been closely linked with intervertebral disc degeneration and that this is associated with inadequate or hindered nutrient supply to the avascular disc [3, 238]. The main nutritional pathway to the disc is through the canal network present in the vertebral endplates (VEPs) [168]. Although changes to the structure of the VEP or the canal network will have direct impact on the disc health, the topology of this network is still poorly understood.

The presence of the canal network and vasculature within this region has been observed using scanning electron microscopy and vascular tracers [63, 239]. However, it is unclear whether all the canals are filled with blood vessels, how the blood vessels are organised within these canals, and specifically, how they terminate at the disc interface.

This chapter aims to image and characterise the topology of the canal network at different locations of the VEP. The work in this chapter also investigates the presence and endings of blood vessels in the canals. Having a clear understanding of the architecture of the canal and their interaction with the blood vessels will provide a comprehensive picture of the nutritional pathway to the disc in its healthy state.

4.2 Materials and Methods

The 54 samples used were the same as in the previous chapter, excised from one mature sheep spine, at 3 spinal levels (L3 to L6), on both sides of the disc (cranial and caudal) and

each VEP was divided into 9 distinct regions (V1 to V9). From the second mature spine, 18 samples were used, V1 to V9 from the cranial and caudal VEPs of level L4/L5 to assess spine to spine variability of recorded trends.

Firstly, the structure of the 3D network was qualitatively characterised to elucidate the architecture and the endings of the blood vessels into the disc. Secondly, the topology of each canal was analysed quantitatively so as to make conclusive remarks on the trends of the network's architecture.

Furthermore, 4 vertebrae from spinal levels L3 to L6 of a cow tail (aged 24 months), sourced from the animal farm of the University of Exeter, were also used as part of the qualitative assessment of the structure and content of the canal network in the VEP.

4.2.1 Qualitative Analysis of 3D Canal Network

3D Rendering of the Canal Network

The reconstructed images of the samples following the micro-CT scanning from the previous chapter were loaded into Simpleware ScanIP software (Synopsys) to create 3D rendered images of the 3D canal network inside the VEP. The region of interest was defined such that only the VEP was selected from the reconstructed images as shown in Step 1 of Figure 4.1. The images were then thresholded from 80-250 to create a mask of the bone only. The mask was then inverted to show the network of the "empty" spaces. The network was smoothed to remove noise while preserving the features of the mesh using a Recursive Gaussian filter for better visualisation and comparison between the different categories of the VEP. The *flood fill* function, which determines the area connected to a given node in a multi-dimensional array, was then used to ensure all the canals were connected to each other in the mask, eliminating stand alone holes and pores. This process is summarised in Figure 4.1.

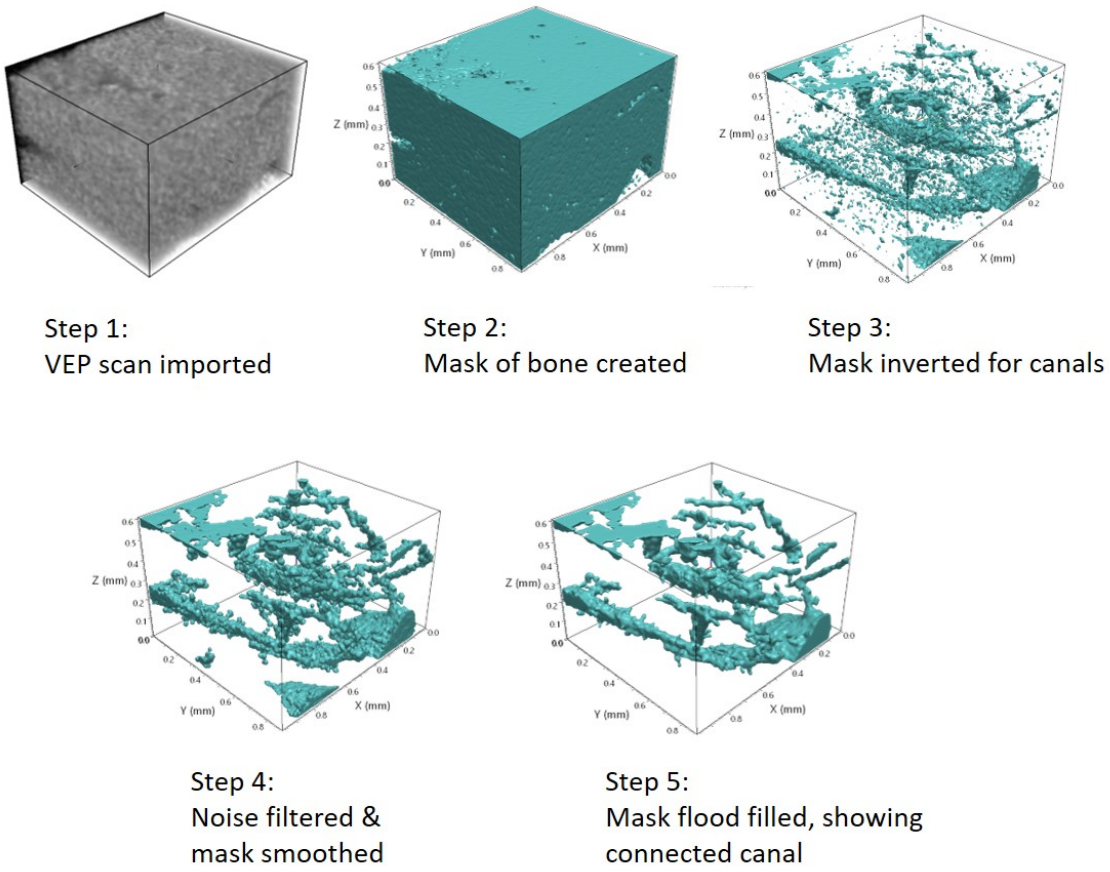

Fig. 4.1 A step by step illustration of how the canals network are visualised from the VEP. The reconstructed image of the VEP scan is loaded into Simpleware. A mask is created of the bone by thresholding the bone with respect to the background. The mask is inverted to show the canal network which is then smoothed using a Recursive Gaussian filter and noise is pruned out using the remote island removal function. Finally, a flood fill function is used to ensure all the canals are connected to form the 3D network observed.

Histology

The V5 samples were scanned in the micro-CT, fixed in formalin and sent to the Norwich Research Park Biorepository for histological analysis where the samples were then decalcified in 4% ethylenediaminetetraacetic acid (EDTA) and embedded in paraffin. Thin slices were sectioned and stained with hematoxylin which stains cell nuclei blue, and eosin which stains the extracellular matrix and cytoplasm pink. Other structures, depending on their compositions appear as combinations of these colours. Histological analysis was carried out to provide a general overview of the soft tissue's structure attached to the boundary of the VEP. The stained slices were then imaged by author with the assistance of Mr. Tom Marjoram MBChB MRCS FRCS, using a ZEISS Observer Z1.

Photoacoustic Imaging of Blood Vessels

A pair of cranial and caudal VEPs from the spinal level L4/L5 from a sheep spine was separated by cutting through the soft tissue of the disc as shown in Figure 4.2. The red circles show the area of focus for the laser for imaging. The 2 whole surfaces of the VEPs were sent to the Bohndiek group at the Cancer Research UK Cambridge Institute, Cambridge. The samples were embedded and imaged with the assistance of Lina Hacker, a PhD student in the Bohndiek group.

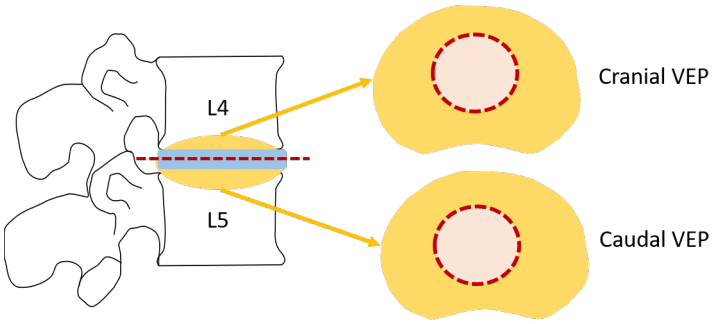

Fig. 4.2 Schematic showing the 2 VEPs used for the photoacoustic imaging. The VEPs were the cranial and caudal ones to the disc at the L4/L5 level of a sheep spine. The red dotted lines show the area of focus of the laser in the central region of the VEP.

The samples were imaged using the Raster Scan Optoacoustic Mesoscopy (RSOM) system (RSOM Explorer P50, iThera Medical GmbH). In the RSOM, laser light is generated by a 532 nm laser and delivered through a customized 2-arm fibre bundle (spot size: 3.5 mm × 5 mm). Optoacoustic signals are detected by a spherically focused LiNbO3 detector (center frequency: 50 MHz; bandwidth: 10-90 MHz; focal diameter: 3 mm; focal distance: 3 mm; f-number: 1). The recorded data are amplified by a low noise amplifier of 63-dB gain. The scanning head is attached to 2 motorized stages.

Images were acquired over a field of view of 12 × 12 mm (step size, 20 μm) at 85 % laser energy and a laser pulse repetition rate of 2 kHz. The scan head was coupled to the sample surface by an interchangeable water-filled (2 ml) interface. For coupling of the sample to the interface, phosphate buffered saline was used. The acquired imaging data were reconstructed by the author using a beam-forming algorithm, which models the sensitivity field of the focused detector and generates 3-dimensional images.

Lugol Staining

It is challenging to visualise the soft tissues of the vasculature walls on the micro-CT due to the low X-ray attenuation of non-mineralised tissues. Contrast agents are commonly used

to counter this effect. Lugol-based dyes have been shown to be well suited for imaging soft tissues in bone samples using the micro-CT [240–242]. Therefore, 10 % lugol's iodine solution (VWR Chemicals) was used for this purpose.

The central region of the caudal VEPs, identified as V5 previously, were shown to be the most porous in the previous chapter. Therefore, the V5 samples from the 3 pairs of caudal and cranial VEPs, from the spinal levels L3/L4, L4/L5 and L5/L6 from the previous chapter were used in this lugol study. They were fixed in 10 ml of 10 % paraformaldehyde, then soaked for 72 hours in excess solution of the prepared lugol solution on a shaker at 500 rpm. The samples were then washed in distilled water and imaged using micro-CT at pixel size 4.5 μm, with the same scanning settings and image reconstruction as described in Section 3.2.2.

The reconstructed images were loaded into the CTAnalyser software. A 3D analysis process of the canal openings was carried out, using the *Trabecular Separation* technique to create a file with images of the holes as opposed to the bone. These files were loaded, alongside the original micro-CT files, into CTVox to create 3D rendered images of the internal structure of the samples. The colours and the transparency were optimised, based on a "scout scan", to isolate and image the soft tissues in the canal network.

Lugol Perfusion of Cow Tail

In order to investigate the closed system of blood circulation connecting the rest of the spine to the VEP, a tracer was used to perfuse a whole bovine tail sample. This experiment was carried out at the Physics Department at the University of Exeter with the assistance of Ellen Green and Fay Manning. The bovine tail used in this study was investigated shortly after slaughter, before the onset of blood clotting. The main artery (median caudal) in the tail was immediately cannulated after excision and flushed through with PBS and heprin solution. The main vein (median caudal) was similarly cannulated and the flushing procedure was carried out until the fluid exiting the vein was clear. A syringe was then attached to the arterial cannula and the 10 % lugol solution was slowly injected into the system. The injection was stopped once the visible soft tissue underlying the tail skin appeared brown.

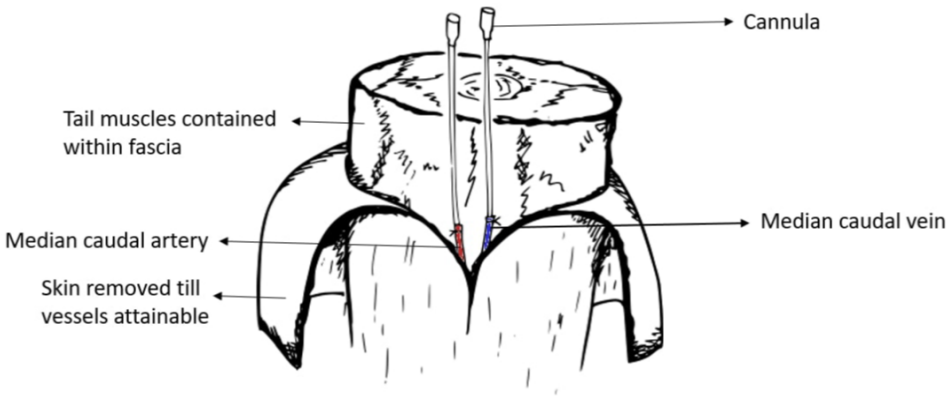

Fig. 4.3 Schematic of the bovine tail with the skin peeled back, far enough to expose the median caudal vein and artery which were cannulated and secured with surgical thread [243].

The 4 vertebrae, from spinal level L3 to L6, were separated by incision through the discs, wrapped separately and frozen at - 80 °C. This provided 4 pairs of caudal and cranial VEPs. Using a Leica light dissection microscope fitted with a Mako camera (WILD M10 G231C IRC PoE), wide fields images of the disc over a range of magnifications were taken by the author. Layers of the discs, 2 mm thick, were then carefully sliced off using a scalpel to image the endings of the canals from the VEP. The frozen samples were then transported to Cambridge and imaged as a whole VEP using the micro-CT with the same settings as described in Section 3.2.2.

4.2.2 Quantitative Analysis of 3D Canal Network

Canal Openings Analysis

The porosity analysis carried out in the previous chapter gave an indication of the porosity across the whole thickness of the VEP. This porosity refers to canals which eventually end at the VEP-disc boundary, appearing as holes, or canal openings. An analysis of the canal openings distribution on the uppermost surface of the VEP, at the boundary with the disc, would indicate the ease of biochemical exchange at the boundary between the VEP and the soft tissues of the cartilage endplate and the disc.

The reconstructed images from the 54 samples were loaded into the CTAnalyser software. A pore analysis was then carried out using the *Individual Object Analysis in 2D* function. For each sample, the topmost 5 image slices were used to calculate average values and the associated standard deviation. This analysis measures the number of openings. The openings per unit area was then calculated as the ratio of number of openings to the surface area of the VEP surface. This was repeated for the 18 samples from the second spine.

The major and minor diameters of each opening were also measured to provide insight into the cross-sectional shape of the openings and to compare with the size of blood vessels. The major diameter is defined as the distance between the two furthest pixels in the openings. The minor diameter is defined as the longest chord through the opening that can be drawn in the perpendicular direction to the major diameter. The aspect ratio was then calculated as the ratio between the major diameter and the minor diameter.

Centreline Analysis

The masks of the canals created in Section 4.2.1. for the 54 samples were used to quantify and compare the structure of each canal. This analysis was repeated for the samples from the second spine. The Simpleware software creates a network of centrelines, lines that run in the middle of each canal with a node at each extremities and at junctions where the canal splits into more than one branch. The canals were then manually pruned to ensure nodes were not inserted in the middle of single lines and to remove loops and incongruent lines.

The length, best fit diameter, orientation with respect to the normal of the VEP surface and vertical position of each line segment between 2 consecutive nodes were measured.

However, the data for each line segment does not clarify the structure of individual canals. The line segments making up the structure of each canal were therefore joined together using a python model created with the assistance of Malavika Nair from the Department of Materials Science and Metallurgy in Cambridge, as shown in Figure 4.4. The model loops through each segment sharing a single node, performing a pair-wise comparison of the angle between each segment of interest and the adjoining lines at the given node. A connection was made between two line segments where the spread between segments were characterised by the smallest angle. Self-intersections were avoided by ensuring that the tolerance for angles between the segment and line were greater than 1°.

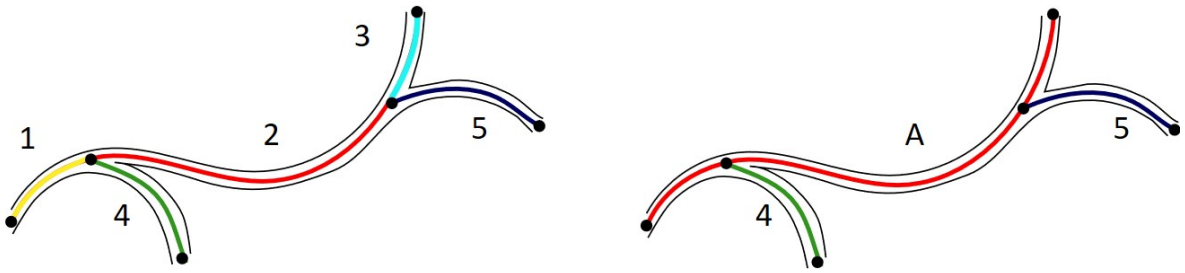

Fig. 4.4 Schematics showing an example of line segments that can be joined together by the python model to create the full canal they represent. The original 5 line segments created from the centerline analysis with their corresponding nodes are shown on the left. After the application of the model, canal A was identified by joining line segments 1, 2 and 3 from the originals, but 4 and 5 still remained as isolated line segments. Therefore the line segments 1, 2 and 3 were parts of the same canal.

The angle between 2 line segments were characterised as shown in Equation 4.1, as the inverse cosine of the scalar product of the unit vectors of the 2 line vectors such that θ_{ij} always lies between 0 °and 180 °. The model calculated the angle between each of the line segments at a node and joined the two with the smallest angle between them. Figure 4.5 exemplifies this with line segments 1 and 2 joined together post processing. Starting from segment 1, at the node, the angle θ_{21} is smaller than both θ_{13} and θ_{23}. The pair 1 and 2 therefore are joined together to form a canal.

$$\theta_{ij} = arccos(V_i.V_j) \tag{4.1}$$

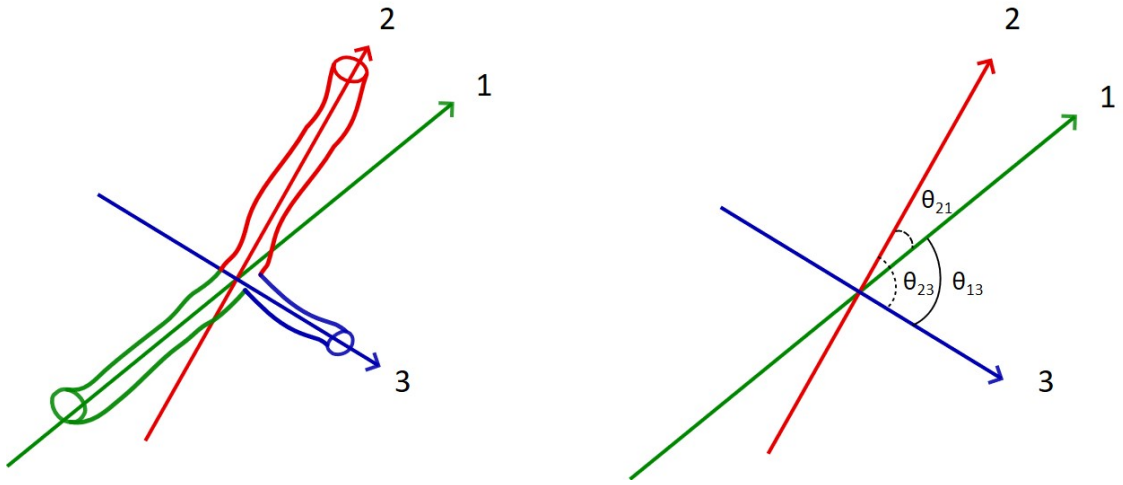

Fig. 4.5 3 line segments with their corresponding vectors are shown (left) with the corresponding angles (right). θ_{21} being the smallest angle would mean that the model will join line segments 1 and 2.

Categories of Canals

The canals were classified into different categories depending on their start and end points, their orientation with respect to the VEP surface's normal direction, and their diameters. A schematic diagram summarising the categories of canals is shown in Figure 4.6. Canals were firstly separated into 2 groups, those starting at the surface of the VEP and those starting in the middle of the VEP layer. Canals starting in the middle of the VEP layer, were subdivided depending on their orientation with respect to the normal of the VEP surface. Canals in the range of 70 °- 110 °to the VEP normal were labelled as "Transverse". Following a comparison of the datasets produced in this study with pre-existing classifications of the larger transverse canals in the literature [131], transverse canals with diameter larger than 0.24 mm were classified as "Large Transverse" canals, that is the cut off radius R_{cutoff} was 0.12 mm. For all canals, their end positions, either back to the VEP surface where their start position were, or in the middle of the VEP layer, or at the trabecular boundary, would also play a role in their classifications. A summary of the criteria for each classification is shown in Figure 4.7. For each category, a breakdown of the parameters in terms of length, diameter and orientation were then compared.

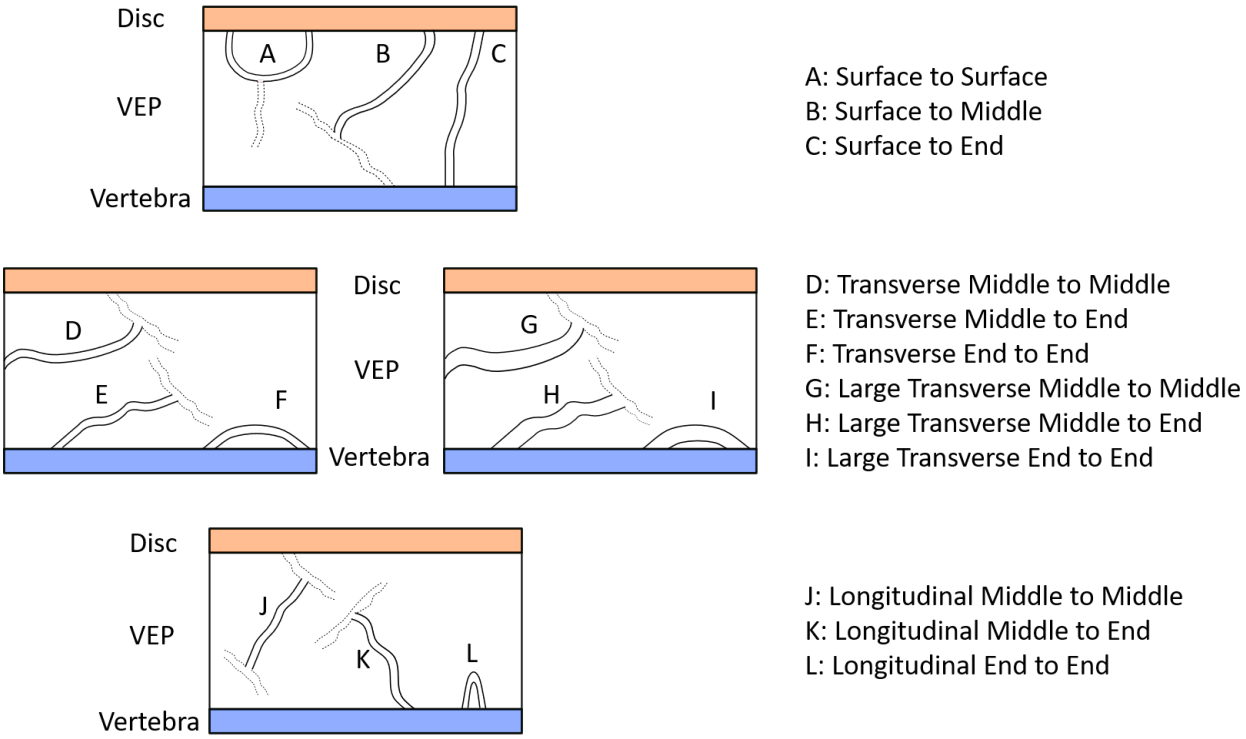

Fig. 4.6 Schematic showing the different categories of canals. The pink strip represents the boundary of the VEP with the disc, which is referred to as the Surface. The blue strip represents the boundary of the VEP with the vertebra and is referred to as the End. The white strip in the middle is the VEP.

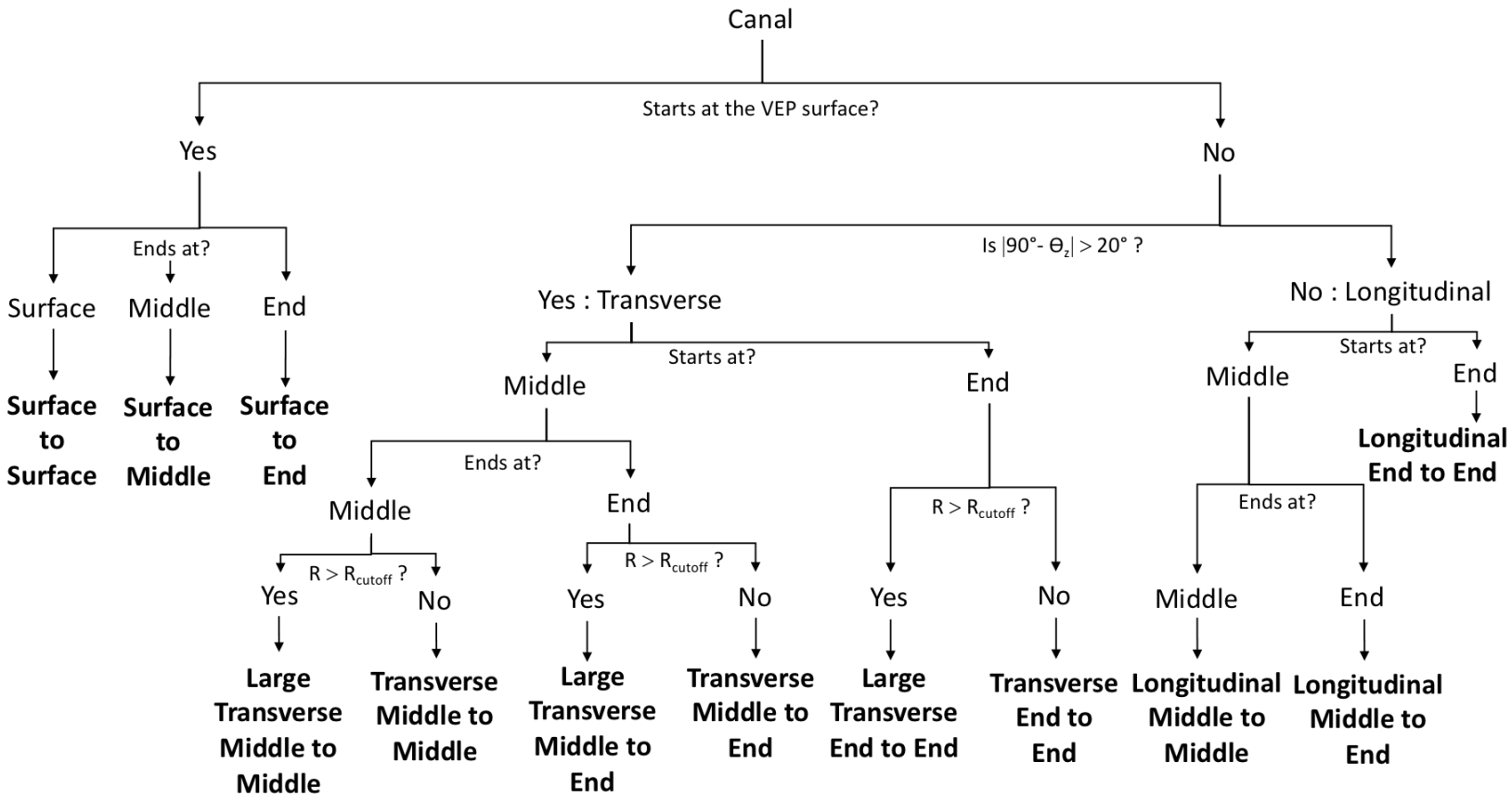

Fig. 4.7 Flow diagram showing the categorisation of 12 different classes of the canals depending on their start and end points, their orientation with respect to the normal of the VEP surface, represented as θ_z, and the radius of the canal, shown as R. R_{cutoff} represents the maximum radius above which the canals are considered larger than normal. The surface refers to the VEP, the end refers to the boundary of the VEP with the underlying trabecular bone and the middle refers to any point in between the surface and end.

4.3 Results

4.3.1 The Canal Network

Figures 4.8 and 4.9 are the representative masks of the anterior V2 section of the caudal VEP from the L4/L5 spinal level. The VEP showed small canal openings distributed along the boundary of the VEP and the disc, which is shown as the empty upper layer space in Figure 4.8. The openings in the transverse slice A are seen to be much smaller than the large pores present in the underlying trabecular bone, shown in slice B. From a side view, the hole can also be seen to be distributed throughout the thickness of the VEP in the zoomed in region C. These canal openings do not exist in the trabecular bone in the vertebra, as shown in the region D, instead they are separated by large porous structures, characteristic of the sponge-like trabecular bone.

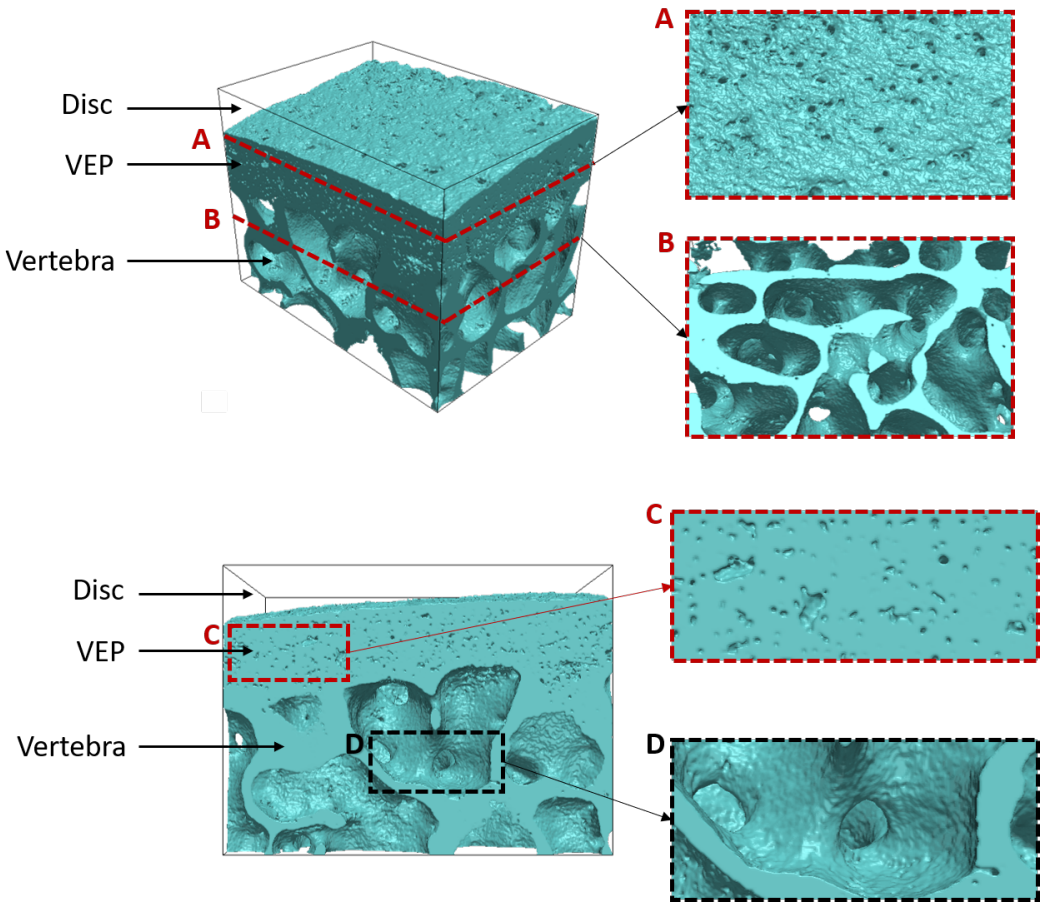

Fig. 4.8 The bone mask of V2 sample from caudal VEP of level L4/L5 shows the disc space, represented by the empty space, the VEP and the trabecular bone of the vertebra. From the ROI at the top, transverse slice A shows the distribution of well-defined openings in the VEP. Slice B shows the trabecular bone in the vertebra separated by large openings. The ROI at the bottom shows the side view and 2 zoomed in areas: C shows the openings distributed across the whole depth of the VEP and D shows the larger pores of the trabecular bone.

When the mask is inverted to show the "empty" spaces, as shown in Figure 4.9, the canal network becomes visible as shown by slices A and C. The openings can therefore be seen to be connected into a complex 3D network, branching from the trabecular bone and sprouting into the canal openings at the disc boundary.

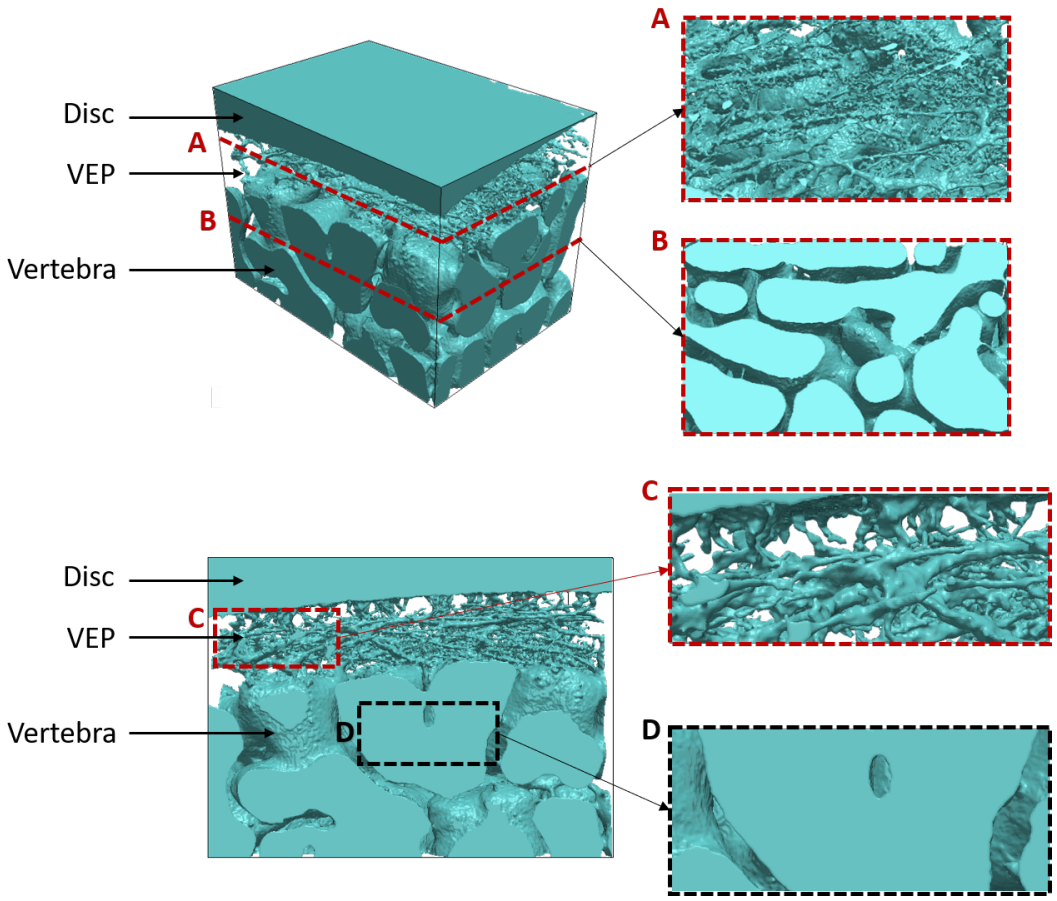

Fig. 4.9 The inverted bone mask of V2 sample from caudal VEP of level L4/L5 shows the disc space, represented by the filled top layer, the VEP space and the trabecular space of the vertebra. From the ROI at the top, transverse slice A shows the canal network connecting the openings present in the VEP. Slice B shows the large trabecular spaces in the vertebra. The ROI at the bottom shows the side view and 2 zoomed in areas: C shows the how the network connects the trabecular spaces and open up into the disc and VEP boundary and D shows the larger trabecular spaces of the trabecular bone.

Figure 4.10 shows the transverse masks of the canals of samples V1 to V9 of the caudal VEP at the L3/L4 level. The central region of the VEP, represented by region V5, had the highest density of canals. Most of the canals lie parallel to the disc and run in concentric directions, as shown in regions V1, V3, V7 and V9. Similar observations were made for all VEPs, irrespective of spinal level or side of the disc.

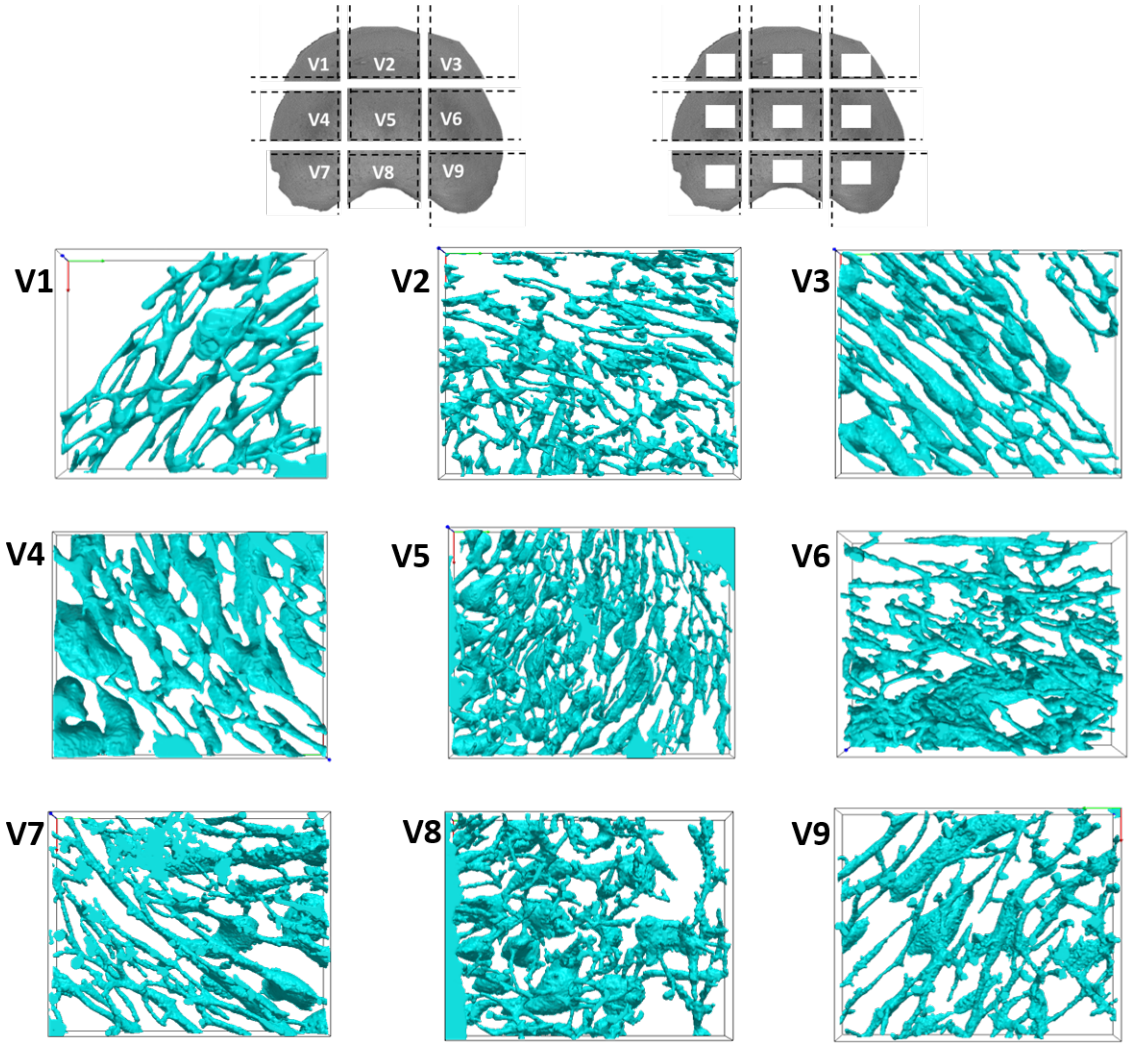

Fig. 4.10 The schematic at the top shows the locations of V1 to V9 on the VEP surface and the white squares represent the regions of interest for which the canals are being shown. The transverse sections of samples V1 to V9 for caudal VEP at L3/L4 level are showing the architecture of the canal networks. The central region, V5, has the highest density of canals and most of the canals are seen to run in concentric directions, parallel to the disc. The square surface of each region represents an area of 4 mm^2.

Given that the central region of the VEP is the most dense with canals and where most biochemical exchange happens with the disc [125], the V5 samples from all 6 VEPs were compared, as shown in Figure 4.11. Moreover, the V5 samples from the second spine are also included, shown in green. Comparing the caudal VEP at levels L3/L4 and L5/L6, it was apparent that the density of canals is lower in the latter. From spinal level L3/L4 to L5/L6, the density of canals appeared to decrease. Most of the canals lie parallel to the disc and run

in circular directions around the central point of the disc. However, visually, it was hard to make any conclusive remarks on the trends of the canal network at this stage.

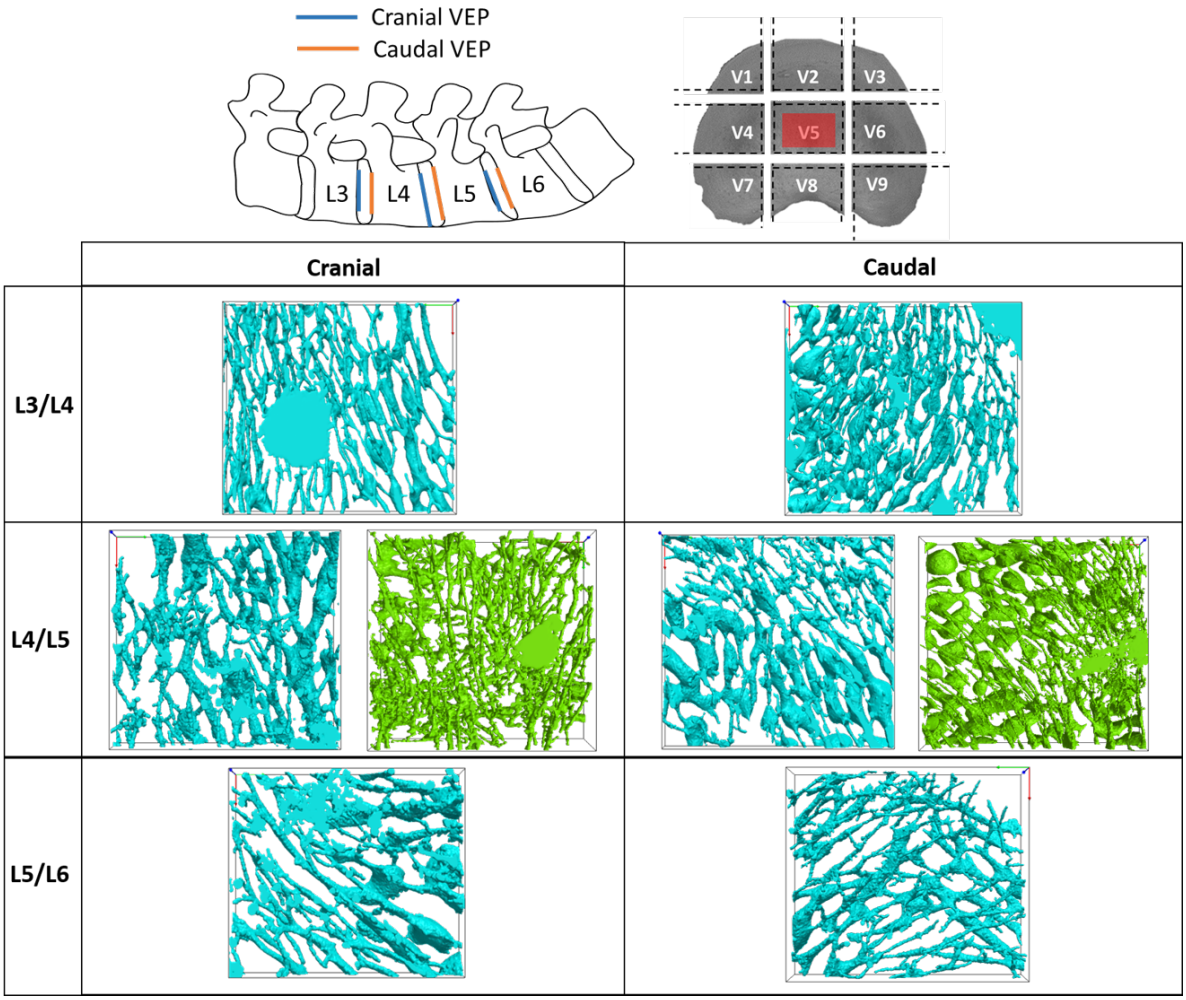

Fig. 4.11 The schematic at the top shows the location of the cranial and caudal VEPs at specific spinal levels and V5 is the sample being shown here, with the red box showing the region of interest. The canal networks in the central region of VEPs, V5, are compared at different spinal levels, sides of the disc and from 2 spines. The networks in blue are from Spine 1, the ones in green are from Spine 2. The regions are all densely populated with canals running parallel to the disc. The patchy regions are due to the uneven surface of the VEP boundary with the disc. The square surface of each region represents an area of $4mm^2$.

4.3.2 Blood Vessels in the Canal Network

Histology

Histology of sample V5 from the cranial VEP of level L4/L5 from the second spine revealed 3 distinct regions of soft tissues that are not seen on the micro-CT scans, as shown in Figure 4.12. These are the calcified cartilage, the cartilage endplate and the disc fibres. A comparable slice from the reconstructed CT images of the same sample can be seen on the right hand side. There is no clear distinction between the bone endplate and the calcified cartilage in the latter. The measured thickness of the visible VEP in the micro-CT image was 0.73 $\pm$ 0.11 mm and from the histology image, the bony endplate region and the calcified cartilage were 0.87 $\pm$ 0.27 mm in thickness. So it can be assumed, from the thickness comparison and the lack of visualisation of 2 types of greyscales in the VEP on the micro-CT, that the micro-CT images only showed the bony endplate region and the calcified cartilage layer was not imaged in the CT scans.

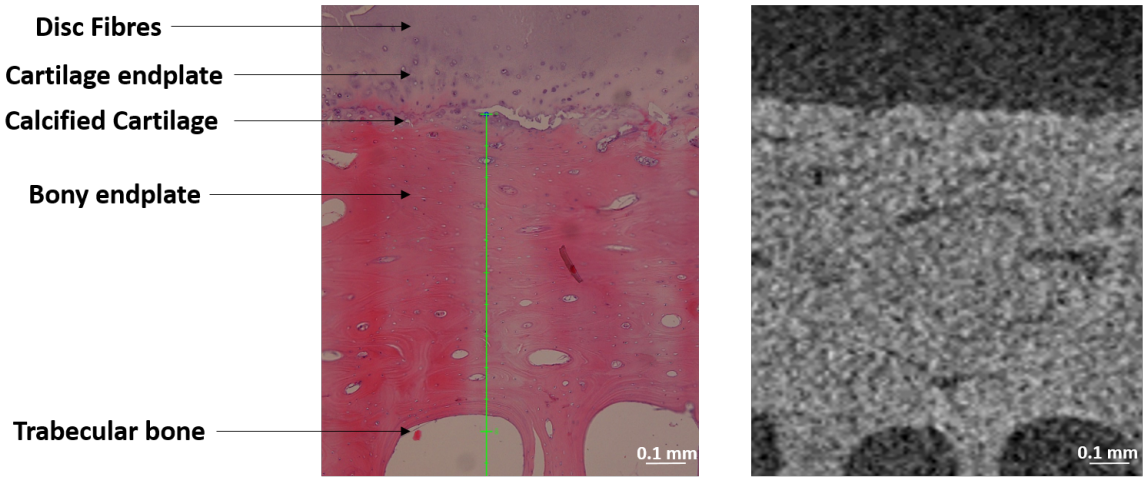

Fig. 4.12 Left: Histology slide of sample V2 from the cranial VEP of level L4/L5 of Spine 2 showing 3 distinct regions of soft tissues. the calcified cartilage layer, the cartilage endplate and the disc fibres, in addition to the bony endplate and the trabecular bone from the vertebra. Right: Reconstructed micro-CT image of a similar slice from the same sample showing only the bony endplate region, in comparison to the image on the left.

Lugol Staining

Lugol solution was used in an attempt to make the content of the canal network visible in the micro-CT scans. As seen in the V5 sample from the cranial L4/L5 sheep VEP in Figure 4.13, the big green pores show the bone marrow stained with lugol inside the trabecular spaces as the bone has been made to appear transparent. The canal network in the VEP can also be

seen poking out of the VEP boundary with the disc. The individual canals can be seen to emerge from the boundary, into what appears to be a bud-like structure.

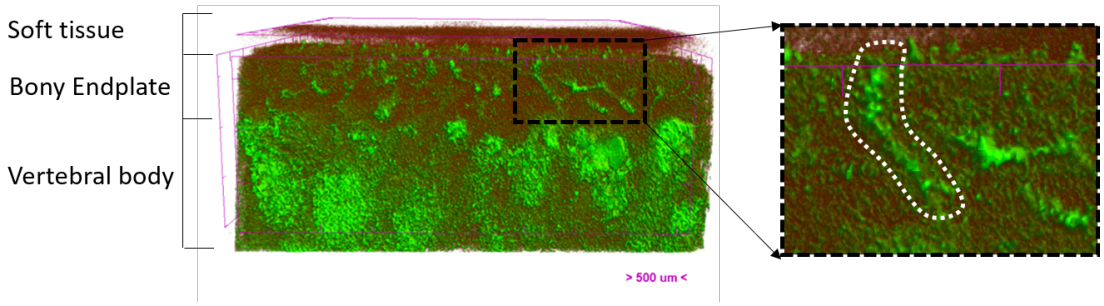

Fig. 4.13 CTVox 3D rendered images of the canals and the trabecular spaces shown in green from the V5 sample of the cranial L4/L5 sheep VEP. The bone has been made transparent and the disc is shown as the red haze. The canals can be seen to be filled with dyed soft tissue originating from the bone marrow and ending into bud-like structure, emerging out of the VEP boundary with the disc. The dotted white outline shows a close-up canal emerging out of the VEP surface.

This is also shown in Figure 4.14. From a top view of the VEP, several small green bumps can be seen poking out of the bone into the red haze which represents the disc. Therefore, the openings that were seen in the VEP boundary in Figure 4.8 are not empty holes and do not contain disc fibres descending into the bone. They appear to be filled with soft tissue, which could be blood vessels, lymphatic vessels or bone marrow, originating from the vertebra and ending into bud-like structures near the disc surface.

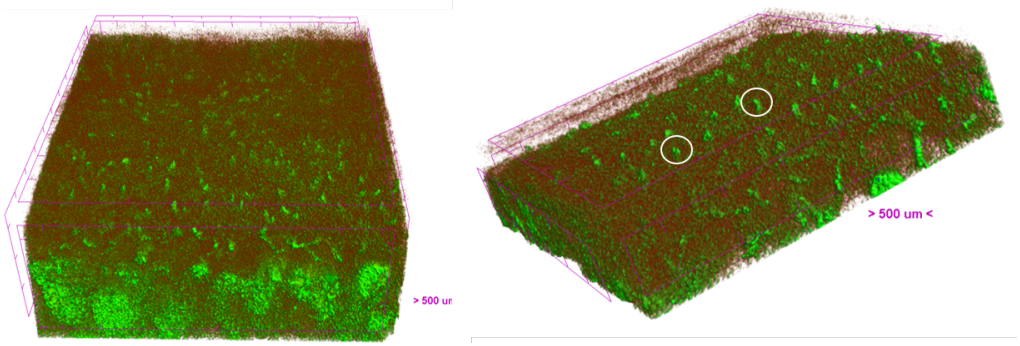

Fig. 4.14 A top view of the CTVox 3D rendered images of the canals and the trabecular spaces shown in green from the V5 sample of the cranial L4/L5 sheep VEP. The bone has been made transparent and the disc is shown as the red haze. Several buds can be seen emerging out of the VEP boundary with the disc and the white circles show 2 of these buds.

Cow Tail Perfusion

The cow tail was injected with lugol solution to test whether the bud-like structures are filled with blood vessels. The penetration of the stain was assumed to be successful given that the inner side of the tail skin showed the blood vessels filled with the yellowish-brown stain when the tail was skinned, as shown in Figure 4.15.

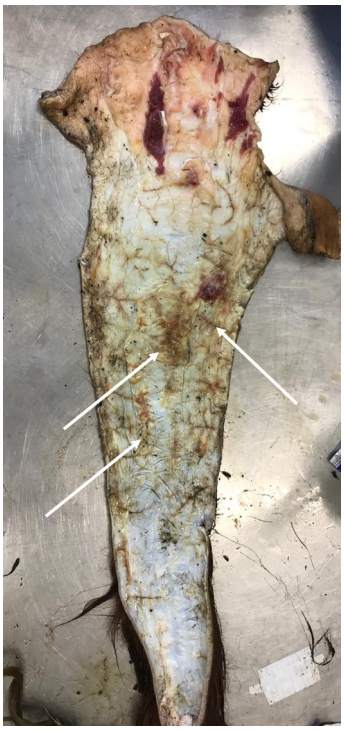

Fig. 4.15 Photograph showing the inner side of the skin of the cow tail post removal. The yellow-brown stains, shown by the white arrows, show the successful penetration of the dye through the small blood vessels on the outer extremities of the tail.

As shown in the top view of a dissection image of the cranial VEP surface from L5 with most of the soft tissue of the disc cut off in Figure 4.16, there are several small reddish-brown spots observed. The spots appear to be filled with a reddish-brown fluid which could either be blood or lugol solution. However,the blood in the whole tail was washed out extensively before the start of the experiment and given the timeframe, it is likely that blood would have clotted by the time of imaging and not still be in liquid form. Therefore, the canals appear to be filled with the lugol dye.

Using a scalpel, 2 mm of more soft tissue was cut off to expose more of the bud-like structures, as shown in Figure 4.17. The white arrowheads in slices B and C showed the presence of a potentially transverse flowing canal, appearing to be thicker than the canals emerging at the surface, underneath the VEP surface, also filled with a reddish fluid.

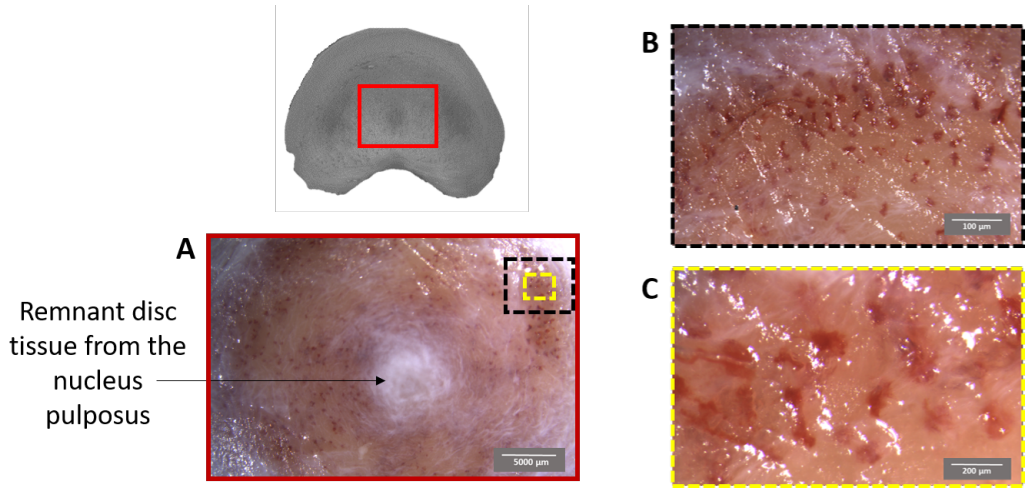

Fig. 4.16 The red square shows the central region of the VEP surface which is shown as a close-up in slice A. A: Top view of the cranial VEP surface from L5 with the disc excised, viewed in the dissection microscope. Some of the nucleus pulposus can be seen as the white fibres at the centre of the image due to the uneven VEP surface. B: Close-up of the black dotted rectangle in slice A, at 16x magnification showing the dots. C: Close-up of the yellow dotted rectangle in slice A, at 80x magnification showing the dots do not look like clots but filled with a liquid.

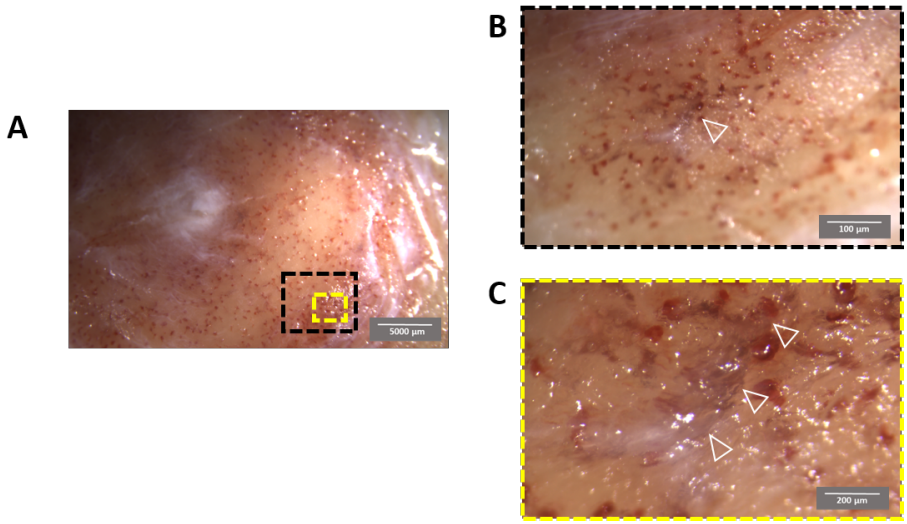

Fig. 4.17 A: Top view of the cranial VEP surface from L5 with an extra 2 mm of the disc excised, viewed in the dissection microscope. B: Close-up of the black dotted rectangle in slice A, at 16x magnification showing the dots. C: Close-up of the yellow dotted rectangle in slice A, at 80x magnification. The white arrowheads in slices B and C show the presence of a transverse thicker canal filled with reddish fluid underneath the upper surface of the VEP.

The cow tail samples were loaded in the micro-CT and the scan of the whole caudal VEP from L4/L5 is shown in Figure 4.18. In the transverse image of the VEP surface, the openings can be seen, however the image appears to be slightly blurry due to the lugol dye interfering with contrast. The soft tissue in the canals cannot be seen in the micro-CT, they still appear as "empty" spaces. Similarly for the trabecular bone in the vertebra underlying the VEP, as shown in Figure 4.19, the internal soft tissues appear as "empty" spaces. The lugol dye failed to stain the tissues enough to create contrast with the bone in the micro-CT. The presence of growth plates were also seen in the vertebral bodies.

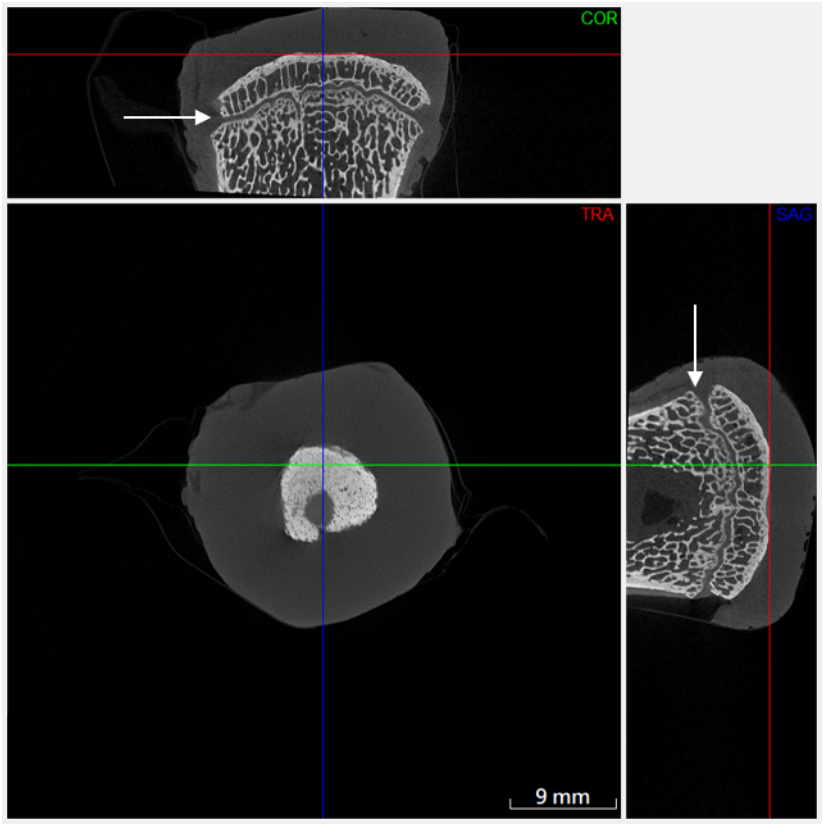

Fig. 4.18 The 3 orthogonal views of the caudal VEP from L5 with the underlying trabecular bone is shown to have a distribution of small openings. However, the openings appear "empty", implying the dye was not strong enough to create contrast with the bone. The outlines of the openings are less well defined due to interference of the dye with contrast. The red lines show the location of the transverse slice, the green line shows the coronal slice and the blue line shows the sagittal slice. The white arrows show the presence of growth plates.

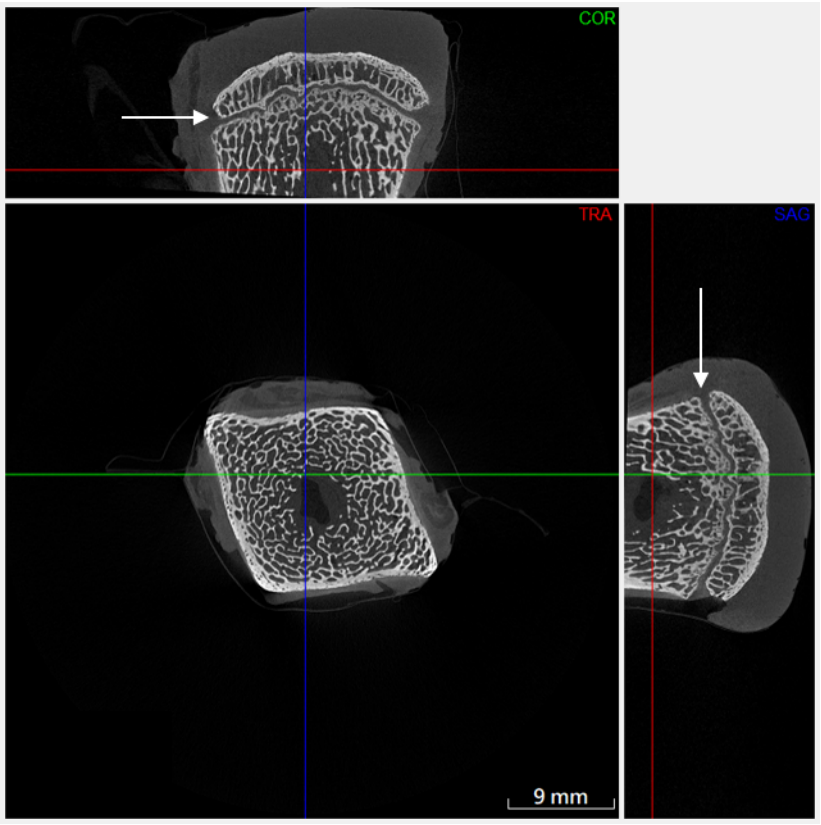

Fig. 4.19 The 3 orthogonal views of the trabecular bone in the underlying vertebra of the caudal VEP from L5 show the open pores of the trabecular space. However, the openings appear "empty", implying the dye was not strong enough to create contrast with the bone. The outlines of the openings are less well defined due to interference of the dye with contrast. The empty space in the middle of the vertebra is loss of pieces of bone material from the sectioning of the samples. The red lines show the location of the transverse slice, the green line shows the coronal slice and the blue line shows the sagittal slice. The white arrows show the presence of growth plates.

Photoacoustic Imaging of Blood Vessels

The photoacoustic imaging of the sheep VEP showed the presence of haemoglobin, as shown in red in Figure 4.20. This implies the presence of blood in the canal network of the VEP layer. However, from the side view, red dots could be seen in the layer where the bony endplate was but without connecting vessels with the vertebra. Even within the VEP, there were no continuous vessels imaged, only isolated dots were seen. This could be because the blood has clotted in the vessels from the cadaveric sheep spine, leading to the imaging of a discontinuous blood flow in the vessels.

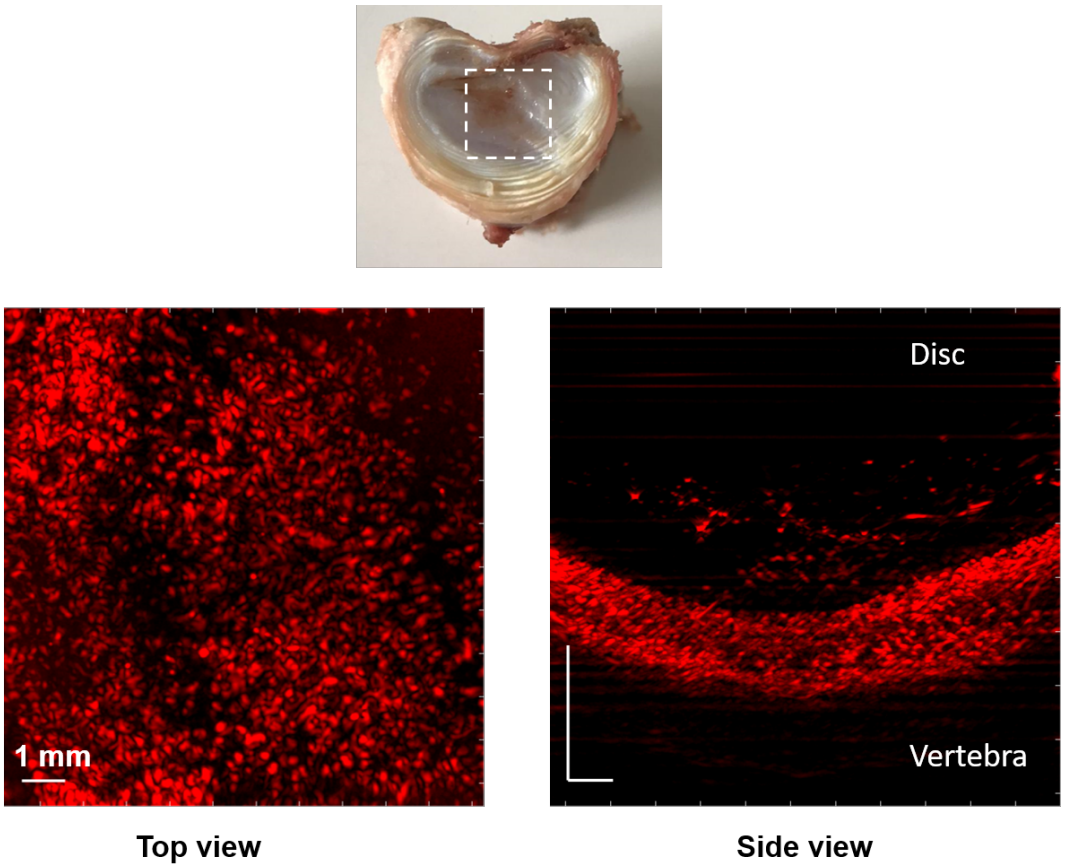

Fig. 4.20 The white dotted square represents the area of focus of the laser. The top view of the VEP central region shows the presence of dispersed red dots, showing the presence of haemoglobin. The side view shows the presences of isolated red dots in the curved central region of the VEP with no connecting vessels. The white scale bars represent 1 mm in both orthogonal directions.

4.3.3 Analysis of the Canal Openings of the VEP surface

Figure 4.21 shows the distribution of the number of openings per area for all 54 samples from Spine 1 and the 18 samples from Spine 2. The central regions of the VEP have the highest density of openings per area for all the VEPs. The canal openings density per area also decreases down the spine from L3/L4 level to L5/L6 and at all levels the caudal VEPs showed significantly more openings than the cranial ones. Samples from the second spine exhibited the same trends as from the first, with opening density in the same range, as shown in Figure 4.22.

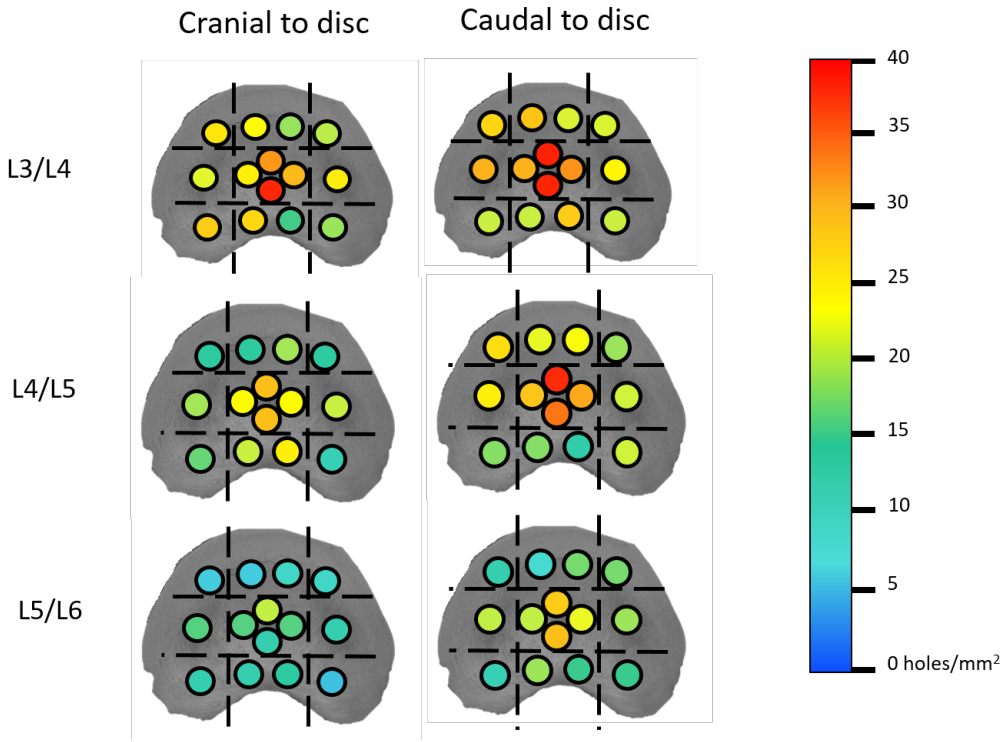

Fig. 4.21 Schematic with colour-coded opening density per unit area of each ROI for the 54 samples from Spine 1. The scale bar on the right shows the opening density per area assigned to the colours. The central regions of each VEP, the higher spinal level L3/L4 and the caudal VEPs showed higher opening density per unit area than their counterparts.

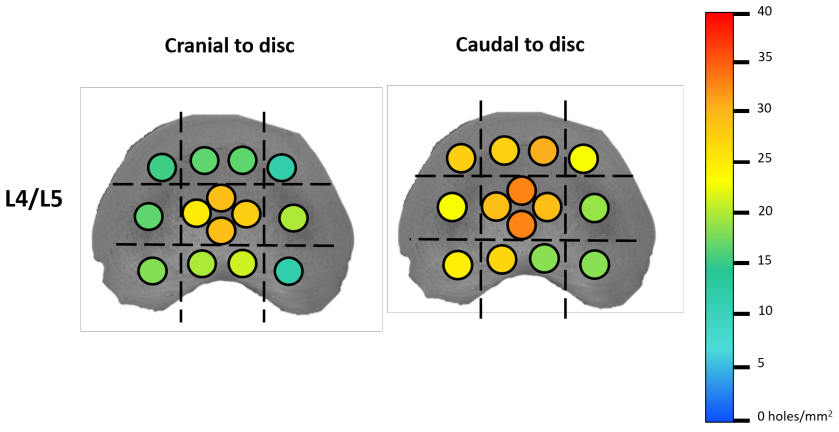

Fig. 4.22 Schematic with colour-coded opening density per unit area of each ROI for the 18 samples from Spine 2. The scale bar on the right shows the opening density per area assigned to the colours. The central regions of each VEP and the caudal VEPs showed higher opening density per unit area than their counterparts.

The average major and minor diameters of the openings for each sample from both spines are shown in Figure 4.23. No apparent trends can be observed, other than the majority of openings not having a perfect circular shape. Few samples had an aspect ratio of 1.0 for their openings implying the openings were close to being perfect circles.

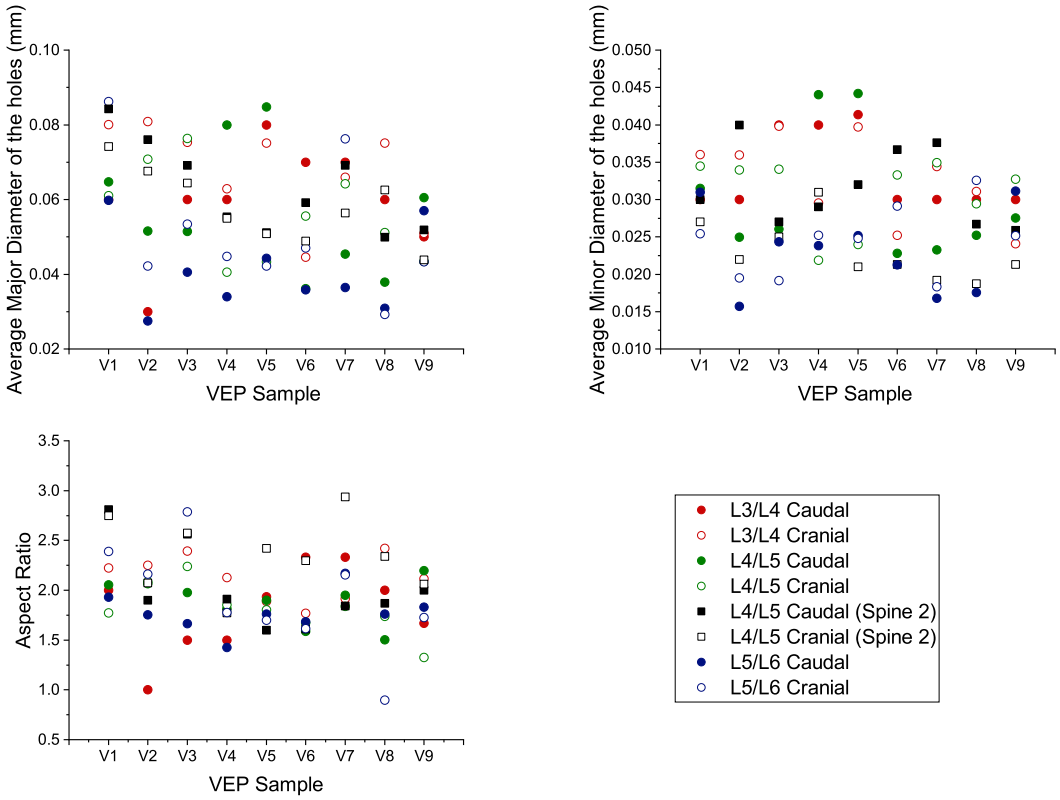

Fig. 4.23 Top Left: The average major diameters of the openings for each sample from both spines are shown. There is no clear trend in how the diameters vary across different samples. Top Right: The average minor diameters of the canal openings for each sample from both spines are shown. There is no clear trend in how the diameters vary across different samples. Bottom Left: The aspect ratio, ratio of the major to minor diameters, for each sample from both spines are shown. Most of the openings appear to be in the range of 1.5 to 2.5, except for a couple with clear to perfect circular shape. Bottom Right: The legend for all 3 graphs.

4.3.4 Quantitative Analysis of the 3D Canal Network

From the centreline analysis of the canal network, the canals were classified into categories as explained in Section 4.2.2. From the results, across all the samples, no canals were classified

as "Longitudinal End to End" or "Large Transverse End to End". The prevalence of each type of the remaining categories can be seen in Figure 4.24. Across all VEPs, the central region V5 showed relatively higher prevalence of the canals starting from surface of the VEP. This implies that the canal network has higher concentration of canals that emerge out of the VEP boundary in the central V5 region. The canals that did not start from the surface are split between longitudinal and transverse canals. No transverse canals were seen in the last spinal level of the VEPs and in the other VEPS, they represented less than 3 % of the total canals.

The "Longitudinal Middle to Middle" and "Transverse Middle to Middle" canals were the most prevalent across all VEPs whereas the "Large Transverse Middle to End", the "Surface to End" and the "Transverse Middle to End" were the least prevalent. The VEP samples from the peripheral areas seemed to consist mostly of canals in the middle of the VEP layer, at all angles, with few large transverse ones and few connecting to the VEP boundaries with the disc and trabecular bone. No significant trends could be seen between caudal and cranial VEPs or at different spinal levels from L3/L4 to L5/L6.

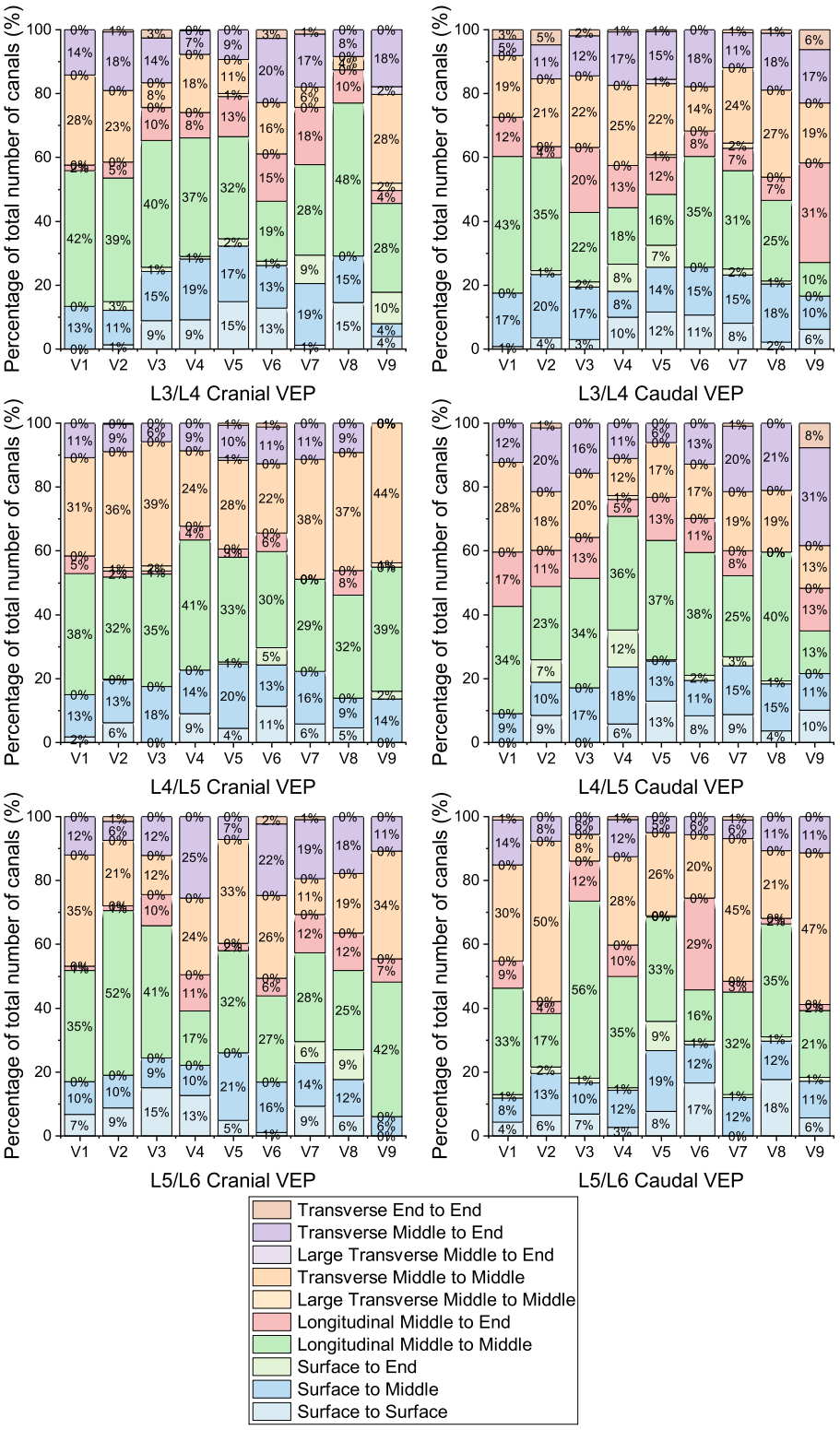

Fig. 4.24 The prevalence of each type of canal as a percentage of the total number of canals is shown for each region V1 to V9 for the 6 VEPs. The 6 graphs represent the 6 VEP locations with respect to the side of the disc and the spinal level.

The canals were broadly classified into 3 groups for the purpose of in-depth analysis: canals starting from the surface, longitudinal canals starting from the middle or the end and transverse canals starting from the middle or end. For each of these 3 groups, the distribution of the structural characteristics of the canals: length and radius, were plotted for the samples V1 to V9 for the 6 VEPs. For the first group, canals starting from the surface of the VEP, this distribution is shown in Figure 4.25. Across all VEPs, the data showed clustering near the origin, implying that most of the canals were relatively short and thin. However, the clusters were seen to be less condensed in the VEPs at lower spinal levels, such that the distributions of lengths and radii were more varied. The concentration of canals which is equivalent to the porosity of the VEP sample, has also been shown to decrease from L3/L4 level to L5/L6 in Figure 3.17 from the previous chapter. The most prominent colour across all the graphs was purple, showing the data points for central samples V5. The caudal VEPs also showed an increased presence of longer canals, upto 2.0 mm. which were more sparse in the cranial VEPs. For the second group, longitudinal canals starting from the middle or the end, the distribution is shown in Figure 4.26. The canals showed a larger distribution in terms of radius of the canal, compared to the surface canals shown in Figures 4.25. The canals also showed a broader distribution of lengths of upto 2.30 ± 0.12 mm. For the third group, transverse canals starting from the middle or end, this distribution is shown in Figure 4.27. The majority of canals seemed to cluster in the region of small radius and short length, with varying concentration across the VEPs. The proportion of canals with radii larger than 0.12 mm decreased from spinal levels L3/L4 to L5/L6, implying the number of large transverse canals decreased, with none in the VEPs at L5/L6 level. However, there were no large and long canals in any of the VEPs samples.

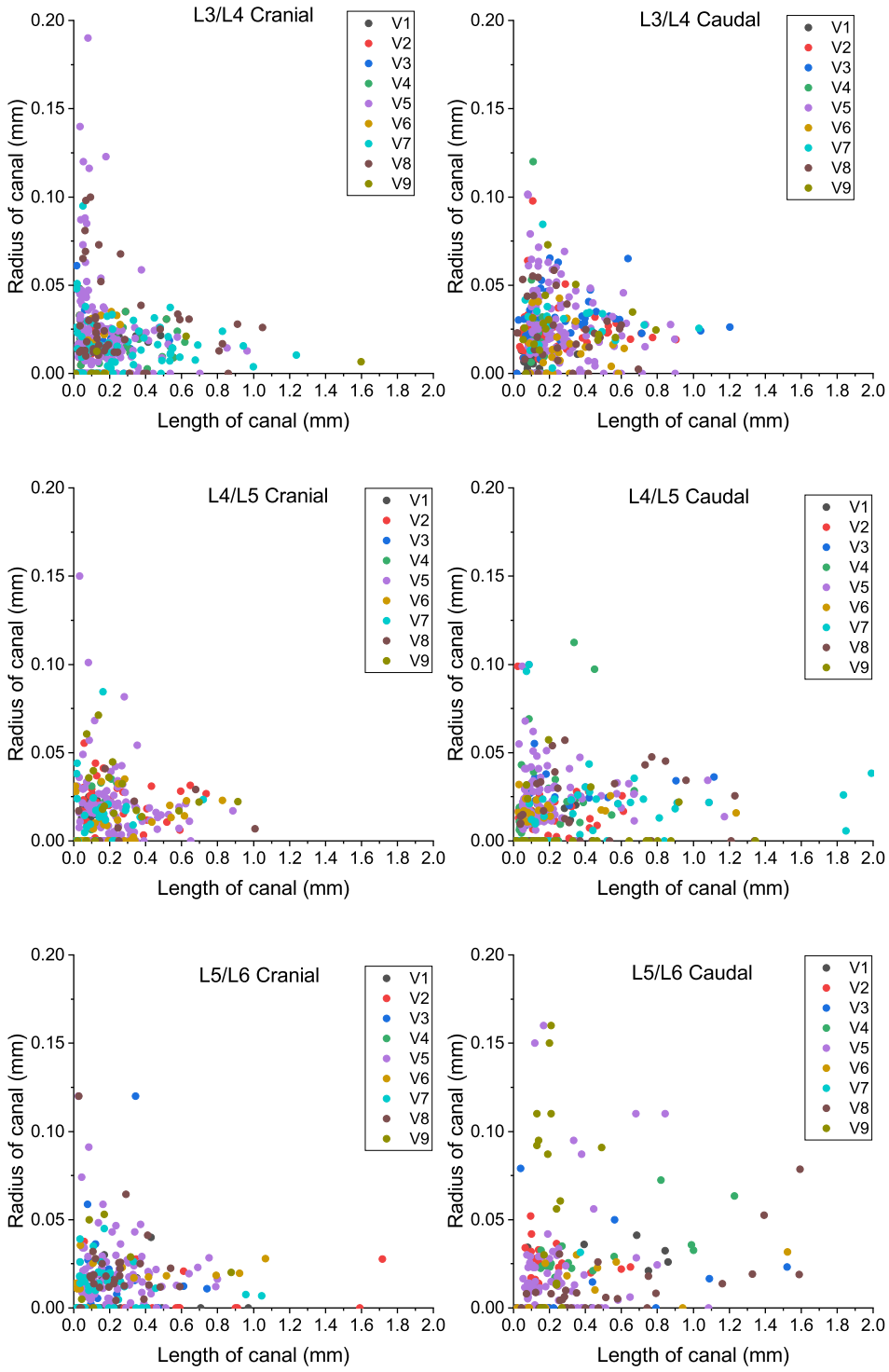

Fig. 4.25 The distribution of the canals originating from the surface of the VEP according to their length and radius are shown for samples V1 to V9 in each graph. The 6 graphs represent the 6 VEP locations with respect to the side of the disc and the spinal level.

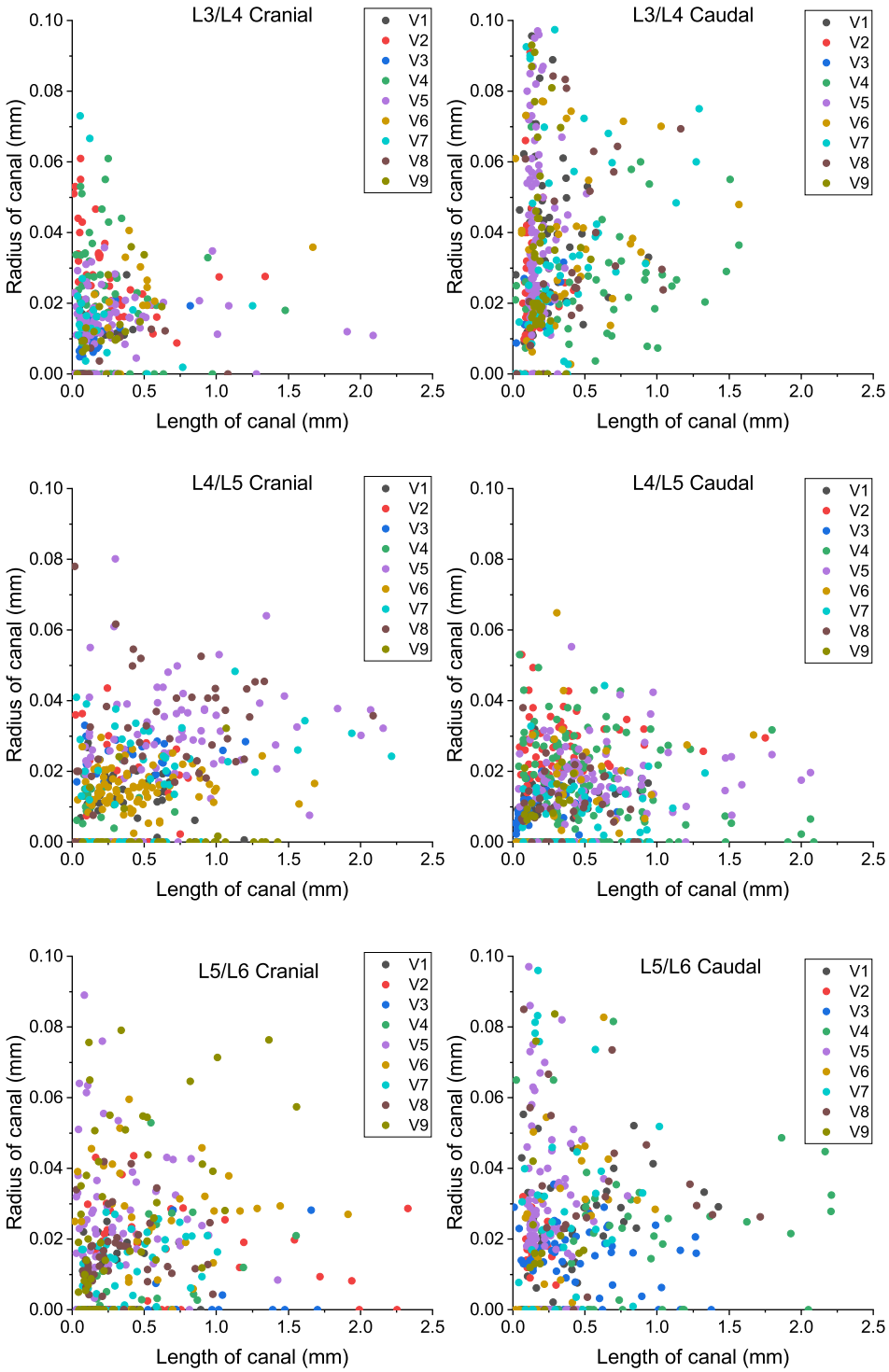

Fig. 4.26 The distribution of the canals originating from the middle or end boundary of the VEP and which were classified as longitudinal canals, are shown for samples V1 to V9 in each graph according to their length and radius. The 6 graphs represent the 6 VEP locations with respect to the side of the disc and the spinal level.

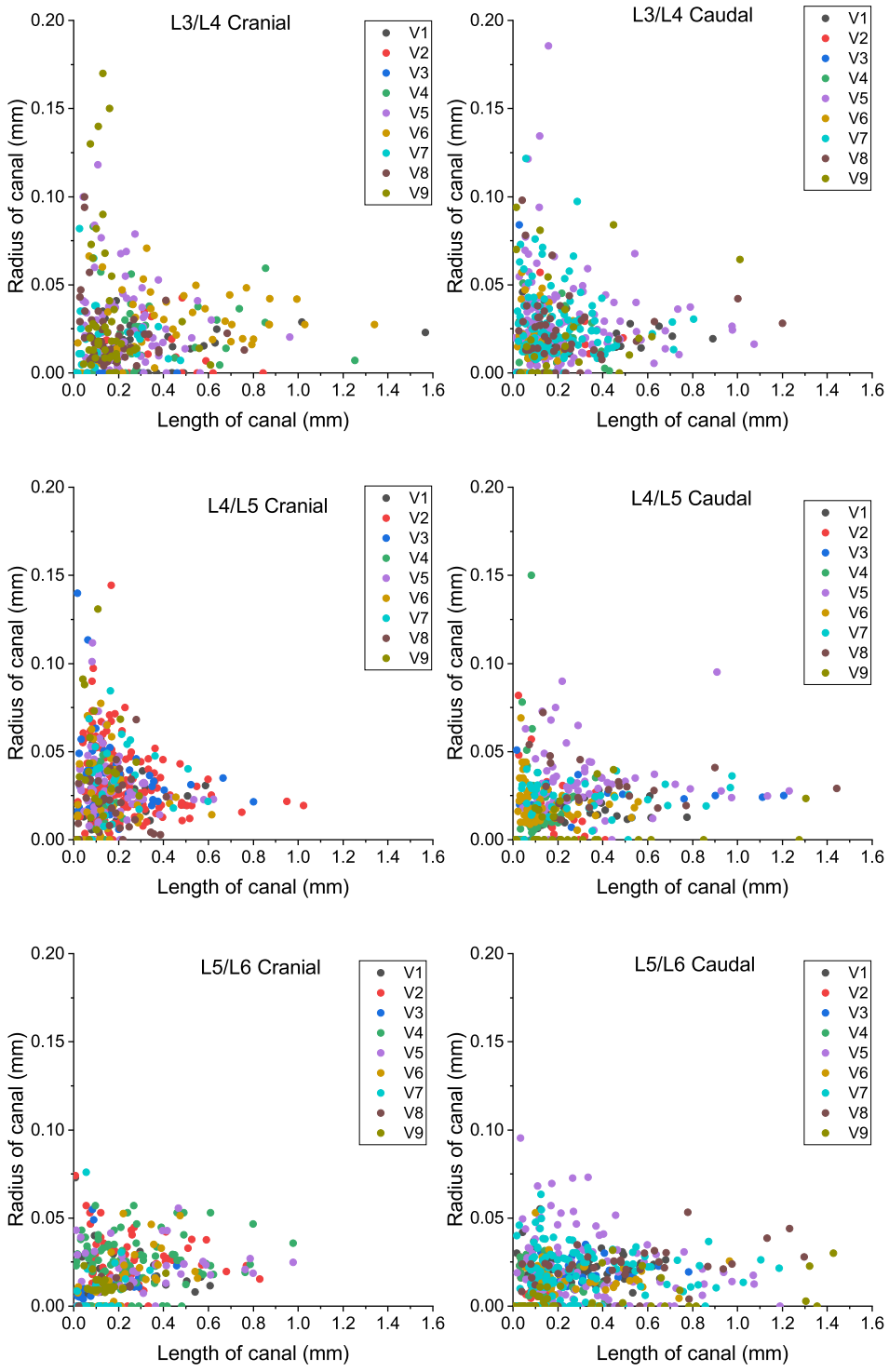

Fig. 4.27 The distribution of the canals originating from the middle or end boundary of the VEP and which were classified as transverse canals, are shown for samples V1 to V9 in each graph according to their length and radius. The 6 graphs represent the 6 VEP locations with respect to the side of the disc and the spinal level.

Comparing the average values of length, radius and orientation for the 3 main categories of canals can provide further insight on how they differ in architecture. This comparison was done for V5 samples from the 6 VEPs as shown in Table 4.1. The large transverse canals were omitted from this analysis so as not to skew the distribution. The data showed that the surface canals were almost perpendicular to the VEP surface, and were shorter than the longitudinal canals but of similar length to the transverse ones. This implies the surface canals are emerging from the transverse canal network and therefore have similar radius but shorter. The transverse canals are seen to be quite short, resulting from the samples being truncated. Across the spinal levels and the caudal/cranial sides of the disc, there were no significant differences or trends between the data for the V5 samples.

Canal Type	Parameters	L3/L4		L4/L5		L5/L6	
		Cranial	Caudal	Cranial	Caudal	Cranial	Caudal
Surface	Length (mm)	0.3 ± 0.2	0.2 ± 0.1	0.2 ± 0.2	0.2 ± 0.2	0.2 ± 0.2	0.3 ± 0.2
	Radius (mm)	0.05 ± 0.02	0.04 ± 0.03	0.03 ± 0.03	0.03 ± 0.02	0.03 ± 0.03	0.02 ± 0.02
	Orientation (°)	33 ± 7	24 ± 6	24 ± 4	20 ± 10	22 ± 9	25 ± 9
Longitudinal	Length (mm)	0.3 ± 0.1	0.6 ± 0.4	0.6 ± 0.4	0.7 ± 0.4	0.5 ± 0.3	0.5 ± 0.3
	Radius (mm)	0.05 ± 0.03	0.03 ± 0.01	0.02 ± 0.02	0.03 ± 0.01	0.04 ± 0.02	0.03 ± 0.02
	Orientation (°)	30 ± 10	50 ± 20	60 ± 10	40 ± 20	50 ± 20	40 ± 20
Transverse	Length (mm)	0.4 ± 0.2	0.3 ± 0.2	0.4 ± 0.3	0.2 ± 0.2	0.5 ± 0.4	0.4 ± 0.3
	Radius (mm)	0.04 ± 0.03	0.03 ± 0.02	0.03 ± 0.03	0.03 ± 0.02	0.03 ± 0.03	0.03 ± 0.02
	Orientation (°)	80 ± 10	90 ± 20	90 ± 20	80 ± 9	100 ± 20	91 ± 8

Table 4.1 Comparison of the length, radius and orientation with respect to the normal to the VEP surface of the 3 main types of canals: surface, longitudinal and transverse, across the V5 samples from the 6 VEPs. The values shown for each parameter are average values and the standard deviation.

4.4 Discussion

This chapter investigated the role of the 3D canal network as a nutritional pathway to the disc. The results of the qualitative analysis of the canal structure will be discussed first, followed by the investigation of the terminations of the canals past the VEP boundary, the presence of blood vessels in the canal network and finally the analysis of the architectural characteristics of individual canals.

4.4.1 The Structure of the Canal Network

The results of this study showed that the canals in the VEP were all connected into a complex 3D network, originating from the trabecular spaces in the vertebral bone and connecting to

the openings present in the boundary of the VEP with the soft tissues of the cartilage endplate and the disc.

The canals, of varying length, sizes and orientations were thinner than the large sponge-like pores present in the trabecular bone. The canals were seen to end into openings at the boundary of the VEP and the disc, as shown in Figure 4.9. This network was similar to the ones reported previously in literature [104, 131, 244]. However, Cao et al. also reported the absence of canals in the central and anterior regions of the caudal VEPs in their mice samples, which was not the case in this study [104]. This could be because of the differences in the maturity of the animal models used in this study and in literature. The blood supply network might be in its formative stages and therefore not completely established in the early years. The canals across the VEP surface were seen to be organised in a circular pattern, running horizontally in the VEP surface surrounding the central region, as shown in Figure 4.10, parallel to the concentric lamellae present in the annulus of the intervertebral disc, with other longitudinal canals connecting the canals from the trabecular bone to the VEP boundary at the disc. Qualitatively, there were no significant differences in the organisation of the canals, as shown in Figures 4.25, 4.26 and 4.27, however, there was a higher density of canals in the central region V5 across all the VEPs. Given that the V5 sample is the middle third portion of the VEP along both the short and long directions of the disc as shown in Figure 4.28, it can be assumed that the V5 samples are the ones in direct contact with the central region of the disc, the nucleus pulposus.

The nucleus pulposus of the disc is where most of the biochemical exchange happens [22], therefore the V5 samples, which had the highest density of canals, are of key importance and were compared for all the VEPs. In Figure 4.11, the canal network was seen to be more dense in spinal level L3/L4 compared to L5/L6. The fewer canals can be explained by the decreasing porosity in the VEP as explained in Section 3.3, at lower spinal levels. The caudal VEPs also have higher porosity than the cranial ones, as shown in Figure 3.17 but this was not apparent from the qualitative data only because of the varying sizes and orientations of the canals. Canals from the second spine showed similar architecture of the canals at level L4/L5.

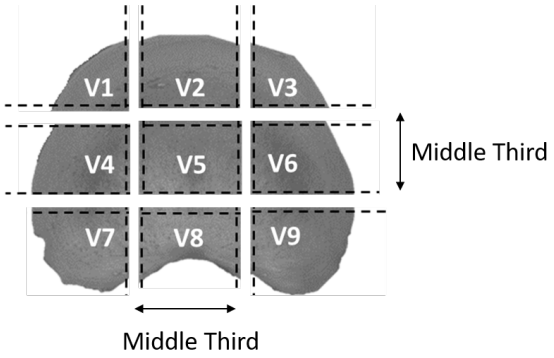

Fig. 4.28 Schematic showing the sides of the V5 sample represent the middle third portion of the VEP surface along both the short and long directions.

After investigating the porosity of the VEP and the organisation of the canals within the VEP, understanding the opening of these canals at the disc and VEP boundary will provide the complete picture of the physical space occupied by the canals. Figure 4.21 reinforced the idea of increased metabolic exchange at the central region of the VEP as the V5 samples had the highest density of openings per area than the surrounding peripheral regions. The openings density per area showed a decreasing trend from spinal level L3/L4 to L5/L6 and from the caudal VEPs to cranial ones. The VEP from the second spine showed similar values for number of openings per area for the L4/L5 VEPs, higher than the L5/L6 VEPS but lower than the L3/L4 VEPs. These trends agreed with the ones shown for the porosity of the VEP, therefore there is a correlation between the porosity of the whole VEP layer and the number of openings at the top surface of the boundary between the VEP and the disc. These openings are the openings of the surface canals that are emerging out of the VEP boundary and therefore could either be the pathway for passive diffusion of nutrients and oxygen to the disc tissues or the canals could be occupied by blood vessels passing through to the other side of the VEP boundary for active diffusion. This will be discussed further in the next section.

To the best of our knowledge, this study is the first to investigate the canal network across the whole VEP surface, at 3 different spinal levels and different sides of the disc, in a large animal model. Cutting the VEP into 9 parts meant that part of the connecting canal network was lost, but it enabled high resolution imaging of the network.

4.4.2 The Soft Tissues and Blood Vessels in the Canal

Histology showed the presence of 3 distinct layers above the VEP: the calcified cartilage, the cartilage endplate and the disc, as shown in Figure 4.12. These layers have been identified previously in different animal models and human cadaveric samples [108, 128, 245].

The disc, made up of a microfibril network of collagen and elastic fibres that anchor into the cartilage endplate, can be seen as a darker shade of purple in Figure 4.12. The cartilage endplate is made of a hydrated proteoglycan gel reinforced by a network of collagen fibrils, similar to the disc, with little to no mineral [246]. The tidemark, seen as the dark purple line, separates the cartilage endplate from the calcified cartilage layer which is considered to be a transition layer from the softer cartilage endplate to the hard bony VEP, as it has a similar structure to the cartilage endplate but with higher mineral content [58]. The latter was seen to be separated from the bony VEP by the cement line where there is a change of colour from pink to purple.

Given that the micro-CT images primarily the hard tissue in the sample, it can be assumed that the disc fibres and the cartilage endplate were not imaged in this current study. Comparing the measurement of the thickness of the VEP of a pre-scanned sample with the thickness of the bony endplate and the calcified cartilage layer confirmed that the calcified cartilage layer was also absent in the micro-CT images. For the rest of this study it was assumed that the only layer observed and under investigation in this study is the bony VEP. The canals observed to be emerging from the VEP boundary could therefore be continuing into either the calcified cartilage or cartilage endplate layers.

Shu et al. used histology to show blood vessels penetrating into the cartilage endplate of Merino Wethers Sheep[247]. Therefore, the canals originating from the VEP, through the boundary, could be continuing till the cartilage endplate, however, the architecture of any blood vessel in the soft tissues still remains unclear.

The lugol study showed the presence of buds that exist outside of the VEP layer, emerging through the canal openings identified earlier from the micro-CT. Lugol solution, or potassium iodide (I_2KI), has a high affinity for carbohydrates and polysaccharides in soft tissues [248]. Lugol's differential affinities for different types of biological tissues would provide different absorbance values and should therefore provide contrast between the soft tissues in the micro-CT [240]. The different penetration depth and affinities of the stain enabled the visualisation of the bone marrow within the trabecular spaces and the soft tissue contained within the canal network in the VEP, as well as the disc. However, lugol stains blood intensely, according to literature, and therefore it was hard to differentiate between the blood vessels and the bone marrow in the VEP and trabecular bone [249]. This could be because the samples were from frozen sheep spines and from the literature, the best results of vasculature staining were seen with fresh specimens [248]. Furthermore, the defrosted samples have clotted blood which would affect the staining time of the blood cells and also block the access of the stain to the blood vessel walls, making visualisation of the blood vessels less clear. The quality of the image was grainy and blurry which could be explained by the shrinkage of tissue caused by

water leaving the tissues to the staining solution due to the osmotic gradient caused by the stain. The presence of any remnant solution within the bone will also affect the quality of the micro-CT image.

The stain was injected into the vascular network of the freshly harvested cow tail with the aim of better staining and penetration of the blood vessels. The reason for using a cow tail was the relative ease to obtain fresh cow tail, straight after the slaughter of the cow, with the main arteries of the spine still intact. Therefore, cannulation of the spine section was easy, to better visualise the complete blood network in the spine especially in the region of the VEP. As for the sheep spines, the lumbar spine was delivered frozen, with skin and surrounding soft tissues removed, therefore making cannulation impossible. The stain was deemed successful given that the inner capillaries of the skin were shown to have been stained, after removal of the skin. The images taken from the dissection microscope identified some bud-like structures, matching the expected colour of lugol stained blood vessels. Given that these images were taken about 6 hours after the time of death of the animal and that blood starts to clot after the first 5 to 8 minutes [250], it is unlikely that the fluid observed as buds in the VEP to be remnant blood after the washing procedure. The fluid seen had a spreading behaviour when the surface was cut, reinforcing the idea that it cannot be blood. This confirms that the canal network in the VEP is the pathway for blood to reach the disc and therefore the main nutritional pathway. The shadow of a larger transverse canal was also imaged in deeper layers of the VEP, however, the central region showed fewer buds than expected and some regions of the VEP showed no bud-like structures. The reason for this observation could be the presence of blood clots in the vascular network, not visible in the VEP, or slow penetration of the stain, which did not have enough time to reach the small vessels in the VEP.

The micro-CT of the lugol stained samples from the cow tail were unsuccessful in identifying the blood vessels in the VEPs. The openings in the VEP surface still appeared as holes, such that the content of the canals were not stained enough to create visible contrast on the micro-CT scans. This suggests that the concentration of the lugol solution was too low. The constant perfusion of the stain could also be causing regions of high pressure in the small vessels, causing them to burst and disrupting the continuous network of blood vessels. It has also been suggested that staining in steps, with incremental concentration of the lugol solution can refresh the concentration gradient aiding the absorption of the stain. Given that the approved and allotted time for this experiment was limited at the host institution in Exeter, optimisation of this experiment was unfortunately not possible at this time.

The lugol solution experiments have therefore shown the presence of bud-like structures emerging out of the VEP into the soft tissues which could be part of the loops which

were reported by Crock and Goldwasser and Oki et al., as discussed in Section 2.6.1. of the Literature Review [123, 137]. These isolated buds as shown in Figure 4.14 could be considered as dead ends given the lack of any connections in between them in the soft tissues. However, blood vessels need to have an inlet and an outlet as blood is finite and needs to be sent back to the heart and lungs for the next cardiac cycle. Blood cannot just exist in a bud or pool without being constantly pumped in an out, to avoid formation of clots. Possible explanations of the bud-like structures are shown in Figure 4.29. The blood vessel could either be looping in the VEP layer, before reaching into the bud protrusion, or looping inside the bud, past the VEP boundary. It is also possible that the bud is occupied by a lymph canal instead. Given that lugol solution has been shown to stain several types of soft tissues [242, 249], with different extents of absorption of the stain, it can be assumed that if lymph vessels were present, they would also be stained in this study.

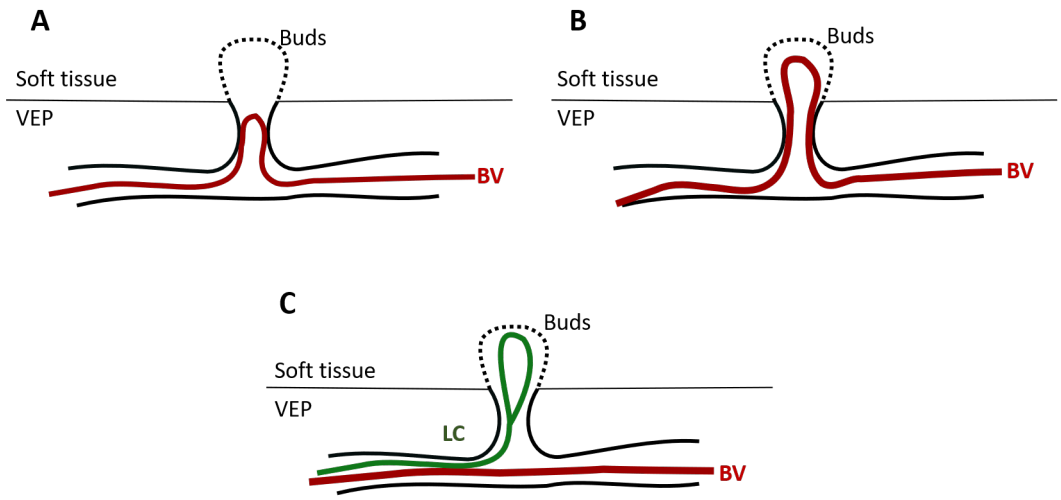

Fig. 4.29 Schematic showing potential pathways of the blood vessels and the content of the bud-like structures. A: The blood vessel (BV) loops within the canal but before the VEP boundary. B: The BV loops inside the bud, past the VEP boundary. C: The bud is occupied by a lymph canal with a closed end (LC) instead, with the BV running parallel.

Histology of the sheep VEP with the appropriate vasculature stain would help identify which of scenarios A or B is true. The presence of vasculature in the calcified cartilage or the cartilage endplate would identify scenario B as most likely. However, in this study, the histology lab was unable to acquire the relevant sheep specific stains or antibodies for vasculature commonly used for the purpose of staining the endothelial cell lining of blood vessels, such as CD31, CD34, von Willebrand factor [251]. Therefore, it is not possible to confidently conclude on which of the two scenarios has the highest likelihood.

Scenario B would also mean having two blood vessel per bud, such that the hole size would be twice the size of a blood vessel. Given that the blood vessel in the VEP layer have been shown previously to be capillaries connected to arterioles and venules, [76, 124], the comparison of the sizes of the openings measured in this study at the VEP surface can be compared to the size of these blood vessels. Capillaries have been reported to be 8 μm wide, venules are about 20 μm and arterioles are around 30 μm [207]. From Figure 4.23, the range of major diameters of the openings were 22 μm to 84 μm and from 15 to 46 μm for the minor diameters. The minor diameters of the openings are comparable to the sizes of blood vessels but the major diameters are considerably larger than only one blood vessel per canal, so it could imply a blood vessel loop. The aspect ratio of blood vessel lumen have been reported to be 2.8, exhibiting slight elliptical cross-sectional area, which enables the blood vessels to withstand the pressure during blood flow [252]. An aspect ratio of 1.0 implies a perfect circle and a ratio of 3.0 refers to an ellipse. The ratios of the openings in this study were all in the range of 1.0 to 3.0, with the majority of openings in the range 1.5 to 2.0, further reinforcing the theory that the majority of the openings might not be occupied by single blood vessels as the aspect ratios do not match those reported previously in literature.

Scenario C suggests the presence of lymph canals. The lymph network runs in parallel to the blood network and Rudert and Tillmann reported the presence of the lymphatic network near the intervertebral discs [124]. However, the distinction between lymph and blood vessels was not achieved in this study. The lymphatic vessels can have "dead-ends". As discussed in detail in the Literature Review, they act as a drainage system for waste materials and water and therefore work alongside the blood flow for normal functioning of cells. Lymphatic capillaries are the terminal canals of the lymph networks and allow free movement of interstitial fluid into the lymphatic system. These vessels are usually intertwined around venules and arterioles of the blood system, in the soft tissue of the body [253]. It would therefore be plausible for the bud-like structures seen protruding out of the VEP to be occupied by lymph capillaries. They could be the main pathway for effective drainage of fluid from the disc during the compression of the spine during daily activities while the blood vessels would offer oxygen and nutrients through passive diffusion from the canals running parallel to the surface of the disc. Lymph capillaries also have the ability to regulate backflow during low pressure situations with their endothelial flaps, which would play a vital role in the movement of water in and out of the disc during loading. However, the presence of lymph vessels in the VEP has not been confirmed yet and remains a challenge due to the complexity of the different types of tissues, and the proximity of the two types of networks makes differentiation harder.

From Figure 4.20, it is clear that blood is present in the VEP layer of the sheep spine. The photoacoustic imaging showed the presence of haemoglobin as red dots in the layer of the VEP. However, the images do not provide distinction between hard and soft tissues, therefore it is likely that the red dots shown are present in both the bony endplate and the cartilage endplate. This confirms the theory that the canals are occupied by blood vessels. However, the dots were seen to be isolated and no continuous vessels were imaged. There could be 2 explanations for this. Firstly, given the timeframe for acquiring the cadaveric sheep spine after the time of death, it is very likely that the blood has already formed clots, hindering the visualisation of continuous blood flow. Secondly, the resolution of the imaging tool could be too low to visualise the smaller connecting canals in the VEP. Given that the resolution of the imaging tool was 10 μm and the majority of the canals were seen be larger than 20 μm across the VEPs, even if the smaller canals would not be imaged, the majority of blood vessels are large enough to be picked up by the imaging tool. Therefore, it is likely that the reason for the imaging of isolated dots instead of continuous vessels could be the presence of blood clots. Injecting the spines with anticoagulant agent, such as heparin, to prevent blood clots from at the time of death of the animal might improve the outcome of the imaging technique.

In the initial trial for this experiment, the excised V5 sample from the central region of the VEP was used preferentially as the associated micro-CT image was also available for comparison purposes. However, very sparse red dots could be seen from the photoacoustic images. Given that the cutting procedure of the VEP includes a constant stream of water, it is likely that the content of the canals is also being washed out resulting in the loss of blood content in the canals. For this reason, a whole VEP surface was used instead to image the undisturbed vessels. However, this meant the inability to compare the photoacoustic images with a pre-scanned micro-CT image of the same samples, as a whole VEP cannot be scanned at the required resolution of 4 μm to visualise the vessels.

Summary of Findings on the Blood Vessels and Buds

As summarised in Figure 4.30, the findings from this study showed the presence of bud-like structures emerging out of the openings on the bony endplate surface into the cartilage endplate, and the presence of haemoglobin in the VEP. The bud-like structures show that the holes in the VEP are not occupied by descending fibres from the disc but instead are occupied by soft tissue protruding out of the VEP-disc boundary. The nature and composition of these buds are still unclear but several hypotheses have been suggested. The functions of these buds are hypothesised to provide closer proximity for the disc cells to the blood supply in the VEP for nutritional exchange. It is also still unclear if all the canals in the VEP are occupied

by blood vessels, or if lymph vessels are present. The arrangement of the blood vessels in the canals is also still unclear.

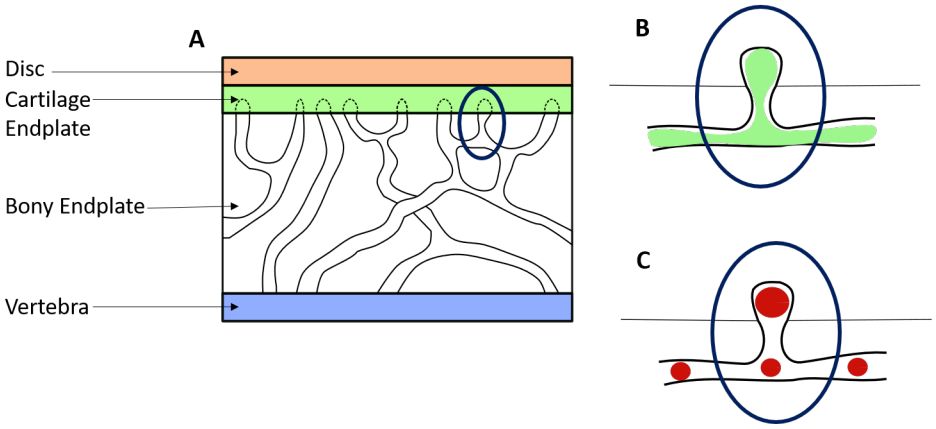

Fig. 4.30 The schematic shows the summary of the findings from this study of the content of the canals in the VEP. A: Schematic showing the canal network in the bony endplate with the ends appearing like buds protruding out of the boundary with the cartilage endplate. B: A close-up schematic of the bud-like structure shown by the lugol experiments. C: The presence of haemoglobin within the canals have been shown by photoacoustic imaging, however it was imaged as isolated dots instead of continuous flowing vessels.

4.4.3 The Individual Canals

Centreline analysis was used to investigate the individual canal of the 3D network in the VEP. The canals were classified into 3 main groups, those starting from the surface of the VEP boundary with the disc, the others were further split into longitudinal and transverse ones. These 3 categories were further split into a total of 12 categories.

The central region of the VEP samples, V5, for the 6 VEPs had higher proportion of surface starting canals than the other samples, as shown in Figure 4.24, closely followed by the neighbouring samples V4 and V6. This can be correlated with the higher density of openings per area in V5 seen in Figure 4.21, such that the canals emerging out of the VEP boundary are in higher numbers. Biologically, it reinforces the concept that the nucleus pulposus requires higher rate of biochemical exchange and therefore, an increased number of surface canals would mean higher volume of oxygen and nutrients exchanged. The surface to middle canals were the most prevalent ones and they matched the description of canals seen previously by Crock and Goldwasser [123]. They described these canals as being "sessile discoid terminations". The surface starting canals were seen to cluster in the region of radius smaller than 0.05 mm and length shorter than 0.8 mm in Figure 4.25. The opening density

has been shown to decrease for VEP at lower spinal levels which would explain the reduced number of canals seen in the surface canals graph in Figure 4.25.

The longitudinal middle to middle and middle to end canals showed the highest prevalence across all the regions of the 6 VEPs. This represents canals which occupy the central portion of the VEP layer and run parallel to the direction of the normal to the VEP surface. These canals showed a wide variation in radius, as shown in Figure 4.26, from very close to zero to 0.10 mm, except for the L4/L5 spinal level. The canals in this category were in a very similar range of radius as the surface starting canals but majority of the canals were longer in the former category. This implies that the longitudinal canals are connecting the surface ones to other canals and to the trabecular spaces in the vertebra while the surface ones are short protrusions.

The third most prevalent canals were the transverse middle to middle canals. As seen in Figure 4.27, these canals were seen to have a dispersed distribution of the lengths of the canals but smaller distribution of radius. These canals match the description of the capillary bed reported in literature, which runs in concentric circles perpendicular to the VEP surface normal, made up of canals of varying lengths but small range of radii [104, 123]. The prevalence of transverse canals with a radius larger than 0.12 mm was very low, and absent in the L5/L6 level. However, the large transverse canals seen in this study were associated with short lengths. This contradicts previous reports, which showed the presence of long and large transverse canals which represent the veinous draining canal for the blood system [131]. One of the reasons for this discrepancy could be the immature nature of the rabbit samples used in literature compared to the mature sheep model used in this study. Furthermore, the VEP was cut into 9 separate samples in this study, which would lead to a proportion of the canals to be sectioned or broken. Similarly, the region of interest used for the application of the centreline analysis also added a limiting factor to the consideration of whole canals.

The aim of characterising the individual canal structure was to add a different dimension to the porosity of the VEP and therefore further understand the permeability of the VEP. Several types of canals were identified, specifically the 3 main ones showed different topologies and prevalence but architecture of the individual canals appeared to be independent of the location of the VEP, based on the data shown in Table 4.1 within the limits of biological variability.

4.4.4 The Role of the Canal Network as a Nutritional Pathway

The results from this study identified the canal network in the VEP, the presence of bud-like protrusions past the VEP boundary and the different topologies of the canals. However, the role of the canal network as a nutritional pathway is still unclear.

It is known that the disc needs oxygen and nutrients and needs the drainage of waste material. The main pathways for this are through the blood vessels surrounding the annulus of the disc but mainly through the VEP to the vertebra. The presence of the canal network supports this concept. However, the exact mechanism and pathway is unclear. Potential mechanisms could be active or passive diffusion processes, as discussed in Section 2.6.1. of the Literature Review, from the nearest source of blood flow, in this case in the VEP layer.

The previous sections explored the potential ways the blood and lymph networks could be occupying these buds and providing the pathway for passive diffusion across the thin walls of the capillaries or the open-end of the lymph canals. Ayotte et al. used fluorescent dye to show that fluid flow to the disc followed the path through the canal network in the VEP, through the openings at the surface [151]. However, the tracers have the ability to diffuse out of the the blood vessels to the disc and therefore the tracers were not indicative of blood vessels path. This could provide a different theory, whereby the bud-like protrusion seen in the current study are not occupied by blood vessels but instead are occupied by blood marrow extending from the trabecular spaces of the vertebra and provide a medium for the diffusing solutes. The lugol injection done in this study was unable to elucidate this because the lugol molecules are too large to pass through capillary walls, making it ideal for blood vessel staining, but it cannot identify the path of the nutrients which diffuse from the blood vessels. However this implies a longer distance for solutes to diffuse across. In contrast, the bud-like protrusions are closer to the anchoring fibres of the disc, making the diffusing distance relatively shorter and the diffusion process more efficient. Further histological analysis and staining investigations should be carried out to test the potential pathways suggested from the findings of this study.

The porosity and the density of the openings at the surface of the VEP sample changed depending on the location of the VEP with respect to the disc and the spinal level. Although the density of canals changed, the proportion of each type of canal and the architecture of individual canals of specific categories do not change considerably at different locations of the VEP. Furthermore, the experimental methods developed in this study can be used to investigate the effect of age and pathological degeneration on the canal network and the topology of the canals.

4.5 Conclusions

This chapter aimed to elucidate the role of the VEP as a nutritional pathway to the disc. This was carried out in 2 parts: the qualitative analysis of the 3D canal network and the quantitative analysis of the individual canals and their openings.

The canal network was successfully isolated and imaged for all the regions of the VEP surface, at different spinal levels and different sides of the disc. The individual canal analysis showed 3 main types of canals, originating from the surface, transverse and longitudinal canals with different functions and characteristic properties but these properties and the prevalence of the canals were not dependent on the VEP location and spinal level. The only exception being the higher prevalence of surface canals in the central region of the VEP. The density of openings per area on the surface of the VEP showed correlation with the porosity of the VEP layer. The V5 samples, directly opposite the nucleus pulposus of the disc, showed highest porosity and number of openings and highest prevalence of the surface starting canals, reinforcing the concept of increased rate of metabolic exchange in the central region of the disc. The capillary bed reported previously in smaller animal models was also successfully imaged, as the transverse canals of varying lengths and longitudinal canals were also identified as longer connections between the VEP boundary and the trabecular bone.

The canal openings were shown to be filled with soft tissue emerging out of the VEP boundary into bud-like structures in the cartilage endplate and calcified cartilage layer. It has been hypothesised that these buds could be filled with blood vessels or lymph vessels but the actual content of the buds remain unclear at this stage. These buds could be filled with blood vessels loops, similar to the ones reported by Oki et al. [137]. Further investigation is required to elucidate the questions raised in this study about the "dead-ends" imaged.

Although the lugol injection experiment was unable to create strong contrast to visualise the blood vessels, it still proved that the dye in the blood system used the canal network in the VEP, confirming the role of the VEP network as a nutritional pathway. However, the diffusion mechanism across the VEP boundary remains unclear owing to the lack of understanding of the organisation of the blood or lymph vessels in close proximity to the disc.

Key Points

The main findings from this chapter can be summarised as shown below:

- The density of openings on the surface of the VEP was highest in the central region of the VEP, in contact with the nucleus pulposus of the disc.
- The 3D network of canal in the VEP layer has a complex structure which was independent of the spinal levels or location with respect to the disc.
- The canal network connects the trabecular spaces of the vertebra to the openings seen at the boundary of the VEP and the soft tissues.

- The canal openings of the VEP were shown to be filled with soft tissues which formed bud-like structures protruding from the bony endplate into the cartilage endplate.
- The canals were shown to contain haemoglobin, confirming the theory that the canals are filled with blood vessels.
- The individual canals could be broadly classified into 3 groups, the ones starting from the surface, the transverse canals and the longitudinal canals.
- The canal network and the bud-like protrusion play a key role as a nutritional pathway to the disc.

Chapter 5

The Effect of Degeneration on Human Vertebral Endplates

5.1 Introduction and Relevance

The previous chapters investigated the structural properties of the vertebral endplates (VEPs) and the role of the canal network in the VEP as a nutritional pathway to the disc. These studies were carried out using a sheep model, of healthy VEP. They were categorised as healthy based on the absence of punctured discs and the preserved discal heights. The VEPs also showed no signs of traumatic fissures or abrasions. Given that the VEP has to balance conflicting biophysical requirements, being strong to provide mechanical stability while also being porous to provide a nutritional pathway to the disc, they are vulnerable to damage. There have been several published reports identifying VEP damage as a precursor for chronic low back pain [174, 254]. However, VEP damage is poorly visualised by current diagnostic imaging [3], as opposed to disc degeneration, which has also been shown to be a precursor of chronic back pain [255]. The effects of degeneration on the structural properties of the VEP therefore remains poorly characterised. Currently, patients suffering from back pain are diagnosed and classified into categories according to the Modic types seen on Magnetic Resonance Imaging (MRI), the Pfirrmann grades of the disc and the VEP erosion grades.

The complexity and range of the aetiology of pathological degeneration coupled with the anatomical differences between humans and animals make the identification of a representative animal model challenging [256]. Although human cadaveric samples have been used in the past, the preservation methods and incomplete medical history can interfere in the complete understanding of the study. This chapter introduces a novel way of assessing

the effect of pathological degeneration on the VEP, using samples harvested from patients undergoing spinal surgeries.

5.2 Materials and Methods

5.2.1 Patient Population and Surgical Harvesting

Ethics Approval for this study was obtained from the NHS Research Ethics Committee (Reference Number:16/EE/0103). The clinical assessment of patients and collection of specimens were carried out by orthopaedic spinal surgeons Mr. David Sharp and Mr. Saaj Khaleel in the Spinal Unit of The Ipswich Hospital NHS Trust.

Patients undergoing anterior lumbar spinal surgery as a treatment plan for their degenerative spine conditions were invited to take part in the study. The surgery involved the implantation of a cage and plate to permanently fuse certain segments of the spine that have a degenerated disc causing pain. The cage is normally held in place with the addition of 3 screws. Patients suffering from spinal infections, tumours and with previous metal fixation of the spine were excluded from the study. As part of the pre-operative assessment of the patients, MRI scans, both T1-weighted and T2-weighted images, of the lumbar spine were recorded by the hospital. From the MRI scans, the protocol for clinical assessment of the degenerative changes of the spine were classified and a grading system was used to record the severity of these observed changes. The protocols for these grading systems will be explained in more details in Sections 5.2.3 to 5.2.5.

During the surgery, a drill was used to make holes for the screws used as part of the normal operative procedures to stabilise the intervertebral cage inserted, as shown in Figure 5.1. For the purpose of sample collection for this study, a 3 mm trephine was used instead of the drill. The slight change in the surgical technique had no impact on the patient. This provided cylindrical specimens with a cross-sectional diameter of 3 mm, each approximately 20 mm in length with the VEP layer sandwiched between a thin layer of disc fibres and trabecular bone from the vertebra. On average, 3 screws are inserted per cage, therefore 3 cores of specimens could be harvested from each patient on average. Care was taken to make clean cuts of the bone samples without creating debris or scratching the VEP. The samples were then wrapped in cling film and stored separately at -70 °C in sterile plastic pathology specimen bottles. The samples were then delivered to the University of Cambridge for further studies. 12 patients were included in this study, as shown in Table 5.1. However, the surgery was not carried out eventually for Patient IPS05, resulting in no samples from this patient.

Samples taken from patient IPS08 were classified as control samples based on their medical history.

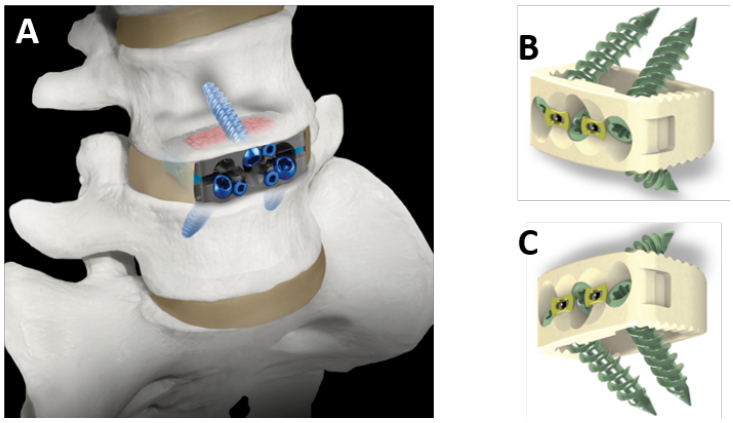

Fig. 5.1 A: Schematic of the cage after insertion with the 3 screws in place. B: Cage with 2 screws on the top surface and 1 on the bottom one. C: Cage with 1 screw on the top surface and 2 on the bottom one. Schematic adapted from OrthoAxis Magnify's website.

Patient Number	Gender	Age	Spinal Level	Side of disc	Postion on VEP
IPS01	M	44	L4/L5	Cranial	Left
			L4/L5	Cranial	Right
			L4/L5	Caudal	Center
			L5/S1	Cranial	Left
			L5/S1	Cranial	Right
			L5/S1	Caudal	Center
IPS02	F	44	L5/S1	Caudal	Left
			L5/S1	Caudal	Right
IPS03	M	37	L5/S1	Caudal	Left
			L5/S1	Caudal	Right
IPS04	M	52	L4/L5	Caudal	Left
			L4/L5	Caudal	Right
			L4/L5	Cranial	Center
IPS05			No Sample		
IPS06	F	33	L5/S1	Caudal	Center
IPS07	M	35	L5/S1	Caudal	Left
			L5/S1	Caudal	Right
			L5/S1	Cranial	Center
IPS08	F	29	L5/S1	Caudal	Left
			L5/S1	Caudal	Right
			L5/S1	Cranial	Center
IPS09	F	42	L5/S1	Cranial	Left
			L5/S1	Cranial	Right
			L5/S1	Caudal	Center
IPS10	M	51	L5/S1	Cranial	Left
			L5/S1	Cranial	Right
			L5/S1	Cranial	Center
			L5/S1	Caudal	Center
IPS11	F	40	L5/S1	Caudal	Left
			L5/S1	Caudal	Right
			L5/S1	Cranial	Center
IPS12	M	40	L5/S1	Cranial	Left
			L5/S1	Cranial	Right
			L5/S1	Caudal	Center

Table 5.1 The samples obtained from the 12 patients in this study are shown with information of the spinal level, the side with respect to the disc, position on the VEP surface, age and gender (M: male, F: female).

5.2.2 Control Samples Harvesting

Control samples from a human cadaver at the Norwich Research Park, with no degenerative condition of the spine, were collected by orthopaedic surgeon Mr Tom Marjoram, following the same pre-operative MRI scanning and similar harvesting protocol as explained in Section 5.2.1. The NHS Research Ethics Committee approval was obtained for the sample collection (Reference Number: 08/h0304/85+5). Table 5.2 shows the characteristics of the 9 samples obtained from the human cadaver.

Patient Number	Gender	Age	Spinal Level	Side of disc	Postion on VEP
Cadaver	F	62	L4/L5	Cranial	Right
			L4/L5	Cranial	Left
			L4/L5	Caudal	Right
			L4/L5	Caudal	Right
			L4/L5	Caudal	Left
			L5/S1	Cranial	Right
			L5/S1	Cranial	Left
			L5/S1	Caudal	Right
			L5/S1	Caudal	Left

Table 5.2 The samples obtained from the human cadaver in this study are shown with information of the spinal level, the side with respect to the disc, position on the VEP surface, age and gender (F: female).

5.2.3 Comparison of the Sheep Model

The structural properties of the control samples in this study were compared with those of the sheep samples, to assess the validity of the sheep model as one for healthy VEP.

The extracted lumbar spine from a mature sheep spine (3 years old) was sent to The Ipswich Hospital NHS Trust where the radiologists did the MRI scanning of the spine. Images were sent back to the author for reconstruction and analysis.

For the human VEPs, samples from the cadaver and from the control patient IPS08 were used and classified as cranial and caudal. For the sheep VEPs, the samples from the anterior region were used, to match the anterior samples harvested during surgeries from patients, as shown in Figure 5.2. Therefore samples V1, V2 and V3 were used from levels L3/L4, L4/L5 and L5/L6, categorised as caudal and cranial.

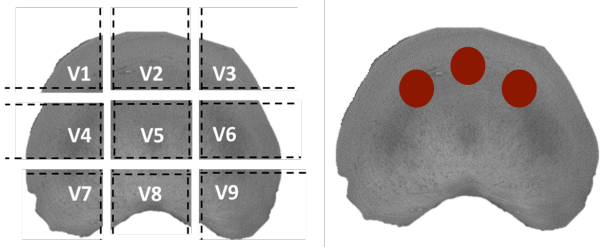

Fig. 5.2 Left: Schematic showing the location of V1, V2 and V3 from sheep VEPs. Right: The 3 red spots show the location of surgical harvesting of samples from the human VEPs.

5.2.4 Assessment of Modic Types

Modic classifications of the vertebral body and the VEP in degenerative conditions of the disc are characterised according to the signal intensity from both the T1-weighted and T2-weighted images, which have been described in more detail in Section 2.7.2 of the Literature Review [190].

Modic type I changes were hypointense on T1-weighted imaging but hyperintense on T2-weighted imaging and were shown to represent bone marrow oedema (swelling due to fluid accummulation) and inflammation. MRI images are in black and white with shades of grey. A hyperintensity is an area that appears lighter in colour than the surrounding tissues; a hypointensity would be darker in colour. Type II changes were hyperintense on T1-weighted imaging, slightly hyperintense on T2-weighted imaging and were associated with conversion of normal red hemopoietic bone marrow into yellow fatty marrow as a result of marrow ischemia, or an inadequate blood supply. Modic type III changes were described as hypointense on both types of imaging and were thought to represent subchondral bone sclerosis which is the formation of new bone. Certain cases of mixed Modic changes, such as I/II and II/III have also been reported, suggesting that these changes can convert from one type to another and that they all present different stages of the same pathologic process [191]. The absence of Modic changes represent a normal anatomic appearance of the disc and VEP on the MRI.

Figure 5.3 summarises the characteristic intensities of each Modic type. The Modic types of each VEP level for this study were recorded by radiologists at the Ipswich Hospital.

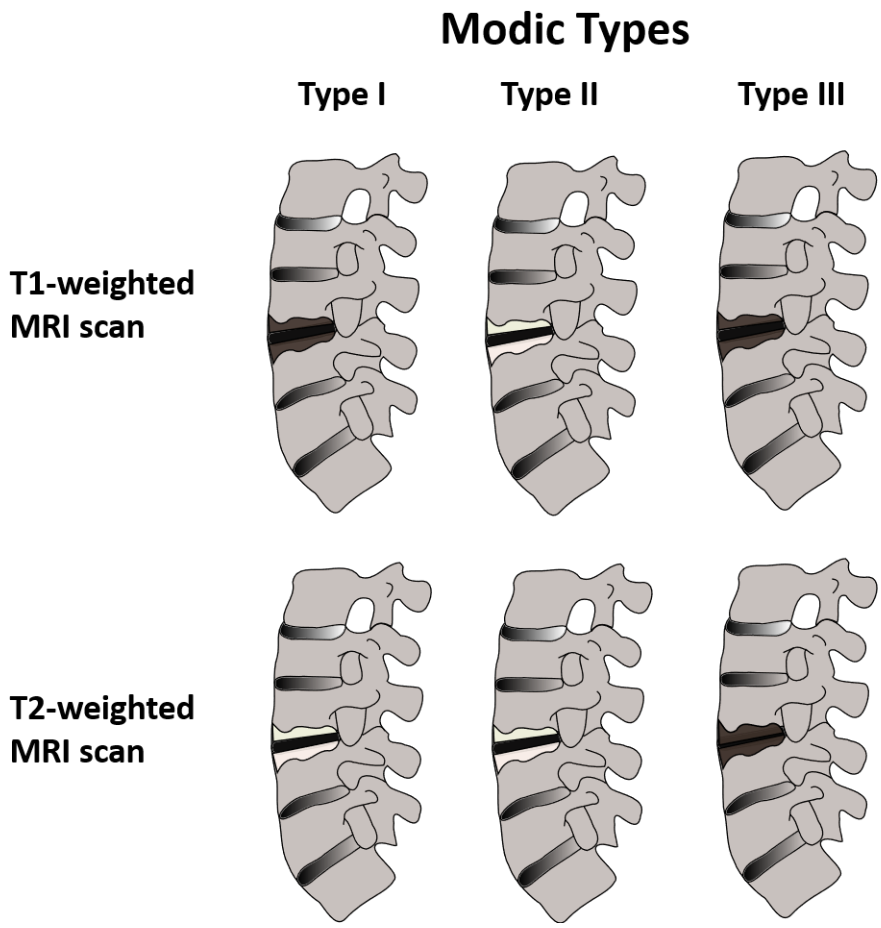

Fig. 5.3 Schematics showing the different types of signal intensities in the T1-weighted and T2-weighted MRI images, characteristics of each Modic type. Adapted from the description of Modic's paper [190].

5.2.5 Assessment of Disc Degeneration

From the MRI imaging, Pfirrmann classification grades were assigned to the degenerate discs by a radiologist at Ipswich Hospital. Pfirrmann et al. identified 5 incremental levels of disc degeneration, based on the homogeneity of the structure of the disc, the distinction between the nucleus pulposus and annulus fibrosus of the disc, and the disc height, as seen on the T2-weighted MRI images [77]. This is summarised in Figure 5.4.

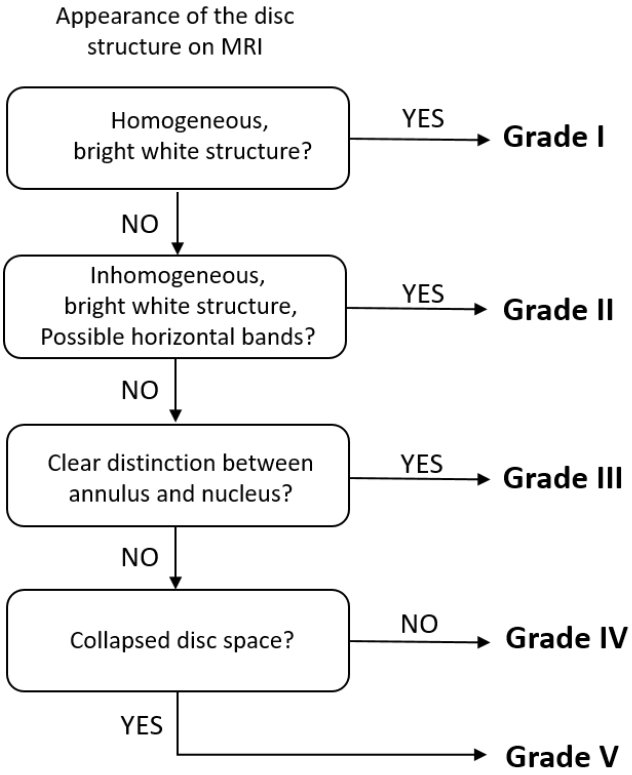

Fig. 5.4 Assessment algorithm used for the classification of the Pfirrmann grades for each disc in this study, from their respective MRI images. Adapted from the description of the Pfirrmann grading system in literature [77, 257].

5.2.6 Assessment of Endplate Erosions

The presence of 3 incremental levels of VEP erosions in degenerative conditions of the spine have been reported in the literature [258]. The description of these grades is shown in Table 5.3 and samples from this study were assigned VEP erosion grades by radiologists at the Ipswich Hospital.

Endplate Erosion Type	Description of Affected Area
I	Central portion of endplate
II	Peripheral portions of endplate
III	Whole endplate surface

Table 5.3 The characteristic of each type of VEP erosion is shown with the description of the VEP area affected for each based on the description found in literature [258].

5.2.7 Micro-CT Imaging

The frozen samples, of both human and sheep, were defrosted overnight in the fridge, wrapped in phosphate-buffered saline (PBS) soaked tissue paper and transferred into sterile 15 ml centrifuge tubes under the fume hood. The samples were then individually scanned, at a pixel size of 4.89 μm, in the micro-CT. The imaging and image reconstruction were carried out following the same protocol as described in Section 2.2. The reconstructed images were transformed into 3D rendered images using the Simpleware software, as explained in Section 4.2.1.

5.2.8 Structural Analysis of the Vertebral Endplates

The thickness, porosity and bone mineral density (BMD) of the VEP layer were measured for each sample following the same protocol as described in Section 3.2.3. The measurements were classified as the cadaveric control samples, the patient control samples from IPS08 and the remaining patients with degenerative disc disease (DDD). The canal openings density per area and distribution of the openings sizes for the VEP surface boundary were also measured following the protocol described in Section 4.2.2. Given that the VEP has to balance conflicting biophysical demands from the disc to be porous but strong, it is prone to damage and degeneration. Therefore, the structural properties of the VEP were compared to all 3 degeneration classifications: Modic changes, Pfirrmann grades and VEP erosions.

5.2.9 Analysis of the Trabecular Bone in the Vertebrae

The porosity, trabecular thickness, trabecular separation and BMD of the trabecular bone in the vertebra were measured following the protocol described in Section 3.2.4. The vertebral bodies are mostly characterised by Modic changes and therefore the structural properties were compared to the latter.

5.2.10 Statistical Analysis

Statistical analysis was carried out using the software OriginLab to check for statistical significance of the results. Normality of the data distributions was first checked, then a Levene's test was used to ensure homogeneity of variances between the different groups of data. If the data passed both tests, a one-way ANOVA parametric test was used. If either one of the two conditions were not met, a non-parametric test, Kruskal-Wallis ANOVA test was used. In both ANOVA tests, the data was considered statistically significant only if the evaluated P-value was smaller than 0.05. When comparing 3 or more groups of data, the

ANOVA test identifies if the results are significant overall, but a post-hoc Tukey test is carried out to identify exactly where those differences lie.

5.3 Results

5.3.1 MRI Imaging

The MRI images showed the presence of Modic Types I, II and III in the patients population, as shown for 3 patients and the cadaver in Figure 5.5. The MRI of the cadaver showed no change in signal intensities in either T1 or T2-weighted images, confirming the absence of degeneration in the lumbar spine. For the classifications of Modic Types I, II or III, the signal intensity profiles seen on T1 and T2-weighted scans were compared to the ones described in Figure 5.3 according to Modic's rules [190].

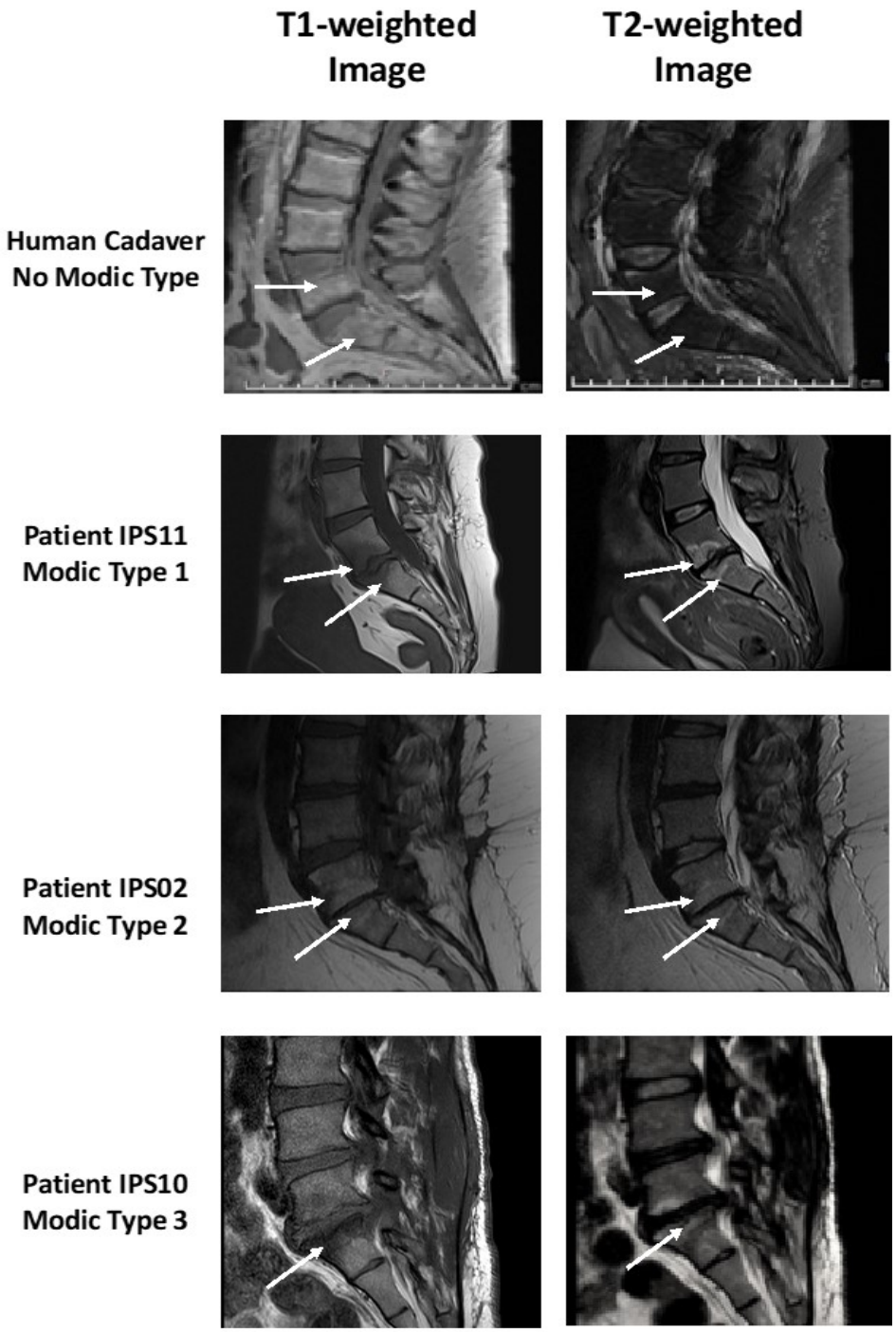

Fig. 5.5 Both T1 and T2-weighted MRI images are shown for the cadaver, and 3 patients showing the differences between no Modic changes and Modic types I, II and III. The white arrows show the VEP from which samples were collected and the area of signal intensities used to assess the Modic changes. Imaging carried out by a radiologist at Ipswich Hospital.

5.3.2 Degeneration Classification

Based on the degeneration assessment from the MRI scans, the different Pfirrmann grades, VEP erosions and Modic types for all patients were assessed by Mr. Tom Marjoram, as reported in Table 5.4.

Patient	Disc Level	Modic Type	Pfirrmann Grade	Endplate Erosion
IPS01	L4/L5	II	V	None
IPS01	L5/S1	II	IV	III
IPS02	L5/S1	II	V	None
IPS03	L5/S1	None	IV	None
IPS04	L4/L5	None	V	I
IPS06	L5/S1	None	IV	II
IPS07	L5/S1	I	IV	III
IPS08	L5/S1	None	I	None
IPS09	L5/S1	I	V	III
IPS10	L5/S1	III	V	II
IPS11	L5/S1	I	V	II
IPS12	L5/S1	II	V	II
Cadaver	L4/L5	None	I	None
Cadaver	L5/S1	None	I	None

Table 5.4 The degenerative classification for each disc level from which VEP samples were harvested for all patients and the cadaver are shown based on the Modic types, Pfirrmann grades and endplate erosions.

5.3.3 Co-Prevalence of different types of Degenerative States

The Pfirrmann grading of Modic changes of intervertebral discs is shown in Table 5.5. Modic type II and Pfirrmann grade V were the most prevalent in this patient population, at 37.9 % and 55.2 %. For the highest grade of Pfirrmann grade, Modic type II was the most prevalent (27.6 %) and Modic type III and no modic changes were the least prevalent at 6.9 %.

	Pfirrmann Grade					
	I	**II**	**III**	**IV**	**V**	**Total**
Modic Type 0 n(%)	3(10.3)	-	-	3(10.3)	2(6.9)	8(27.6)
Modic Type I n(%)	-	-	-	3(10.3)	4(13.8)	7(24.1)
Modic Type II n(%)	-	-	-	3(10.3)	8(27.6)	11(37.9)
Modic Type III n(%)	-	-	-	1(3.4)	2(6.9)	3(10.3)
Total n(%)	3(10.3)	-	-	10(34.5)	16(55.2)	**29(100)**

Table 5.5 Relationship between Modic changes and Pfirrmann grades of vertebral disc degenerative changes, where n represents the number of samples and the representative percentage as a ratio of the total number of samples is shown in brackets. The red colour represents the highest values, followed in descending order by orange, yellow and finally the green colour representing the lowest values.

The Pfirrmann grading of VEP erosion changes of intervertebral discs is shown in Table 5.6. Erosion grade II and Pfirrmann grade V were the most prevalent in this patient population, at 27.6 % and 55.2 %. For the highest grade of Pfirrmann grade, erosion type II was the most prevalent (20.7 %) and erosion grade zero and I were the least prevalent at 10.3 %.

	Pfirrmann Grade					
	I	**II**	**III**	**IV**	**V**	**Total**
Erosion Grade 0 n(%)	3(10.3)	-	-	5(17.2)	3(10.3)	11(37.9)
Erosion Grade I n(%)	-	-	-	-	3(10.3)	3(10.3)
Erosion Grade II n(%)	-	-	-	2(6.9)	6(20.7)	8(27.6)
Erosion Grade III n(%)	-	-	-	3(10.3)	4(13.8)	7(24.1)
Total n(%)	3(10.3)	-	-	10(34.5)	16(55.2)	**29(100)**

Table 5.6 Relationship between VEP erosion grades and Pfirrmann grades of vertebral disc degenerative changes, where n represents the number of samples and the representative percentage as a ratio of the total number of samples is shown in brackets. The red colour represents the highest values, followed in descending order by orange, yellow and finally the green colour representing the lowest values.

The VEP erosion grading of Modic changes of intervertebral discs is shown in Table 5.7. Erosion grade zero and Modic type II were the most prevalent in this patient population, both at 37.9 %.

	VEP Erosion Grade				
	0	**I**	**II**	**III**	**Total**
Modic Type 0 n(%)	5(17.2)	2(6.9)	1(3.4)	-	8(27.6)
Modic Type I n(%)	-	-	2(6.9)	5(17.2)	7(24.1)
Modic Type II n(%)	6(20.7)	1(3.4)	2(6.9)	2(6.9)	11(37.9)
Modic Type III n(%)	-	-	3(10.3)	-	3(10.3)
Total n(%)	11(37.9)	3(10.3)	8(27.6)	7(24.1)	**29(100)**

Table 5.7 Relationship between Pfirrmann grades and Modic changes of vertebral disc degenerative changes, where n represents the number of samples and the representative percentage as a ratio of the total number of samples is shown in brackets. The red colour represents the highest values, followed in descending order by orange, yellow and finally the green colour representing the lowest values.

5.3.4 Micro-CT Imaging

The micro-CT images of all the control samples from the cadaver showed a thin layer of VEP with sparse but large openings as shown in a representative sample from L5 cranial VEP in Figure 5.6. Across all the cadaveric samples, the trabecular bone in the vertebra beneath the VEP surface showed thin trabeculae separated by large distances. The micro-CT images of the L5 cranial VEP from Patient IPS08 with no degenerative conditions had a thicker VEP than the cadaveric control and thicker trabeculae in the vertebra as shown in Figure 5.6. The comparison of the absolute values of the thickness of VEPs will be discussed further in Section 5.3.6. For both samples, the openings on the VEP surface showed a range of sizes.

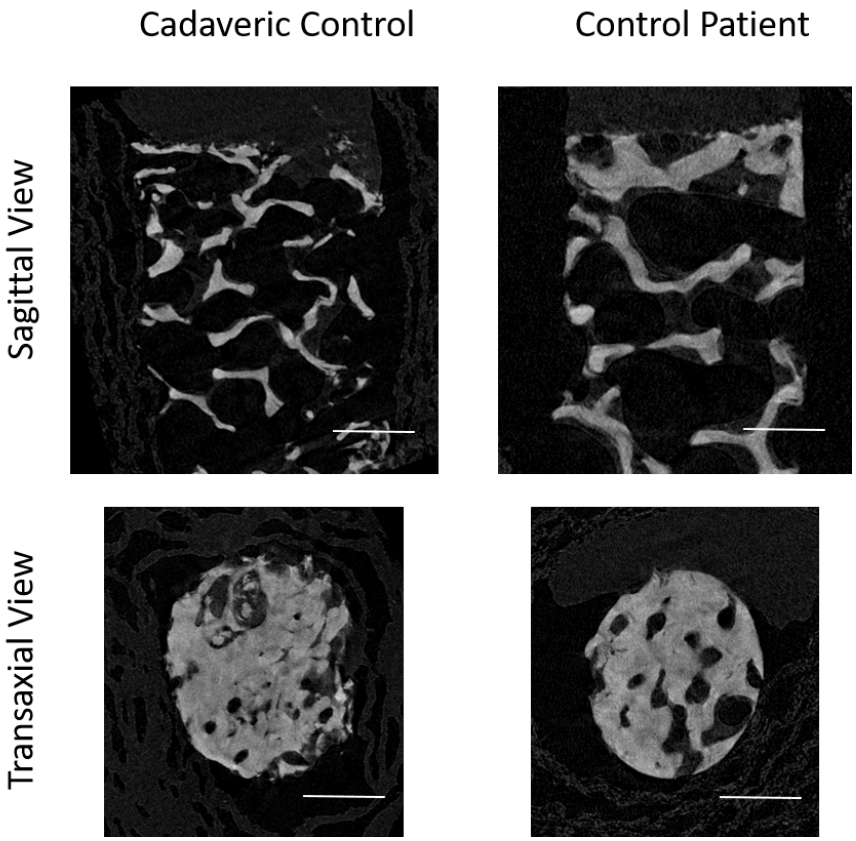

Fig. 5.6 The micro-CT images show the sagittal and transaxial views of 2 VEPs samples both from L5 cranial VEP, one from the cadaveric control (left) and the other from the control patient IPS08 (right). The scale bar represents 1 mm. The trabecular in the patient were thicker than the ones seen in the cadaver and the VEP was thinner in the latter, with openings of varied sizes.

Comparing the VEP from 3 patients (IPS02,07,10 respectively), which displayed Modic types I, II and II respectively showed variations in thickness and openings distribution on the VEP surface, as shown in Figure 5.7. In Modic I, the VEP showed a high concentration of openings at the surface, with larger openings connecting the middle of the VEP layer to the boundary, as shown by the dotted white circles. In Modic II, the VEP was seen to be thicker than the one with Modic I but was also more porous, with large pores extending all the way to the VEP boundary with the disc, from the vertebra. The presence of fissures could also be seen in the transaxial view of the VEP layer, as indicated by the white arrow. In Modic III, the VEP was thick, showing two different shades of grey, indicating different type of bony structure. The transition line between the 2 areas are annotated by the white arrow heads. The surface of the VEP showed irregular thresholding, with varied sizes of openings. The VEP surface also appeared to be rough at the edge.

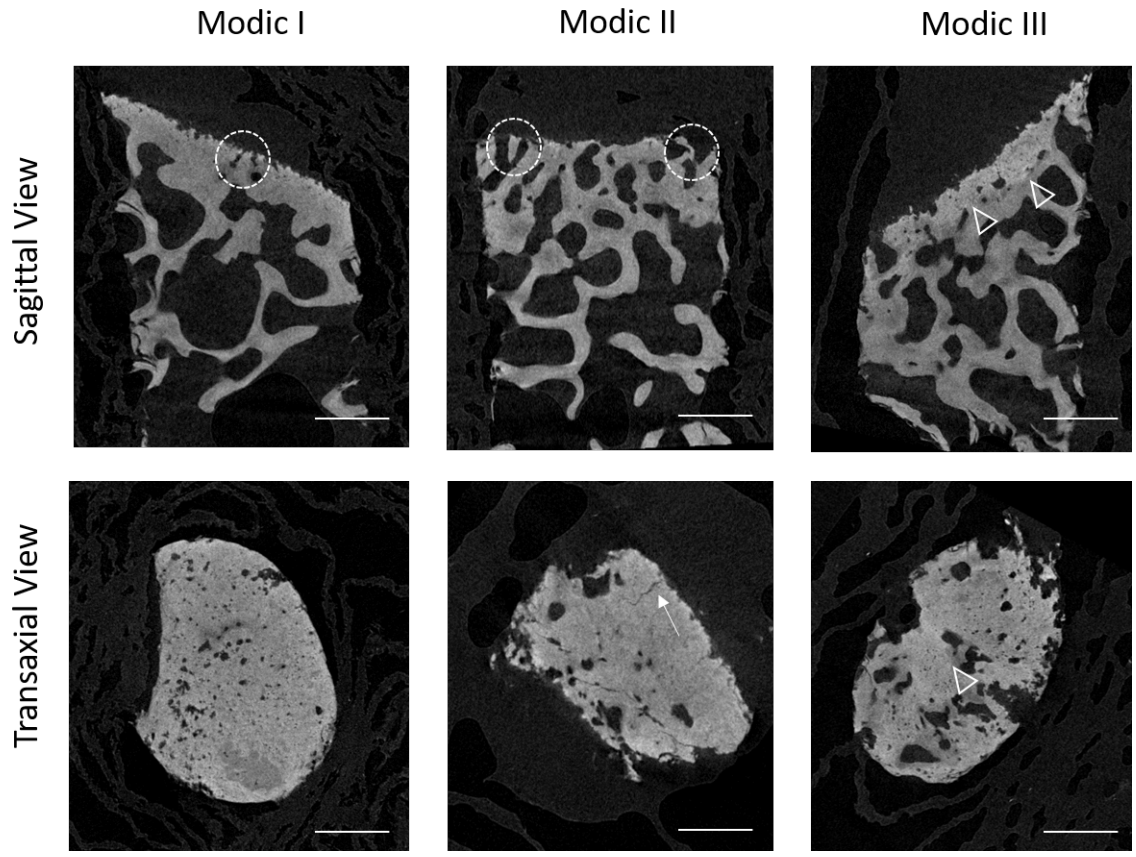

Fig. 5.7 The micro-CT images show the sagittal and transaxial views of VEPs samples from 3 different patients, IPS02, 07 and 10, with Modic types I, II and III respectively. In Modic I, the VEP showed a high concentration of openings at the surface, with larger openings connecting the middle of the VEP layer to the boundary, as shown by the dotted white circles. In Modic II, the VEP was thicker and more porous than the one with Modic I, with large pores extending all the way to the VEP boundary with the disc, from the vertebra, as shown by the dotted white circle. The presence of fissures could also be seen in the transaxial view of the VEP layer, as indicated by the white arrow. In Modic III, the VEP was thick, showing two different shades of grey. The transition line between the 2 areas are annotated by the white arrow heads. The surface of the VEP had openings of varying sizes. The scale bar represents 1 mm.

5.3.5 3D Rendered Images of the VEP

The 3D rendered images of the caudal VEPs from L4 from both the cadaveric control and patient IPS08 showed structural differences. As shown in Figure 5.8, the surface of the VEP appeared rougher, with more bony protrusion in the cadaveric samples than in the healthy patient. Furthermore, the trabeculae of the vertebra appeared thinner and further apart in the cadaver than in the patient. Both showed openings on the VEP surface, of different sizes.

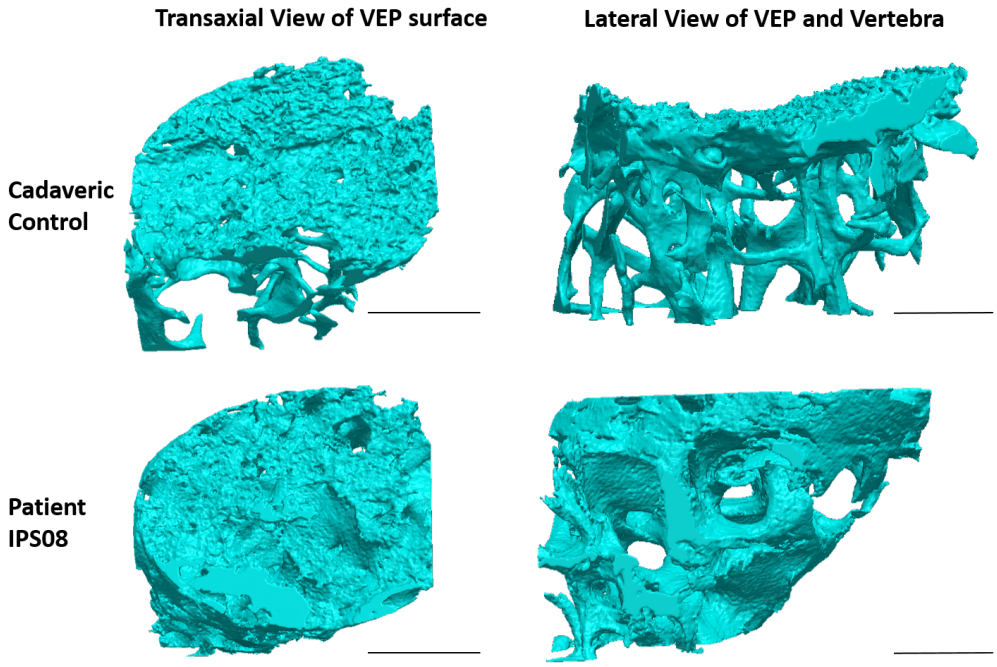

Fig. 5.8 The 3D rendered images of the L4 caudal VEPs from the cadaver and patient IPS08 are shown. The transaxial views show higher roughness and more bony protrusions on the surface of the cadaveric VEP. Both VEPs showed the presence of large openings on the surface. The lateral views show the trabeculae of the vertebra from the cadaver to be thinner and further apart than in the patient. The scale bar represents 1 mm.

The comparison of the VEP surface for different grades of VEP erosion is shown in Figure 5.9. With no erosion grade, the VEP from patient IPS02 showed a relatively smooth surface with dispersed holes of small to medium sizes. With VEP erosion Grade I in the central L4 VEP from patient IPS04, the openings appeared larger and covered most of the VEP surface. The L5 peripheral VEP from patient IPS10 showed VEP erosion grade II, characterised by even larger openings than grade I, covering all of the VEP surface. Finally, grade III erosions showed the loss of the VEP's structural integrity, shown by the missing chunk in the middle of the VEP surface and several bony protrusions as seen in the S1 VEP from patient IPS07.

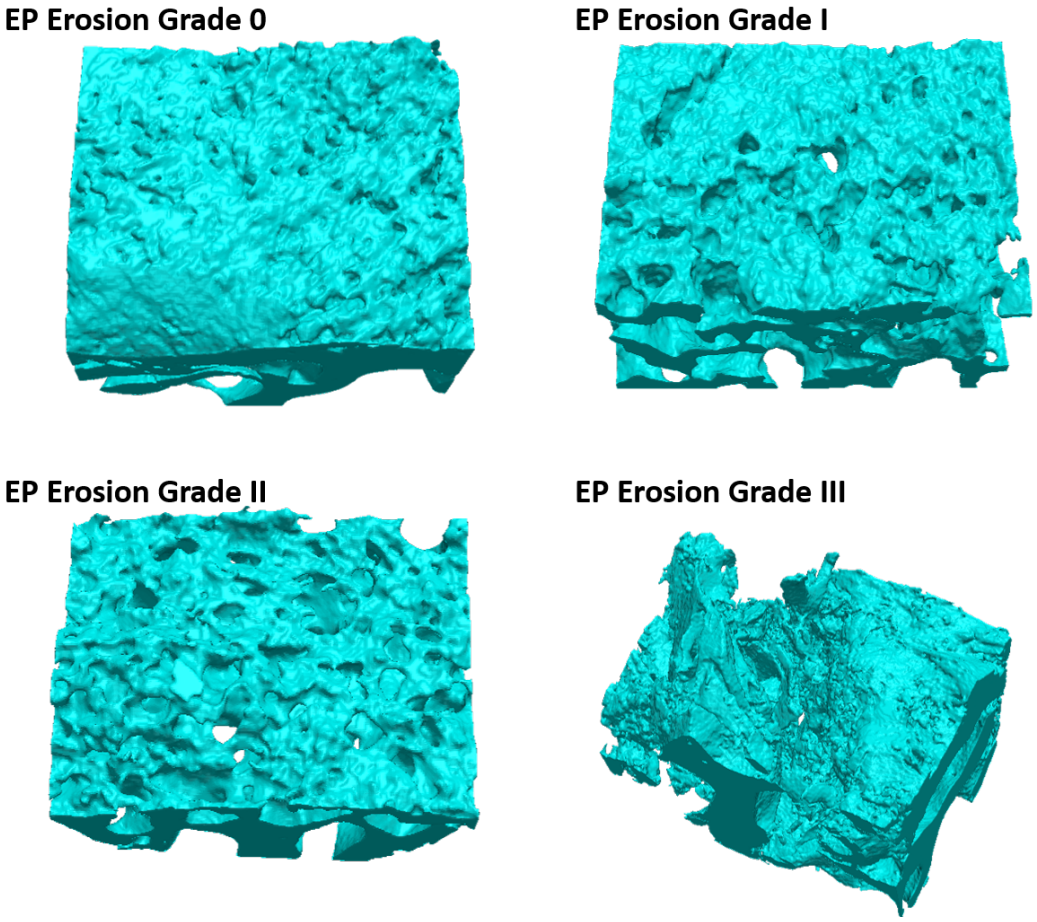

Fig. 5.9 The 3D rendered images of VEPs from 4 different patients with increasing VEP erosions grades are shown. Patient IPS02 showed no erosion grades, with relatively small openings dispersed on the VEP surface. The central VEP from L4 in patient IPS04 had grade I VEP erosion and displayed larger openings covering most of the VEP surface. The peripheral L5 VEP sample from patient IPS10 had grade II VEP erosion, characterised by even larger openings, covering the whole VEP surface. In patient IPS07, the S1 VEP erosion grade III showed loss of the structural integrity of the VEP surface, with a chunk of VEP missing and the presence of bony protrusions. Each VEP rectangular region of interest was 1.0 mm x 1.5 mm.

5.3.6 Thickness of VEP

The average thickness of caudal and cranial VEPs with respect to the disc showed no statistical difference ($P > 0.05$), as shown in Figure 5.10. Similarly, the thickness of VEPs at different spinal levels showed no significant differences ($P > 0.05$). Therefore, while comparing the effect of degeneration on structural parameters of the VEP, the spinal level and position with respect to the disc were not considered.

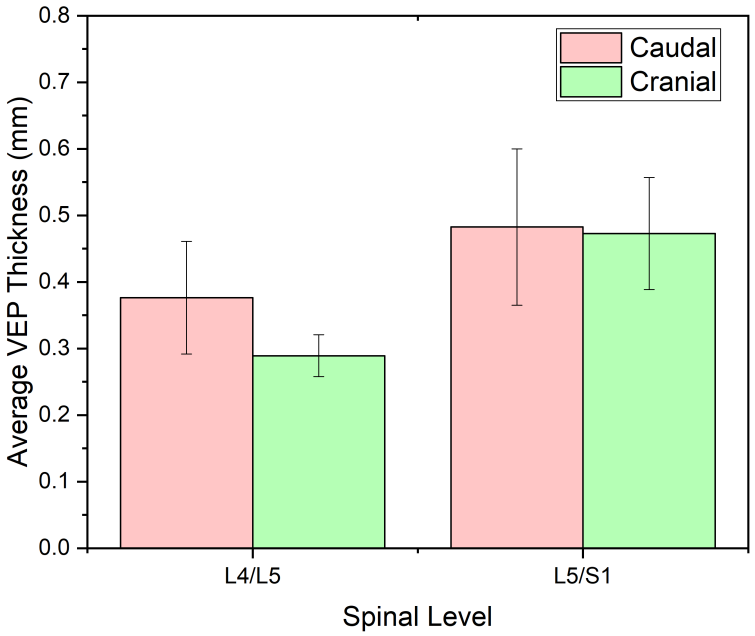

Fig. 5.10 The average VEP thickness showed no statistical differences between cranial and caudal VEPs or at different spinal levels for all patients samples. The error bars represent the standard deviation.

The thickness variation of the VEPs with Modic types is shown in Figure 5.11. The samples with Modic type II were significantly thinner ($P < 0.05$) than the VEPs of patients with DDD exhibiting no Modic changes and Modic type I. Conversely, samples with Modic type III were significantly thicker ($P < 0.05$) than samples with Modic type II. The thickness of the cadaveric control were low compared to the control patient and the patients with DDD.

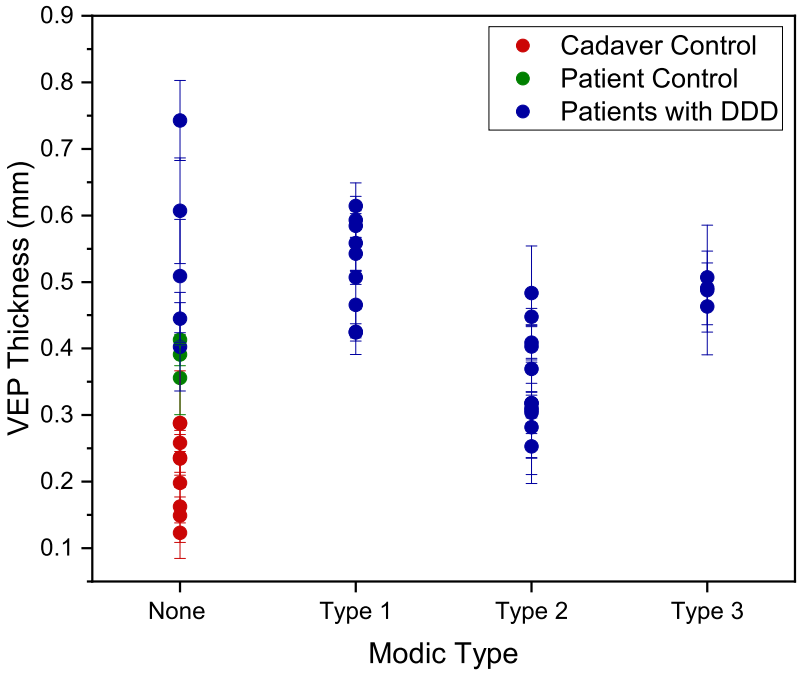

Fig. 5.11 Graph showing the variation of the VEP thickness with the Modic changes observed on the MRI images. The cadaveric controls showed the thinnest VEPs, compared to the control patient and the patients with DDD. The VEP thickness of the patients with DDD showed a decrease from no Modic changes to Modic II, but a significant increase in thickness for Modic III. The error bars represent the standard deviation for each sample. (DDD: Degenerative Disc Disease)

Thickness of the VEP was shown to be higher in the samples with Pfirrmann grades of degeneration compared to normal discs, but the thickness differences between the grades did not show statistical significance ($P > 0.05$), as shown in Figure 5.12. However, this study only had discs with Pfirrmann grade IV and V and none with II and III. The VEP thickness showed a similar range of thicknesses for both grades IV and V, with a couple of thicker samples in grade IV.

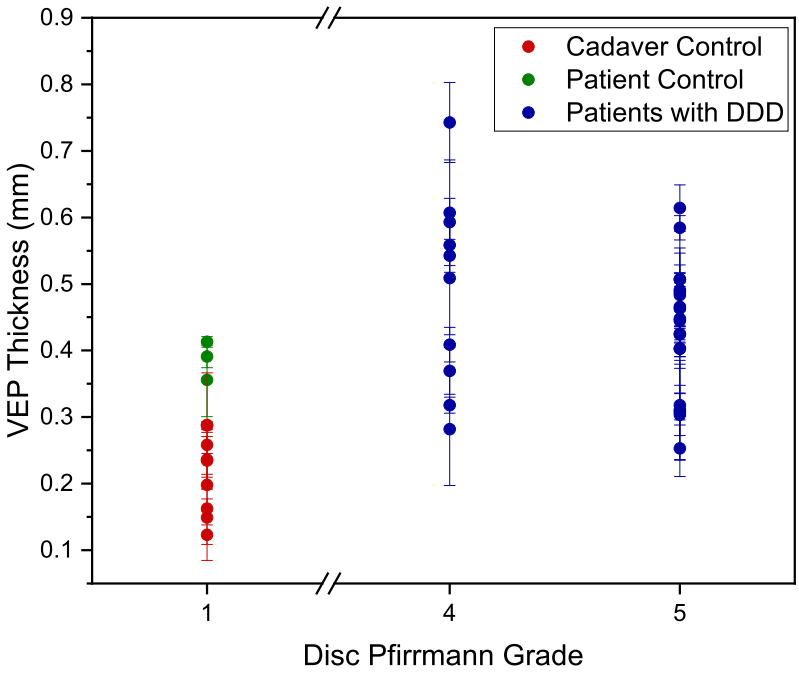

Fig. 5.12 Graph showing the distribution of VEP thickness with the Pfirrmann grade of the disc. Samples from patients with DDD showed higher thicknesses than the control ones, with a subtle decreasing trend from grade IV to V influenced by couple of thicker VEP samples from grade IV. The difference in thickness measurements was not statistically significant, with $P > 0.05$, between the different Pfirrmann grades. The error bars represent the standard deviation for each sample. (DDD: Degenerative Disc Disease)

Thickness of samples with the same Modic types and Pfirrmann grades were averaged to provide simultaneous comparison to both the Modic changes and the Pfirrmann grades, as shown in Table 5.8. The lowest thickness was recorded for Modic type III at both Pfirmann grades IV and V. It appears that the thickest VEPs were the ones with no Modic changes or type I with the Pfirrmann grade IV, but these were even thicker than the healthy samples with no sign of degeneration. However, there was no clear trend of how thickness was changing with advancing stages of degeneration.

	Pfirrmann Grade		
	I	IV	V
No Modic Type (mm)	0.37 ± 0.05	0.62 ± 0.07	0.42 ± 0.07
Modic Type I (mm)	-	0.56 ± 0.04	0.50 ± 0.06
Modic Type II (mm)	-	0.36 ± 0.06	0.45 ± 0.06
Modic Type III (mm)	-	0.51 ± 0.08	0.49 ± 0.06

Table 5.8 Table comparing the thickness of the VEP, taking into account the Modic types and the Pfirrmann grades for each sample. The thickness values are shown as average values of samples with the same combination of Modic and Pfirrmann with the associated standard deviation. The red colour represents the highest values, followed in descending order by orange, yellow and finally the green colour representing the lowest values.

Thickness of the VEP did not show any clear trend with different grades of VEP erosions and the thickness difference was not statistically significant with $P > 0.05$, as shown in Figure 5.13.

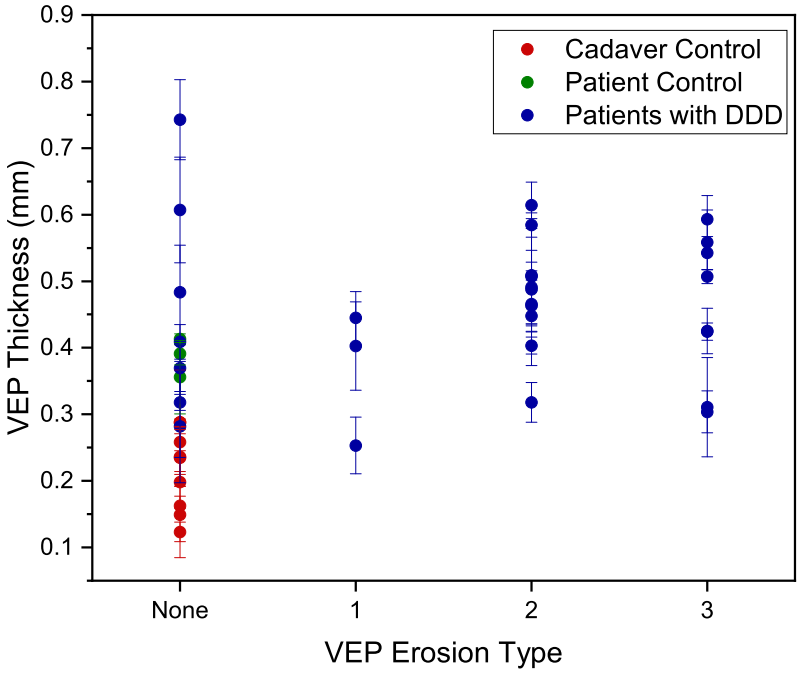

Fig. 5.13 Graph showing the VEP thickness distribution with the VEP erosion types. The thickness difference was not statistically significant, with $P > 0.05$, between the different VEP erosion types. The error bars represent the standard deviation for each sample. (DDD: Degenerative Disc Disease)

5.3.7 Porosity of VEP

The differences in average porosity of caudal and cranial VEPs with respect to the disc showed no statistical significance. Similarly, the porosity of VEPs at different spinal levels showed no significant differences ($P > 0.05$), as shown in Figure 5.14. This means that the trends observed in VEPs on different sides of the disc and at different spinal levels showed no significant trends. Therefore, while comparing the effect of degeneration on the porosity of the VEP, the spinal level and position with respect to the disc were not considered.

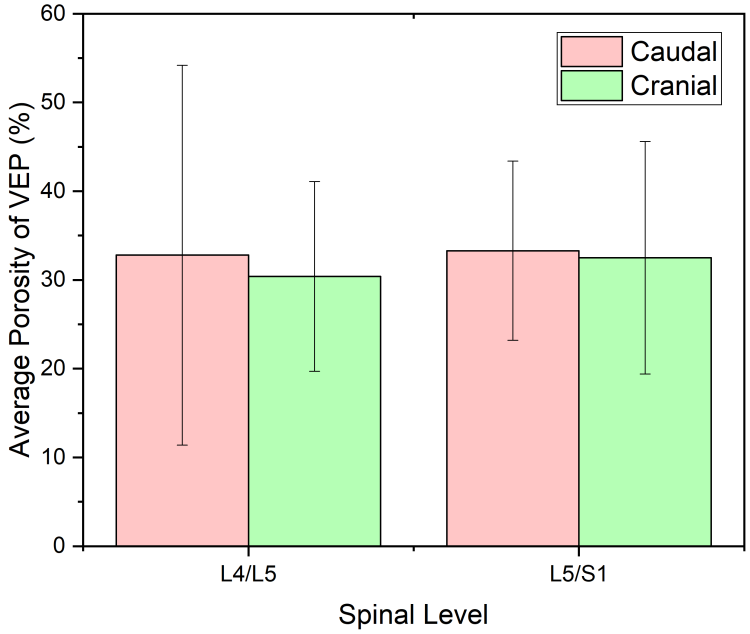

Fig. 5.14 The average VEP porosity showed no statistical differences between cranial and caudal VEPs or at different spinal levels for all patients samples. The error bars represent the standard deviation.

The porosity variation of the VEPs with Modic types in Figure 5.15 showed no clear trend, with no significant differences across the different Modic types, although Modic types I and III had a larger distribution of data compared to the others, with some samples exhibiting very small porosity values, up to 9 ± 7 % in Modic type II .

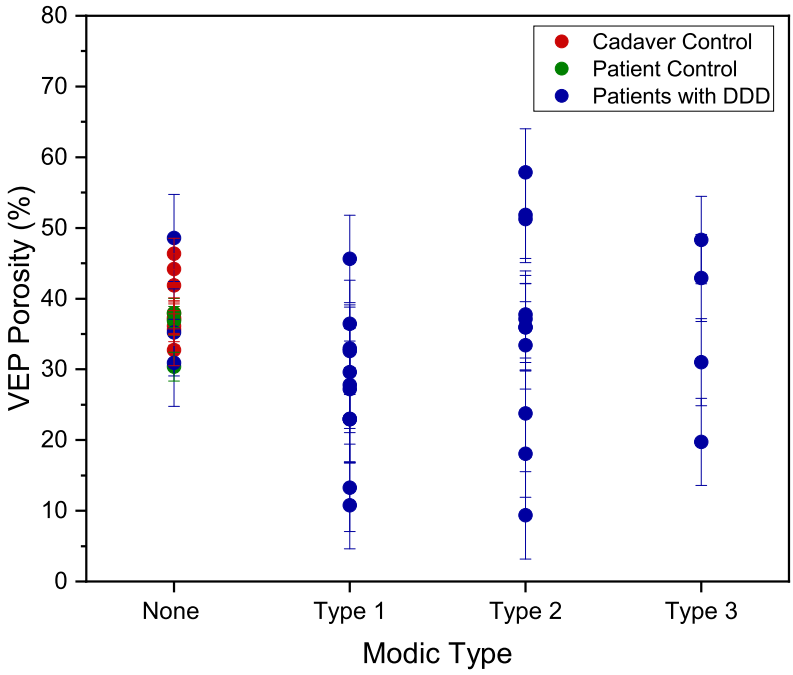

Fig. 5.15 Graph showing the variation of the VEP porosity with the Modic changes observed on the MRI images. The differences in porosity were not statistically significant, with $P > 0.05$, between the different Modic types. Samples with Modic types greater than zero showed larger distribution of porosity, with some samples exhibiting very small porosity compared to the controls. The error bars represent the standard deviation for each sample. (DDD: Degenerative Disc Disease)

Similarly, porosity of the VEP showed no clear trend or significant differences with Pfirrmann grades of degeneration, as shown in Figure 5.16. The data for grade V showed a larger distribution of the data as the majority of the samples used in this study were harvested from patients needing surgery due to the worst state of their disc. Samples with grade V also showed the most and least porous samples in this study.

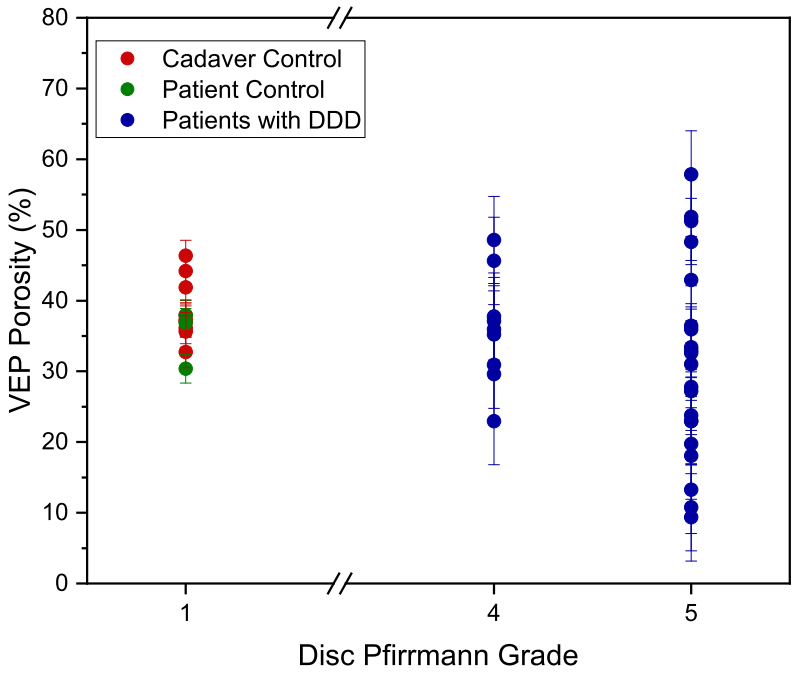

Fig. 5.16 Graph showing the distribution of VEP porosity with the Pfirrmann grade of the disc. Samples from patients with DDD showed a larger distribution of porosity than the control ones, with grade V samples showing the smallest and largest porosities of this sample population. The differences in porosity data was not statistically significant, with $P > 0.05$, between the different Pfirrmann grades. The error bars represent the standard deviation. (DDD: Degenerative Disc Disease)

Porosity of samples with the same Modic types and Pfirrmann grades were averaged to provide simultaneous comparison to both the Modic changes and the Pfirrmann grades, as shown in Table 5.9. The highest porosity was recorded for Modic type III and Pfirmann grade IV. However, there was no clear trend of how porosity was changing with advancing stages of degeneration, implying changes in porosity are not directly correlated with increasing degeneration.

	Pfirrmann Grade		
	I	IV	V
No Modic Type (%)	35 ± 7	38.24	30 ± 4
Modic Type I (%)	-	32 ± 8	27 ± 6
Modic Type II (%)	-	31 ± 7	33 ± 7
Modic Type III (%)	-	42 ± 4	33 ± 7

Table 5.9 Table comparing the porosity of the VEP, taking into account the Modic types and the Pfirrmann grades for each sample. The porosity values are shown as average values of samples with the same combination of Modic and Pfirrmann with the associated standard deviation. The red colour represents the highest values, followed in descending order by orange, yellow and finally the green colour representing the lowest values.

Porosity of the VEP did not show any clear trend or significant differences with different grades of VEP erosions either, as shown in Figure 5.17.

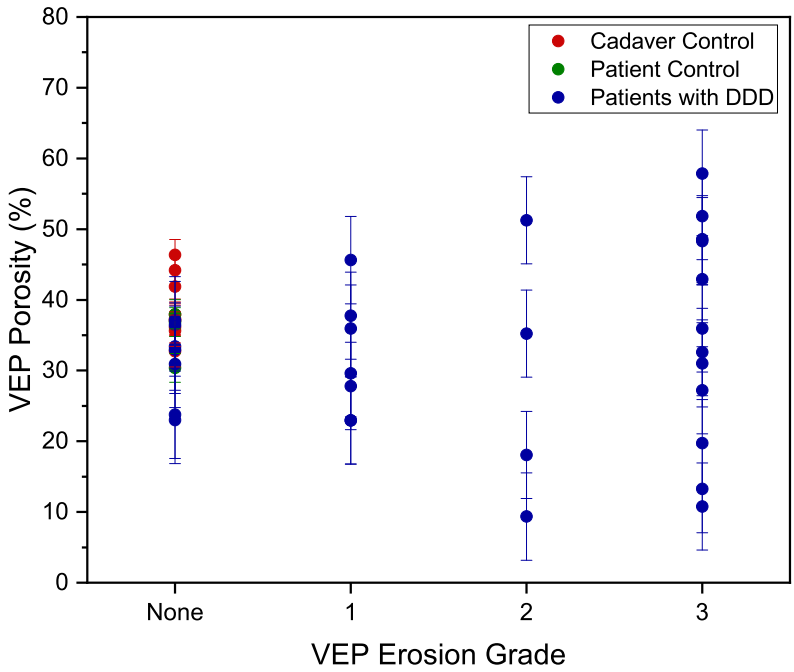

Fig. 5.17 Graph showing the VEP porosity distribution with the VEP erosion types. The porosity data was not significantly different, with $P > 0.05$, between the different VEP erosion types. The error bars represent the standard deviation for each sample. (DDD: Degenerative Disc Disease)

5.3.8 Bone Mineral Density of VEP

The average BMD of caudal and cranial VEPs with respect to the disc showed no significant differences. Similarly, the BMD of VEPs at different spinal levels showed no significant differences, as shown in Figure 5.18. This means that the trends observed in VEPs on different sides of the disc and at different spinal levels showed no significant trends and therefore, while comparing the effect of degeneration on the bone mineral density of the VEP, the spinal level and position with respect to the disc were not considered.

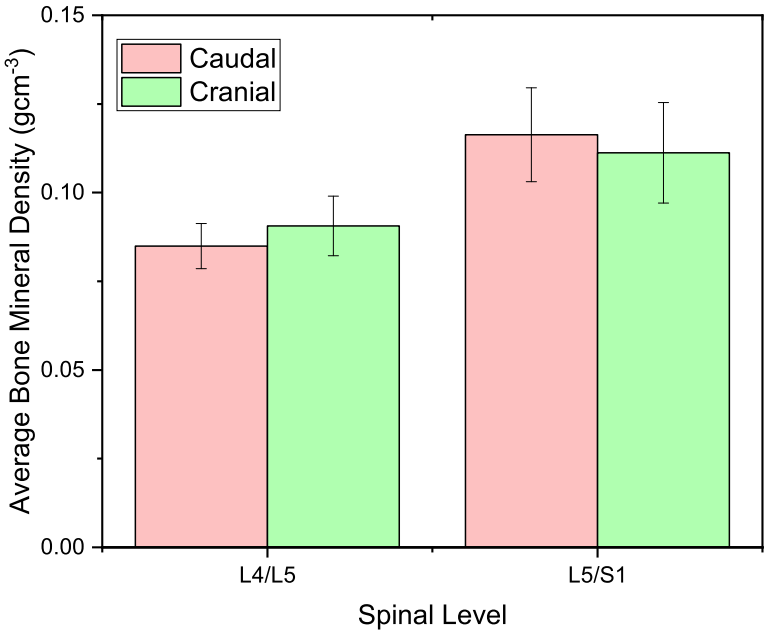

Fig. 5.18 The average VEP BMD showed no statistical differences between cranial and caudal VEPs or at different spinal levels for all patients samples. The error bars represent the standard deviation.

The BMD variation of the VEPs with Modic types in Figure 5.19 showed an increasing trend from Modic type I to type III, and the differences were statistically significant ($P < 0.05$). The BMD of the samples from Modic type III closely match the ones for the control samples from both the cadaver and patient IPS08. The error bars represent the standard deviation for each subgroup of samples as the standard deviation for each sample's measurements were too small to be apparent.

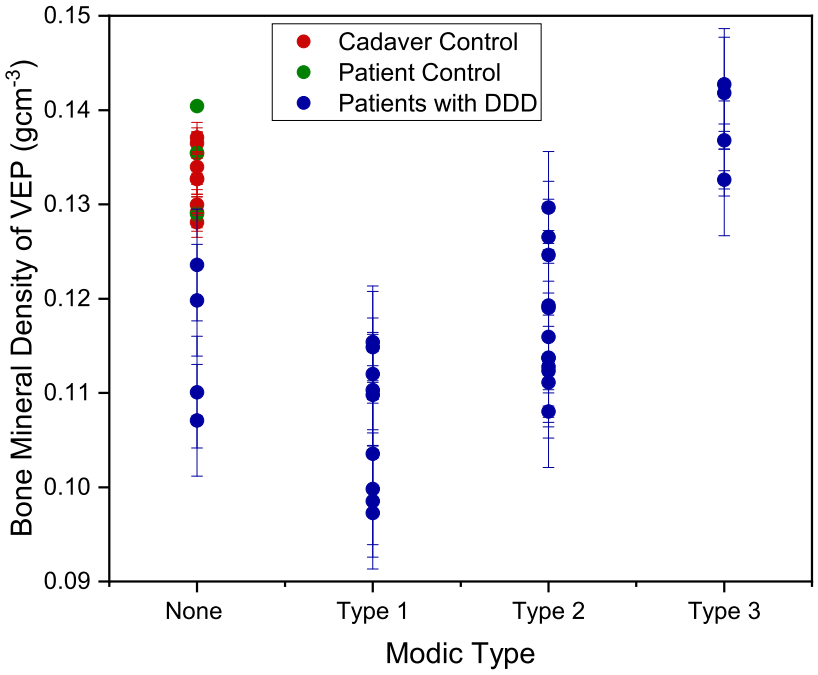

Fig. 5.19 Graph showing the variation of the VEP BMD with the Modic changes observed on the MRI images. There is an apparent increasing trend from Modic type I to III, with samples from the subgroup of Modic type II having bone densities in close range to the control samples. The data showed a significant increase, with $P < 0.05$, from Modic type I to type III. The error bars represent the standard deviation for each subgroup of samples. (DDD: Degenerative Disc Disease)

The BMD of the VEPs was shown to be significantly higher ($P < 0.05$) in the control samples from both the cadaver and patient IPS08 than the samples with degenerate discs of Pfirrmann grades III and IV, as shown in Figure 5.20. Samples with Pfirrmann grade V showed a wide distribution of BMD, with the majority of samples exhibiting bone densities lower than the controls, but no significant differences between samples with grades IV and V were seen. The datasets with grade I was statistically different from the degenerative ones.

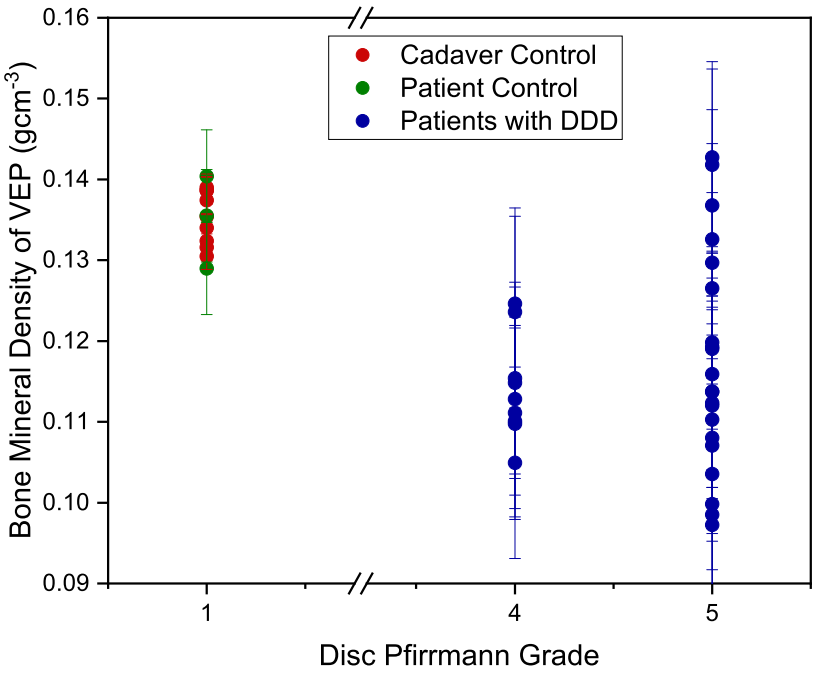

Fig. 5.20 Graph showing the variation of the VEP BMD with the Pfirrmann grades of the intervertebral discs. The datasets with grade I was statistically different from the degenerative ones. The error bars represent the standard deviation for each subgroup of samples. (DDD: Degenerative Disc Disease)

BMD of samples with the same Modic types and Pfirrmann grades were averaged to provide simultaneous comparison to both the Modic changes and the Pfirrmann grades, as shown in Table 5.10. There was a clear observation of highest BMD of samples shown at Modic type III and Pfirrmann grade V. The highest BMD was therefore measured at the worst case of degeneration while the lowest BMD measured were for samples with no Modic changes but the lowest Pfirrmann grades included in this study: IV and V. The samples with no degeneration showed a BMD higher than those of Modic types I and II, but lower than those with Modic III.

	Pfirrmann Grade		
	I	IV	V
No Modic Type (gcm^{-3})	0.125 ± 0.009	0.113 ± 0.004	0.113 ± 0.005
Modic Type I (gcm^{-3})	-	0.113 ± 0.005	0.118 ± 0.008
Modic Type II (gcm^{-3})	-	0.117 ± 0.005	0.119 ± 0.006
Modic Type III (gcm^{-3})	-	0.137 ± 0.006	0.139 ± 0.006

Table 5.10 Table comparing the BMD of the VEP, taking into account the Modic types and the Pfirrmann grades for each sample. The BMD values are shown as average values of samples with the same combination of Modic and Pfirrmann with the associated standard deviation. The red colour represents the highest values, followed in descending order by orange, yellow and finally the green colour representing the lowest values.

The BMD of the VEP did not show any clear trend or significant differences with the different grades of VEP erosions, as shown in Figure 5.21.

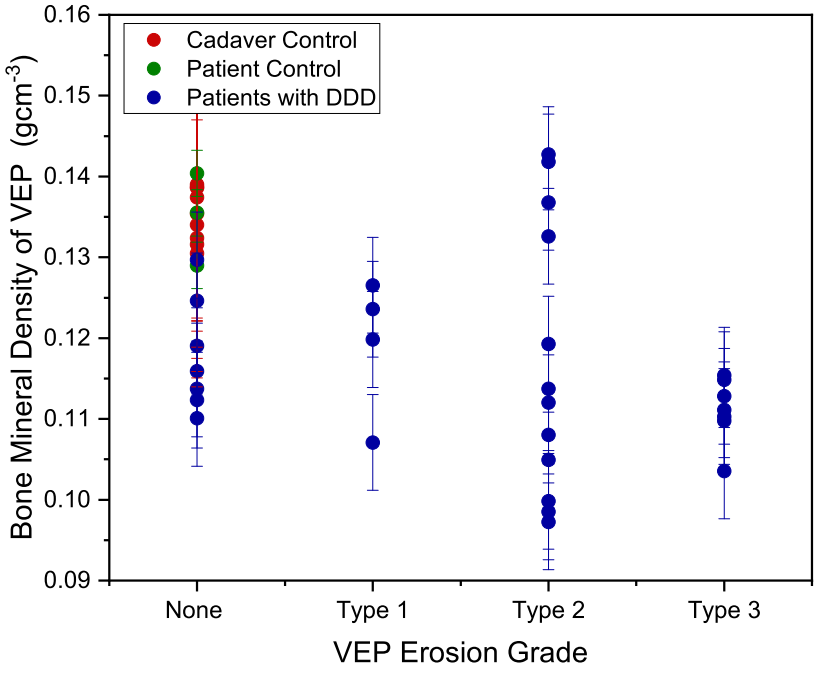

Fig. 5.21 Graph showing the variation of the VEP BMD with the VEP erosion grades. The datasets showed no statistically significant difference with each other. The error bars represent the standard deviation for each subgroup of samples. (DDD: Degenerative Disc Disease)

5.3.9 VEP Canal Openings Analysis

The distribution of the canal opening density per unit area for the samples is shown with respect to the Modic types in Figure 5.22. There is an apparent trend of decreasing openings per area from Modic type II to type III, however no statistical significance was found between the different subgroups of no Modic type, and Modic types I, II and III.

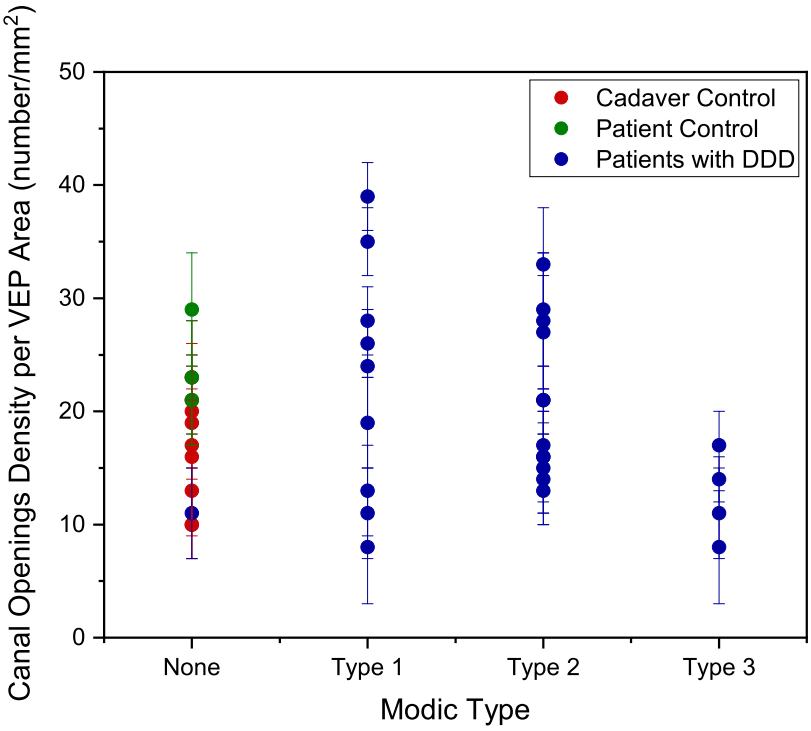

Fig. 5.22 Graph showing the variation of the openings density per area with the Modic changes observed on the MRI images. There is an apparent decreasing trend from Modic type II to III. The datasets showed no statistically significant difference with each other. The error bars represent the standard deviation for each sample. (DDD: Degenerative Disc Disease)

The distribution of the openings density per unit area for the samples is shown with respect to the Pfirrmann grades of the intervertebral discs in Figure 5.23. There was no clear trend or significant difference in terms of how the openings density changed with the Pfirrmann grades.

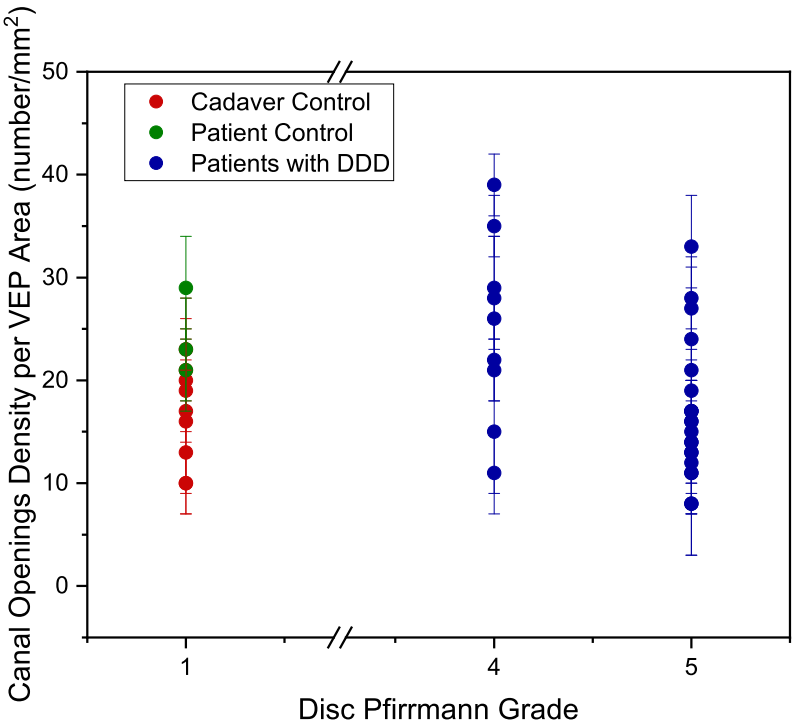

Fig. 5.23 Graph showing the variation of the openings density per area with the Pfirrmann grades of the disc. There is no clear trend observed. The datasets showed no statistically significant difference with each other. The error bars represent the standard deviation for each sample. (DDD: Degenerative Disc Disease)

The distribution of the canal openings density per unit area for the samples is shown with respect to the VEP erosion grades in Figure 5.24. VEP erosion grade II was in the same range as the control samples but grade I and III showed larger distributions of the openings density. Samples from patients with DDD with no erosion showed similar openings density as the control samples. The data did not show any significant differences between the subgroups of different VEP erosion grades.

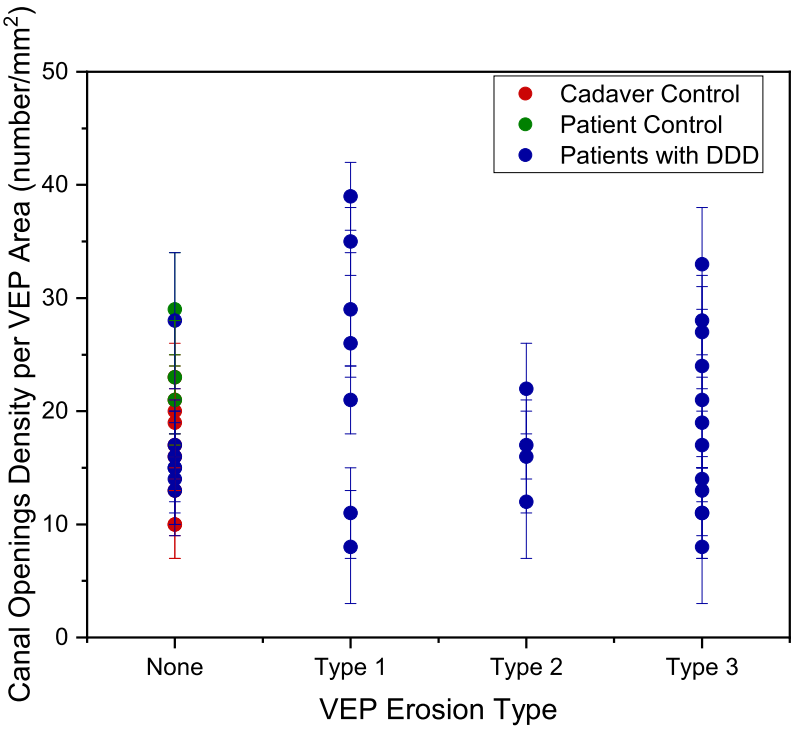

Fig. 5.24 Graph showing the variation of the openings density per area with the VEP erosion grades. There is no clear trend observed but samples from patients with DDD but with no erosion showed similar openings density as the control samples. The datasets showed no statistically significant difference with each other. The error bars represent the standard deviation for each sample. (DDD: Degenerative Disc Disease)

The variation of the average major diameters of the canal openings for each sample with respect to the Modic changes are shown in Figure 5.25. The cadaveric control samples showed large distributions of the opening diameters, compared to the patient IPS08. There was a subtle trend of increasing diameter from Modic type I to III, but the differences between the Modic types showed no statistical significance.

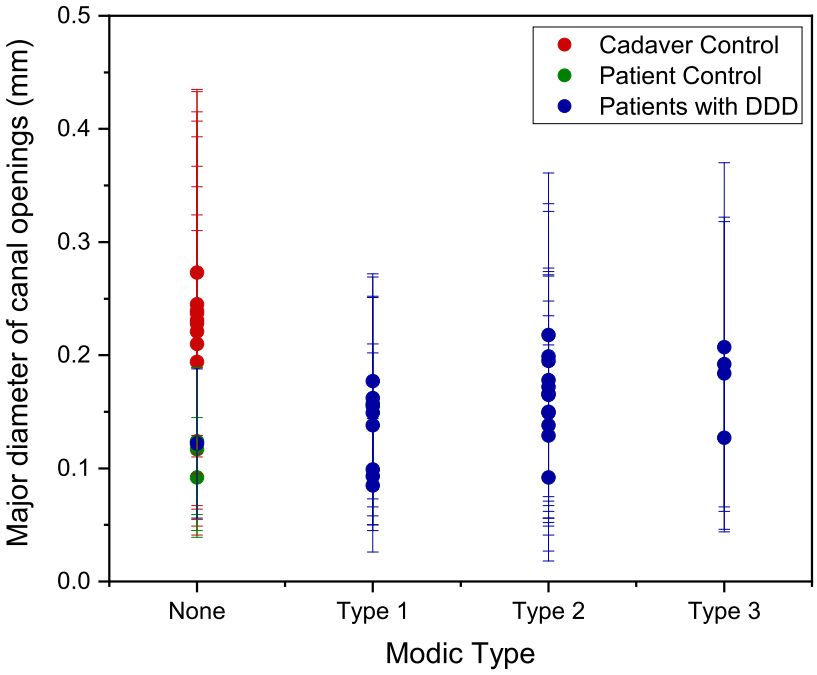

Fig. 5.25 Graph showing the variation of the major diameter of the openings on the VEP surface with the Modic changes observed on the MRI images. There is an apparent increasing trend from Modic type I to III, however the datasets showed no statistically significant differences with each other. The error bars represent the standard deviation for each sample. (DDD: Degenerative Disc Disease)

The variation of the average major diameters of the openings for each sample with respect to the Pfirrmann grade of the intervertebral discs are shown in Figure 5.26. The range of diameters showed no significant differences with grades IV and V of degeneration.

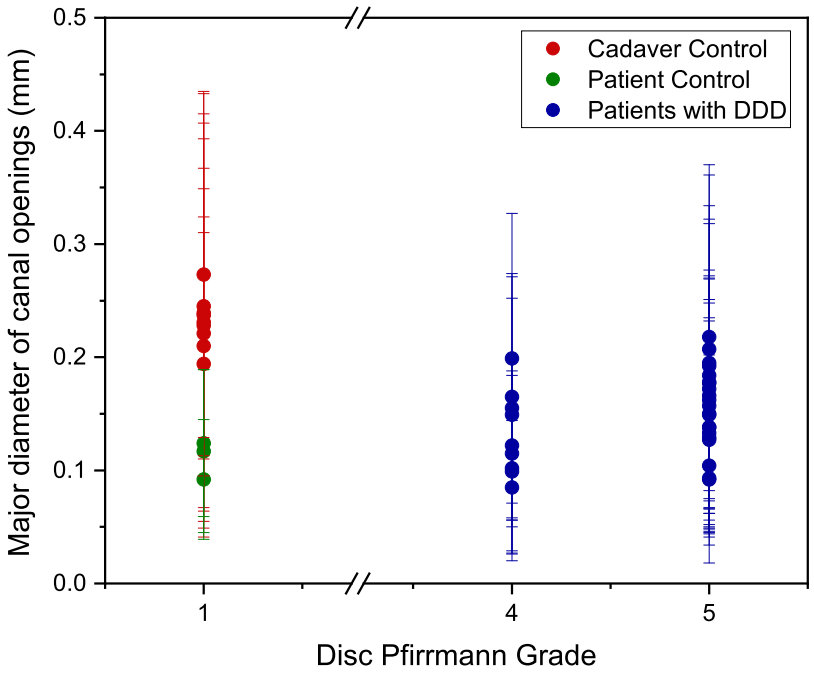

Fig. 5.26 Graph showing the variation of the major diameters of the openings on the VEP surface with the Pfirrmann grades of the disc. There is no clear trend observed. The datasets showed no statistically significant difference with each other. The error bars represent the standard deviation for each sample. (DDD: Degenerative Disc Disease)

The variation of the average major diameters of the openings for each sample with respect to the VEP erosion grades are shown in Figure 5.27. The openings in EP erosion III were significantly larger than the ones from EP erosion I and II, matching the size of the openings in the cadaver.

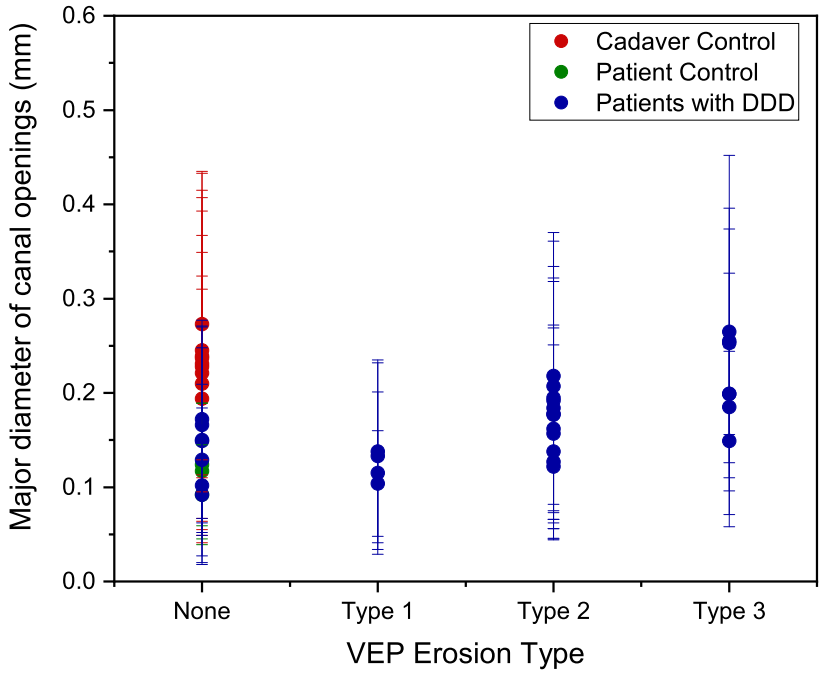

Fig. 5.27 Graph showing the variation of the major diameter of the openings in the VEP surface with the VEP erosion grades. The canal openings in type III were significantly larger than the ones from grade I and II, matching the size of the openings in the cadaver. The error bars represent the standard deviation for each sample. (DDD: Degenerative Disc Disease)

5.3.10 Effect of Ageing on the VEP

The thickness of the VEP did not show a clear trend with increasing age of the patient or cadaver. However, the control samples from the cadaver, aged 62 years old, had thinner VEPs than the control samples from patient IPS08, aged 29 years old. This is shown in Figure 5.28.

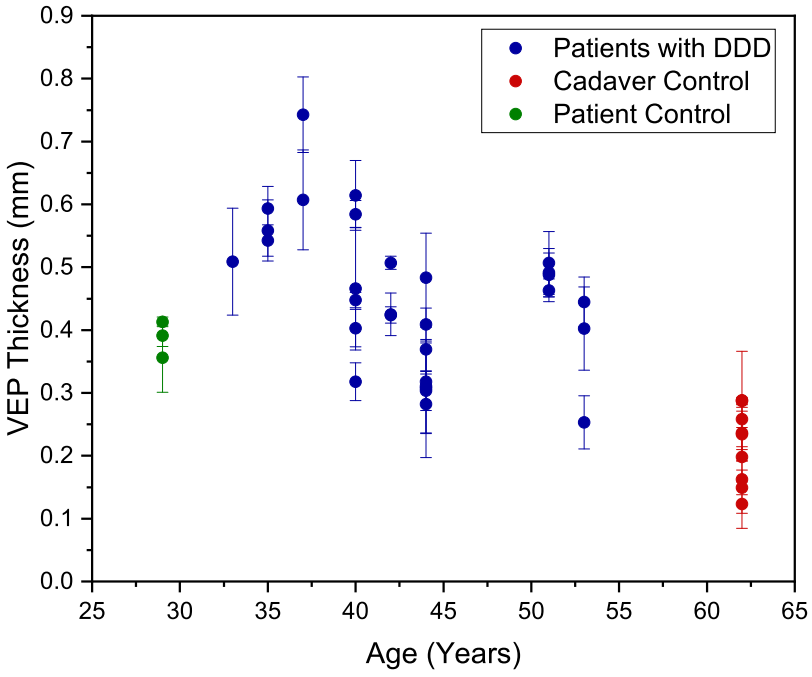

Fig. 5.28 Graph showing the VEP thickness distribution with age of the patients and cadaver. The error bars represent the standard deviation for each sample. (DDD: Degenerative Disc Disease)

Porosity of the VEP did not show a clear trend with increasing age of the patient or cadaver. However, the control samples from the cadaver had more porous VEPs than the control samples from patient IPS08. This is shown in Figure 5.29.

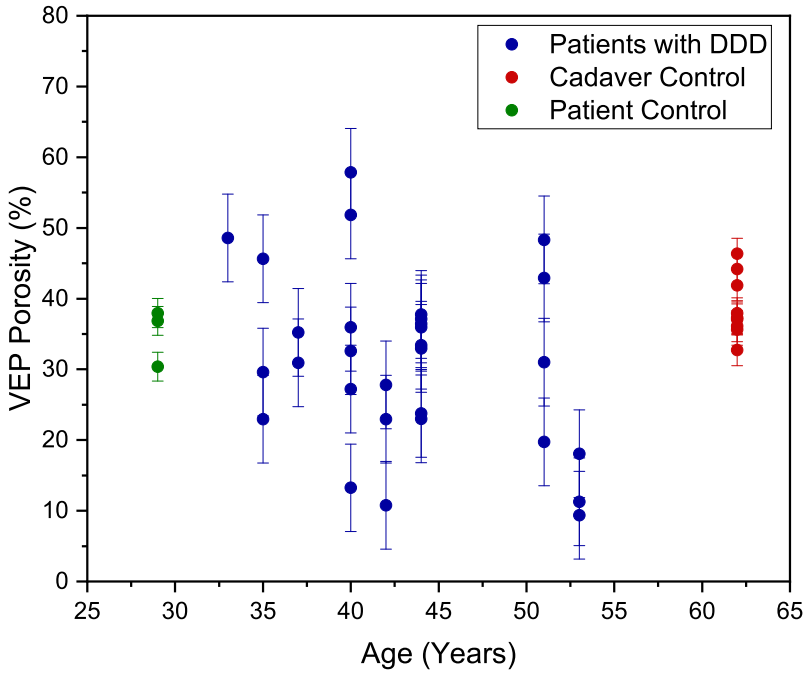

Fig. 5.29 Graph showing the VEP porosity distribution with age of the patients and cadaver. The error bars represent the standard deviation for each subgroup of samples. (DDD: Degenerative Disc Disease)

The BMD of the VEP did not show a clear trend with increasing age of the patient or cadaver. However, the control samples from both the cadaver and IPS08 showed high BMD compared to the patients with DDD, with the exception of the patient IPS10 (51 years old), who was diagnosed with Modic type III and therefore bony sclerosis, as shown in Figure 5.30.

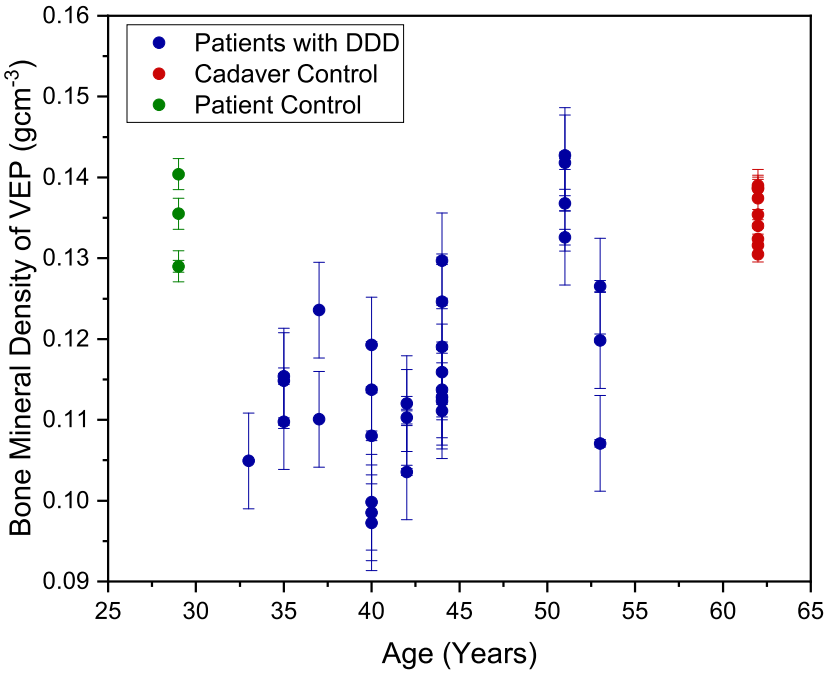

Fig. 5.30 Graph showing the VEP BMD distribution with age of the patients and cadaver. The error bars represent the standard deviation of each subgroup of samples. (DDD: Degenerative Disc Disease)

5.3.11 Structural Properties of the Trabecular Bone from the Vertebra

The porosity of the trabecular bone from the underlying vertebra was seen to be highest in the samples from tge cadaveric control, and significantly ($P < 0.05$) higher than the samples from control IPS08. The variation of the trabeculae porosity with Modic changes is shown in Figure 5.31. There were no clear difference between Modic types I and II but samples with type III showed significantly lower porosity than the other Modic types. Samples from patients with DDD but with no Modic changes closely matched the porosity of the non-diseased patient IPS08.

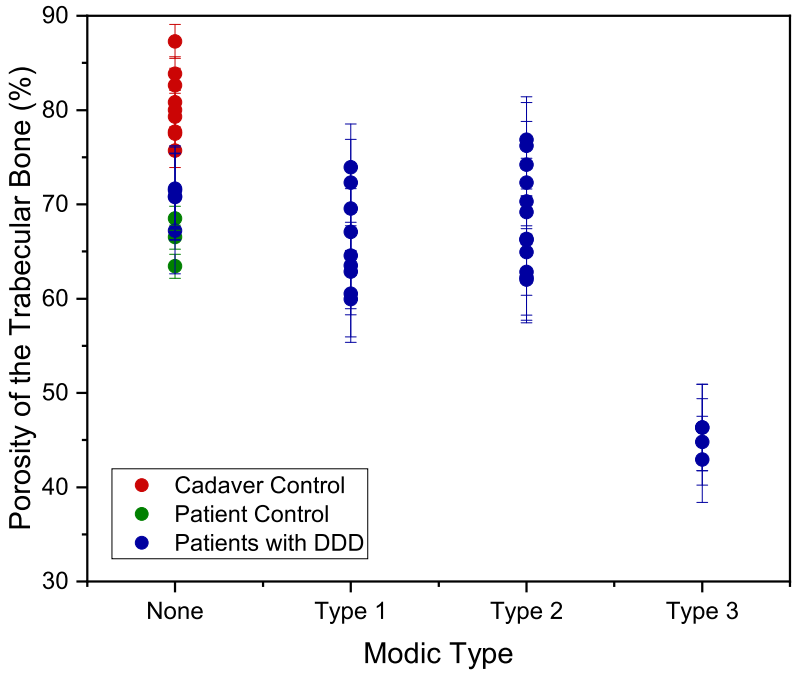

Fig. 5.31 Graph showing the distribution of the porosity of the trabecular bone with Modic changes seen on the MRI scans. Samples from the cadaver showed the highest porosity. Patients with DDD but exhibiting no Modic changes closely matched the porosity of samples from the control patients. Samples with Modic type III showed the smallest porosity. The error bars represent the standard deviation for each subgroup of data. (DDD: Degenerative Disc Disease)

The BMD of the trabecular bone showed the same trends as the variation of the BMD of the VEP (Figure 5.19) with the Modic changes as shown in Figure 5.32. The cadaver and the control patient showed similar BMD values, significantly higher than the patient with DDD showing no Modic changes, Modic types I and II. Samples with Modic type III showed significantly higher bone densities than types I and II, in the same range as the control samples.

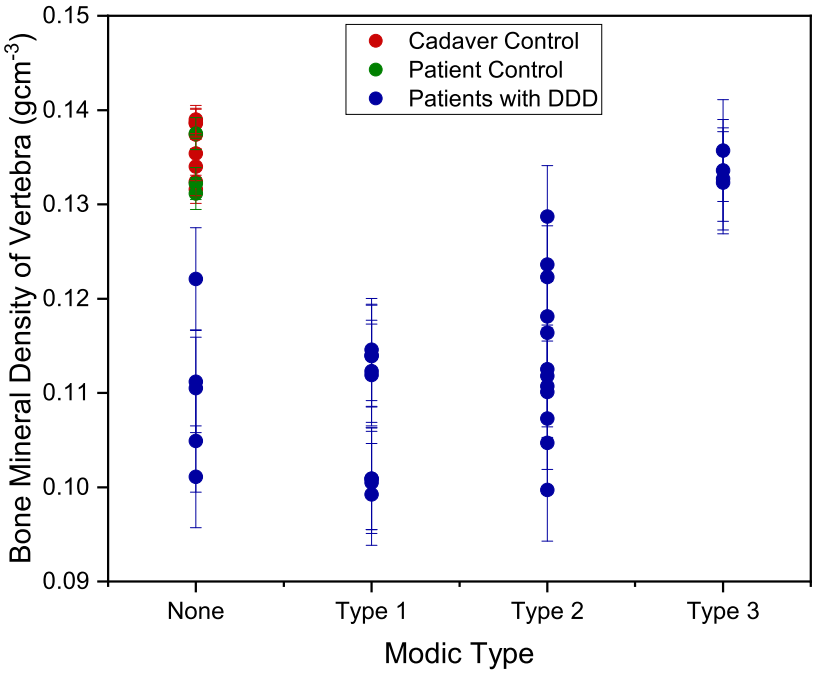

Fig. 5.32 Graph showing the distribution of the BMD of the trabecular bone with Modic changes seen on the MRI scans. Samples from the cadaver and the control patients showed the highest bone densities. Samples with Modic type III showed higher bone densities than types I and II, in the same range as the control samples. The datasets showed no statistically significant difference with Modic types. The error bars represent the standard deviation for each subgroup of data. (DDD: Degenerative Disc Disease)

The distributions of the trabecular thickness and separation of the trabecular bone with Modic changes are shown in Figure 5.33. The cadaveric samples showed the thinnest trabeculae, separated by the largest distances. Conversely, samples with Modic type III showed the thickest trabeculae packed closest. Samples from patients with DDD but with no Modic changes showed the same range of thickness and separation as the control patient IPS08.

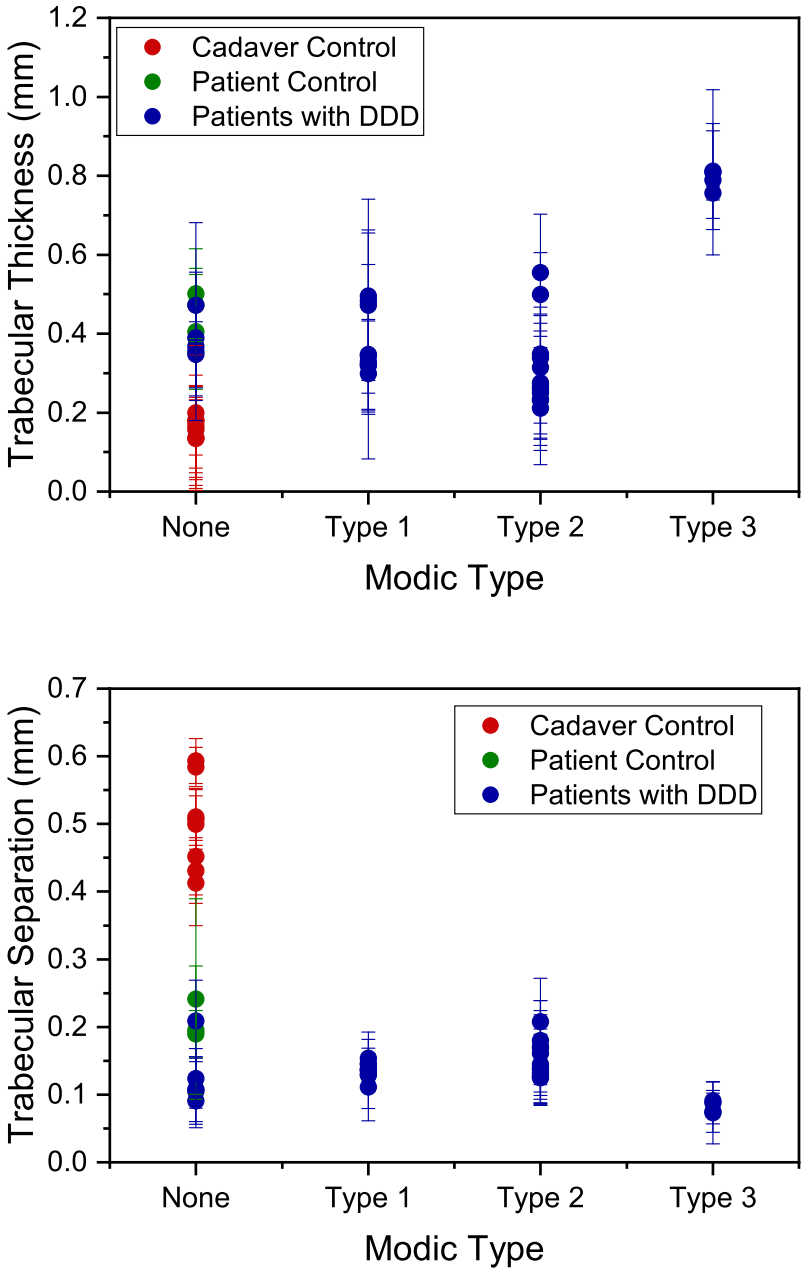

Fig. 5.33 Top: Graph showing the distribution of the trabecular thickness of the trabecular bone with Modic changes seen on the MRI scans. The cadaveric samples showed the smallest thickness while Modic type III showed the thickest trabeculae. The datasets showed no statistically significant differences with Modic types. Bottom: Graph showing the distribution of the trabecular separation of the trabecular bone with Modic changes seen on the MRI scans. The cadaveric samples showed the largest separation while Modic type III showed the closest trabeculae. The datasets showed no statistically significant difference with different Modic types. (The error bars represent the standard deviation for each sample and DDD means Degenerative Disc Disease)

5.3.12 MRI and Micro-CT Imaging of Sheep VEP

MRI scanning of the ex-vivo sheep spine showed the healthy states of the discs and VEPs in the lower lumbar region, as seen in Figure 5.34. The discs appeared grey in T1-imaging and bright in T2-imaging, indicating intact and hydrated discs. The boundaries of the VEP appeared smooth and unbroken. The large white shadow is a fluid-filled bag attached to the spine to provide contrast to the ex-vivo spine.

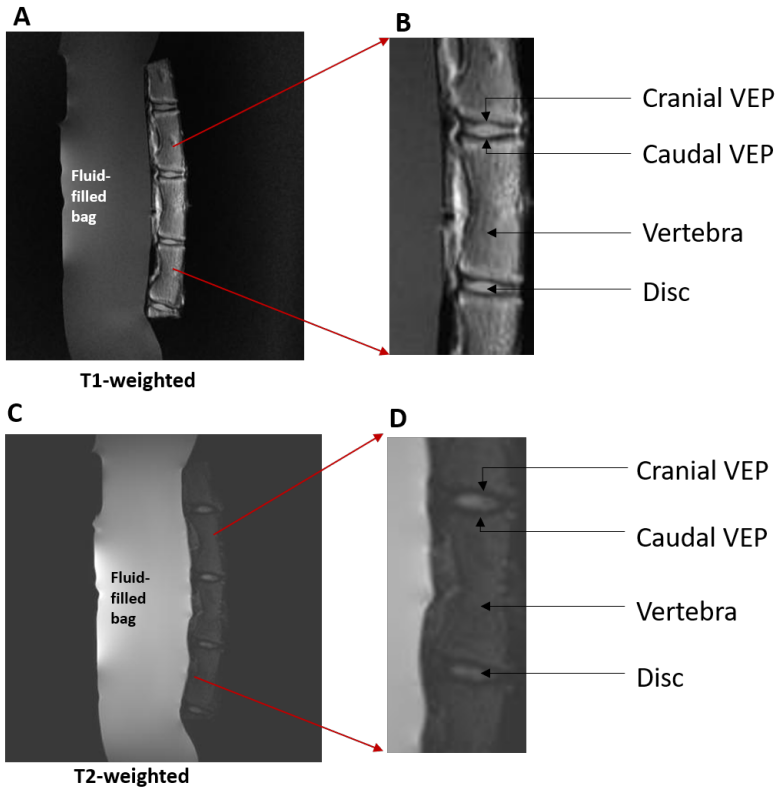

Fig. 5.34 T1-weighted and T2-weighted MRI images of ex-vivo sheep spine showing intact and healthy discs, and intact VEPs. A: T1-weighted MRI scan of the sheep spine is shown. B: A zoomed-in section from the scan in A shows the intact disc as grey and the boundaries of the VEPs can be seen as intact. C: The T2-weighted MRI scan of the sheep spine is shown. D: A zoomed-in section of C shows the disc as bright compared to the bones, and the VEP boundaries are intact. The fluid-filled bag was used to provide contrast to the sample.

A representative sheep VEP (V1 from caudal L3/L4 to represent anterior region) micro-CT image is shown in Figure 5.35. The VEP can be seen as a thick layer of much denser bone than the underlying trabecular bone, with a distribution of small openings on the surface.

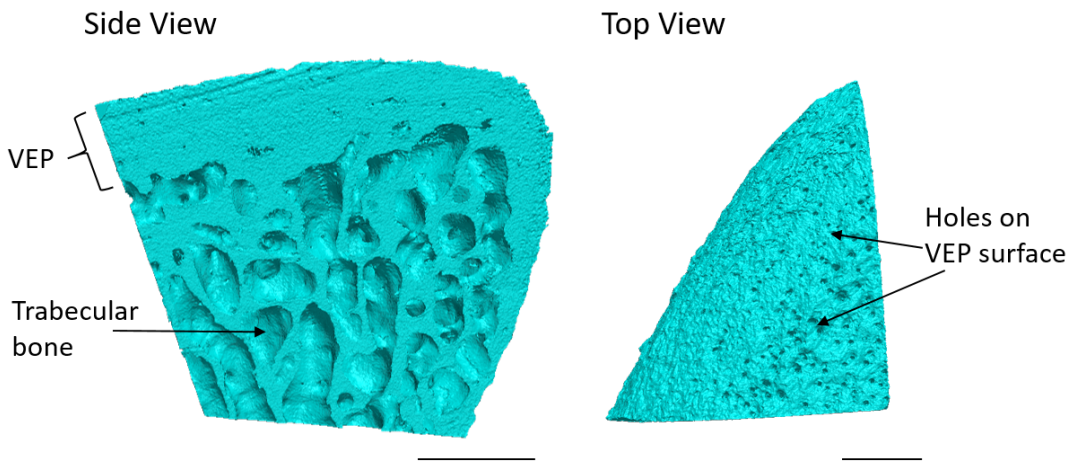

Fig. 5.35 3D rendered images of anterior region of Caudal L3/L4 sheep VEP showing clear demarcation of the denser, thick layer of VEP from the trabecular bone in the side view, with openings on the surface of the dense VEP, in the top view. The scale bars represents 2.5 mm.

5.3.13 Structural Properties of Sheep VEP and Human VEP

From this preliminary study, the sheep VEPs were thicker, less porous with less BMD than the VEPs from the healthy control human samples. The average thickness of the VEPs from the sheep spine were significantly different ($P < 0.05$) from both the cadaveric and non-cadaveric human samples, for both caudal and cranial subgroups, as shown in Figure 5.36. The cadaveric and non-cadaveric human samples showed no statistically significant difference between the caudal and cranial VEPs.

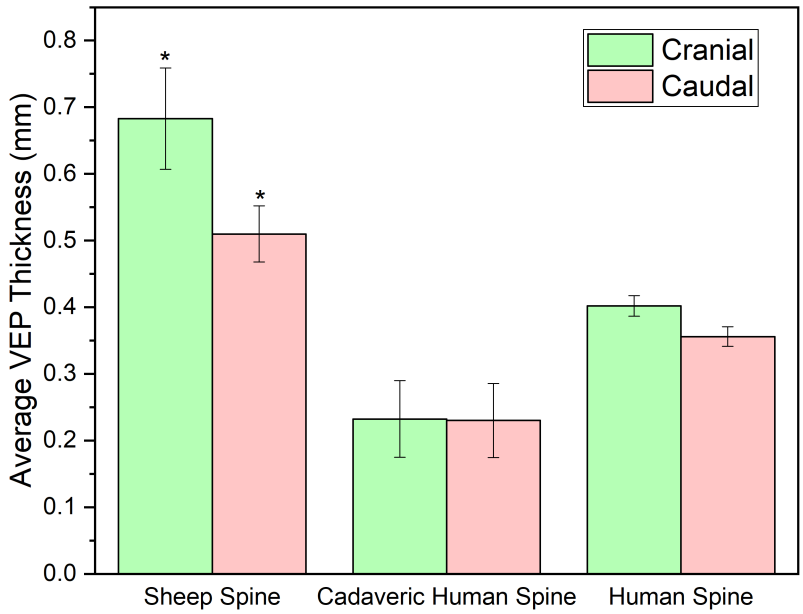

Fig. 5.36 The average thickness data for caudal and cranial VEPs are shown for the sheep spine, the cadaveric human and non-cadaveric human spines. The * represent statistical significance for the 2 bars of the sheep spine with $P < 0.05$, compared to both human spines. In all 3 categories, cranial VEPs were thicker than caudal ones. There were no statistically significant differences between the 2 types of human spines. The error bars show the standard deviation for each dataset.

The average porosity of the VEPs from the sheep spine were significantly different ($P < 0.05$) from the porosity of both types of human spines, for both caudal and cranial subgroups, as shown in Figure 5.37. The cadaveric and non-cadaveric human samples showed no statistically significant difference between the caudal and cranial VEPs.

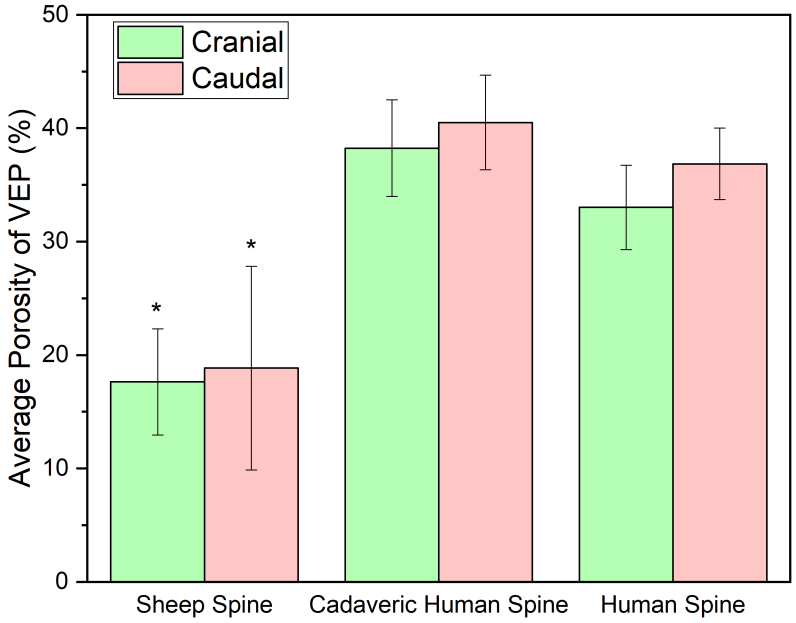

Fig. 5.37 The average porosity data for caudal and cranial VEPs are shown for the sheep spine, cadaveric and non-cadaveric human spines. The * represent statistical significance for the 2 bars of the sheep spine with $P < 0.05$, compared to both human spines. In all 3 categories, cranial VEPs were less porous than caudal ones. There were no statistically significant differences between the 2 types of human spines. The error bars show the standard deviation for each dataset.

The average BMD of the VEPs from the sheep spine were significantly different ($P < 0.05$) from the average BMD of both types of human spines, for both caudal and cranial subgroups, as shown in Figure 5.38. The cadaveric and non-cadaveric human samples showed no statistically significant difference between the caudal and cranial VEPs.

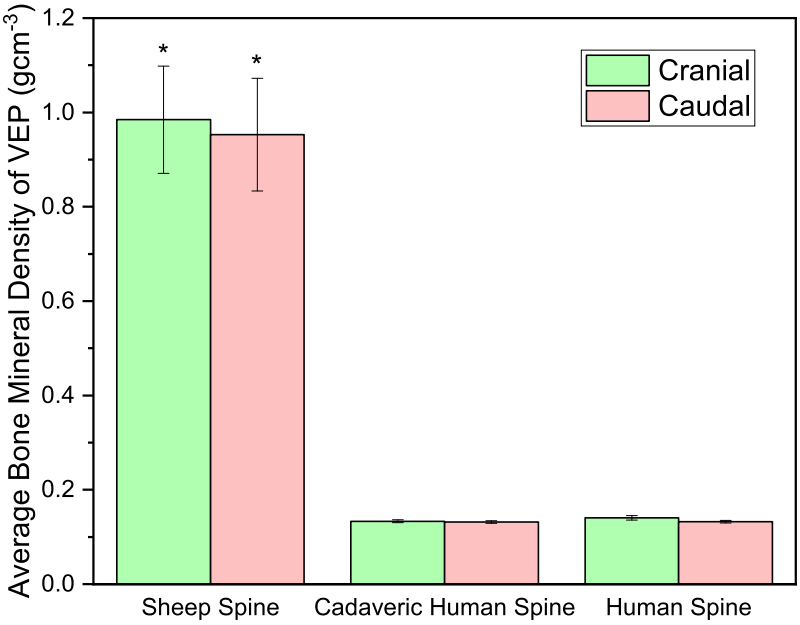

Fig. 5.38 The average BMD data for caudal and cranial VEPs are shown for the sheep spine and the healthy human samples. The * represent statistical significance for the 2 bars of the sheep spine with $P < 0.05$, compared to both human spines. In all 3 categories, the cranial VEPS were more dense than the caudal ones. There were no statistically significant differences between the 2 types of human spines. The error bars show the standard deviation for each dataset.

5.4 Discussion

This chapter investigated the effect of pathological degeneration on the VEP in humans. This study is the first to investigate the effect of degeneration on the VEPs and the underlying trabecular bone, using samples from patients, making the correlation between laboratory findings and clinical data possible. The observed effects of degeneration on the structural properties of the VEP will be discussed first, followed by the effect on the trabecular bone of the vertebra and finally analysis of the changes on the nutritional pathway will be discussed.

5.4.1 Prevalence of Degenerative State

The extent of Modic changes was associated with the severity of disc degeneration of the adjacent intervertebral discs, as shown in Table 5.5. This agrees with previous findings by Jensen et al. and Kokkonen et al. [259, 260]. The highest prevalence was seen for Modic II and Pfirrmann grade V, implying that Modic III is a stable phase compared to Modic II, where peak degeneration occurs.

Although there were close associations between high Pfirrmann grades and VEP erosion grades and between the advanced Modic types and VEP erosion grades, as shown in Tables 5.6 and 5.7, this study only had samples from patients with highly degenerated discs and healthy discs. Therefore the study did not include samples with less advanced degeneration, making it harder to make conclusive remarks on the association between different degeneration grades.

5.4.2 Effects of Degeneration on the Structural Properties of the VEP

Samples from patient IPS08 were classified as healthy as they showed no Modic changes on the MRI scans and showed healthy disc with Pfirrmann grade I and no VEP erosion grade. The patient was undergoing corrective surgery for their spine alignment and therefore did not suffer from pathological degeneration. Given that in this study, the healthy condition is defined as no Modic change, disc Pfirrmann grade 1 and no VEP erosion grade, the samples from the patient satisfy all the requirements and were therefore also used as controls.

Furthemore, 9 samples from a cadaver were also used as controls. However, the cadaveric samples showed different structural characteristics than samples from IPS08 on the micro-CT, as shown in Figure 5.6. The thickness of the VEPs from the cadaver were 0.23 ± 0.06 mm, which were thinner than the 0.77 ± 0.04 mm and 0.69 ± 0.04 mm reported previously in literature [261, 262]. Although the VEPs from the cadaver were thinner with rougher surfaces and larger openings, the VEP samples showed the same range of porosity, opening density at the disc boundary, and BMD to the samples from the healthy patient. Samples from both control groups showed no statistical difference between the distributions of the VEP thickness, porosity and bone densities. Similarly, the vertebrae from the cadaver were more porous with thinner trabeculae but with similar bone densities. The thinner VEP and trabeculae could be explained by the advanced age of the cadaver, 62 years old, compared to the patients. Age-related bone loss and osteoporosis in older people have been reported by several studies [263–265]. Owing to the incomplete medical history of the cadaver, these observations could have also been caused by other medical conditions such as osteoporosis. However, the BMD values of the trabecular bone of the cadaver, 0.133 ± 0.003 gcm^{-3}, do

not indicate osteoporosis given that they closely matched the BMD of the samples from the healthy patient: 0.135 ± 0.006 gcm^{-3}. The BMD values of vertebrae reported by Bruno et al. in the literature using quantitative computed tomography were 0.137 ± 0.001 gcm^{-3} for healthy men and 0.150 ± 0.001 gcm^{-3} for healthy women [266]. Furthermore, using the same methods, Gezer et al. reported BMD values of 0.119 ± 0.003 gcm^{-3} in the lumbar region [267]. Therefore, the BMD values for the non-degenerate samples from this study was in the same range as values previously reported in literature and the cadaveric samples can be assumed to be exhibiting healthy BMD.

Samples classified as caudal/cranial with respect to the intervertebral discs showed no statistical difference for all of the structural properties of the VEP. The samples harvested during surgery were all from the anterior region of the VEP, either from the central anterior region or the peripheral anterior region. Therefore it was not possible to compare the structural properties of the VEP across the whole VEP surface. Furthermore, no statistical difference were seen for samples from the middle or peripheral regions of the VEP. This could be explained by the degenerative states of these VEPs. Therefore, the structural analysis for the rest of this study did not take into account the physical location of the VEP as defined by caudal/cranial and central/peripheral, but only the degenerative classifications.

Variation with Modic Changes

According to Modic, the presence of Modic type I refers to inflammation and oedema which is acute swelling due to accumulation of fluid in the bone marrow [190]. Oedema is usually a response to an injury, and it has been reported that in Modic I, mechanical trauma can lead to disruption of the disc or appearance of fissures in the VEP which lead to the development of vascular granulation tissue causing oedema as a result of the trauma [268].This leads to higher vascular permeability and innervation of the VEP which explains the high prevalence of back pain in patients with Modic type I [269]. Pro-inflammatory material from the disc nucleus may diffuse into the adjacent marrow, through the more porous VEP, leading to a cascade of inflammatory mediators, further oedema, and neo-vascularization (formation of new blood vessels). From Figure 5.15, no significant differences were observed between the porosity changes across the different Modic types, but from Figure 5.7, for Modic I, the samples showed increased interconnectivity between the pores which would support the clinical descriptions. The BMD was lowest in the samples with Modic change I, which is explained by the close association between loss of bone mineral and inflammation as the latter affects the bone remodelling cycle [270]. The bone remodelling cycle refers to the coordinated interaction between osteoclasts and osteoblasts to remove an area of existing bone and replace it with new bone matrix. However, inflammation stimulates osteoclasts

production, therefore increasing the rate of bone resorption but also inhibits osteoblasts formations therefore slowing down the process of bone formation.

Modic type II represents the conversion of bone marrow to fatty marrow as a result of ischaemia, which is the restriction in blood supply to the tissue. Modic type II is considered a more stable and chronic phase of the degenerative state, in contrast to the inflammatory stage of Modic type I. From this study, samples with Modic II were seen to be thinner than those with Modic I, with the presence of fissures in Modic II, however no significant differences were recorded for porosity. The BMD of VEP samples with Modic type II was higher than Modic type I but lower than the control samples with no Modic changes. The higher bone densities than Modic I can be explained by the absence or reduced concentration of inflammation mediators, therefore less bone loss. It was not possible to compare the values of BMD of the VEP measured in this study as previous studies in the literature has reported BMD of samples with Modic changes measured by the dual-energy X-ray absorptiometry (DEXA), in different units: kgcm^{-2} [271, 272] and there were no studies reporting the changes in the BMD of VEPs with deterioration of Modic changes. It has been shown that a sample with Modic type I can convert to type II and vice versa [190]. This could explain the closely similar range of porosity seen in Modic II to Modic I as it could be resultant porosity during the previous stage of Modic I. The presence of fissures as seen in the micro-CT scans of Modic II samples as shown in Figure 5.7 provides further evidence to the transitional nature of the Modic changes as they are similar to the ones expected in Modic I, which could be the result of biomechanical trauma leading to the onset of degeneration.

In Modic III, the VEP was thick, showing two different shades of grey, indicating deposition of a new layer of bony structure, as shown in Figure 5.7. This stage of degeneration is assigned to bony sclerosis which is the deposition of new bone mineral, leading to the stiffening of the cartilaginous tissues near the VEP. This would explain the increased thickness observed in this study, as shown in Figure 5.11 and the high bone mineral density seen in Figure 5.19.

It has been suggested in literature that all Modic changes represent different stages of the same pathological process and mixed Modic changes can be assumed to develop before the conversion from one Modic type to another [273, 274]. There has been recent evidence showing the presence of bony sclerosis, in varying degrees, in all the Modic types [268]. The mixed effects of oedema, fat and sclerosis and the overlapping nature of the Modic types make the identification of structural trends hard to see. Samples were collected from people of different ages, with different levels of physical activity and lifestyles which could also explain why no clear trends could be seen in the thickness and porosity variations 5.11.

Variation with Pfirrmann Grades

The results from this study did not show any conclusive correlation between the structural properties of the VEP, thickness, porosity and BMD with the Pfirrmann grades. Given that patients undergoing surgery in this study only reported Pfirrmann grades IV and V, it was not possible to investigate the stepwise progression of degeneration from grade I to V. At grade IV, the boundary between the nucleus pulposus and the annulus fibrosus of the disc is lost and the disc height is decreased. At grade V, the disc has completely collapsed [77]. This degeneration grading system is based on the structural integrity of the intervertebral disc and this study showed no significant trend with the changes observed in the structure of the VEPs.

Although, it is not possible to infer causality in this study, the evidence from literature suggests that VEP microfracture can initiate disc degeneration, and the reverse is less likely to be true [77, 275]. This is because degenerated discs are collapsed, with reduced discal heights, such that the discal pressure is lower than in healthy discs. This means that compressive forces during mechanical loading of the spine will be transmitted through the annulus of the disc instead of through the VEP, where it is less likely to cause damage to the VEP. As structural integrity of the VEP is key to providing mechanical stability and a nutritional pathway to the disc, it is reasonable to assume the VEP defects could be the initiator for the disc degeneration and ultimately back pain.

Co-variation of Modic Changes and Pfirrmann Grades

As shown in Table 5.10, there was a clear trend of highest BMD observed in the worst degenerative states, which were in Modic type III and Pfirrmann grades IV and V. On the contrary, the lowest BMD was seen in the absence of Modic changes but at high Pfirrmann grades. The healthy samples, with no Modic changes and Pfirrmann grade I, exhibited BMD in the range between samples with Modic type II and type III. Therefore, the BMD drops with increasing Modic changes from the healthy state, but then increases at Modic III, which is in line with the current understanding of the Modic types.

From Table 5.8, the data showed a general decreasing trend with incremental degenerative conditions but the trend was not conclusive. Conversely, in Table 5.9, the data showed an increasing trend of porosity with increasing degenerative conditions. However, given the lack of all the Pfirrmann grades, it is not possible to have conclusive trends at this stage.

Furthermore, the results from this study show that considering only the Pfirrmann grade of the disc does not provide a holistic image of the pathology involved. Samples exhibiting the same Pfirrmann grade showed different structural properties depending on their Modic

changes. Therefore, it is crucial to consider the degenerative states of both the disc and the vertebra when assessing their combined effect on the VEPs.

Variation with Endplate Erosions

The results from this study suggest that VEP erosions are closely associated with adjacent disc degeneration, as shown in Table 5.6. The data showed that greater affected VEP area of lesion, that is higher grades of VEP erosions, were associated with higher Pfirrmann grades of the adjacent discs. Similarly, as shown by the data in Table 5.7, VEP erosion was present across all Modic types, with a high prevalence of 17.2 % for VEP erosion grade III and Modic type I. This supports previous work in the literature suggesting close association between VEP erosions and back pain [276]. Modic type I is strongly associated with back pain. The central portion of the VEP and the adjacent vertebral marrow are innervated, in contrast to the nucleus pulposus of the disc [174, 277]. Therefore, lesions and erosions of the VEP expose these sensory receptors, producing pain. Moreover, the inhomogeneous VEP boundary with the disc and inflammation can lead to altered stress distributions which could in turn lead to the innervation of the VEP. These suggested mechanisms for degeneration could explain the occurrence of pain.

The inhomogeneous nature of the VEP-disc boundary as a result of VEP erosion made it hard to see any clear trend in the structural properties of the VEP with different grades of VEP erosions. The disruption of the VEP's structural integrity could be initiating the degenerative conditions of the disc. The nucleus pulposus is likely to protrude into the vertebra through the eroded VEP causing a loss of water and proteoglycan of the disc and loss of discal heights, all contributing to the degeneration of the disc [278]. Furthermore, in an attempt to repair the VEP erosions, the bone remodelling cycle could lead to obstruction of the vascular network in the VEP, leading to limited nutrition to the disc.

5.4.3 Effects of Degeneration on the Trabecular Bone of the Vertebra

To assess the effect of degeneration on the trabecular bone, only Modic changes were considered as the Pfirrmann grades of the disc and the VEP erosion grades affect the disc and the VEP only, but Modic changes also affect the trabecular bone in the verterbra. Comparing the structural properties of the underlying trabecular bone in the vertebra with Modic changes showed no clear trends for the types I and II. The BMD of the controls and samples with Modic type III were highest. As explained in the previous section, this increase in BMD from Modic type II to type III could be explained by bony deposition or mineralisation of the cartilage tissues due to the pathological nature of Modic type III. The cadaveric

samples had the highest porosity and therefore the largest trabecular separation and thinnest trabeculae. This further implies that the cadaver must have had other pre-existing medical conditions which would explain the uncharacteristic structural properties of the samples, despite having no disc degeneration. Conversely, samples with Modic type III showed the lowest porosity, with thickest trabeculae and smallest trabecular separation. This could mean that sclerosis or bone deposition is happening throughout the vertebra as the cells involved in the bone remodelling cycle could be infiltrating through the damaged VEP-disc boundary and reaching the trabecular bone in the vertebra. This agrees with the findings of Perilli et al. showing increased bone volume and trabecular thickness compared to Modic I and II, which they explained by increased bone formation and reduced bone resorption [279]. Another explanation could be that the samples with Modic type III, given that they are all from the same patient, could be an individual characteristic of this particular patient, therefore making it harder to make conclusive remarks at this stage.

5.4.4 Effects of Degeneration on the Nutritional Pathway of the VEP

It is still unclear whether the VEP or the disc is the initiator of degeneration. However, as discussed in the previous sections, given that the VEP provides a nutritional pathway to the avascular disc, it is hypothesised that hindrance of this blood supply would lead to the degeneration of the disc. In this study, the nutritional pathway was characterised by the openings density per area on the surface of the VEP in contact with the disc and the sizes of the openings. The effects of degeneration on these parameters will be compared for each of the degeneration categories.

Variation with Modic Changes

The cadaveric samples showed lower canal openings density than the healthy patients but had larger openings, the major diameter of the openings were actually largest for the cadaver, as shown in Figure 5.25. Samples with Modic I showed the largest spread for openings density, with the values higher than other Modic types, as shown in Figure 5.22. This is because oedema present in Modic I is accompanied by an increased vascular density along with an increase in the number of nerve endings as a result of the VEP microcracks [191]. Conversely, samples with Modic III had the lowest openings density per area, which implies that sclerosis could be obstructing some of the openings. The diameters of the openings did not show considerable variations across all Modic types.

Variation with Pfirrmann Grades

The openings density per area and the diameter of the openings showed no specific variation with the disc Pfirrmann grades, as shown in Figures 5.23 and 5.26. This implies that the degeneration grades of the disc are not contibuting factors to the normal functioning of the nutritional pathway of the VEP. Given that samples were excised from patients undergoing surgery, their discs were at higher grades, Pfirrmann grades IV and V. Therefore this study had no samples from grades II and III, making it harder to make a conclusive remark on the effect of Pfirrmann grades on the nutritional pathway.

Variation with Endplate Erosions

The canal openings density per area showed no clear trend with VEP erosion grade, as shown in Figure 5.24. This is because of the different extents of influence from the different types of degeneration as well as individual characteristics of each patients. However, the openings in samples with Modic type III had larger diameters than the ones in types I and II, which is also reflected in the 3D rendered images shown in Figure 5.9. The standard deviation of the diameters were also large in Modic III, implying the openings are of very different sizes, with some very large ones, due to the loss of the VEP's structural integrity. The diameter of the openings in VEP erosion type II were also larger than the ones in type I which shows the openings get larger with increasing erosion of the VEP. These larger openings are the result of the VEP layer being eroded and might not necessarily contain vascular vessels but could be filled with bone marrow and descending matrix of the nucleus pulposus of the disc [258, 280].

5.4.5 Clinical Significance

Modic changes have been associated with the presence of external pressure from the loading of the spine, hindrance of the nutritional pathway and genetic factors by Emch et al. [281] whereas Crock et al. linked Modic changes with the inflammation in the VEP resulting from disruption of the intervertebral discs [175]. From this study, we saw a close association between Modic changes and the structural properties of the VEP. It has been reported that lumbar spinal segmental instability, which occurs when an applied force produces displacement of part of a motion segment exceeding that found in a normal spine, could play a major role in the onset of the pathological degeneration of the disc [282]. Furthermore, degenerated discs also contribute to the spinal segmental instability, worsening the condition. It has been shown previously that Modic I is more prone segmental instability, which explains the conditions worsening to Modic II in some patients [283].

It is not possible to make conclusive remarks about the effect of only the Modic changes on the structural properties of the VEP due to varying degrees of Pfirrmann grades and VEP erosions in the samples from this study. Furthermore, the Pfirrmann grading system does not take age into consideration, given that it was devised with a sample group with average age 40 years [77], and there is also inter-observer disagreement on grades II and III due to the ambiguity of the description provided for the grading system. It has also been shown that there is considerable variation in discal heights, making the grading system relatively non-discriminatory for grades III and IV. To address these shortcomings, Griffith et al. devised a modified Pfirrmann grading system, adding grades VI to VIII, expanding the visual representation and description of the new grades [284]. Yu et al. showed that there was a significant difference in the Pfirrmann grade and the modified Pfirrmann grade among Modic type 0, I and II changes [282]. Therefore, hospitals and radiologists should consider using the modified Pfirrmann grades to assess degeneration levels of the discs. This could have provided a clearer picture of the association between the Modic changes and the Pfirrmann grades in this study.

Similarly with the Modic changes, due to the occurrence of mixed Modic types and transitional phases between Modic I and II, modified Modic classification has been suggested [285]. However, it is still undecided which of the two grading systems have better inter and intra observer reliability. Therefore, it might be essential to improve the sensitivity and precision in assessing MRI signal changes of VEPs, given that the Modic classification was devised in 1988.

Regarding the VEP, morphological changes were evident with advancing age but also in association with pathological changes of the intervertebral discs in incremental stages of degeneration. In early stages of degeneration, fissures were seen on the VEP with increasing porosity. These were assumed to be linked to increased blood vessels during the inflammation stages, as a result of the ossification of the VEP and the cartilage endplate in the more advanced stages of degeneration.

Brown et al. showed the proliferation of vascularity and sensory nerves in the VEP region and the vertebra adjacent to the degenerate discs. This increase in nerve endings was linked with an increase in blood flow, perhaps as an attempt to increase the nutrition of the degenerated disc [176]. The neuropeptides responsible for the innervation process are also pain transmitting. Therefore, the increase in sensory nerves and the presence of VEP erosions strongly suggest that VEP are sources of pain. In conclusion, the VEP plays an important role in maintaining the healthy conditions of the disc and the spine. From this study, we have a better understanding of the VEP and the structural changes that occur as

part of degeneration. The VEPs have to balance physiological challenges which contribute to its failure. However, the exact cause and initial stages of degeneration still remain unclear.

Although disc degeneration is not the only cause of back pain, the findings from this study strongly support previous results from literature which highlighted the strong correlation that exists between the two. As a result of the increased understanding of the cellular processes that lead to disc degeneration and the structural properties of the VEP, there is also more development in the field of regenerative medicine. The regenerations of the VEP under development involve the disc as a whole, due to the complex interactions between the individual components of the disc and the VEP [286]. However, these approaches should take into account several factors such as the individual patient's weight, activity, other medical conditions and a clearer understanding of the progressing stages of degeneration is required.

5.4.6 Physiological Degeneration of the VEP

According to literature, the physiological degeneration of the VEP with age would mean a decrease in thickness, an increase in porosity and a increase in the BMD [129]. This can be explained by the constant loading of the spine leading to a decrease in discal thickness and therefore VEP thickness [104]. Furthermore, with age, the cartilage VEP undergoes calcification, therefore increasing the BMD of the VEP which can impede the nutritional pathway, leading to an increased porosity as a coping mechanism.

The results from this study also indicated a decreasing trend for the VEP thickness, with the cadaver at 62 years old having the thinnest VEP, as shown in Figure 5.28. The porosity showed a less clear trend. For the BMD, shown in Figure 5.30, the control patient and cadaver had the highest values and a generally increasing trend for the other samples. Because these samples were excised from patients with different degrees of disc degeneration, with different levels of physical activity and lifestyles which are all contributors to the structural properties of the VEP, finding a trend with age proved to be hard. The physiological degeneration is not the biggest factor in determining the structural properties of the VEP, in this study.

Given that the VEP provides the main nutritional pathway to the avascular disc, it would make more sense for this pathway to be first hindered, causing the eventual degeneration to the disc. It is less likely for the disc to degenerate first, causing a blockage of the nutritional pathway. Moreover, the degeneration grades of the disc, assessed by the Pfirrmann grading system, did not show any clear trend with the structural properties of the VEP. However, the VEP showed clear trends with the Modic changes, which are based on the bony changes of the VEP and the trabecular bone. The occurrence of fissures, as shown in the micro-CT images in Figure 5.7, from constant loading of the spine could lead to disruption of the mechanical stability of the VEP which in turn affect the calcification and bone remodelling

processes. This could lead to the changes observed in the porosity and nutritional pathway of the VEP, eventually leading to the degeneration of the disc. However, this still remains a theory, requiring further investigation into the pathologies involved in the different levels of disc degeneration.

5.4.7 Validity of the Sheep Model

From the MRI scans of the sheep spine in Figure 5.34, the discs and VEP were shown as healthy and therefore are comparable to samples from the cadaver and from the healthy patient IPS08. However, the VEP in the sheep are thicker with smaller openings on the surface as shown in the 3D rendered images in Figure 5.35. The defining structural properties of the VEP, namely the thickness, porosity and BMD of the sheep samples were significantly different from the control human samples. The cadaveric and healthy patient samples were considered separately and there were no significant differences between these two groups, as shown in Figure 5.36, 5.37 and 5.38. This further reinforces the validity of the cadaveric samples as control in this study. However, the results from this study indicate that the sheep model does not provide an accurate representation of the human spine. Although the trends with respect to cranial and caudal VEPs might be similar, the actual values are different, given the size difference of the spine and the fact that sheep are quadrupeds. Therefore, it is safe to say that using a sheep model is a good way of perfecting experimental protocols and is useful to understand the trends in the structural properties and the nutritional pathway of the VEP. However, they have limitations and should be used with extreme caution for comparison with data from human spines or for designing implants due to the size differences.

5.5 Conclusions

This chapter aimed to assess the effect of pathological degeneration on the VEP, using a novel approach comparing the laboratory findings with clinical observations of samples harvested from patients undergoing spinal surgeries.

The results successfully showed a direct association between disc degeneration and VEP structure. Although Modic changes and Pfirrmann grades are useful grading systems to assess the progress of the degenerative state of the disc, they are still limited in their description making targeted identification of a specific grade less specific. However, the VEP samples showed expected trends with the Modic changes, showing increased porosity and decreased BMD with inflammation in Modic I and II but increased BMD and increased thickness of

the VEP in Modic III, highlighting the bony sclerosis. However, the lack of samples from each incremental grade of degeneration in this study made the findings inconclusive.

Similarly, the VEP erosion grades showed a direct association with the size of the openings on the surface of the VEP in contact with the disc, both on the micro-CT images and in the quantitative analysis of the openings. It was clear that with advancing erosion grade, the openings get bigger in size, leading to loss of the structural integrity of the VEP in the worst cases. The VEP erosion grades showed correlation with the Modic and Pfirrmann changes, however, due to the lack of samples from all grades, it is not possible to make conclusive remarks on the trends from this study. Furthermore, the underlying trabecular bone in the vertebra showed the same trends in structural properties as the VEP, in both healthy samples and samples with Modic type III, implying the cells causing the pathological degeneration could be breaching the damaged disc-VEP boundary and infiltrating the VEP and the vertebra. It also became clear in this study that the weight, level of physical activity, smoking and drinking habits and other pre-existing medical conditions should all be considered before making assumptions about the trends with disc degeneration. The cadaveric samples, for instance, qualified as healthy samples based on the assessment of disc degeneration but clearly showed some uncharacteristic features compared to samples from the healthy patient. Therefore, all factors have to be taken into account before making conclusive remarks.

The sheep model showed the same trends as the ones seen for cranial and caudal VEPs in both the cadaveric and healthy patient samples, however, there was a significant difference in the magnitude of the results. Therefore, sheep models can be used for perfecting experimental protocols and predicting trends, however, absolute values are not comparable to those from human spines.

Key Points

The main findings from this chapter can be summarised as shown below:

- The results of this study suggest that the hindrance of the nutritional pathway of the VEP as the initiator to disc degeneration, rather than the degenerated disc causing changes in the VEP.
- Increased BMD and increased thickness of the VEP in Modic III could be caused by the pathological process of bony sclerosis.
- The Pfirrmann grading system and the Modic changes are limited in their assessment of degenerative states.

- With advancing VEP erosion grades,the size of the canal openings on the surface of the VEP in contact with the disc were seen to be larger, both on the micro-CT images and in the quantitative analysis of the openings.
- The underlying trabecular bone showed the same trends in structural properties as the VEP, in healthy samples and samples with Modic type III.
- The sheep model is valuable for perfecting experimental methods but the structural properties are significantly different in magnitude to those measured in the healthy human samples.

Chapter 6

Conclusions and Future Work

6.1 Summary of Main Findings

The work presented in this thesis described the experimental investigations of the vertebral endplate (VEP) with respect to its structural properties and main biophysical functions. Furthermore, the effect of degenerative conditions of the intervertebral disc on the structural properties of the VEPs were also investigated. In each of the experimental chapters, the methods developed and used, the results obtained, and the discussion of those results were presented. The main findings will be summarised below.

Structural Properties of the Endplate

In Chapter 3, a characterisation protocol was optimised for the sheep VEPs, using the micro-CT imaging technique. The novel aspect of this study was the simultaneous assessment of different structural properties of the same VEP, and the comparison of different VEP locations from the same spine on the structural properties. The VEP was shown to have structural properties, adapted to enable it to fulfil its 2 main biophysical functions of providing mechanical support and a nutritional pathway to the disc. The central region of the VEP was thinner and more porous to allow for increased biochemical exchange with the nucleus pulposus of the disc while the peripheral regions were thicker and less porous to enable better anchorage of the fibres from the annulus pulposus of the disc. The VEP has been shown to be part of a complex multi-component systems, consisting of the epiphyseal ring, the vertebra, the cartilage endplate and the intervertebral disc. The size of the epiphyseal ring also adapted to the loading of the spine, being thicker in the anterior region of the spine to allow the spine to bend and twist without slippage of the disc by providing strong anchorage of the discal fibres. Furthermore, the VEP was also shown to have different structural properties

depending on their location with respect to the disc and the spinal level. The cranial and caudal VEPs had different properties, as did the VEP at higher spinal levels compared to those at the lower ones of the lumbar spine. The cranial VEPs were thicker, more porous and showed higher BMD than their caudal counterparts. The thickness of the VEP increased from spinal level L3 to L6, whereas the porosity and the BMD decreased in the same direction. This once again highlights the close correlation between the loading of the spine and the structural properties of the VEP.

The bone health of the trabecular bone in the underlying vertebra was also investigated. Although there were no significant changes in the average porosity, trabecular thickness and separation in different vertebrae, the BMD increased from spinal level L3 to L6. Given that all 54 samples were harvested from the same sheep spine, this study provided a reliable means of assessing the effect of locations on the structural properties of the VEPs.

Nutritional Pathway within the Endplate

An intricate 3D network of canals was found in the VEP layer, which was imaged, isolated and analysed. This study was the first to quantitatively characterise the structure of the individual canals, and simultaneously investigate the contents and the endings of these canals. The canals originated from the trabecular bone and ended at the boundary of the VEP with the soft tissues of the disc. Chapter 4 introduced a new method using the centreline analysis for the quantitative analysis of the individual canals in the VEP. The canals were classified into 3 groups, the ones starting from the surface of the VEP, the transverse canals with respect to the normal direction to the VEP surface, and the longitudinal canals. The canals emerging at the surface of the VEPs were in high concentrations at the central region of the VEP, which was also indicated by the higher density of canal openings in the same region. This reinforces the theory of a higher rate of biochemical exchange with the nucleus pulposus of the disc from the central region of the VEP.

The ending of these canals were shown to emerge as bud-like, soft tissue structures into the cartilage endplate. Furthermore, this study successfully showed the presence of blood in the VEP layer, within the canal network. Therefore, it can be assumed that the canal network within the VEP layer is host to the capillary network carrying blood close to the disc. However, blood capillaries do not possess the ability to be open-ended or intertwined into bud-like structures. Given the requirement of blood systems to be closed ones, the blood flow in the VEP, especially at the boundary with the soft tissue of the cartilage endplate and the disc remains unclear. Therefore, it is known that nutrients and oxygen reach the disc through the blood vessels which flow within the canal network in the VEP. However, the

mechanism of exchange at the VEP-disc boundary and the architecture of the endings of the blood vessels are still unclear.

Degenerative Conditions of the Endplate

The study in Chapter 5 showed a novel approach for the comparison of the clinical assessments of disc degenerations, from magnetic resonance imaging (MRI) scans, to laboratory characterisation of the human VEP from micro-CT imaging, using samples from patients undergoing elective surgeries.The results identified the VEP as being more likely to be the cause of disc degeneration rather than the effect. Given that it provides nutrients and oxygen and provides mechanical support to the disc, it plays a crucial role in maintaining the healthy state of the disc. Therefore, it is likely that hindered nutritional exchange will lead to degeneration of the disc. The structural properties of the VEP were seen to change with different levels of disc degeneration, assessed by Modic types, Pfirrmann grades and VEP erosion grades. Modic types I and II are the result of inflammation and oedema in the trabecular bone while bony deposition is characteristic of Modic type III. Modic types I and II were characterised by higher porosity and lower BMD than healthy VEPs, while Modic type III was characterised with high BMD and low porosity, and increased thickness. The Pfirrmann grading system, being limited in its assessment of ascending levels of disc degeneration, did not show clear association with the changes seen in the VEP structure. Conversely, advancing VEP erosion grades showed a strong correlation with the size of the openings and the VEP area corroded. Therefore, the degeneration in the VEP structure showed correlation with the clinical assessments of the degeneration in the trabecular bone (Modic changes) and the VEP itself (VEP erosion grades), but not with the state of the disc, which could be due to the efficiency of the grading system or the complexity of the pathological process of disc degeneration.

The findings from this study also showed that the sheep model is not a realistic representation of the human spine. The magnitude of the absolute values were higher than those measured in the human spine, due to the larger size of the sheep spine. It provided a good means for identifying the main trends in terms of the structural properties of the VEPs with respect to their physical location and for optimising the testing protocols.

Overall Implications

The VEP has been underappreciated in its role in the normal functioning of the spine, and in its role in the occurrence of back pain. The results from this work have highlighted the importance of the VEP in maintaining the healthy functioning of the intervertebral disc and

has provided evidence for changes in the structural properties of the VEP in degenerative conditions of the spine. In relation to the aims of this thesis, the findings have successfully:

- characterised the structural properties of the VEP,
- isolated and quantitatively characterised the nutritional canal within the VEP,
- identified the presence of blood in the 3D canal network,
- imaged the endings of the canals out of the bony VEP as bud-like structures
- showed significant changes in some of the structural properties of the VEP in degenerative conditions of the spine, characterised by clinical observations.

Given that the VEP has been shown to provide mechanical support to both the disc and the vertebra, and to provide a nutritional pathway to the disc, it should be given due consideration during diagnosis of back pain. Unfortunately, current diagnostic tools do not identify subtle VEP damage associated with innervation, and consequently the role of VEP damage in the onset of back pain may be underappreciated. Therefore, more research is needed to clarify the role of VEPs in disc degeneration and discogenic pain. Ultimately, the association between clinical observations from back pain patients and scientific investigations of the disc cells, structural and biomechanical properties need to be investigated in greater details.

Furthermore, the VEP has to be considered as part of disc implant design and surgical procedures, such as in the case of interbody spinal fusions, as discussed in Section 2.8. The results from this thesis showed how the structural properties change with spinal level, side of the disc and association with central or peripheral regions of the disc. Therefore, implants for the disc or the VEP have to be tailor-made depending on specific locations where they are meant to be fitted into the spine.

6.2 Future Work

The work from this thesis has highlighted the importance of the VEP in providing mechanical stability and a nutritional pathway to the disc, and identified the role of the VEP in degeneration of the spine. However, it has also highlighted many interesting questions to further clarify the role of the VEP in the spine. Future work should be focused on 3 main goals: correlating the mechanical properties of the VEP with the structure, clarifying the blood flow within the VEP layer and understanding the mechanism for the onset of pathological degeneration of the disc.

6.2.1 Mechanical Properties of the Endplate

Given that the structural properties of the VEPs have been associated with the mechanical loading of the spine, it is important to understand the mechanical strength of the VEPs. Furthermore, a clearer understanding of the mechanical properties of the VEP is essential to ensure the development of new implants have the potential to minimise or avoid subsidence of the implants into the bone, causing further damage. An in-depth knowledge of the hardness, stiffness and Young's modulus would enable clinicians to assess the risk of subsidence related complications post surgerical interventions. It would also improve the identification of the optimal implant placement to avoid areas of low mechanical strength of the VEP [287].

Several studies have investigated the mechanical strength of the VEP, at the microscopic level, for example measuring the modulus of the VEP using nano- and micro-indentations of the microstructures of the bone tissues [68, 288, 289]. However, the findings from these studies do not accurately represent the behaviour of the VEP at the macroscopic level, or how the microstructural properties translate to the likelihood of subsidence of implants into the VEP [287]. Studies including indentation techniques at the microscopic level do not take into consideration the combined effects of VEP thickness, the bone health of the underlying trabecular bone or the presence of bone defects. However, other studies have considered the stiffness of the VEP at the macroscopic level but this property is not directly relatable to implants materials and is dependent on the geometry of the indenter used in the study [288, 290].

The in-situ compression testing stage in the micro-CT scanner offers a useful means of observing changes to the microstructure as a result of pressure in situ and of identifying the nucleation points of cracks and damage before failure of the bone sample. In the case of the VEP, this would enable the correlation of measured mechanical properties at the microscopic levels with observed changes in the bone. It would also provide a representation of the compressive pressure of implants to model the point at which subsidence occurs and the weak areas of cracks nucleation in the VEP.

6.2.2 Blood Flow within the Endplate

A crucial extension of the current study on the nutritional pathway within the VEP layer involves finding evidence of blood vessels in the VEP and imaging the endings of these vessels at the VEP-disc boundary. A few of the techniques that could be used will be discussed briefly below.

Histology

Histological staining would provide a useful way of identifying the presence of blood in the different layers of the endplate: the bony endplate (VEP) and the cartilage endplate. Using the appropriate staining for blood vessels, and a series of incremental histological slides, it would be possible to identify the presence of blood vessels in the different layers of the endplate. Furthermore, if coupled with pre-scanning of the sample in the micro-CT it would be possible to correlate the architecture of the 3D canal network in the VEP layer with the presence of blood vessels from histology to assess whether all the canals are filled with blood vessels or not.

Staining methods could also be used to investigate the presence of lymph vessels in the VEP. Lymph vessels are generally lined by one cell layer. Morphologically, if a red blood cell can be seen within a lumen, then it is very likely to be a capillary and not a lymph vessel. However, if white blood cells can be seen, that is indicative of a lymph vessel. Podoplanin has been used to stain lymphatics. However, podoplanin also stains a small proportion of capillaries and there is no absolute immunohistochemical marker that has the ability to accurately differentiate blood vessels and lymphatics [291, 292]. Therefore, this would be a challenge to find a reproducible way to differentiate the stains for the blood vessels and the lymph vessels.

Photoacoustic Imaging of Blood Flow

The photoacoustic imaging used in Chapter 4 to visualise the blood vessels within the VEP was shown to be useful for showing the presence of haemoglobin but was limited by the cadaveric nature of the VEP samples. In order to visualise the continuous flow within the blood system present in the VEP, especially at the VEP-disc boundary, anti-coagullants, such as heparin or ethylenediaminetetraacetic acid injections could be used [293, 294]. This would ensure the blood does not form clots and therefore a continuous 3D flow of the blood could be visualised. This could also be compared with the canal structure seen from pre-scanning of the VEP in the micro-CT. This would provide an approach to understand the endings of the blood vessels and the blood flow within the VEP layer.

Computational Modelling of Blood Flow

An understanding of the deformation and flow of blood within the canals of the VEP can provide an understanding of how nutrients and oxygen are carried to the disc and waste products removed, giving an insight into the vulnerable areas for the onset of degeneration. Investigations of the macroscopic blood properties consist of rheometric experiments. Com-

putational modelling offers a method to simulate the hemorheology of the VEP, which is the study of the interactions between blood components and the endothelial cells lining the blood vessels. Studies have shown that uncharacteristic hemorheological properties can be strong indicators of inhibited circulation or pathological interference [295].

The canal networks obtained from the analysis of the micro-CT images through the Simpleware software could be turned into a finite element model. This model could then be used in the COMSOL software to create a simulation of the blood flow within the canal network. Simulations are based on restricted domains with only a few vessels from a network of blood circulation. Therefore, an understanding of the nature of the endings of the blood vessels at the VEP-disc boundary is crucial to provide the artificial boundary conditions of the model. Another challenge is to estimate the model parameters of the VEP bone, such as the vessel wall compliance, from measurements or preliminary simulations. The non-Newtonian nature of blood as a fluid, the viscosity and the different components of blood also have to be included into the model. The interaction of patient specific geometry and physiological flows often leads to a complex flow, creating numerical instabilities at the artificial boundaries. Therefore, the model used should be able to handle this complexity, perturbing as least as possible the natural flow. Important information such as the vessel wall shear stress can be computed from the model. The effect of increased pressure on the VEP and clogged pores on the blood flow within the VEP could also be investigated this way, leading to an understanding of the onset of pathological degeneration of the disc.

6.2.3 Pathological Mechanism of Degeneration

The pathology of disc degeneration is still unclear, despite having been extensively investigated. From the results in this study, it has been suggested that various factors are at play in the aetiology, including mechanical loading, compressive forces, shear stress, as well as ageing and genetic factors. However, there is still no clear evidence indicating whether ageing or repetitive injury has a greater influence on degeneration. Mechanical factors can trigger biochemical reactions which can lead to the initiation of biological changes of the normal ageing process. This process can also be accelerated by genetics. Degradation of the structure of the disc as part of the ageing process also makes the disc more susceptible to mechanical injuries. Which factors initiate the degenerative cascade is a question that remains unanswered, but most evidence points to an age-related process influenced primarily by mechanical and genetic factors [296].

Given that the Modic changes, the Pfirrmann grade and the VEP erosion grade can be assessed based on MRI scans, the correlation between these observed degenerative states could provide a clearer picture of the aetiology of degeneration. A clinical based study

could be carried out with a considerably large group of patients with chronic back pain, with long-term follow-up and normalized measurement. The study would only require the MRI scans and would therefore be non-intrusive. It would also enable the inclusion of patients with early stages of chronic back pain, not requiring surgical interventions, which was not available in the present study. The statistical dependence of the different states of degeneration could provide an insight on the aetiology of degenerative conditions. For example, if the presence of advanced endplate erosion grade is seen in patients with early onset of Pfirrmann grade or Modic change, it would imply the VEP is the initiation point of degeneration. Furthermore, the age, genetic factors and other pre-existing medical conditions should be factored into the study to ensure reliability of data.

6.2.4 Summary of Future Avenues of Investigation

Understanding the healthy state of the VEP is crucial to identifying the causes leading to the degenerative states of the VEP. In this study, the structural properties have been characterised in depth. However, there are still many important avenues for further investigation. Investigating the mechanical properties of the VEP would provide further information on how the VEPs are able to fulfil their biophysical functions in relation to providing mechanical support to the intervertebral disc. Furthermore, imaging and quantifying the blood flow in the VEP layer will provide an understanding of the nutritional pathway to the disc and the biochemical exchange of nutrients, oxygen and waste products with the disc. Equipped with the right knowledge of the structure and functions of the VEP, it will be possible to identify the areas prone to damage and therefore the aetiology of degeneration can be clarified. Further investigations of the degenerated VEPs will provide evidence concerning the sites of initiation of degeneration. If it can be shown that the VEP is the initiation point of disc degeneration, for example by identifying the hindered nutritional pathway to the disc as the cause for the disc to degenerate, novel targeted treatments of back pain might be designed. Previously, the VEP has been underappreciated in the literature and clinical assessment of back pain. The work in this thesis highlights the importance of a holistic understanding of the role of the VEP in the normal function of the spine and could lead to the improvement of diagnostic tools to take into account the health of the VEP, as well as the disc and the vertebra.

References

[1] T. Driscoll, G. Jacklyn, J. Orchard, E. Passmore, T. Vos, G. Freedman, S. Lim, and L. Punnett, "The global burden of occupationally related low back pain: estimates from the Global Burden of Disease 2010 study," *Annals of the Rheumatic Diseases*, vol. 73, no. 6, pp. 975–981, 2014.

[2] J. K. Freburger, G. M. Holmes, R. P. Agans, A. M. Jackman, J. D. Darter, A. S. Wallace, L. D. Castel, W. D. Kalsbeek, and T. S. Carey, "The Rising Prevalence of Chronic Low Back Pain," *Archives of Internal Medicine*, vol. 169, no. 3, p. 251, 2009.

[3] J. C. Lotz, A. J. Fields, and E. C. Liebenberg, "The role of the vertebral end plate in low back pain.," *Global spine journal*, vol. 3, no. 3, pp. 153–64, 2013.

[4] J. P. Urban and S. Roberts, "Development and degeneration of the intervertebral discs.," *Molecular medicine today*, vol. 1, no. 7, pp. 329–335, 1995.

[5] D. S. Schultz, A. G. Rodriguez, P. K. Hansma, and J. C. Lotz, "Mechanical profiling of intervertebral discs," *Journal of Biomechanics*, vol. 42, no. 8, pp. 1154–1157, 2009.

[6] J. A. Buckwalter, R. R. Cooper, and J. A. Maynard, "Elastic fibers in human intervertebral discs.," *The Journal of bone and joint surgery. American volume*, vol. 58-A, no. 1, pp. 73–6, 1976.

[7] G. B. Andersson, "Epidemiological features of chronic low-back pain," *Lancet*, vol. 354, no. 9178, pp. 581–585, 1999.

[8] J. Rapoport, P. Jacobs, N. R. Bell, and S. Klarenbach, "Refining the measurement of the economic burden of chronic diseases in Canada," *Chronic Diseases in Canada*, vol. 25, no. 1, pp. 13–21, 2004.

[9] M. A. Adams and P. Dolan, "Spine biomechanics," *Journal of Biomechanics*, vol. 38, p. 5, 2005.

[10] Nikolai Bogduk, "Clinical Anatomy of the Lumbar Spine and Sacrum," in *The effects of brief mindfulness intervention on acute pain experience: An examination of individual difference*, vol. 1, pp. 1689–1699, Churchill Livingstone, 2015.

[11] F. H. Netter, "Atlas of Human Anatomy," in *Muscle Nerve*, p. 612, Elsevier Ltd, 2006.

[12] G. P. Grieve, "Clinical Anatomy of the Lumbar Spine and Sacrum," *Physiotherapy*, vol. 83, no. 9, p. 495, 1997.

[13] U. Zehra, K. Robson-Brown, M. A. Adams, and P. Dolan, "Porosity and Thickness of the Vertebral Endplate Depend on Local Mechanical Loading," *Spine (Phila Pa 1976)*, vol. 40, no. 15, pp. 1173–1180, 2015.

[14] P. P. Raj, "Intervertebral disc : pathophysiology-treatment.," *Pain Practice*, vol. 8, no. 1, pp. 18–44, 2008.

[15] M. A. Adams, B. Derby, and R. Akhtar, "Intervertebral Disc Tissues," in *Mechanical Properties of aging soft tissues*, ch. 2, pp. 268–288, Springer, sixth ed., 2015.

[16] F. Marchand and A. M. Ahmed, "Investigation of the laminate structure of lumbar disc anulus fibrosus.," *Spine*, vol. 15, no. 5, pp. 402–410, 1990.

[17] M. A. Adams and W. C. Hutton, "The effect of posture on the fluid content of lumbar intervertebral discs.," *Spine*, vol. 8, no. 6, pp. 665–671, 1983.

[18] J. Antoniou, T. Steffen, F. Nelson, N. Winterbottom, A. P. Hollander, R. A. Poole, M. Aebi, and M. Alini, "The human lumbar intervertebral disc: Evidence for changes in the biosynthesis and denaturation of the extracellular matrix with growth, maturation, ageing, and degeneration," *Journal of Clinical Investigation*, vol. 98, no. 4, pp. 996–1003, 1996.

[19] V. Mahadevan, "Anatomy of the vertebral column," *Surgery (United Kingdom)*, vol. 36, no. 7, pp. 327–332, 2018.

[20] G. Dar, Y. Masharawi, S. Peleg, N. Steinberg, H. May, B. Medlej, N. Peled, and I. Hershkovitz, "The epiphyseal ring: A long forgotten anatomical structure with significant physiological function," *Spine*, vol. 36, no. 11, pp. 850–856, 2011.

[21] M. Bick and J. W. Copel, "The ring apophysis of the human vertebra; contribution to human osteogeny. II.," *The Journal of bone and joint surgery.*, vol. 33, no. A3, pp. 783–787, 1951.

[22] M. Coventry, R. Ghormley, and J. Kernohan, "The intervertebral disc: its microscopic anatomy and pathology: Part I. Anatomy, Development, and Physiology," *Journal of Bone and Joint Surgery*, vol. 27, no. 1, p. 105, 1945.

[23] M. M. Panjabi, "The stabilizing system of the spine. Part I. Function, dysfunction, adaptation, and enhancement.," *Journal of spinal disorders*, vol. 5, no. 4, pp. 383—-389; discussion 397, 1992.

[24] M. A. Adams and W. C. Hutton, "The effect of posture on the role of the apophysial joints in resisting intervertebral compressive forces.," *The Journal of bone and joint surgery. British volume*, vol. 62B, no. 3, pp. 358–362, 1980.

[25] R. Stevens, "Gray's Anatomy for Students," in *Annals of the Royal College of Surgeons of England*, pp. 513–514, Elsevier Ltd, 2006.

[26] H. Granhed, R. Jonson, and T. Hansson, "Mineral content and strength of lumbar vertebrae. A cadaver study.," *Acta orthopaedica Scandinavica*, vol. 60, no. 1, pp. 105–109, 1989.

[27] P. Brinckmann, M. Biggemann, and D. Hilweg, "Prediction of the compressive strength of human lumbar vertebrae.," *Spine*, vol. 14, no. 6, pp. 606–610, 1989.

[28] W. C. Hutton, B. M. Cyron, and J. R. Stott, "The compressive strength of lumbar vertebrae.," *Journal of anatomy*, vol. 129, no. Pt 4, pp. 753–8, 1979.

[29] M. A. Adams, D. S. McNally, and P. Dolan, "'Stress' distributions inside intervertebral discs. The effects of age and degeneration.," *The Journal of bone and joint surgery. British volume*, vol. 78, no. 6, pp. 965–972, 1996.

[30] J. Nachemson, A., & Morris, "Lumbar Discometry Lumbar Intradiscal Pressure Measurements in Vivo," *The Lancet*, vol. 281, no. 7291, pp. 1140–1142, 1963.

[31] A. Nachemson, "Lumbar mechanics as revealed by lumbar intradiscal pressure measurements," in *The Lumbar Spine and Back pain*, ch. 9, pp. 157–170, Churchill Livingstone, fourth ed., 1992.

[32] P. Lama, U. Zehra, C. Balkovec, H. A. Claireaux, L. Flower, I. J. Harding, P. Dolan, and M. A. Adams, "Significance of cartilage endplate within herniated disc tissue," *European spine journal : official publication of the European Spine Society, the European Spinal Deformity Society, and the European Section of the Cervical Spine Research Society*, vol. 23, no. 9, pp. 1869–1877, 2014.

[33] R. J. Moore, "The vertebral end-plate: what do we know?," *European Spine Journal*, vol. 9, no. 2, pp. 92–96, 2000.

[34] T. Brown, R. J. Hansen, and A. Yorra, "Some mechanical tests on the lumbosacral spine with particular reference to the intervertebral discs; a preliminary report.," *The Journal of bone and joint surgery. American volume*, vol. 39-A, no. 5, pp. 1135–64, 1957.

[35] H. Yang, M. G. Jekir, M. W. Davis, and T. M. Keaveny, "Effective modulus of the human intervertebral disc and its effect on vertebral bone stress," *Journal of Biomechanics*, vol. 49, no. 7, pp. 1134–1140, 2016.

[36] J. Galante, "Tensile Properties of the Human Lumbar Annulus Fibrosus," *Acta orthopaedica Scandinavica*, vol. 38, no. sup100, pp. 1–91, 1967.

[37] J. C. Iatridis, S. Kumar, R. J. Foster, M. Weidenbaum, and V. C. Mow, "Shear mechanical properties of human lumbar annulus fibrosus.," *Journal of Orthopaedic Research*, vol. 17, no. 5, pp. 732–737, 1999.

[38] S. Ebara, J. C. Iatridis, L. a. Setton, R. J. Foster, V. C. Mow, and M. Weidenbaum, "Tensile properties of nondegenerate human lumbar anulus fibrosus.," *Spine*, vol. 21, no. 4, pp. 452–461, 1996.

[39] A. I. Maroudas, "Balance between swelling pressure and collagen tension in normal and degenerate cartilage.," *Nature*, vol. 260, no. 5554, pp. 808–809, 1976.

[40] J. R. Taylor, "Growth of human intervertebral discs and vertebral bodies.," *Journal of anatomy*, vol. 120, no. Pt 1, pp. 49–68, 1975.

[41] E. W. Donisch and W. Trapp, "The cartilage endplates of the human vertebral column (some considerations of postnatal development)," *The Anatomical Record*, vol. 169, no. 4, pp. 705–715, 1971.

[42] A. J. Fields, F. Sahli, A. Rodriguez, and J. Lotz, "Seeing double: a comparison of microstructure, biomechanical function, and adjacent disc health between double- and single-layer vertebral endplates," *Spine (Phila Pa 1976)*, vol. 37, no. 21, pp. E1310–E1317, 2012.

[43] A. Polikeit, S. J. Ferguson, L. P. Nolte, and T. E. Orr, "The importance of the endplate for interbody cages in the lumbar spine," *European Spine Journal*, vol. 12, no. 6, pp. 556–561, 2003.

[44] A. Maroudas, R. A. Stockwell, A. Nachemson, and J. Urban, "Factors involved in the nutrition of the human lumbar intervertebral disc: cellularity and diffusion of glucose in vitro.," *Journal of Anatomy*, vol. 120, no. Pt 1, pp. 113–130, 1975.

[45] R. M. Aspden, D. S. Hickey, and D. W. L. Hukins, "Determination of Collagen Fibril Orientation in the Cartilage of Vertebral End Plate," *Connective Tissue Research*, vol. 9, no. 2, pp. 83–87, 2009.

[46] W. M. Erwin and K. E. Hood, "The cellular and molecular biology of the intervertebral disc: A clinician's primer.," *The Journal of the Canadian Chiropractic Association*, vol. 58, no. 3, pp. 246–57, 2014.

[47] A. J. Fields, F. Sahli, A. G. Rodriguez, and J. C. Lotz, "Seeing double: a comparison of microstructure, biomechanical function, and adjacent disc health between double- and single-layer vertebral endplates.," *Spine*, vol. 37, no. 21, pp. E1310–7, 2012.

[48] K. Wade, P. Robertson, and N. Broom, "On how nucleus-endplate integration is achieved at the fibrillar level in the ovine lumbar disc," *Journal of Anatomy*, vol. 221, no. 1, pp. 39–46, 2012.

[49] P. Trisi and W. Rao, "Bone classification: clinical-histomorphometric comparison," *Clinical Oral Implants Research*, vol. 10, no. 1, pp. 1–7, 1999.

[50] D. W. Dempster, "Histomorphometric Analysis of Bone Remodeling," in *Principles of Bone Biology, Two-Volume Set*, pp. 447–463, Academic Press, 2008.

[51] M. Tosta, A. R. Cortes, L. Corrêa, D. d. S. Pinto, I. Tumenas, and E. Katchburian, "Histologic and histomorphometric evaluation of a synthetic bone substitute for maxillary sinus grafting in humans," *Clinical Oral Implants Research*, 2013.

[52] R. Müller, S. C. Gerber, and W. C. Hayes, "Micro-compression: a novel technique for the nondestructive assessment of local bone failure," *Technology and Health Care*, vol. 6, no. 5, pp. 433–444, 1998.

[53] M. Silva, C. Wang, T. Keaveny, and W. Hayes, "Direct and computed tomography thickness measurements of the human, lumbar vertebral shell and endplate," *Bone*, vol. 15, no. 4, pp. 409–14, 1994.

[54] W. T. Edwards, N. R. Ordway, Y. Zheng, G. McCullen, Z. Han, and H. a. Yuan, "Peak stresses observed in the posterior lateral anulus.," *Spine*, vol. 26, no. 16, pp. 1753–1759, 2001.

[55] S. Roberts, I. W. McCall, J. Menage, M. J. Haddaway, and S. M. Eisenstein, "Does the thickness of the vertebral subchondral bone reflect the composition of the intervertebral disc?," *European Spine Journal*, vol. 6, no. 6, pp. 385–389, 1997.

[56] Y. Hou and Z. Luo, "A study on the structural properties of the lumbar endplate: histological structure, the effect of bone density, and spinal level.," *Spine*, vol. 34, no. 12, pp. E427–33, 2009.

[57] H. J. Wilke, A. Kettler, K. H. Wenger, and L. E. Claes, "Anatomy of the sheep spine and its comparison to the human spine," *Anatomical Record*, vol. 247, no. 4, pp. 542–555, 1997.

[58] S. Roberts, J. Menage, and J. P. G. Urban, "Biochemical and structural properties of the cartilage end-plate and its relation to the intervertebral disc," *Spine*, vol. 14, no. 2, pp. 166–174, 1989.

[59] E. B. Van Der Houwen, P. Baron, A. G. Veldhuizen, J. G. M. Burgerhof, P. M. A. Van Ooijen, and G. J. Verkerke, "Geometry of the intervertebral volume and vertebral endplates of the human spine," *Annals of Biomedical Engineering*, vol. 38, no. 1, pp. 33–40, 2010.

[60] Y. Wang, M. C. Battié, and T. Videman, "A morphological study of lumbar vertebral endplates: radiographic, visual and digital measurements.," *European Spine Journal*, vol. 21, no. 11, pp. 2316–2323, 2012.

[61] M. L. Bouxsein, S. K. Boyd, B. A. Christiansen, R. E. Guldberg, K. J. Jepsen, and R. Müller, "Guidelines for assessment of bone microstructure in rodents using micro-computed tomography," *Journal of Bone and Mineral Research*, vol. 25, no. 7, pp. 1468–1486, 2010.

[62] Y. Wang, M. C. Battié, S. K. Boyd, and T. Videman, "The osseous endplates in lumbar vertebrae: Thickness, bone mineral density and their associations with age and disk degeneration," *Bone*, vol. 48, no. 4, pp. 804–809, 2011.

[63] H. E. Gruber, N. Ashraf, J. Kilburn, C. Williams, H. J. Norton, B. E. Gordon, and E. N. Hanley, "Vertebral endplate architecture and vascularization: application of micro-computerized tomography, a vascular tracer, and immunocytochemistry in analyses of disc degeneration in the aging sand rat.," *Spine*, vol. 30, no. 23, pp. 2593–2600, 2005.

[64] H. E. Gruber, B. Gordon, C. Williams, H. J. Norton, and E. N. Hanley, "Bone mineral density of lumbar vertebral end plates in the aging male sand rat spine," *Spine*, vol. 28, no. 16, pp. 1766–1772, 2003.

[65] H. E. Gruber, B. Gordon, C. Williams, H. J. Norton, and E. N. Hanley, "Vertebral endplate and disc changes in the aging sand rat lumbar spine: Cross-sectional analyses of a large male and female population," *Spine*, vol. 32, no. 23, pp. 2529–2536, 2007.

[66] M. D. Antonacci, D. S. Hanson, and M. H. Heggeness, "Pitfalls in the measurement of bone mineral density by dual energy x-ray absorptiometry.," *Spine (Phila Pa 1976)*, vol. 21, no. 1, pp. 87–91, 1996.

[67] M. Ito, K. Hayashi, M. Yamada, M. Uetani, and T. Nakamura, "Relationship of osteophytes to bone mineral density and spinal fracture in men," *Radiology*, vol. 189, no. 2, pp. 497–502, 1993.

[68] J. P. Grant, T. Oxland, and M. Dvorak, "Mapping the structural properties of the lumbosacral vertebral endplate," *Spine*, vol. 26, no. 8, pp. 889–896, 2001.

[69] S. A. Rodrigues, K. R. Wade, A. Thambyah, and N. D. Broom, "Micromechanics of annulus-end plate integration in the intervertebral disc," *Spine Journal*, vol. 12, no. 2, pp. 143–150, 2012.

[70] G. M. Campbell and A. Sophocleous, "Quantitative analysis of bone and soft tissue by micro-computed tomography: applications to ex vivo and in vivo studies," *Bonekey reports*, vol. 3, p. 564, 2014.

[71] L. T. Hall, S. I. Esses, P. C. Noble, and E. Kamaric, "Morphology of the lumbar vertebral endplates.," *Spine*, vol. 23, no. 14, pp. 1517–22; discussion 1522–3, 1997.

[72] S. Zhou, I. McCarthy, A. McGregor, R. Coombs, and S. Hughes, "Geometrical dimensions of the lower lumbar vertebrae—analysis of data from digitised CT images," *Eur Spine J.*, vol. 9, no. 3, pp. 242–248, 2000.

[73] D. W. Holdsworth and M. M. Thornton, "Micro-CT in small animal and specimen imaging," *Trends in Biotechnology*, vol. 20, no. 8, pp. S34–S39, 2002.

[74] S. R. Buchman, D. G. Sherick, R. W. Goulet, and S. a. Goldstein, "Use of microcomputed tomography scanning as a new technique for the evaluation of membranous bone.," *The Journal of craniofacial surgery*, vol. 9, no. 1, pp. 48–54, 1998.

[75] P. A. Hulme, S. J. Ferguson, and S. K. Boyd, "Determination of vertebral endplate deformation under load using micro-computed tomography," *Journal of Biomechanics*, vol. 41, no. 1, pp. 78–85, 2008.

[76] A. G. Rodriguez, A. E. Rodriguez-Soto, A. J. Burghardt, S. Berven, S. Majumdar, and J. C. Lotz, "Morphology of the human vertebral endplate," *Journal of Orthopaedic Research*, vol. 30, no. 2, pp. 280–287, 2012.

[77] C. W. Pfirrmann, A. Metzdorf, M. Zanetti, J. Hodler, and N. Boos, "Magnetic resonance classification of lumbar intervertebral disc degeneration," *Spine*, vol. 26, no. 17, pp. 1873–1878, 2001.

[78] J. M. Laffosse, T. Odent, F. Accadbled, T. Cachon, C. Kinkpe, E. Viguier, J. S. De Gauzy, and P. Swider, "Micro-computed tomography evaluation of vertebral endplate trabecular bone changes in a porcine asymmetric vertebral tether," *Journal of Orthopaedic Research*, vol. 28, no. 2, pp. 232–240, 2010.

[79] C. H. Turner and D. B. Burr, "Basic biomechanical measurements of bone: A tutorial," *Bone*, vol. 14, no. 4, pp. 595–608, 1993.

[80] M. Hahn, M. Vogel, M. Pompesius-Kempa, and G. Delling, "Trabecular bone pattern factor-a new parameter for simple quantification of bone microarchitecture," *Bone*, vol. 13, no. 4, pp. 327–330, 1992.

[81] A. Odgaard, "Three-dimensional methods for quantification of cancellous bone architecture," *Bone*, vol. 20, no. 4, pp. 315–328, 1997.

[82] A. Parfitt, "Age-related structural changes in trabecular and cortical bone: cellular mechanisms and biomechanical consequences.," *Calcified tissue international*, vol. 36, no. 1, pp. S123–S128, 1984.

[83] L. Mosekilde, A. Viidik, and L. Mosekilde, "Correlation between the compressive strength of iliac and vertebral trabecular bone in normal individuals," *Bone*, vol. 6, no. 5, pp. 291–295, 1985.

[84] L. Mosekilde, "Sex differences in age-related loss of vertebral trabecular bone mass and structure-biomechanical consequences," *Bone*, vol. 10, no. 6, pp. 425–432, 1989.

[85] L. Mosekilde, C. C. Danielsen, and U. B. Knudsen, "The effect of aging and ovariectomy on the vertebral bone mass and biomechanical properties of mature rats," *Bone*, vol. 14, no. 1, pp. 1–6, 1993.

[86] A. Boyde and S. J. Jones, "Scanning electron microscopy of bone: Instrument, specimen, and issues," *Microscopy Research and Technique*, vol. 33, no. 2, pp. 92–120, 1996.

[87] C. Whitehouse, WJ, Dyson, ED, Jackson, "The scanning electron microscope in studies of trabecular bone from a human vertebral body," *Journal of Anatomy*, vol. 108, no. 3, pp. 481–496, 1971.

[88] Y. S. Nosikova, J. P. Santerre, M. Grynpas, G. Gibson, and R. A. Kandel, "Characterization of the annulus fibrosus-vertebral body interface: Identification of new structural features," *Journal of Anatomy*, vol. 221, no. 6, pp. 577–589, 2012.

[89] M. Hayat, "Principles and techniques of electron microscopy: biological applications (Chapter 9: Plant Tissues)," in *Toxicologic Pathology*, p. 543, Cambridge University Press, 2000.

[90] W. J. Howat and B. A. Wilson, "Tissue fixation and the effect of molecular fixatives on downstream staining procedures," *Methods*, vol. 70, no. 1, pp. 12–19, 2014.

[91] b. Q. Huang and E. C. Yeung, "Chemical and physical fixation of cells and tissue: an overview," in *Plant Microtechniques and Protocols*, pp. 23–32, Springer, 2015.

[92] S. Davies and A. Forge, "Preparation of the mammalian organ of Corti for scanning electron microscopy," *Journal of Microscopy*, vol. 147, no. 1, pp. 89–101, 1987.

[93] T. W. Gilbert, T. L. Sellaro, and S. F. Badylak, "Decellularization of tissues and organs," *Biomaterials*, vol. 27, no. 19, pp. 3675–3683, 2006.

[94] D. W. Jackson, E. S. Grood, S. P. Arnoczky, D. L. Butler, and T. M. Simon, "Cruciate reconstruction using freeze dried anterior cruciate ligament allograft and a ligament augmentation device (LAD). An experimental study in a goat model.," *The American journal of sports medicine*, vol. 15, no. 6, pp. 528–538, 1987.

[95] P. Lin, W. C. Chan, S. F. Badylak, and S. N. Bhatia, "Assessing Porcine Liver-Derived Biomatrix for Hepatic Tissue Engineering," *Tissue Engineering*, vol. 10, no. 7-8, pp. 1046–1053, 2004.

[96] K. Schenke-Layland, O. Vasilevski, F. Opitz, K. König, I. Riemann, K. J. Halbhuber, T. Wahlers, and U. A. Stock, "Impact of decellularization of xenogeneic tissue on extracellular matrix integrity for tissue engineering of heart valves," *Journal of Structural Biology*, vol. 143, no. 3, pp. 201–208, 2003.

[97] G. Falke, J. J. Yoo, T. G. Kwon, R. Moreland, and A. Atala, "Formation of Corporal Tissue Architecture in Vivo Using Human Cavernosal Muscle and Endothelial Cells Seeded on Collagen Matrices," *Tissue Engineering*, vol. 9, no. 5, pp. 871–879, 2003.

[98] J. S. Cartmell and M. G. Dunn, "Effect of chemical treatments on tendon cellularity and mechanical properties," *Journal of Biomedical Materials Research*, vol. 49, no. 1, pp. 134–140, 2000.

[99] E. Rieder, G. Seebacher, M. T. Kasimir, E. Eichmair, B. Winter, B. Dekan, E. Wolner, P. Simon, and G. Weigel, "Tissue engineering of heart valves: Decellularized porcine and human valve scaffolds differ importantly in residual potential to attract monocytic cells," *Circulation*, vol. 111, no. 21, pp. 2792–2797, 2005.

[100] P. G. Gamba, M. T. Conconi, R. Lo Piccolo, G. Zara, R. Spinazzi, and P. P. Parnigotto, "Experimental abdominal wall defect repaired with acellular matrix," *Pediatric Surgery International*, vol. 18, no. 5-6, pp. 327–331, 2002.

[101] P. S. McFetridge, J. W. Daniel, T. Bodamyali, M. Horrocks, and J. B. Chaudhuri, "Preparation of porcine carotid arteries for vascular tissue engineering applications.," *Journal of biomedical materials research. Part A*, vol. 70, no. 2, pp. 224–234, 2004.

[102] S. L. M. Dahl, J. Koh, V. Prabhakar, and L. E. Niklason, "Decellularized native and engineered arterial scaffolds for transplantation," *Cell Transplantation*, vol. 12, no. 6, pp. 659–666, 2003.

[103] J. Hu, S. Ni, Y. Cao, X. Wang, S. Liao, and H. Lu, "Comparison of Synchrotron Radiation-based Propagation Phase Contrast Imaging and Conventional Micro-computed Tomography for Assessing Intervertebral Discs and Endplates in a Murine Model," *Spine*, vol. 42, no. 15, pp. E883–E889, 2017.

[104] Y. Cao, S. Liao, H. Zeng, S. Ni, F. Tintani, Y. Hao, L. Wang, T. Wu, H. Lu, C. Duan, and J. Hu, "3D characterization of morphological changes in the intervertebral disc and endplate during aging: A propagation phase contrast synchrotron micro-tomography study," *Scientific Reports Nature Research*, vol. 7, p. 43094, mar 2017.

[105] M. Alini, S. M. Eisenstein, K. Ito, C. Little, A. A. Kettler, K. Masuda, J. Melrose, J. Ralphs, I. Stokes, and H. J. Wilke, "Are animal models useful for studying human disc disorders/degeneration?," *European Spine Journal*, vol. 17, no. 1, pp. 2–19, 2008.

[106] B. M. Boszczyk, A. A. Boszczyk, and R. Putz, "Comparative and functional anatomy of the mammalian lumbar spine," *Anatomical Record*, vol. 264, no. 2, pp. 157–168, 2001.

[107] J. C. Lotz, "Animal models of intervertebral disc degeneration: Lessons learned," *Spine*, vol. 29, no. 23, pp. 2742–2750, 2004.

[108] Y. Zhang, B. a. Lenart, J. K. Lee, D. Chen, P. Shi, J. Ren, C. Muehleman, D. Chen, and H. S. An, "Histological Features of Endplates of the Mammalian Spine: From Mice to Men," *Spine*, vol. 39, no. 5, pp. E312–7, 2014.

[109] A. Nachemson, T. Lewin, A. Maroudas, and M. Freeman, "In Vitro Diffusion of DYE Through the End-Plates and the Annulus Fibrosus of Human Lumbar Inter-Vertebral Discs," *Acta orthopaedica Scandinavica*, vol. 41, no. 6, pp. 589–607, 1970.

[110] M. Mageed, D. Berner, H. Jülke, C. Hohaus, W. Brehm, and K. Gerlach, "Is sheep lumbar spine a suitable alternative model for human spinal researches? Morphometrical comparison study," *Laboratory Animal Research*, vol. 29, no. 4, pp. 183–189, 2013.

[111] E. Newman, A. S. Turner, and J. D. Wark, "The potential of sheep for the study of osteopenia: Current status and comparison with other animal models," *Bone*, vol. 16, no. 4, pp. 277S–284S, 1995.

[112] A. S. Turner, "Experiences with sheep as an animal model for shoulder surgery: Strengths and shortcomings," *Journal of Shoulder and Elbow Surgery*, vol. 16, no. 5, pp. S158–S163, 2007.

[113] M. Egermann, J. Goldhahn, and E. Schneider, "Animal models for fracture treatment in osteoporosis," *Osteoporosis International*, vol. 16, no. 2, pp. S129–S138, 2005.

[114] T. H. Smit, "The use of a quadruped as an in vivo model for the study of the spine - Biomechanical considerations," *European Spine Journal*, vol. 11, no. 2, pp. 137–144, 2002.

[115] C. Daly, P. Ghosh, G. Jenkin, D. Oehme, and T. Goldschlager, "A Review of Animal Models of Intervertebral Disc Degeneration: Pathophysiology, Regeneration, and Translation to the Clinic," *BioMed Research International*, p. 5952165, 2016.

[116] S. Holm, a. Maroudas, J. P. Urban, G. Selstam, and a. Nachemson, "Nutrition of the intervertebral disc: solute transport and metabolism.," *Connective Tissue Research*, vol. 8, no. 2, pp. 101–119, 1981.

[117] D. Eyre, B. Caterson, and P. Benya, "The intervertebral disc," in *New Perspectives on Low back pain* (S. Gordon and J. Frymoyer, eds.), pp. 147–209, American Institute of Orthopaedic Surgeons, 1991.

[118] H. Brodin, "Paths of nutrition in articular cartilage and intervertebral discss," *Acta orthopaedica Scandinavica*, vol. 24, no. 1-4, pp. 177–183, 1955.

[119] H. Ohshima, H. Tsuji, and N. Hirano, "Water diffusion pathway, swelling presure and biomechanical properties of the intervertebral disc during com- pression loading," *Spine*, vol. 14, no. 11, pp. 1234–1244, 1991.

[120] M. Adams and W. Hutton, "The effect of posture on diffusion into lumbar intervertebral discs.," *Journal of anatomy*, vol. 147, pp. 121–34, 1986.

[121] W. Drescher, H. Li, D. Qvesel, S. D. Jensen, C. Flo, E. S. Hansen, and C. Bünger, "Vertebral blood flow and bone mineral density during long-term corticosteroid treatment: An experimental study in immature pigs.," *Spine*, vol. 25, no. 23, pp. 3021–3025, 2000.

[122] K. Ogata and L. Whiteside, "Nutrition pathways in the intervertebral disc: an experimental study using hydrogen wash-out technique," *Spine*, vol. 6, no. 3, pp. 211–216, 1981.

[123] H. V. Crock and M. Goldwasser, "Anatomic studies of the circulation in the region of the vertebral end-plate in adult Greyhound dogs.," *Spine*, vol. 9, no. 7, pp. 702–706, 1984.

[124] M. Rudert and B. Tillmann, "Detection of lymph and blood vessels in the human intervertebral disc by histochemical and immunohistochemical methods," *Annals of Anatomy*, vol. 175, no. 3, pp. 237–242, 1993.

[125] H. Crock and H. Yoshizawa, "The blood supply of the lumbar vertebral column," *Clinical orthopaedics and related research*, vol. 115, pp. 6–21, 1976.

[126] J. P. Urban, S. Holm, A. Maroudas, and A. Nachemson, "Nutrition of the intervertebral disk. An in vivo study of solute transport.," *Clinical orthopaedics and related research*, no. 129, pp. 101–114, 1977.

[127] J. P. G. Urban, S. Holm, and A. I. Maroudas, "Diffusion of small solutes into the intervertebral disc. An in vivo study.," *Biorheology*, vol. 15, no. 3-4, pp. 203–221, 1978.

[128] S. Roberts, J. P. G. Urban, and H. Evans, "Transport properties of the human cartilage endplate in relation to its composition and calcification," *Spine*, vol. 21, no. 4, pp. 415–420, 1996.

[129] S. Bernick and R. Cailliet, "Vertebral end-plate changes with aging of human vertebrae.," *Spine*, vol. 7, no. 2, pp. 97–102, 1982.

[130] J. Oda, H. Tanaka, and N. Tsuziki, "Intervertebral Disc Changes with Aging of Human Cervical Vertebra: From the Neonate to the Eighties," *Spine*, vol. 13, no. 11, pp. 1205–1211, 1988.

[131] T. Yamaguchi, S. Goto, Y. Nishigaki, A. A. E. Orías, W. C. Bae, K. Masuda, and N. Inoue, "Microstructural analysis of three-dimensional canal network in the rabbit lumbar vertebral endplate," *Journal of Orthopaedic Research*, vol. 33, no. 2, pp. 270–276, 2015.

[132] D. M. Cooper, A. L. Turinsky, C. W. Sensen, and B. Hallgrímsson, "Quantitative 3D analysis of the canal network in cortical bone by micro-computed tomography," *Anatomical Record - Part B New Anatomist*, vol. 274, no. 1, pp. 169–179, 2003.

[133] S. K. Mirza and A. A. White, "Anatomy of intervertebral disc and pathophysiology of herniated disc disease," *Journal of Clinical Laser Medicine and Surgery*, vol. 13, no. 3, pp. 131–142, 1995.

[134] M. Bendtsen, C. Bunger, P. Colombier, C. Le Visage, S. Roberts, D. Sakai, and J. P. Urban, "Biological challenges for regeneration of the degenerated disc using cellular therapies," *Acta Orthopaedica*, vol. 87, no. 363, pp. 39–46, 2016.

[135] F. Paneni, "The ESC Textbook of Vascular Biology," *European heart journal*, vol. 38, pp. 2868–2870, 2017.

[136] H. V. Crock, H. Yoshizawa, and S. K. Kame, "Observations on the venous drainage of the human vertebral body," *Journal of Bone and Joint Surgery - Series B*, vol. 55, no. 3, pp. 528–533, 1973.

[137] S. Oki, Y. Matsuda, T. Itoh, T. Shibata, H. Okumura, and J. Desaki, "Scanning electron microscopic observations of the vascular structure of vertebral end-plates in rabbits," *Journal of Orthopaedic Research*, vol. 12, no. 3, pp. 447–449, 1994.

[138] R. P. Kumar, F. Albregtsen, M. Reimers, B. Edwin, T. Langø, and O. J. Elle, "Three-Dimensional Blood Vessel Segmentation and Centerline Extraction based on Two-Dimensional Cross-Section Analysis," *Annals of Biomedical Engineering*, vol. 43, no. 5, pp. 1223–1234, 2015.

[139] D. Fleischmann, T. J. Hastie, F. C. Dannegger, D. S. Paik, M. Tillich, C. K. Zarins, and G. D. Rubin, "Quantitative determination of age-related geometric changes in the normal abdominal aorta," *Journal of Vascular Surgery*, vol. 33, no. 1, pp. 97–105, 2001.

[140] F. Rengier, T. F. Weber, F. L. Giesel, D. Böckler, H. U. Kauczor, and H. Von Tengg-Kobligk, "Centerline analysis of aortic CT angiographic examinations: Benefits and limitations," *American Journal of Roentgenology*, vol. 192, no. 5, pp. W255–W263, 2009.

[141] J. W. Breslin, Y. Yang, J. P. Scallan, R. S. Sweat, S. P. Adderley, and W. L. Murfee, "Lymphatic vessel network structure and physiology," *Comprehensive Physiology*, vol. 9, no. 1, pp. 207–299, 2018.

[142] M. Rudert and B. Tillmann, "Lymph and blood supply of the human intervertebral disc: Cadaver study of correlations to discitis," *Acta orthopaedica Scandinavica*, vol. 64, no. 1, pp. 37–40, 1993.

[143] T. G. Kashima, A. Dongre, and N. A. Athanasou, "Lymphatic involvement in vertebral and disc pathology," *Spine (Phila Pa 1976)*, vol. 36, no. 11, pp. 899–904, 2011.

[144] M. M. Katz, A. R. Hargens, and S. R. Garfin, "Intervertebral disc nutrition. Diffusion versus convection," *Clinical Orthopaedics and Related Research*, vol. 210, pp. 243–245, 1986.

[145] E. M. Bartels, J. C. Fairbank, C. P. Winlove, and J. P. Urban, "Oxygen and lactate concentrations measured in vivo in the intervertebral discs of patients with scoliosis and back pain," *Spine*, vol. 23, no. 1, pp. 1–7, 1998.

[146] M. R. Urban, J. C. Fairbank, P. J. Etherington, L. Loh, C. P. Winlove, and J. P. Urban, "Electrochemical measurement of transport into scoliotic intervertebral discs in vivo using nitrous oxide as a tracer," *Spine*, vol. 26, no. 8, pp. 984–990, 2001.

[147] S. J. Ferguson, K. Ito, and L. P. Nolte, "Fluid flow and convective transport of solutes within the intervertebral disc," *Journal of Biomechanics*, vol. 37, no. 2, pp. 213–221, 2004.

[148] J. P. Urban and J. F. McMullin, "Swelling pressure of the lumbar intervertebral discs: Influence of age, spinal level, composition, and degeneration," *Spine*, vol. 13, no. 2, pp. 179–187, 1988.

[149] D. S. McNally and M. A. Adams, "Internal intervertebral disc mechanics as revealed by stress profilometry," *Spine*, vol. 17, no. 1, pp. 66–73, 1992.

[150] H. J. Wilke, P. Neef, M. Caimi, T. Hoogland, and L. E. Claes, "New in vivo measurements of pressures in the intervertebral disc in daily life," *Spine*, vol. 24, no. 8, pp. 755–762, 1999.

[151] D. C. Ayotte, K. Ito, and S. Tepic, "Direction-dependent resistance to flow in the endplate of the intervertebral disc: An ex vivo study," *Journal of Orthopaedic Research*, vol. 19, no. 6, pp. 1073–1077, 2001.

[152] N. Arjmand, A. Plamondon, A. Shirazi-Adl, M. Parnianpour, and C. Larivière, "Predictive equations for lumbar spine loads in load-dependent asymmetric one- and two-handed lifting activities," *Clinical Biomechanics*, vol. 27, no. 6, pp. 537–544, 2012.

[153] T. Oxland, J. Grant, and C. Fisher, "Effects of endplate removal on the structural properties of the lower lumbar vertebral bodies," *Spine (Phila Pa 1976)*, vol. 28, no. 8, pp. 771–7, 2003.

[154] P. Brinckmann, W. Frobin, E. Hierholzer, and M. Horst, "Deformation of the vertebral end-plate under axial loading of the spine.," *Spine*, vol. 8, no. 8, pp. 851–856, 1983.

[155] A. J. van der Veen, M. G. Mullender, I. Kingma, J. H. Van, and T. H. Smit, "Contribution of vertebral bodies, endplates, and intervertebral discs to the compression creep of spinal motion segments," *Journal of Biomechanics*, vol. 41, no. 6, pp. 1260–1268, 2008.

[156] P. Brinckmann, N. Johannleweling, D. Hilweg, and M. Biggemann, "Fatigue fracture of human lumbar vertebrae," *Clinical Biomechanics*, vol. 2, no. 2, pp. 94–96, 1987.

[157] A. Holmes, D. W. L. Hukins, and A. Freemont, "End-Plate Displacement During Compression of Lumbar Vertebra-Disc-Vertebra Segments and the Mechanism of Failure," *Spine*, vol. 18, no. 1, pp. 128–135, 1993.

[158] P. B. Bishop and R. H. Pearce, "The proteoglycans of the cartilaginous end???plate of the human intervertebral disc change after maturity," *Journal of Orthopaedic Research*, vol. 11, no. 3, pp. 324–331, 1993.

[159] T. Aigner, K. R. Gresk-otter, J. C. Fairbank, K. von der Mark, and J. P. Urban, "Variation with age in the pattern of type X collagen expression in normal and scoliotic human intervertebral discs," *Calcif Tissue Int*, vol. 63, no. 3, pp. 263–268, 1998.

[160] M. Wong, M. Siegrist, and K. Goodwin, "Cyclic tensile strain and cyclic hydrostatic pressure differentially regulate expression of hypertrophic markers in primary chondrocytes," *Bone*, vol. 33, no. 4, pp. 685–693, 2003.

[161] F. D. Zhao, P. Pollintine, B. D. Hole, M. A. Adams, and P. Dolan, "Vertebral fractures usually affect the cranial endplate because it is thinner and supported by less-dense trabecular bone," *Bone*, vol. 44, no. 2, pp. 372–379, 2009.

[162] N. Yoganandan, D. J. Maiman, F. Pintar, G. Ray, J. B. Myklebust, A. Sances, and S. J. Larson, "Microtrauma in the lumbar spine: A cause of low back pain," *Neurosurgery*, vol. 23, no. 2, pp. 162–168, 1988.

[163] B. Vernon-Roberts and C. J. Pirie, "Healing trabecular microfractures in the bodies of lumbar vertebrae.," *Annals of the rheumatic diseases*, vol. 32, no. 5, pp. 406–12, 1973.

[164] A. G. Rodriguez, C. K. Slichter, F. L. Acosta, A. E. Rodriguez-Soto, A. J. Burghardt, S. Majumdar, and J. C. Lotz, "Human disc nucleus properties and vertebral endplate permeability.," *Spine*, vol. 36, no. 7, pp. 512–20, 2011.

[165] T. S. Keller, I. Ziv, E. Moeljanto, and D. M. Spengler, "Interdependence of lumbar disc and subdiscal bone properties: a report of the normal and degenerated spine.," *Journal of Spinal Disorders*, vol. 6, no. 2, pp. 106–113, 1993.

[166] J. Aoki, I. Yamamoto, N. Kitamura, T. Sone, H. Itoh, K. Torizuka, and K. Takasu, "End plate of the discovertebral joint: degenerative change in the elderly adult.," *Radiology*, vol. 164, no. 2, pp. 411–4, 1987.

[167] K. M. C. Cheung, J. Karppinen, D. Chan, D. W. H. Ho, Y.-Q. Song, P. Sham, K. S. E. Cheah, J. C. Y. Leong, and K. D. K. Luk, "Prevalence and pattern of lumbar magnetic resonance imaging changes in a population study of one thousand forty-three individuals.," *Spine*, vol. 34, no. 9, pp. 934–40, 2009.

[168] M. A. Adams and P. J. Roughley, "What is Intervertebral Disc Degeneration, and What Causes It?," *Spine*, vol. 31, no. 18, pp. 2151–2161, 2006.

[169] M. C. Battié, T. Videman, and E. Parent, "Lumbar Disc Degeneration Epidemiology and Genetic Influences," *Spine*, vol. 29, no. 23, pp. 2679–2690, 2004.

[170] S. M. F. Pluijm, H. W. van Essen, N. Bravenboer, A. G. Uitterlinden, J. H. Smit, H. A. P. Pols, and P. Lips, "Collagen type I alpha1 Sp1 polymorphism, osteoporosis, and intervertebral disc degeneration in older men and women.," *Annals of the rheumatic diseases*, vol. 63, no. 1, pp. 71–77, 2004.

[171] S. D. Boden, K. D. Riew, K. Yamaguchi, T. P. Branch, D. Schellinger, and S. W. Wiesel, "Orientation of the lumbar facet joints: association with degenerative disc disease.," *The Journal of bone and joint surgery. American volume*, vol. 78, no. 3, pp. 403–411, 1996.

[172] M. H. Coppes, E. Marani, R. T. Thomeer, and G. J. Groen, "Innervation of 'painful' lumbar discs," *Spine*, vol. 22, no. 20, pp. 2349–2350, 1997.

[173] B. Peng, J. Hao, S. Hou, W. Wu, D. Jiang, X. Fu, and Y. Yang, "Possible pathogenesis of painful intervertebral disc degeneration," *Spine*, vol. 31, no. 5, pp. 560–566, 2006.

[174] A. Fagan, R. Moore, B. Vernon Roberts, P. Blumbergs, and R. Fraser, "ISSLS prize winner: The innervation of the intervertebral disc: a quantitative analysis.," *Spine*, vol. 28, no. 23, pp. 2570–2576, 2003.

[175] H. Crock, "Internal disc disruption. A challenge to disc prolapse fifty years on.," *Spine (Phila Pa 1976)*, vol. 11, no. 6, pp. 650–653, 1986.

[176] M. F. Brown, M. V. Hukkanen, I. D. McCarthy, D. R. Redfern, J. J. Batten, H. V. Crock, S. P. Hughes, and J. M. Polak, "Sensory and sympathetic innervation of the vertebral endplate in patients with degenerative disc disease," *Journal of Bone & Joint Surgery, British Volume*, vol. 79, no. 1, pp. 147–153, 1997.

[177] S. Ohtori, G. Inoue, T. Ito, T. Koshi, T. Ozawa, H. Doya, T. Saito, H. Moriya, and K. Takahashi, "Tumor necrosis factor-immunoreactive cells and PGP 9.5-immunoreactive nerve fibers in vertebral endplates of patients with discogenic low back pain and modic type 1 or type 2 changes on MRI," *Spine*, vol. 31, no. 9, pp. 1026–1031, 2006.

[178] S. Rajasekaran, J. N. Babu, R. Arun, B. R. W. Armstrong, A. P. Shetty, and S. Murugan, "ISSLS prize winner: A study of diffusion in human lumbar discs: A serial magnetic resonance imaging study documenting the influence of the endplate on diffusion in normal and degenerate discs," *Spine*, vol. 29, no. 23, pp. 2654–2667, 2004.

[179] J. Niinimäki, A. Korkiakoski, O. Parviainen, M. Haapea, M. Kuisma, R. O. Ojala, J. Karppinen, R. Korpelainen, O. Tervonen, and M. T. Nieminen, "Association of lumbar artery narrowing, degenerative changes in disc and endplate and apparent diffusion in disc on postcontrast enhancement of lumbar intervertebral disc," *Magnetic Resonance Materials in Physics, Biology and Medicine*, vol. 22, no. 2, pp. 101–109, 2009.

[180] M. E. Katz, S. L. Teitelbaum, L. A. Gilula, D. Resnick, and S. J. Katz, "Radiologic and pathologic patterns of end-plate–based vertebral sclerosis," *Investigative Radiology*, vol. 23, no. 6, pp. 447–454, 1988.

[181] A. Stäbler, M. Bellan, C. Gärtner, J. Brossmann, and M. F. Reiser, "MR imaging of enhancing intraosseous disk herniation (Schmorl's nodes)," *American Journal of Roentgenology*, vol. 168, no. 4, pp. 933–938, 1997.

[182] L. Benneker and P. Heini, "Correlation of radiographic and MRI parameters to morphological and biochemical assessment of intervertebral disc degeneration.," *Eur Spine J.*, vol. 14, no. 1, pp. 27–35, 2005.

[183] F. P. Mok, D. Samartzis, J. Karppinen, K. D. Luk, D. Y. Fong, and K. M. Cheung, "ISSLS prize winner: Prevalence, determinants, and association of schmorl nodes of the lumbar spine with disc degeneration: A population-based study of 2449 individuals," *Spine*, vol. 35, no. 21, pp. 1944–1952, 2010.

[184] K. Singer, S. Edmondston, R. Day, P. Breidahl, and R. Price, "Prediction of thoracic and lumbar vertebral body compressive strength: correlations with bone mineral density and vertebral region," *Bone*, vol. 17, no. 2, pp. 167–174, 1995.

[185] T. H. Hansson, T. S. Keller, and D. M. Spengler, "Mechanical behavior of the human lumbar spine. II. Fatigue strength during dynamic compressive loading," *Journal of Orthopaedic Research*, vol. 5, no. 4, pp. 479–487, 1987.

[186] Y. Wang, T. Videman, and M. Battie, "ISSLS Prize Winner: Lumbar vertebral endplate lesions: associations with disc degeneration and back pain history," *Spine*, vol. 37, no. 17, pp. 1490–96, 2012.

[187] R. C. Hilton and J. Ball, "Vertebral rim lesions in the dorsolumbar spine," *Annals of the Rheumatic Diseases*, vol. 43, no. 2, pp. 302–307, 1984.

[188] B. Vernon-Roberts, "Pathology of intervertebral discs and apophyseal joints," in *The Lumbar Spine and Back pain*, pp. 37–55, Churchill-Livingstone, London, 1987.

[189] B. Grignon, Y. Grignon, D. Mainard, M. Braun, P. Netter, and J. Roland, "The structure of the cartilaginous end-plates in elder people," *Surgical and Radiologic Anatomy*, vol. 22, no. 1, pp. 13–9, 2000.

[190] M. T. Modic, P. M. Steinberg, J. S. Ross, T. J. Masaryk, and J. R. Carter, "Degenerative disk disease: assessment of changes in vertebral body marrow with MR imaging.," *Radiology*, vol. 166, no. 1, pp. 193–199, 1988.

[191] R. Rahme and R. Moussa, "The modic vertebral endplate and marrow changes: Pathologic significance and relation to low back pain and segmental instability of the lumbar spine," *American Journal of Neuroradiology*, vol. 29, no. 5, pp. 838–842, 2008.

[192] R. M. Kanna, R. Shanmuganathan, V. R. Rajagopalan, S. Natesan, R. Muthuraja, K. M. C. Cheung, D. Chan, P. Y. P. Kao, A. Yee, and A. P. Shetty, "Prevalence, patterns, and genetic association analysis of modic vertebral endplate changes," *Asian Spine Journal*, vol. 11, no. 4, pp. 594–600, 2017.

[193] T. S. Jensen, T. Bendix, J. S. Sorensen, C. Manniche, L. Korsholm, and P. Kjaer, "Characteristics and natural course of vertebral endplate signal (Modic) changes in the Danish general population," *BMC Musculoskeletal Disorders*, vol. 10, no. 1, p. 81, 2009.

[194] J. Lotz, V. Haughton, and S. Boden, "New treatments and imaging strategies in degenerative disease of the intervertebral disks," *Radiology*, vol. 264, no. 1, pp. 6–19, 2012.

[195] J. Stergar, L. Gradisnik, T. Velnar, and U. Maver, "Intervertebral disc tissue engineering: A brief review," *Bosnian Journal of Basic Medical Sciences*, vol. 19, no. 2, pp. 130–137, 2019.

[196] T. Steffen, a. Tsantrizos, and M. Aebi, "Effect of implant design and endplate preparation on the compressive strength of interbody fusion constructs.," *Spine*, vol. 25, no. 9, pp. 1077–1084, 2000.

[197] M. Zindrick and D. Selby, "Lumbar spinal fusion: different types and indications," in *Wiesel SW, Weinstein JN, Herkowitz H, Dvorak J, Bell G (eds)The Lumbar Spine*, Saunders, Philadelphia, second ed., 1996.

[198] J. P. Hollowell, D. G. Vollmer, C. R. Wilson, F. A. Pintar, and N. Yoganandan, "Biomechanical analysis of thoracolumbar interbody constructs. How important is the endplate?," *Spine*, vol. 21, no. 9, pp. 1032–6, 1996.

[199] W. J. Elias, N. E. Simmons, G. J. Kaptain, J. B. Chadduck, and R. Whitehill, "Complications of posterior lumbar interbody fusion when using a titanium threaded cage device.," *Journal of neurosurgery*, vol. 93, no. 1 Suppl, pp. 45–52, 2000.

[200] S.-J. Liu, Z. Zou, J.-S. Pan, and S. Liao, "Mice endplate segmentation from micro-CT data through graph-based trabecula recognition.," *EURASIP Journal on Image and Video Processing*, no. 60, 2019.

[201] H. T. Hee, Y. J. Chuah, B. H. M. Tan, T. Setiobudi, and H. K. Wong, "Vascularization and morphological changes of the endplate after axial compression and distraction of the intervertebral disc," *Spine*, vol. 36, no. 7, pp. 505–511, 2011.

[202] M. Wojtkow, Z. Kiełbowicz, J. Bieżyński, and C. Pezowicz, "Quantitative and qualitative assessment of the impact of osteoporosis on endplate layers," *Biocybernetics and Biomedical Engineering*, vol. 39, no. 3, pp. 797–805, 2019.

[203] C. Ludtka, S. Schwan, A. Friedmann, W. Brehm, I. Wiesner, and F. Goehre, "Micro-CT evaluation of asymmetrical ovine intervertebral disc height loss from surgical approach," *European Spine Journal*, vol. 26, no. 8, pp. 2031–2037, 2017.

[204] M. Mageed, D. Berner, H. Jülke, C. Hohaus, W. Brehm, and K. Gerlach, "Morphometrical dimensions of the sheep thoracolumbar vertebrae as seen on digitised CT images," *Laboratory Animal Research*, vol. 29, no. 3, pp. 138–147, 2013.

[205] B. M. Carlson, "The Skeleton," in *The Human Body*, ch. 4, pp. 87–110, Academic Press, 2018.

[206] C. Hasler, C. M. Sprecher, and S. Milz, "Comparison of the immature sheep spine and the growing human spine: A spondylometric database for growth modulating research," *Spine*, vol. 35, no. 23, pp. E1262–E1272, 2010.

[207] H. Gray, "The classic collector's edition grays anatomy," in *Anatomy descriptive and surgical*, Gramercy, 1901.

[208] T. H. Smit, E. Schneider, and A. Odgaard, "Star length distribution: A volume-based concept for the characterization of structural anisotropy," *Journal of Microscopy*, vol. 191, no. 3, pp. 249–257, 1998.

[209] L. Salvagno and U. Albarella, "A morphometric system to distinguish sheep and goat postcranial bones," *PLoS ONE*, vol. 12, no. 6, 2017.

[210] N. H. Hart, S. Nimphius, T. Rantalainen, A. Ireland, A. Siafarikas, and R. U. Newton, "Mechanical basis of bone strength: Influence of bone material, bone structure and muscle action," *Journal of Musculoskeletal Neuronal Interactions*, vol. 17, no. 3, pp. 114–139, 2017.

[211] W. T. Edwards, "Structural features and thickness of the vertebral cortex in the thoracolumbar spine," *Spine (Phila Pa 1976)*, vol. 26, no. 2, pp. 218–25, 2001.

[212] H. M. Frost, "Wolff's Law and bone's structural adaptations to mechanical usage: an overview for clinicians.," *Angle Orthodontist*, vol. 64, no. 3, pp. 175–188, 1994.

[213] H. Inoue, "Three-dimensional architecture of lumbar intervertebrai discs," *Spine*, vol. 6, no. 2, pp. 139–146, 1981.

[214] A. O. Ortiz and R. Bordia, "Injury to the vertebral endplate-disk complex associated with osteoporotic vertebral compression fractures," *American Journal of Neuroradiology*, vol. 32, no. 1, pp. 125–130, 2011.

[215] G. C. Tender, "Caudal vertebral body fractures following lateral interbody fusion in nonosteoporotic patients," *Ochsner Journal*, vol. 14, no. 1, pp. 123–130, 2014.

[216] H. K. Genant, K. Engelke, T. Fuerst, C.-C. Glüer, S. Grampp, S. T. Harris, M. Jergas, T. Lang, Y. Lu, S. Majumdar, A. Mathur, and M. Takada, "Noninvasive assessment of bone mineral and structure: State of the art," *Journal of Bone and Mineral Research*, vol. 11, no. 6, pp. 707–730, 2009.

[217] F. Xie, H. Zhou, W. Zhao, and L. Huang, "A comparative study on the mechanical behavior of intervertebral disc using hyperelastic finite element model," *Technology and Health Care*, vol. 25, no. 1, pp. 177–187, 2017.

[218] S. Zahaf, B. Mansouri, A. Belarbi, and Z. Azari, "The Effects Induced by a Backpack Eccentric Load on the Spine of Children," *Biomedical Science and Engineering*, vol. 4, no. 1, pp. 6–22, 2016.

[219] N. A. Langrana, S. P. Kale, W. T. Edwards, C. K. Lee, and K. J. Kopacz, "Measurement and analyses of the effects of adjacent end plate curvatures on vertebral stresses," *Spine Journal*, vol. 6, no. 3, pp. 267–268, 2006.

[220] M. Hongo, E. Abe, Y. Shimada, H. Murai, N. Ishikawa, and K. Sato, "Surface strain distribution on thoracic and lumbar vertebrae under axial compression: The role in burst fractures," *Spine*, vol. 24, no. 12, pp. 1197–1202, 1999.

[221] Y. Masharawi, K. Salame, Y. Mirovsky, S. Peleg, G. Dar, N. Steinberg, and I. Hershkovitz, "Vertebral body shape variation in the thoracic and lumbar spine: Characterization of its asymmetry and wedging," *Clinical Anatomy*, vol. 21, no. 1, pp. 46–54, 2008.

[222] F. Zhao, P. Pollintine, B. D. Hole, P. Dolan, and M. A. Adams, "Discogenic origins of spinal instability," *Spine*, vol. 30, no. 23, pp. 2621–2630, 2005.

[223] K. A. Gillespie and J. P. Dickey, "Biomechanical role of lumbar spine ligaments in flexion and extension: Determination using a parallel linkage robot and a porcine model," *Spine*, vol. 29, no. 11, pp. 1208–1216, 2004.

[224] T. Asazuma, M. Nobuta, M. Sato, M. Yamagishi, K. Fujikawa, and W. A. Taylor, "Lumbar disc herniation associated with separation of the posterior ring apophysis: Analysis of five surgical cases and review of the literature," *Acta Neurochirurgica*, vol. 145, no. 6, pp. 461–6, 2003.

[225] I. Beggs and J. Addison, "Posterior vertebral rim fractures," *British Journal of Radiology*, vol. 71, no. 5, pp. 567–572, 1998.

[226] Z. Wu, W. Lei, Y. Hu, H. Wang, S. Wan, Z. Ma, H. Sang, S. Fu, and Y. Han, "Effect of ovariectomy on BMD, micro-architecture and biomechanics of cortical and cancellous bones in a sheep model," *Medical Engineering and Physics*, vol. 30, no. 9, pp. 1112–1118, 2008.

[227] M. R. Zarrinkalam, H. Beard, C. G. Schultz, and R. J. Moore, "Validation of the sheep as a large animal model for the study of vertebral osteoporosis," *European Spine Journal*, vol. 18, no. 2, pp. 244–253, 2009.

[228] P. Augat, S. Schorlemmer, C. Gohl, S. Iwabu, A. Ignatius, and L. Claes, "Glucocorticoid-treated sheep as a model for osteopenic trabecular bone in biomaterials research," *Journal of Biomedical Materials Research - Part A*, vol. 66, no. 3, pp. 457–462, 2003.

[229] P. Tranquilli Leali, C. Doria, A. Zachos, A. Ruggiu, F. Milia, and F. Barca, "Bone fragility: Current reviews and clinical features," *Clinical Cases in Mineral and Bone Metabolism*, vol. 6, no. 2, pp. 109–113, 2009.

[230] R. Oftadeh, M. Perez-Viloria, J. C. Villa-Camacho, A. Vaziri, and A. Nazarian, "Biomechanics and Mechanobiology of Trabecular Bone: A Review," *Journal of Biomechanical Engineering*, vol. 137, no. 1, pp. 210–215, 2015.

[231] K. S. Jensen, L. Mosekilde, and L. Mosekilde, "A model of vertebral trabecular bone architecture and its mechanical properties," *Bone*, vol. 11, no. 6, pp. 417–423, 1990.

[232] G. H. Bell, O. Dunbar, J. S. Beck, and A. Gibb, "Variations in strength of vertebrae with age and their relation to osteoporosis," *Calcified Tissue Research*, vol. 1, no. 1, pp. 75–86, 1967.

[233] S. D. Rockoff, E. Sweet, and J. Bleustein, "The relative contribution of trabecular and cortical bone to the strength of human lumbar vertebrae," *Calcified Tissue Research*, vol. 3, no. 2, pp. 163–175, 1969.

[234] N. L. Fazzalari, B. Manthey, and I. H. Parkinson, "Intervertebral disc disorganisation and its relationship to age adjusted vertebral body morphometry and vertebral bone architecture," *Anatomical Record*, vol. 262, no. 3, pp. 331–339, 2001.

[235] O. D. Kennedy, O. Brennan, S. M. Rackard, F. J. O'Brien, D. Taylor, and T. C. Lee, "Variation of trabecular microarchitectural parameters in cranial, caudal and mid-vertebral regions of the ovine L3 vertebra," *Journal of Anatomy*, vol. 214, no. 5, pp. 729–735, 2009.

[236] S. A. Rodrigues, A. Thambyah, and N. D. Broom, "How maturity influences annulus-endplate integration in the ovine intervertebral disc: a micro- and ultra-structural study," *Journal of Anatomy*, vol. 230, no. 1, pp. 152–164, 2017.

[237] X. Wu and W. Ma, "Posterior lumbar ring apophysis fracture.," *Orthopaedic surgery*, vol. 3, no. 1, pp. 72–77, 2011.

[238] M. A. Adams and P. Dolan, "Intervertebral disc degeneration: Evidence for two distinct phenotypes," *Journal of Anatomy*, vol. 221, no. 6, pp. 497–506, 2012.

[239] L. M. Benneker, P. F. Heini, M. Alini, S. E. Anderson, and K. Ito, "2004 Young investigator award winner: Vertebral endplate marrow contact channel occlusions and intervertebral disc degeneration," *Spine*, vol. 30, no. 2, pp. 167–173, 2005.

[240] B. D. Metscher, "MicroCT for developmental biology: A versatile tool for high-contrast 3D imaging at histological resolutions," *Developmental Dynamics*, vol. 238, no. 3, pp. 632–640, 2009.

[241] B. D. Metscher, "MicroCT for comparative morphology: Simple staining methods allow high-contrast 3D imaging of diverse non-mineralized animal tissues," *BMC Physiology*, vol. 9, no. 11, 2009.

[242] P. Heimel, N. V. Swiadek, P. Slezak, M. Kerbl, C. Schneider, S. Nürnberger, H. Redl, A. H. Teuschl, and D. Hercher, "Iodine-Enhanced Micro-CT Imaging of Soft Tissue on the Example of Peripheral Nerve Regeneration," *Contrast Media and Molecular Imaging*, no. 3, pp. 1–15, 2019.

[243] F. Manning, *The vertebral endplate: its structure and function*. PhD thesis, University of Exeter, 2019.

[244] H. Xu, Y. Wang, H. Jin, D. Xu, J. Xuan, J. Chen, A. Goswami, Z. Tao, F. Zhou, X. Zhang, and X. Wang, "A novel micro-CT-based method to monitor the morphology of blood vessels in the rabbit endplate," *European Spine Journal*, vol. 26, no. 1, pp. 221–227, 2017.

[245] S. Roberts, B. Caterson, H. Evans, and S. M. Eisenstein, "Proteoglycan components of the intervertebral disc and cartilage endplate: an immunolocalization study of animal and human tissues," *The Histochemical Journal*, vol. 26, no. 5, pp. 402–411, 1994.

[246] K. Wade, "Vertebral Endplates," in *Biomechanics of the Spine*, ch. 8, pp. 125–140, Academic Press, 2018.

[247] C. C. Shu, M. M. Smith, S. M. Smith, A. J. Dart, C. B. Little, and J. Melrose, "A histopathological scheme for the quantitative scoring of intervertebral disc degeneration and the therapeutic utility of adult mesenchymal stem cells for intervertebral disc regeneration," *International Journal of Molecular Sciences*, vol. 18, no. 5, p. 1049, 2017.

[248] P. M. Gignac, N. J. Kley, J. A. Clarke, M. W. Colbert, A. C. Morhardt, D. Cerio, I. N. Cost, P. G. Cox, J. D. Daza, C. M. Early, M. S. Echols, R. M. Henkelman, A. N. Herdina, C. M. Holliday, Z. Li, K. Mahlow, S. Merchant, J. Müller, C. P. Orsbon, D. J. Paluh, M. L. Thies, H. P. Tsai, and L. M. Witmer, "Diffusible iodine-based contrast-enhanced computed tomography (diceCT): An emerging tool for rapid, high-resolution, 3-D imaging of metazoan soft tissues," *Journal of Anatomy*, vol. 228, no. 6, pp. 889–909, 2016.

[249] K. Degenhardt, A. C. Wright, D. Horng, A. Padmanabhan, and J. A. Epstein, "Rapid 3D phenotyping of cardiovascular development in mouse embryos by micro-CT with iodine staining," *Circulation: Cardiovascular Imaging*, vol. 3, no. 3, pp. 314–322, 2010.

[250] R. I. Lee and P. D. White, "A clinical study of the coagulation time of blood," *The American Journal of the Medical Sciences*, vol. 145, no. 4, pp. 495–503, 1913.

[251] S. Dekker, D. van Geemen, A. J. van den Bogaerdt, A. Driessen-Mol, E. Aikawa, and A. I. Smits, "Sheep-Specific Immunohistochemical Panel for the Evaluation of Regenerative and Inflammatory Processes in Tissue-Engineered Heart Valves," *Frontiers in Cardiovascular Medicine*, vol. 5, p. 105, 2018.

[252] M. K. Lichtenberg, "Lumen Shape: A new measurement to consider in the treatment of iliofemoral venous outflow obstruction," *Supplement to Endovascular Today Europe*, vol. 6, no. 5, pp. 9–12, 2018.

[253] M. C. Hsu and M. Itkin, "Lymphatic Anatomy," *Techniques in Vascular and Interventional Radiology*, vol. 19, no. 4, pp. 247–254, 2016.

[254] J. H. Van Dieën, H. Weinans, and H. M. Toussaint, "Fractures of the lumbar vertebral endplate in the etiology of low back pain: A hypothesis on the causative role of spinal compression in aspecific low back pain," *Medical Hypotheses*, vol. 53, no. 3, pp. 246–252, 1999.

[255] K. Luoma, H. Riihimäki, R. Luukkonen, R. Raininko, E. Viikari-Juntura, and A. Lamminen, "Low back pain in relation to lumbar disc degeneration," *Spine*, vol. 25, no. 4, pp. 487–492, 2000.

[256] Y. Kotani, B. W. Cunningham, K. Abumi, A. E. Dmitriev, M. Ito, N. Hu, Y. Shikinami, P. C. McAfee, and A. Minami, "Multidirectional flexibility analysis of cervical artificial disc reconstruction: in vitro human cadaveric spine model.," *Journal of neurosurgery. Spine*, vol. 2, no. 2, pp. 188–194, 2005.

[257] J. Urrutia, P. Besa, M. Campos, P. Cikutovic, M. Cabezon, M. Molina, and J. P. Cruz, "The Pfirrmann classification of lumbar intervertebral disc degeneration: an independent inter- and intra-observer agreement assessment," *European Spine Journal*, vol. 25, no. 9, pp. 2728–2733, 2016.

[258] K. Yamada, A. Suzuki, S. Takahashi, H. Yasuda, M. Tada, Y. Sugioka, T. Okano, T. Koike, and H. Nakamura, "MRI evaluation of lumbar endplate and facet erosion in rheumatoid arthritis," *Journal of Spinal Disorders and Techniques*, vol. 27, no. 4, pp. 128–135, 2014.

[259] S. M. Kokkonen, M. Kurunlahti, O. Tervonen, E. Ilkko, and H. Vanharanta, "Endplate degeneration observed on magnetic resonance imaging of the lumbar spine: Correlation with pain provocation and disc changes observed on computed tomography diskography," *Spine*, vol. 27, no. 20, pp. 2274–2278, 2002.

[260] T. S. Jensen, P. Kjaer, L. Korsholm, T. Bendix, J. S. Sorensen, C. Manniche, and C. Leboeuf-Yde, "Predictors of new vertebral endplate signal (Modic) changes in the general population," *European Spine Journal*, vol. 19, no. 1, pp. 129–135, 2010.

[261] S. M. Moon, J. H. Yoder, A. C. Wright, L. J. Smith, E. J. Vresilovic, and D. M. Elliott, "Evaluation of intervertebral disc cartilaginous endplate structure using magnetic resonance imaging," *European Spine Journal*, vol. 22, no. 8, pp. 1820–1828, 2013.

[262] J. F. DeLucca, J. M. Peloquin, L. J. Smith, A. C. Wright, E. J. Vresilovic, and D. M. Elliott, "MRI quantification of human spine cartilage endplate geometry: Comparison with age, degeneration, level, and disc geometry," *Journal of Orthopaedic Research*, vol. 34, no. 8, pp. 1410–1417, 2016.

[263] H. Chen, X. Zhou, H. Fujita, M. Onozuka, and K. Y. Kubo, "Age-related changes in trabecular and cortical bone microstructure," *International Journal of Endocrinology*, pp. 1–9, 2013.

[264] P. Pietschmann, M. Rauner, W. Sipos, and K. Kerschan-Schindl, "Osteoporosis: An age-related and gender-specific disease - A mini-review," *Gerontology*, vol. 55, no. 1, pp. 3–12, 2009.

[265] J. Jasien, C. M. Daimon, S. Maudsley, B. K. Shapiro, and B. Martin, "Aging and bone health in individuals with developmental disabilities," *International Journal of Endocrinology*, pp. 1–10, 2012.

[266] A. G. Bruno, K. E. Broe, X. Zhang, E. J. Samelson, C. A. Meng, R. Manoharan, J. D'Agostino, L. A. Cupples, D. P. Kiel, and M. L. Bouxsein, "Vertebral size, bone density, and strength in men and women matched for age and areal spine BMD," *Journal of Bone and Mineral Research*, vol. 29, no. 3, pp. 562–569, 2014.

[267] N. S. Gezer, A. Balcı, O. Kalemci, N. Köremezli, I. Başara Akın, and K. Ur, "Vertebral body bone mineral density in patients with lumbar spondylolysis: A quantitative CT study," *Diagnostic and Interventional Radiology*, vol. 23, no. 5, pp. 385–389, 2017.

[268] L. Xu, B. Chu, Y. Feng, F. Xu, and Y. F. Zou, "Modic changes in lumbar spine: Prevalence and distribution patterns of end plate oedema and end plate sclerosis," *British Journal of Radiology*, vol. 89, no. 1060, p. 20150650, 2016.

[269] M. T. Crockett, B. S. Kelly, S. Van Baarsel, and E. C. Kavanagh, "Modic type 1 vertebral endplate changes: Injury, inflammation, or infection?," *American Journal of Roentgenology*, vol. 209, no. 1, pp. 167–170, 2017.

[270] R. Hardy and M. S. Cooper, "Bone loss in inflammatory disorders," *Journal of Endocrinology*, vol. 201, no. 3, pp. 309–320, 2009.

[271] A. M. Briggs, P. B. O'Sullivan, D. Foulner, and J. D. Wark, "Vertebral bone mineral measures and psychological wellbeing among individuals with Modic changes," *Clinical Medicine Insights: Case Reports*, vol. 5, no. 1, pp. 35–41, 2012.

[272] S. Teboul-Coré, C. Roux, D. Borderie, S. Kolta, M. M. Lefèvre-Colau, S. Poiraudeau, F. Rannou, and C. Nguyen, "Bone mineral density and bone remodeling markers in chronic low back pain patients with active discopathy: A case-control exploratory study," *PLoS ONE*, vol. 13, no. 6, p. e0196536, 2018.

[273] C. Sun, H. Wang, J. Jiang, F. Lu, X. Ma, and X. Xia, "The Pathology of Type II Modic Changes: Fat Deposition or Osteosclerosis? A Study Using CT Scan," *BioMed Research International*, pp. 1–6, 2018.

[274] H. B. Albert, P. Kjaer, T. S. Jensen, J. S. Sorensen, T. Bendix, and C. Manniche, "Modic changes, possible causes and relation to low back pain," *Medical Hypotheses*, vol. 70, no. 2, pp. 361–368, 2008.

[275] M. Rade, J. Määttä, M. Freidin, O. Airaksinen, J. Karppinen, and F. Williams, "Vertebral Endplate Defect as Initiating Factor in Intervertebral Disc Degeneration; Strong Association between Endplate Defect and Disc Degeneration in the General Population," *Spine*, vol. 43, no. 6, pp. 412–419, 2017.

[276] I. Braithwaite, J. White, A. Saifuddin, P. Renton, and B. A. Taylor, "Vertebral endplate (Modic) changes on lumbar spine MRI: Correlation with pain reproduction at lumbar discography," *European Spine Journal*, vol. 7, no. 5, pp. 363–368, 1998.

[277] I. K. Ashton, S. Roberts, D. C. Jaffray, J. M. Polak, and S. M. Eisenstein, "Neuropeptides in the human intervertebral disc," *Journal of Orthopaedic Research*, vol. 12, no. 2, pp. 186–192, 1994.

[278] R. H. Pearce, B. J. Grimmer, and M. E. Adams, "Degeneration and the chemical composition of the human lumbar intervertebral disc," *Journal of Orthopaedic Research*, vol. 5, no. 2, pp. 198–205, 1987.

[279] E. Perilli, I. H. Parkinson, L. H. Truong, K. C. Chong, N. L. Fazzalari, and O. L. Osti, "Modic (endplate) changes in the lumbar spine: bone micro-architecture and remodelling," *European Spine Journal*, vol. 24, no. 9, pp. 1926–1934, 2015.

[280] Y. Kawaguchi, H. Matsuno, M. Kanamori, H. Ishihara, K. Ohmori, and T. Kimura, "Radiologic findings of the lumbar spine in patients with rheumatoid arthritis, and a review of pathologic mechanisms," *Journal of Spinal Disorders and Techniques*, vol. 16, no. 1, pp. 38–43, 2003.

[281] T. M. Emch and M. T. Modic, "Imaging of lumbar degenerative disk disease: History and current state," *Skeletal Radiology*, vol. 40, no. 9, pp. 1175–1189, 2011.

[282] L. P. Yu, W. W. Qian, G. Y. Yin, Y. X. Ren, and Z. Y. Hu, "MRI Assessment of Lumbar Intervertebral Disc Degeneration with Lumbar Degenerative Disease Using the Pfirrmann Grading Systems," *PLoS ONE*, vol. 7, no. 12, p. 48074, 2012.

[283] T. Toyone, K. Takahashi, H. Kitahara, M. Yamagata, M. Murakami, and H. Moriya, "Vertebral bone-marrow changes in degenerative lumbar disc disease: An MRI study of 74 patients with low back pain," *Journal of Bone and Joint Surgery - Series B*, vol. 76, no. 5, pp. 757–764, 1994.

[284] J. F. Griffith, Y. X. J. Wang, G. E. Antonio, K. C. Choi, A. Yu, A. T. Ahuja, and P. C. Leung, "Modified Pfirrmann grading system for lumbar intervertebral disc degeneration," *Spine*, vol. 32, no. 24, pp. 708–712, 2007.

[285] F. Fayad, M. M. Lefevre-Colau, J. L. Drapé, A. Feydy, N. Chemla, N. Quintéro, F. Rannou, S. Poiraudeau, J. Fermanian, and M. Revel, "Reliability of a modified Modic classification of bone marrow changes in lumbar spine MRI," *Joint Bone Spine*, vol. 76, no. 3, pp. 289–289, 2009.

[286] R. J. Moore, "The vertebral endplate: Disc degeneration, disc regeneration," *European Spine Journal*, vol. 15, no. 3, pp. 333–337, 2006.

[287] R. R. Patel, A. Noshchenko, R. D. Carpenter, T. Baldini, C. P. Frick, V. V. Patel, and C. M. Yakacki, "Evaluation and Prediction of Human Lumbar Vertebrae Endplate Mechanical Properties Using Indentation and Computed Tomography," *Journal of Biomechanical Engineering*, vol. 140, no. 10, pp. 111–119, 2018.

[288] J. P. Grant, T. R. Oxland, M. F. Dvorak, and C. G. Fisher, "The effects of bone density and disc degeneration on the structural property distributions in the lower lumbar vertebral endplates," *Journal of Orthopaedic Research*, vol. 20, no. 5, pp. 115–120, 2002.

[289] E. Dall'Ara, C. Karl, G. Mazza, G. Franzoso, P. Vena, M. Pretterklieber, D. Pahr, and P. Zysset, "Tissue properties of the human vertebral body sub-structures evaluated by means of microindentation," *Journal of the Mechanical Behavior of Biomedical Materials*, vol. 25, no. 1, pp. 23–32, 2013.

[290] A. Noshchenko, A. Plaseied, V. V. Patel, E. Burger, T. Baldini, and L. Yun, "Correlation of vertebral strength topography with 3-dimensional computed tomographic structure," *Spine*, vol. 38, no. 4, pp. 339–349, 2013.

[291] P. Birner, A. Obermair, M. Schindl, H. Kowalski, G. Breitenecker, and G. Oberhuber, "Selective immunohistochemical staining of blood and lymphatic vessels reveals independent prognostic influence of blood and lymphatic vessel invasion in early-stage cervical cancer," *Clinical Cancer Research*, vol. 7, no. 1, pp. 93–97, 2001.

[292] L.-L. Kong, N.-Z. Yang, L.-H. Shi, G.-H. Zhao, W. Zhou, Q. Ding, M.-H. Wang, and Y.-S. Zhang, "The optimum marker for the detection of lymphatic vessels," *Molecular and Clinical Oncology*, vol. 7, no. 4, pp. 515–520, 2017.

[293] E. Gray, J. Hogwood, and B. Mulloy, "The anticoagulant and antithrombotic mechanisms of heparin," *Handbook of Experimental Pharmacology*, vol. 207, pp. 43–61, 2012.

[294] G. Banfi, G. L. Salvagno, and G. Lippi, "The role of ethylenediamine tetraacetic acid (EDTA) as in vitro anticoagulant for diagnostic purposes," *Clinical Chemistry and Laboratory Medicine*, vol. 45, no. 5, pp. 565–576, 2007.

[295] N. Bessonov, A. Sequeira, S. Simakov, Y. Vassilevskii, and V. Volpert, "Methods of Blood Flow Modelling," *Mathematical Modelling of Natural Phenomena*, vol. 11, no. 1, pp. 1–25, 2016.

[296] A. G. Hadjipavlou, M. N. Tzermiadianos, N. Bogduk, and M. R. Zindrick, "The pathophysiology of disc degeneration: A critical review," *Journal of Bone and Joint Surgery - Series B*, vol. 90, no. 10, pp. 1261–1270, 2008.